

Patricia Hernández López

In silico analysis of the process of atheroma plaque formation and growth in arteries

Director/es

Peña Baquedano, Estefanía
Cilla Hernández, Myriam

<http://zaguan.unizar.es/collection/Tesis>



Universidad
Zaragoza

Tesis Doctoral

IN SILICO ANALYSIS OF THE PROCESS OF
ATHEROMA PLAQUE FORMATION AND GROWTH
IN ARTERIES

Autor

Patricia Hernández López

Director/es

Peña Baquedano, Estefanía
Cilla Hernández, Myriam

UNIVERSIDAD DE ZARAGOZA
Escuela de Doctorado

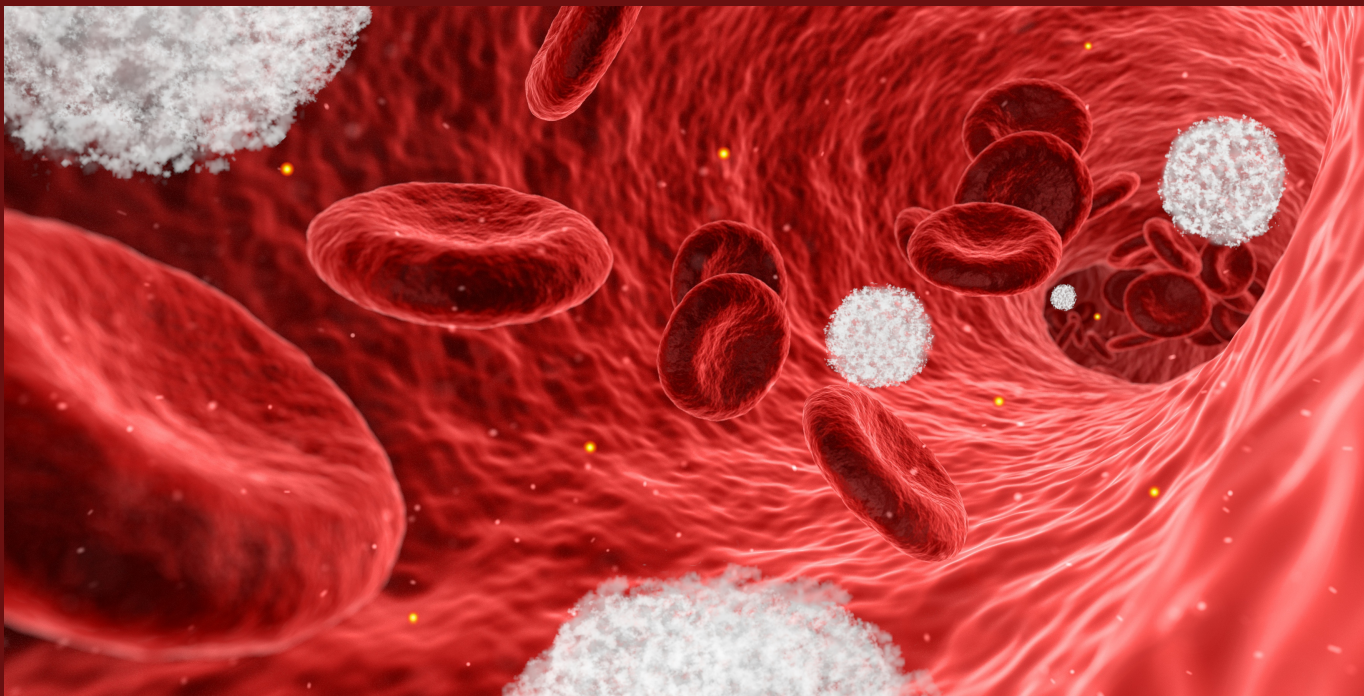
Programa de Doctorado en Ingeniería Mecánica

2023

In silico analysis of the process of atheroma plaque formation and growth in arteries

PhD thesis by

Patricia Hernández López



Doctoral advisors

Dr. Estefanía Peña Baquedano

Dr. Myriam Cilla Hernández

PhD Programme in Mechanical Engineering

May 2023

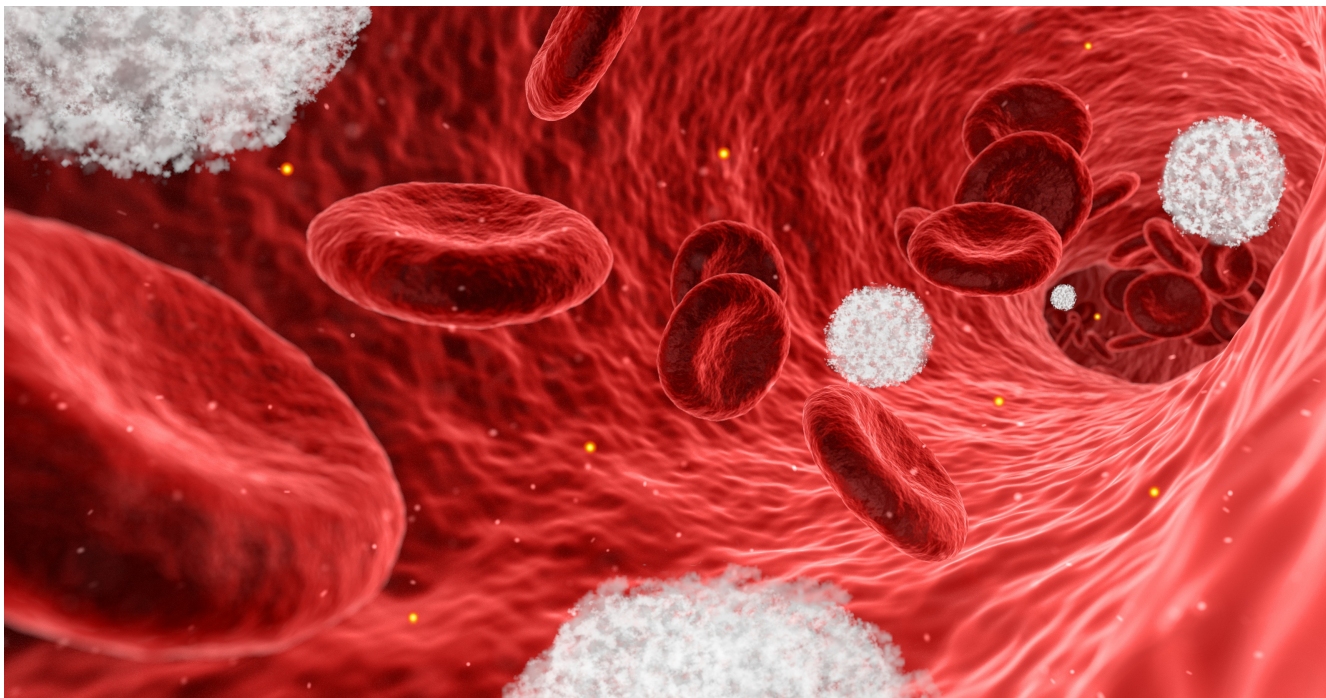


Universidad
Zaragoza

In silico analysis of the process of atheroma plaque formation and growth in arteries

PhD thesis by

Patricia Hernández López



Doctoral advisors

Dr. Estefanía Peña Baquedano

Dr. Myriam Cilla Hernández

PhD Programme in **Mechanical Engineering**

May 2023



Universidad
Zaragoza

A mis padres
A mi hermano
A Adrián

Agradecimientos

En primer lugar, me gustaría agradecer a mis directoras, Fany y Myriam, la oportunidad, el apoyo y la atención que me han dado, guiándome a lo largo de todo este camino. Hace ya 9 años entré en el despacho de Fany para comenzar mi Trabajo Final de Grado, y en ese momento no podía ni imaginar cuánto me iba a gustar todo lo relacionado con la biomecánica. Muchas gracias por la confianza depositada en mí desde entonces. También querría agradecer a Miguel Ángel, mi director en la sombra, toda la ayuda, orientación y comprensión. Me gustaría también dar las gracias a Mauro, por darme la oportunidad de realizar mi estancia de investigación con él, por su amabilidad y buenos consejos.

Quiero darle las gracias también a Itziar, que empezó y termina conmigo esta aventura, por su alegría contagiosa y por ser también la mejor compañera de habitación en todos los congresos. A Nico el haber confiado en mí como co-directora de su Trabajo Final de Máster cuando yo todavía estaba empezando este camino. Muchas gracias a Ricardo, por todo el apoyo, la ayuda y los ánimos que me ha brindado durante este año y medio desde su comienzo de Tesis. Gracias también a Álvaro por transmitirme su templanza en los momentos difíciles, y por todas sus bromas que han hecho más fácil este camino. También quiero dar las gracias a todos mis otros compañeros que han estado conmigo durante todo este tiempo, por hacerme más ameno mi tiempo durante estos años. Algunos de ellos se han convertido también en mis amigos después de muchas aventuras vividas juntos. Esta Tesis no habría sido lo mismo sin ellos.

A mis amigos que, aunque a veces no entienden todo lo que hago me apoyan siempre y me animan en todo lo que decido hacer. Por último, querría agradecerles a mis padres, Begoña y Francisco, su esfuerzo por proporcionarnos siempre lo mejor tanto a mi hermano como a mí, por su apoyo incondicional y por hacer de mí la persona que soy hoy en día. A mi hermano, Fran, por su complicidad y por su franqueza que tanto me ayuda. A Adrián, que apareció en mi vida haciéndome reír y no ha parado de hacerlo desde entonces. Muchas gracias por estar siempre a mi lado ofreciéndome tu apoyo y ánimo y compartiendo todos tus logros conmigo. Esta Tesis también tiene una parte de todos vosotros.

Abstract

Cardiovascular diseases are currently one of the main causes of mortality globally. They include atherosclerosis disease, which is a pathology that consists of the development of lipid deposits in the arterial wall, called atheroma plaques, that cause a reduction in the space available for blood circulation. Depending on the artery in which this disease is developed, it can lead to severe consequences, such as ischaemia or stroke. However, the process by which these plaques are developed is not completely understood, so any advances in the understanding of this process will have an important relevance.

Therefore, this thesis studies the process of atheroma plaques formation in arteries through the development of a mechanobiological model, which is applied to carotid arteries models, with the aim of predicting the areas of plaque growth, as well as their development.

Since there are different types of plaque according to their vulnerability, a model of vulnerable atheroma plaques in an axisymmetric geometry has been developed and considered as the reference model. Additionally, by modifying some of the equations of this reference model, a non-vulnerable plaques growth model has also been developed. Due to the large variability in the values of the parameters involved in the inflammatory process of the arterial wall found in the literature, a sensitivity analysis of the model to variations in these parameters has been performed. With this sensitivity analysis, it has been concluded that the parameters of the model have a large influence in the results.

The validation of the vulnerable plaque model has been performed with three dimensional patient-specific geometries, which correspond to bifurcations of the carotid arteries of four pathological patients and one healthy volunteer. To perform this validation, the area of the real arteries with atheroma plaque was artificially repaired to obtain the equivalent healthy geometries on which the mechanobiological model of plaque growth has been simulated. Finally, the simulated plaques in each of the geometries have been compared with the real plaques of the patients, also validating that the geometry of the healthy patient does not develop any atheroma plaque. In addition, the validation of the non-vulnerable model has been carried out attending to the composition of the plaques by comparison with real images of atheroma plaques obtained by intravascular ultrasound of the literature.

In addition, since it is widely accepted that the initiation of atheroma plaques depends on some haemodynamic factors, the influence of the two most commonly used stimuli

(TAWSS and OSI) has been analysed on the real patient geometries. A new stimulus that combines the action of both stimuli has been developed and also modelled. It has been observed that this new stimulus predicts the resulting plaques more accurately than the use of only one of the two stimuli commonly used in the literature, because it combines the strengths of both of them.

On the other hand, it has been observed that some of the plaques present in real patients were not predicted by any of the haemodynamic stimuli analysed, which is caused, as observed in the obtained results, by not considering the fluid-structure interaction of the blood flow with the arterial wall. For this reason, two different models of fluid-structure interaction have been performed, considering different properties for endothelial repair produced by changes in the haemodynamic stimuli caused by plaque growth. Finally, it has been concluded that the effect of fluid-structure interaction on atheroma plaques cannot be neglected.

During this Thesis, two mechanobiological models capable of predict atheroma plaques development attending to their vulnerability have been developed and validated. This could contribute to improve the knowledge and diagnosis of the disease in clinical practice in the future.

Resumen

Actualmente, las enfermedades cardiovasculares son una de las principales causas de mortalidad a nivel global. Entre ellas se encuentra la aterosclerosis, una patología que consiste en el desarrollo de depósitos lipídicos en la pared arterial, denominados placas de ateroma, que causan una reducción del espacio disponible para la circulación de la sangre. Dicha patología puede derivar en consecuencias muy graves, dependiendo de la arteria en la cual se desarrolle, como isquemias o infartos. Sin embargo, el proceso de desarrollo de estas placas todavía no se conoce completamente, por lo cual cualquier avance en el conocimiento del proceso de formación de placas de ateroma resulta de una gran importancia.

Por ello, a lo largo de esta Tesis se estudia el proceso de formación de placas de ateroma en arterias mediante el desarrollo de un modelo mecanobiológico, el cual se aplica a diferentes modelos computacionales de arteria carótida, con el objetivo de predecir las zonas de crecimiento de placas, así como su desarrollo.

Dado que existen diferentes tipos de placa atendiendo a su vulnerabilidad, se ha desarrollado un modelo de placa de ateroma vulnerable en una geometría axisimétrica, considerado como modelo de referencia. Adicionalmente, mediante modificaciones en algunas de las ecuaciones del modelo de referencia, se ha desarrollado también un modelo de crecimiento de placas no vulnerables. Debido a la gran variabilidad de los valores de los parámetros involucrados en el proceso inflamatorio de la pared arterial que se ha encontrado en la literatura, se ha realizado un análisis de sensibilidad del modelo ante variaciones en los mismos. Con este análisis de sensibilidad se ha concluido que los parámetros del modelo tienen una gran influencia en los resultados obtenidos.

La validación del modelo de placa vulnerable se ha realizado con geometrías en tres dimensiones de paciente específico, las cuales corresponden a bifurcaciones de arteria carótida de cuatro pacientes patológicos y un voluntario sano. Para realizar dicha validación, se ha reparado artificialmente la zona de las arterias reales con presencia de placa para obtener las geometrías sanas equivalentes sobre las cuales se ha aplicado el modelo mecanobiológico de crecimiento de placa. Finalmente, se han contrastado las placas obtenidas mediante la simulación en cada una de las geometrías con las placas reales de los pacientes, comprobando además que la geometría correspondiente al paciente sano no desarrolla placa de ateroma. Por otra parte, la validación del modelo de placa no vulnerable se ha realizado atendiendo a la composición de las placas obtenidas mediante su

comparación con imágenes reales de placas de ateroma de la literatura, obtenidas mediante ultrasonido intravascular.

Dado que está ampliamente aceptado que el inicio de las placas de ateroma depende de factores hemodinámicos, se ha analizado la influencia sobre las geometrías de paciente real de los dos estímulos más empleados (TAWSS y OSI), realizando también un modelo con un nuevo estímulo que combina la acción de ambos. Se puede concluir que este nuevo estímulo predice las placas resultantes de una manera más precisa que el uso de únicamente uno de los dos estímulos empleados comúnmente en la literatura, debido a que combina las fortalezas de ambos.

Por otra parte, se ha observado que algunas de las placas presentes en los pacientes reales no se lograban predecir con ninguno de los estímulos hemodinámicos analizados, lo cual se debe, como se observa en los resultados obtenidos, a que no se considera una actualización de las variables hemodinámicas durante el proceso de crecimiento. Por ello, se han realizado dos modelos diferentes de interacción fluido-estructura, considerando distintas propiedades para la reparación endotelial producida por los cambios en los estímulos hemodinámicos ocasionados por el crecimiento de la placa. Finalmente, se concluye que el efecto de la actualización de las variables hemodinámicas sobre las placas de ateroma no puede ser despreciado.

A lo largo de esta Tesis se han desarrollado dos modelos mecanobiológicos capaces de predecir el crecimiento de placas de ateroma, atendiendo a su vulnerabilidad. Esto podría contribuir en el futuro a mejorar el conocimiento y diagnóstico de la enfermedad en la práctica clínica.



Table of contents

Contents

Thesis	1
0 Nomenclature	3
0.1 Abbreviations	3
0.2 Subscripts	4
0.3 Nomenclature list	5
0.4 Nomenclature list: Greek alphabet	7
0.5 Mathematical symbols	8
1 Introduction	9
1.1 General Overview and motivation	9
1.2 Arteries and their composition	11
1.2.1 Carotid arteries	13
1.3 Atherosclerosis	14
1.3.1 Composition of atheroma plaques	16
1.3.2 Types of atheroma plaques	16
1.4 State of the art	17
1.5 Objectives	23
1.6 Thesis structure	23
2 Mathematical modelling	25
2.1 General Overview	25
2.2 Blood flow in the lumen	26
2.2.1 Boundary conditions	27
2.3 Plasma flow across the arterial wall	28
2.3.1 Boundary conditions	34
2.4 Substances flow along the lumen	35

2.4.1	Boundary conditions	36
2.5	Inflammatory process of the arterial wall	37
2.5.1	Evolution of LDL Concentration	38
2.5.2	Evolution of Oxidised LDL Concentration	40
2.5.3	Evolution of Monocyte Concentration	41
2.5.4	Evolution of Macrophage Concentration	42
2.5.5	Evolution of Cytokine Concentration	42
2.5.6	Evolution of Contractile Smooth Muscle Cell Concentration	43
2.5.7	Evolution of Synthetic Smooth Muscle Cell Concentration	43
2.5.8	Evolution of Foam Cell Concentration	43
2.5.9	Evolution of Collagen Fibres	44
2.5.10	Boundary conditions	46
2.6	Arterial wall mechanical model	49
2.6.1	Boundary conditions	49
2.7	Plaque initiation and growth	49
2.8	Summary of the improvements	50
2.8.1	Substances diffusion coefficients	51
2.8.2	Plasma flow	51
2.8.3	LDL molecules	52
2.8.4	Monocyte	53
2.8.5	Macrophage	54
2.8.6	Contractile Smooth Muscle Cells	54
2.8.7	Synthetic Smooth Muscle Cells	55
2.8.8	Foam Cells	56
2.8.9	Conversion parameters	56
3	Two-dimensional axisymmetric model	59
3.1	General Overview	59
3.2	Geometry	59
3.3	Reference vulnerable model	61
3.3.1	Governing equations	61
3.3.2	Boundary conditions	61
3.3.3	Haemodynamical stimulus	62
3.3.4	Numerical methods	62
3.3.5	Sensitivity analysis of the mesh	63
3.3.6	Analysis of the geometry length	69

3.3.7	Vulnerable plaque model results	70
3.4	Mathematical modelling for non-vulnerable plaques	77
3.4.1	Governing equations	77
3.4.2	Non-vulnerable plaque model results	79
3.4.3	Validation of the non-vulnerable model	81
3.5	Vulnerable vs non-vulnerable plaque models	82
3.6	Sensitivity analysis of the parameters of the model	85
3.7	Conclusions	92
4	Effects of haemodynamical stimuli in patient-specific geometries	95
4.1	General Overview	95
4.2	Geometries	96
4.3	Boundary conditions	101
4.3.1	Murray's law	101
4.3.2	LDL and monocyte concentration in lumen	103
4.4	Haemodynamical stimuli	103
4.5	Numerical methods	109
4.6	Mesh sensitivity analysis	110
4.7	Analysis of the number of cardiac cycles	116
4.8	Results	116
4.8.1	Healthy geometry results	118
4.8.2	Pathological geometries results	119
4.8.3	Plaque growth updating the geometry	132
4.9	Conclusions	133
5	Fluid-Structure Interaction analysis	137
5.1	General Overview	137
5.2	Geometry	138
5.3	Boundary conditions of transient blood flow	138
5.4	Haemodynamical stimulus	139
5.5	Reference model with transient blood flow	139
5.5.1	Numerical methods	140
5.5.2	Sensitivity analysis of the mesh	140
5.5.3	Results	144
5.6	Fluid-Structure Interaction	144
5.6.1	Numerical methods	145
5.6.2	Model with endothelial repair	147
5.6.3	Model without endothelial repair	150
5.7	Comparison of the results	153
5.8	Conclusions	155

6	Conclusions	157
6.1	General overview	157
6.2	General conclusions	157
6.3	Thesis contributions	161
6.4	Future research lines	162
6.5	Publications and other contributions	163
6.5.1	Journal contributions	163
6.5.2	Communications in scientific conferences	164
7	Conclusiones	169
7.1	Introducción	169
7.2	Conclusiones finales	169
7.3	Contribuciones	173
7.4	Líneas de trabajo futuras	174
7.5	Publicaciones y otras contribuciones	176
7.5.1	Publicaciones en revistas científicas	176
7.5.2	Presentaciones en congresos científicos	176
	Appendices	181
A	Parameters	183
A.1	Blood flow	183
A.2	Plasma flow	183
A.2.1	Physic properties	183
A.2.2	Dimensions	184
A.2.3	Pressures	185
A.3	Substances flow along lumen	185
A.4	Inflammatory process	185
A.4.1	Substances properties and dimensions	185
A.4.2	Initial and threshold concentrations	189
A.4.3	Lumen-Arterial wall flows	190
A.4.4	Parameters of reactive terms	190
A.4.5	Conversion parameters	192
A.5	Arterial wall mechanical model	193
A.6	Plaque growth	193
B	Darcy's law for plasma flow	195
	Bibliography	199

List of Figures

1.1	Percentages of deaths in 2019 due to the leading 10 causes	9
1.2	Millions of deaths due to the top 10 causes of mortality in the years 2000 and 2019	10
1.3	Structure of the arterial wall	12
1.4	Scheme of the right carotid artery	13
1.5	Different shapes of endothelial cells	14
1.6	Substances considered in the computational model of atherosclerosis developed in this Thesis	15
1.7	Process of atheroma plaques formation	16
2.1	Workflow of the computational process for the base model.	25
2.2	Fluid classification chart	26
2.3	Structure of the arterial wall	29
2.4	Correlation between Shape Index and Wall Shear Stress	31
2.5	Distribution of leaky cells and leaky junctions in the endothelium	33
2.6	Evolution of monocyte concentration	53
2.7	Evolution of the SMCs differentiation from the contractile phenotype into the synthetic one	55
3.1	Two-dimensional axisymmetric geometry	60
3.2	LDL concentration profile limits of the mesh 1	68
3.3	LDL concentration profile limits of the mesh 2	68
3.4	Details of the lumen and arterial wall meshes	69
3.5	Velocity of the blood flow for the axisymmetric model in two dimensions	71
3.6	Streamlines of blood flow downstream the obstacle plaque	71
3.7	WSS profile along the hole geometry	72
3.8	Distribution of LDL and monocyte concentrations in the lumen of the artery	72
3.9	Velocity of plasma in the arterial wall	73

3.10	Flows of LDL and monocytes across the endothelium	73
3.11	LDL distribution obtained in a healthy area of the geometry	74
3.12	Arterial wall thickness increase and concentrations of all substances obtained with the reference vulnerable model for a simulation time of 10 years	75
3.13	Volumetric growth of the plaque due to FCs, CSMCs, collagen fibres and total for a total time of 10 years of the reference vulnerable model	76
3.14	Volumetric growth of the plaque due to FCs, CSMCs and collagen fibres with the reference model without threshold of SSMCs and reducing pss to $0.0202 d^{-1}$ and r_{apop} to $8.011 \cdot 10^{-8} s^{-1}$	78
3.15	Volumetric growth of the plaque due to FCs, CSMCs and collagen fibres with the reference model without threshold of SSMCs and reducing pss to $0.0202 d^{-1}$ and r_{apop} to $8.011 \cdot 10^{-8} s^{-1}$, without natural degradation of collagen	79
3.16	Arterial wall thickness increase and concentrations of all substances obtained with the reference non-vulnerable model for a simulation time of 10 years	80
3.17	Evolution of substances concentration for a total time of 10 <i>years</i> for the vulnerable and non-vulnerable models	84
3.18	Variation of the volume of FC, SSMC and collagen when increasing and decreasing the parameters by 10 %	89
3.19	Variation of the stenosis ratio when increasing and decreasing the parameters by 10 %	89
4.1	Example of an image of a bifurcation of carotid artery	96
4.2	Example of the thresholding of an image of a bifurcation of carotid artery	97
4.3	Geometry in 3D of the artery of the real patient with a detail of the area near the atheroma plaque and the calcification	97
4.4	Reconstructed geometry of the real patient with a detail of the area near the bifurcation	98
4.5	Details of the bifurcation area of all the patients with atheroma plaque ("A"–"G") and the healthy volunteer ("H")	100
4.6	Details of the bifurcation area of all the reconstructed geometries	100
4.7	Blood mass flow at the inlet of the CCA of the geometry "A" and pressure at the outlets of the ICA and ECA	102
4.8	Correlation between the shape index and oscillatory shear index	104
4.9	Correlation surface among the shape index, time average wall shear stress and oscillatory shear index	105
4.10	Correlation between the flow of monocytes across the endothelium and OSI	107

4.11	Correlation surface among the flow of monocytes across the endothelium, TAWSS and OSI	108
4.12	Workflow of the computational process	109
4.13	Details of the selected mesh for patient "A" in the areas of the bifurcation and in the inlet of the geometry	110
4.14	Mesh sensibility for the lumen of geometry "A", depending on the element size	112
4.15	Mesh sensibility for the lumen of geometry "A", depending on the number of boundary layers	113
4.16	Shape index distribution and a detail of the wall thickness increase in the bifurcation area in the healthy geometry ("H") with the different mechanical stimuli studied	118
4.17	Shape index distribution in all the geometries ("A"–"G") with the different mechanical stimuli studied	121
4.18	LDL, oxidised LDL and monocyte concentration for the patient "A" considering TAWSS, OSI and NV	122
4.19	Macrophage, cytokine and foam cells concentration for the patient "A" considering TAWSS, OSI and NV	123
4.20	CSMC, SSMC and collagen concentration for the patient "A" considering TAWSS, OSI and NV	124
4.21	Wall thickness increase due to plaques apparition in all the geometries ("A"–"G") with the different mechanical stimuli studied	127
4.22	Results for wall thickness increase due to the apparition of plaques in patient B with 30 and 15 years of continuous process, the updated geometry after 15 years of the growth process, the wall thickness increase after 30 years in the updated geometry and the real plaque of the patient	133
5.1	Blood mass flow at the inlet and pressure imposed at the inlet and outlet of the geometry, respectively	139
5.2	Workflow of the computational process for the 2D axisymmetric model with transient blood flow	140
5.3	Arterial wall thickness increase for the uncoupled model with NV, for a time of simulation of 10 years	144
5.4	Workflow of the computational process for the FSI models	146
5.5	Plaque area obtained for the uncoupled and FSI with endothelial repair models, for all the temporal intervals of geometry updating	148
5.6	Stenosis ratio obtained for the uncoupled and FSI with endothelial repair models, for all the temporal intervals of geometry updating	148

5.7	Geometry and maximum wall thickness increase for all the time intervals of geometry updating every 1.25 years, for the case of FSI considering endothelial repair	149
5.8	Plaque area obtained for the uncoupled and FSI without endothelial repair models, for all the temporal intervals of geometry updating	150
5.9	Stenosis ratio obtained for the uncoupled and FSI without endothelial repair models, for all the temporal intervals of geometry updating	151
5.10	Geometry and maximum wall thickness increase for all the time intervals of geometry updating every 1.25 years, for the case of FSI without considering endothelial repair	152
5.11	Concentration of foam cells, SSMCs and collagen after <i>10 years</i> of simulation for the uncoupled and the two FSI developed models	153
5.12	LDL concentration after <i>10 years</i> of simulation for the uncoupled and the two FSI developed models	154

List of Tables

1.1	Summary of the atherosclerosis development models in the literature . .	22
2.1	List of the parameters needed to calculate blood flow in the arterial lumen	27
2.2	List of the parameters necessary to calculate plasma flow through the endothelium	35
2.3	List of the parameters needed to calculate substances flow in lumen . . .	36
2.4	Summary of the equations of the inflammatory process in the arterial wall	45
2.5	List of the parameters that are needed to calculate the inflammatory process in arterial wall	48
2.6	List of constants of the Yeoh's model in the arterial wall	49
2.7	List of the parameters that are needed to calculate plaque growth in the arterial wall	50
3.1	Values of the geometrical and blood flow parameters, and substance concentrations considered in the lumen for the reference model	62
3.2	Characteristics of the predefined meshes of COMSOL Multiphysics for domains with fluid mechanics	63
3.3	Results obtained for the length of WSS lower than $2 Pa$ and maximum velocities in the hole lumen and in the area of the obstacle plaque depending on the mesh	64
3.4	Variation of the length of WSS lower than $2 Pa$ and of the maximum velocities in the hole lumen and in the area of the obstacle plaque depending on the mesh	65
3.5	Results obtained for the length of WSS lower than $2 Pa$ and maximum velocities in the hole lumen and in the area of the obstacle plaque depending on the number of boundary layers	65
3.6	Variation of the length of WSS lower than $2 Pa$ and of the maximum velocities in the hole lumen and in the area of the obstacle plaque depending on the number of boundary layers	66

3.7	Number of mesh, nodes and wall thickness increase for the analysed meshes in the arterial wall	67
3.8	Details of the selected mesh for the arterial wall	69
3.9	Number of nodes and boundary layers of the selected meshes for the lumen and the arterial wall.	69
3.10	Results obtained for the three different total lengths analysed for the reference model	70
3.11	Changes in the equations and parameters for the non-vulnerable reference model	79
3.12	Areas of the lipidic nucleus and of the fibrous layer of the plaques used to validate the non-vulnerable model	82
3.13	Analysed parameters and their respective values for the cases of increase and decrease them by 25 % and 10 %	86
3.14	Foam cells, synthetic smooth muscle cells, collagen volume and stenosis ratio variation by reducing and increasing the values of the parameters by 25%	87
3.15	Foam cells, synthetic smooth muscle cells, collagen volume and stenosis ratio variation by reducing and increasing the values of the parameters by 10%	87
4.1	Correspondence between patients and each one of the computed geometries	99
4.2	Results of Murray's law in all the carotid arteries	102
4.3	Adjustment parameters for the correlation of SI as a function of TAWSS, OSI and NV	105
4.4	Multiplying function values respective to the considered cases of TAWSS and OSI	106
4.5	Characteristics of the analysed meshes for the lumen	111
4.6	Results of the areas of geometry "A" with $TAWSS < 2 Pa$ and $OSI > 0.1910$, obtained with the three different analysed element sizes for the meshes of the lumen	113
4.7	Results of the areas of geometry "A" with $TAWSS < 2 Pa$ and $OSI > 0.1910$, with the different number of boundary layers analysed	114
4.8	Results of maximum LDL concentration in the arterial wall and maximum wall thickness increase, obtained with the different meshes analysed for the arterial wall with TAWSS and OSI as main mechanical stimuli	115
4.9	Characteristics of the mesh selected for the arterial wall	115
4.10	Number of nodes of the lumen and the arterial wall meshes of all the geometries	115

4.11	Results of TAWSS and OSI obtained for five cardiac cycles in the geometry "A"	116
4.12	Results obtained for the two plaques of the geometry "A"	128
4.13	Results obtained for the two plaques of the geometry "B"	128
4.14	Results obtained for the two plaques of the geometry "C"	129
4.15	Results obtained for the plaque of the geometry "D"	129
4.16	Results obtained for the plaque of the geometry "E"	129
4.17	Results obtained for the plaque of the geometry "F"	130
4.18	Results obtained for the two plaques of the geometry "G"	130
4.19	Stenosis ratio of all the real plaques, the plaques predicted with the computational model for the different mechanical stimuli and stenosis difference between them	131
5.1	Number of nodes and resolution time of the lumen meshes analysed for the case of transient blood flow	141
5.2	Results obtained, attending to the considered mesh, for the length of SI higher than 0.3085 for NV as haemodynamical stimulus, and maximum velocities of transient blood flow in the hole lumen and in the area of the obstacle plaque	141
5.3	Variation (%), attending to the considered mesh, of the length of SI higher than 0.3085 for the case of consider NV as haemodynamical stimulus, and of the maximum velocities of transient blood flow in the hole lumen and in the area of the obstacle plaque	142
5.4	Results obtained, attending to the number of boundary layers, for the length of SI higher than 0.3085 for NV as haemodynamical stimulus, and maximum velocities of transient blood flow in the hole lumen and in the area of the obstacle plaque	142
5.5	Variation (%), attending to the number of boundary layers, of the length of SI higher than 0.3085 for the case of consider NV as haemodynamical stimulus, and of the maximum velocities of transient blood flow in the hole lumen and in the area of the obstacle plaque	143
5.6	Number of nodes and boundary layers of the selected meshes for the lumen and the arterial wall in the case of transient blood flow	143
A.1	Parameters to determine the value of K_{lag}	188
A.2	Arterial wall compressibility analysis	193



Thesis

Nomenclature

Chapter 0

0.1 Abbreviations

ABM	Agent-based models
BDF	Backwards differentiation formula
CFD	Computational fluid dynamics
CSMC	Contractile smooth muscle cells
CT	Computed tomography
FC	Foam cells
FSI	Fluid–structure interaction
GMRES	Generalized minimum residual iterative solver
IVUS	Intravascular ultrasound
LC	Leaky cells
LDL	Low-density lipoproteins
MC	Mitotic cells
MRI	Magnetic Resonance Imaging
MUMPS	Multi-frontal massively parallel sparse direct solver
NV	New variable dependent on TAWSS and OSI
OSI	Oscillatory shear index

PARDISO	Parallel direct sparse solver
SI	Shape index
SMC	Smooth muscle cells
SSMC	Synthetic smooth muscle cells
TAWSS	Time-averaged wall shear stress
WSS	Wall shear stress
WHO	World Health Organisation

0.2 Subscripts

<i>adv</i>	Adventitia
<i>b</i>	Blood
<i>c</i>	Cytokine
<i>Cf</i>	Central filament of hyaluronic
<i>Cg</i>	Collagen
<i>Cp</i>	Proteoglycan core proteins
<i>CSMC</i>	Contractile Smooth Muscle Cells
<i>End</i>	Endothelium
<i>FC</i>	Foam Cells
<i>G</i>	Glycosaminoglycan fibres
<i>LDL</i>	Low-density lipoproteins
<i>lj</i>	Leaky junctions
<i>m</i>	Monocyte
<i>M</i>	Macrophage
<i>nj</i>	Normal junctions
<i>oxLDL</i>	Oxidised LDL

p	Plasma
Pg	Proteoglycan matrix
Pm	Proteoglycan monomers
SMC	Smooth muscle cells
$SSMC$	Synthetic Smooth Muscle Cells
vp	Vesicular pathways
w	Arterial wall
r	Radial direction
θ	Circumferential direction
z	Longitudinal direction

0.3 Nomenclature list

$\frac{A_p}{S}$	Endothelial area occupied by leaky junctions
A_{slj}	Area of a single leaky junction
A_{unit}	Unit area
$C_{0,i}$	Initial concentration of the substance i
$C_{c,w}^{th}$	Cytokine threshold in the arterial wall
C_i	i concentration
C_{LDLdep}	LDL deposited in the arterial wall across the endothelium
C_r	Cytokine production rate in the arterial wall
$C_{SSMC,w}^{th}$	SSMC maximum threshold in the arterial wall
$C_{Yeoh,i}$	Constant number i of the Yeoh's material model
d_c	Cytokine degradation rate in the arterial wall
d_{Cg}	Collagen degradation rate in the arterial wall
D_H	Hydraulic diameter
D_i	Diffusion coefficient of the substance i
d_{LDL}	Degradation rate of LDL in the arterial wall
D_{lj}	Diffusion coefficient of leaky junctions
d_m	Monocyte differentiation rate in the arterial wall
F_b	Internal forces of blood
G_r	Collagen secretion rate in the arterial wall

I_1	First invariant of the right Cauchy-Green deformation tensor
J	Jacobian
$J_{S,i}$	i flow across the endothelium
J_v	Plasma flow across the endothelium
k_c	Saturation constant
k_i	Permeability of i
$K_{lag,i}$	Solute lag coefficient of i in the arterial wall
$k_{(LDL-oxLDL)}$	Parameter for the unit conversion from LDL into oxLDL
$k_{(M-FC)}$	Parameter for the unit conversion from macrophages into FC
$k_{(m-M)}$	Parameter for the unit conversion from monocytes into macrophages
$k_{(SMC)}$	Parameter for the unit conversion from CSMCs into SSMCs
K_w	Initial compression modulus of the arterial wall
$LDL_{ox,r}$	LDL that a macrophage can ingest
l_i	Length of i
L_{pi}	Hydraulic conductivity of i
Lp_{slj}	Hydraulic conductivity of a single leaky junction
m_d	Monocyte natural death in the arterial wall
m_r	Monocyte recruitment from lumen
Mw_i	Molecular weight of the substance i
n_{FC}	Quantity of oxLDL that a macrophage has to ingest to turn into a FC
N_i	Flow of the substance i
$P_{app,i}$	Apparent permeability of i
Pe_{lj}	Modified Péclet number in the leaky junctions
P_i	Pressure of i
P_{lj}	Diffusive permeability of leaky junctions
P_{slj}	Diffusive permeability of a single leaky junction
p_{ss}	SSMC proliferation rate in the arterial wall
r_{Apop}	SSMC apoptosis rate in the arterial wall
R_{cell}	Endothelial cell radius
Re	Reynolds number
R_i	Radius of i
S_r	SSMC differentiation rate in the arterial wall

t	Time
$t_{0,intima}$	Thickness of the intima layer for the zero pressure case
t_{intima}	Thickness of the intima layer for a pressure different to zero
T	Cardiac cycle period
T_A	Transversal area
u_i	Velocity of i
v_i	Volume of i
w_l	Half-width of a leaky junction
W_p	Wetted perimeter
WSS_0	Reference WSS
Z_{lj}	Reduction factor of leaky junctions

0.4 Nomenclature list: Greek alphabet

α_{lj}	Pore area occupied by LDL transport
α_{Pm-Cf}	Ratio between the lengths of Pm and Cf
β_{G-Cp}	Ratio between the lengths of G and Cp
ΔP_{End}	Pressure drop in the endothelium
$\Delta \Pi$	Osmotic pressure difference across the endothelium
ϵ_i	Porosity of i
ϵ_{oi}	Porosity of i for the zero pressure case
ε_{lj}	Leaky junction permeability
μ_i	Dynamic viscosity of i
ρ_i	Density of i
σ_d	Osmotic reflection coefficient of plasma
$\sigma_{f,lj}$	Solvent-drag coefficient of leaky junctions
τ	Blood flow tangential stresses

Φ_{lj}	Endothelial fraction of leaky cells
χ	Fraction of endothelial cells separated by leaky junctions
Ψ	Strain energy density
Ω_{intima}	Partition coefficient of the intima layer

0.5 Mathematical symbols

Bold symbols	Vector or matrix
i^T	Transpose of i
I	Identity tensor
∇	Nabla operator: $\left(\frac{\partial}{\partial x}, \frac{\partial}{\partial y}, \frac{\partial}{\partial z} \right)^T$
$i \cdot \nabla$	$i_x \frac{\partial}{\partial x} + i_y \frac{\partial}{\partial y} + i_z \frac{\partial}{\partial z}$
∇i	Gradient of i : $\left(\frac{\partial i}{\partial x}, \frac{\partial i}{\partial y}, \frac{\partial i}{\partial z} \right)^T$
$\nabla \cdot i$	Divergence of i : $\frac{\partial i_x}{\partial x} + \frac{\partial i_y}{\partial y} + \frac{\partial i_z}{\partial z}$



Chapter 1

Introduction

Chapter 1

1.1 General Overview and motivation

Cardiovascular diseases are one of the main causes of mortality worldwide. According to the World Health Organisation (WHO), in 2019 there were a total of 55.4 million deaths in all the world. In the WHO's 2019 annual report, approximately 55 % of annual deaths are attributable to the 10 leading causes of death. These top 10 causes of death can be classified as: Cardiovascular diseases (composed of ischaemic heart disease and strokes), chronic obstructive pulmonary disease, lower respiratory infections, neonatal conditions, trachea, bronchus and lung cancers, alzheimer disease and other dementias and others (which includes diabetes mellitus, kidney diseases and diarrhoeal diseases) (World Health Organisation, 2019). Figure 1.1 represents the percentages of deaths globally due to each one of these causes in 2019, respect the total number of deaths due to them.

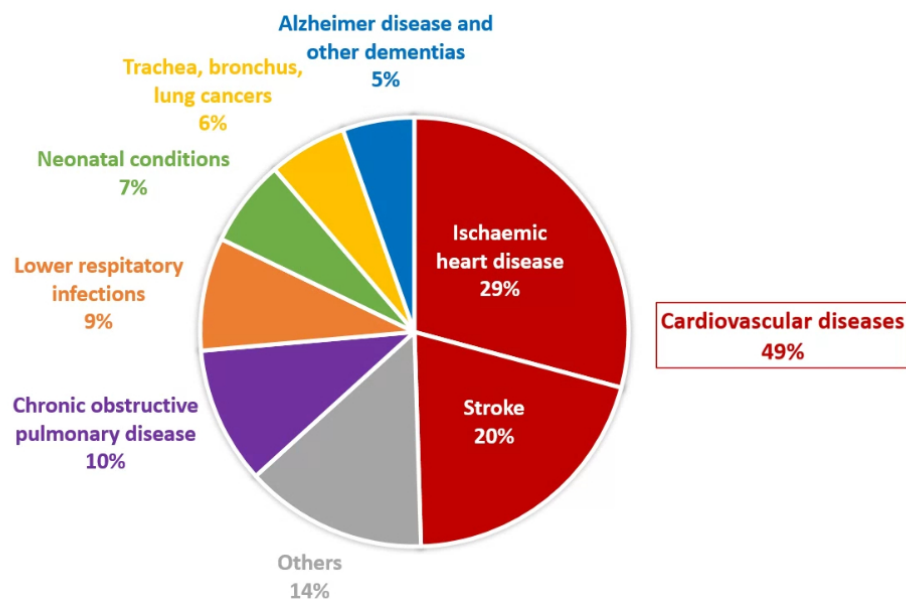


Figure 1.1: Percentages of deaths in 2019 due to the leading 10 causes. Data from: <https://www.who.int/news-room/fact-sheets/detail/the-top-10-causes-of-death>.

In Figure 1.1 it can be seen that the 49 % of these deaths was due to cardiovascular diseases and, in particular, to ischaemic heart disease and strokes. The first leading cause of

deaths in the world in 2019 corresponds to the ischaemic heart disease which, in that year, was the responsible for 16 % of deaths globally, with more than 8.9 million deaths. The second leading cause of deaths worldwide that year were strokes, which, in fact, caused more than 6 million deaths, being responsible for almost 11 % of the deaths globally that year.

In Figure 1.2, the millions of deaths in the world for each of the analysed leading causes of death is represented, for the years 2000 and 2019, so it is possible to analyse their evolution over time (World Health Organisation, 2019). As can be observed, the number of deaths due to cardiovascular diseases has increased over the years, which can be associated with an increase in life expectancy. In this line, a significant increase has been observed for other diseases associated with the increase in life expectancy, such as the case of Alzheimer disease and other dementias. The opposite is true for deaths due to neonatal conditions and for lower respiratory infection, which have decreased over time.

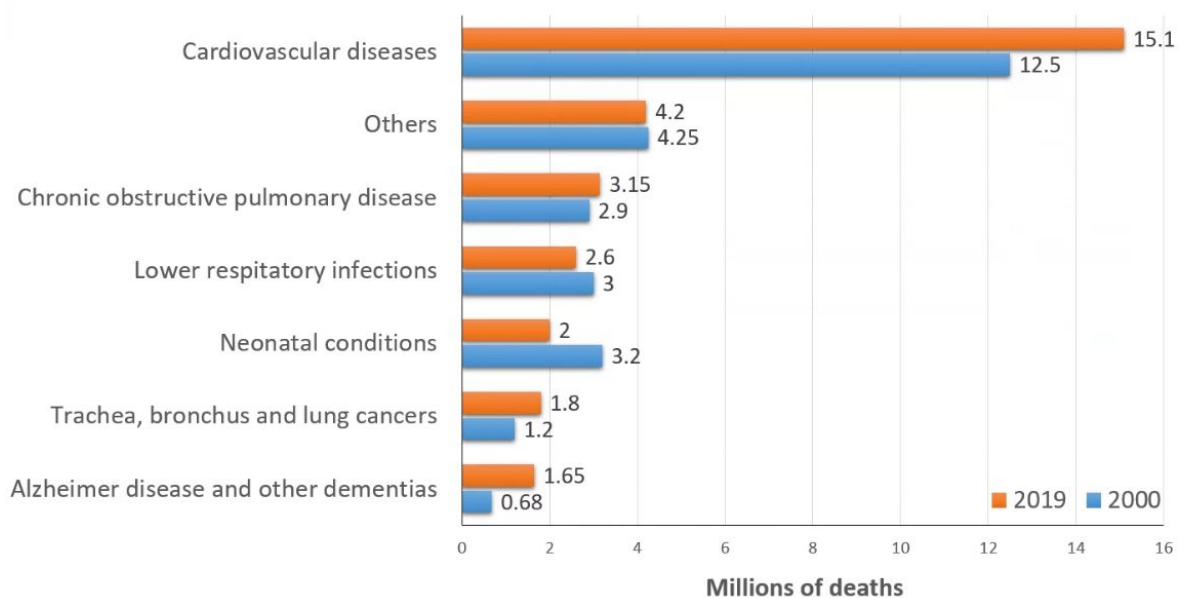


Figure 1.2: Millions of deaths due to the top 10 causes of mortality in the years 2000 and 2019 (blue and orange bars, respectively. Data from: <https://www.who.int/news-room/fact-sheets/detail/the-top-10-causes-of-death>.

As can be seen in Figures 1.1 and 1.2, cardiovascular diseases are the leading cause of mortality nowadays. In addition, they represent a mortality comparable to the sum of the other leading causes of death. Therefore, all the efforts to improve knowledge about them, including their development and diagnosis, will have a great impact in the society.

As commented before, the deaths in Figures 1.1 and 1.2 due to cardiovascular diseases are referred to ischaemic heart disease and strokes, which are both consequences derived from atherosclerosis. Therefore, atherosclerosis is a pathology that produces several events with important consequences and accounts for a large number of deaths annually.

Atherosclerosis is a pathology which consist in the formation of deposits and plaques in the arterial wall due to lipid deposition in it, called atheroma plaques. These plaques lead to an increase of the arterial wall thickness and, therefore, a decrease of the area where blood flows, called lumen. In addition, plaques can break and cause a blood clot that can travel along the circulatory system. For these causes, atherosclerosis can result in several consequences that are dependent on the artery affected, e.g., myocardial attacks, ischaemias, or ictus, among others.

There are multiple factors evolved in the formation of atherosclerosis. Some of these factors can be lesions in the endothelium of the arterial wall (that can cause an increase in its permeability), haemodynamic factors (which produce a change in the shape of the endothelial cells) and high levels of low density lipoproteins (LDL) in blood. Although this pathology has been widely studied, it has not been completely understood yet. Therefore, it is relevant to study the process of formation of atheroma plaques and to determine how these mechanical stimuli can affect the growth and location of atheroma plaques. It can be useful to foresee the locations susceptible of apparition of plaques and to early detect or even prevent their apparition.

With this in mind, the main motivation of this Thesis is stated. The aim of the Thesis is to develop a computational model of the process of atherosclerosis development in arteries to better understand the process of atheroma plaques formation and growth.

In this chapter, an introduction to the composition and properties of arteries are presented. Then, the development process of atherosclerosis is detailed, including an analysis of the different types of atheroma plaques. A revision of the state-of-the-art of atherosclerosis computational models is presented, by differentiating between continuous and agent-based models. For the case of the continuous models, two and three dimensional geometries, as well as patient specific models of the literature are revised too. Furthermore, some models of atherosclerosis with parameters sensitivity analysis and models with fluid-structure interaction (FSI) of blood flow with the arterial wall are included.

Finally, next to the state-of-the-art of atherosclerosis computational models, the objectives of this Thesis, as well as its structure, are explained.

1.2 Arteries and their composition

Arteries are the blood vessels responsible of distribute oxygen-rich blood throughout the body. They are composed of the lumen, through which blood flows, and the arterial wall, which surrounds the lumen and provides resistance to the artery (Humphrey, 2002). The structure of the arterial wall depends on the considered artery, due to that there are elastic and muscular arteries. Elastic arteries correspond to bigger arteries that are near to the heart (like the aorta or the pulmonary artery), while muscular arteries correspond to smaller vessels. However, in both cases, the arterial wall is composed of different concentric layer, which are represented in Figure 1.3:

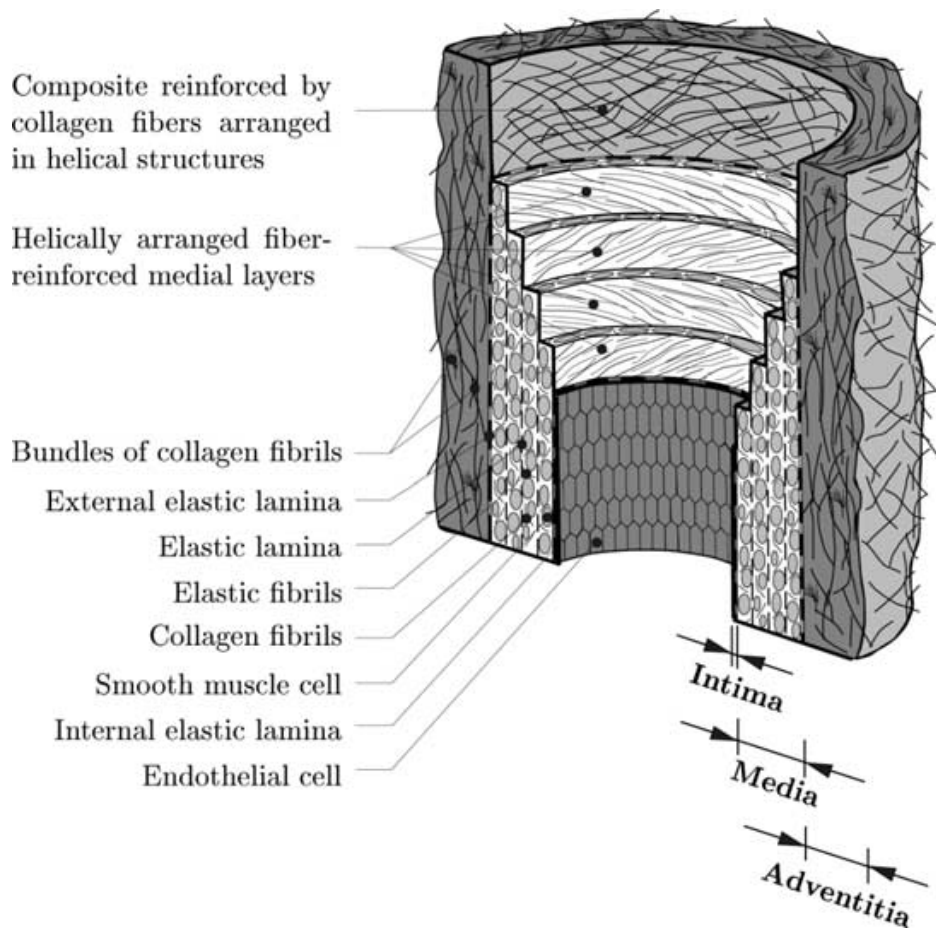


Figure 1.3: Structure of the arterial wall. Figure extracted from [Holzapfel et al. \(2000\)](#).

These concentric layers by which the arterial wall is composed of are, from the lumen to the outer part of the arterial wall, the tunica intima, the tunica media and the tunica adventitia:

- The tunica intima of the arteries consists of the endothelium, the subendothelial space and the internal elastic lamina. The endothelium is a semi-permeable and non-thrombogenic membrane that separates the blood flow from the arterial wall, allowing the flow of some substances through it, such as nutrients and oxygen. It plays a key role in the process of atherosclerosis, as will be discussed below. On the other hand, the subendothelial space is mostly composed of collagen, while the internal elastic lamina is a membrane that separates the intima and media layers of the arterial wall.
- The tunica media of the arterial wall has a bigger thickness, and it is composed of circumferentially arranged smooth muscle cells, collagen and elastin. Finally, the external elastic lamina separates the media and adventitia layers.

- The tunica adventitia is the outer layer of the arterial wall. It is composed of collagen and elastin fibres, and has the function of providing stiffness to the artery.

1.2.1 Carotid arteries

In this Thesis different mechanobiological models of carotid arteries, whose function is to supply oxygen-rich blood to the neck and head, are developed. The human body has two carotid arteries (right and left): The right carotid artery arises from the brachiocephalic trunk, next to the right subclavian artery, while the left carotid artery arises directly from the aortic arch.

Moreover, each one of the carotid arteries bifurcate into two smaller arteries, called the internal and external carotid arteries (ICA and ECA, respectively). Additionally, the branch of the carotid artery before the bifurcation is named common carotid artery (CCA). The ICA is responsible of supply oxygen-rich blood to the corresponding hemisphere of the brain and eye orbit (right or left), while the ECA supplies oxygen-rich blood to the corresponding side of the face (Gray, 1918).

In Figure 1.4, the bifurcation of the right carotid artery is represented. It is possible to observe its origin, next to the right subclavian artery, and to distinguish the CCA, ICA and ECA branches.

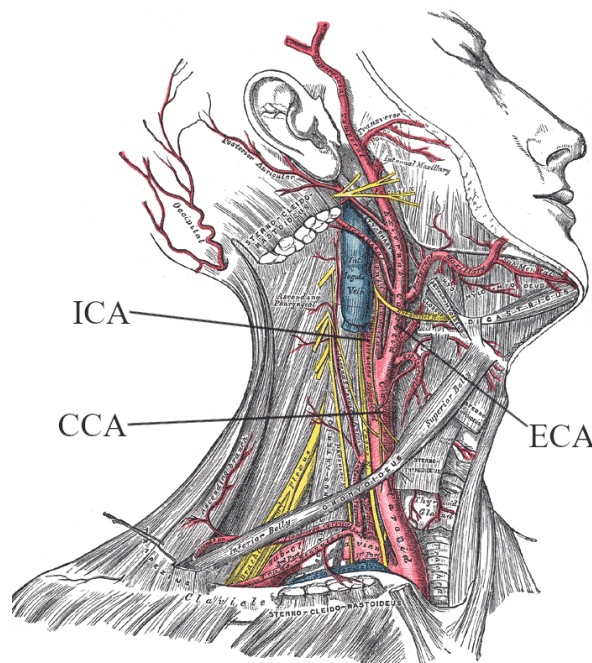


Figure 1.4: Scheme of the right carotid artery. Figure extracted from Gray (1918).

1.3 Atherosclerosis

Atherosclerosis is a pathology which causes the increase of the arterial wall thickness due to an accumulation of some substances in it. Therefore, it results in a decrease of the lumen area in which blood flows, and it can derive in several events, such as heart attacks, ischaemias or strokes. As commented before, it is one of the global main causes of mortality currently, and the most common acquired vascular disease (Humphrey, 2002).

One of the trigger factors of the disease is an increase of the endothelial permeability, which can be caused by a variety of factors. As previously mentioned, the endothelium is a semi-permeable membrane that naturally allows the flow of certain substances into the arterial wall. However, due to its developed increased permeability in some areas, some substances such as LDL molecules are deposited into the arterial wall, initiating the process of atheroma plaques formation.

It has been noticed that this increase in the endothelial permeability is due to the change of shape of the endothelial cells depending on the conditions of the cardiac cycle (Chien, 2008; Dai et al., 2004; Levesque et al., 1986), as can be seen in Figure 1.5. Therefore, the effect of haemodynamical stimuli on the endothelium results crucial in the development of atheroma plaques.

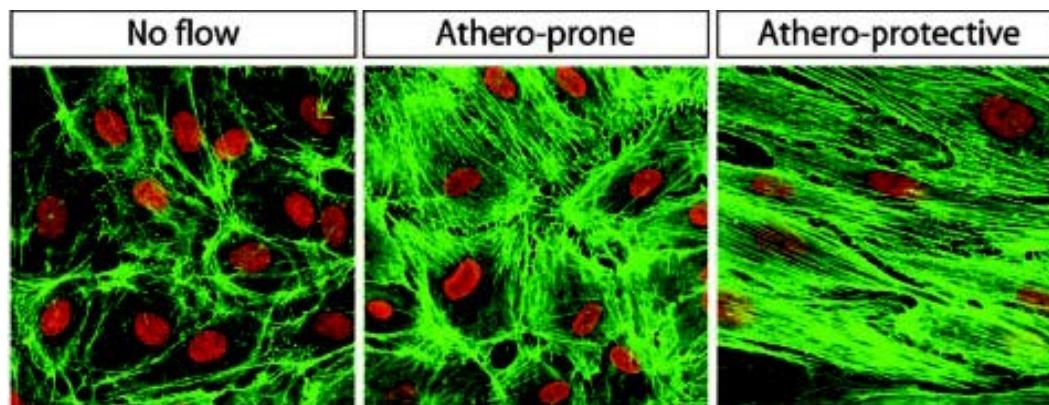


Figure 1.5: Different shapes of endothelial cells. Figure extracted from Dai et al. (2004).

The main risk factors to develop atherosclerosis can be due to genetics and external causes, and include high levels of LDL in blood and low levels of high density lipoproteins (HDL). The process of atheroma plaques formation is a complex problem, in which a large quantity of substances and processes are involved. Therefore, only those substances considered to be the most important of the process have been included in the models developed in this Thesis. Among these substances, low density lipoproteins (LDL) and oxidised low density lipoproteins (oxLDL), cells like monocytes (m), macrophages (M), foam cells (FC), contractile and synthetic smooth muscle cells (CSMCs and SSMCs, respectively),

cytokines (c) and collagen fibres (Cg) are considered. These substances are represented in Figure 1.6.

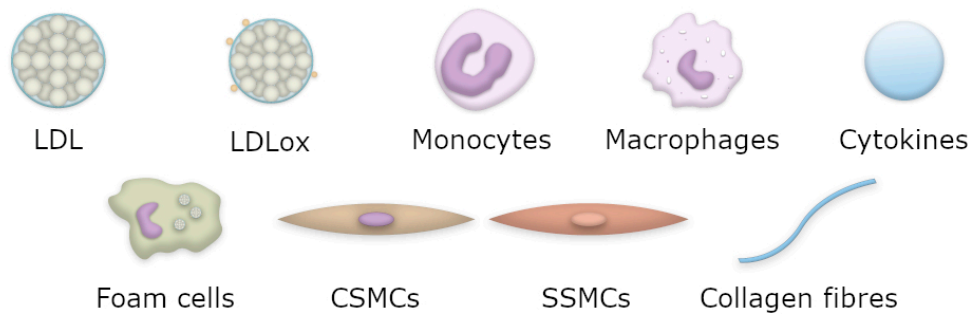


Figure 1.6: Substances considered in the computational model of atherosclerosis developed in this Thesis.

Blood is composed of a liquid component, named plasma, which includes different elements in suspension, among which LDL molecules and cells such as monocytes are included. Thus, all these substances and cells are dragged along the lumen by the blood flow. However, due to the increase in the endothelial permeability caused by changes in the haemodynamical conditions, a flow of substances like plasma and LDL molecules can be generated across the endothelium. Therefore, these substances can penetrate into the arterial wall.

Once that LDL molecules are in the arterial wall, they are no longer in contact with the antioxidants that the blood has, so LDL molecules are oxidised, resulting in oxidised LDL molecules inside the arterial wall. Oxidised LDL is more dangerous than normal LDL, since it can react with other tissues and cause damage in them. Therefore, due to the presence of oxidised LDL in the arterial wall, an immune response is initiated, allowing the flow of monocytes (a kind of white globules) from the blood into the arterial wall. Once in the arterial wall, the objective of monocytes is to eliminate oxidised LDL molecules. Thus, due to the presence of some arterial wall proteins, monocytes differentiate into macrophages. Macrophages are the responsible of the elimination of dangerous substances like oxidised LDL by their phagocytosis, process in which in addition, they segregate cytokines. Once that macrophages cannot ingest more quantity of oxidised LDL, they become foam cells, forming the lipidic nucleus of the plaque. These foam cells are not dangerous, but they can suppose an accumulation of lipid in some areas with a high concentration of them.

Concurrently, at the beginning of the inflammatory process, all the muscular cells on the arterial wall are contractile, i.e., they cannot move or react with any other of the substances. However, due to the presence of cytokines in the arterial wall (segregated by macrophages), these muscle cells change their phenotype and become synthetic smooth muscle cells, which can move and interact with other substances in the arterial wall. Then, synthetic smooth muscle cells surround the foam cells, macrophages and oxidised LDL,

and segregate collagen fibres to isolate the lipid core, forming the fibrous layer of the plaque. The size of these plaques can increase over the time, leading to a reduction in the space available for the arterial lumen, with its correspondent previously commented consequences (Libby, 2021; Libby et al., 2011).

The process of atheroma plaque formation is schematically represented in Figure 1.7, taking into account the introduced substances represented in Figure 1.6.

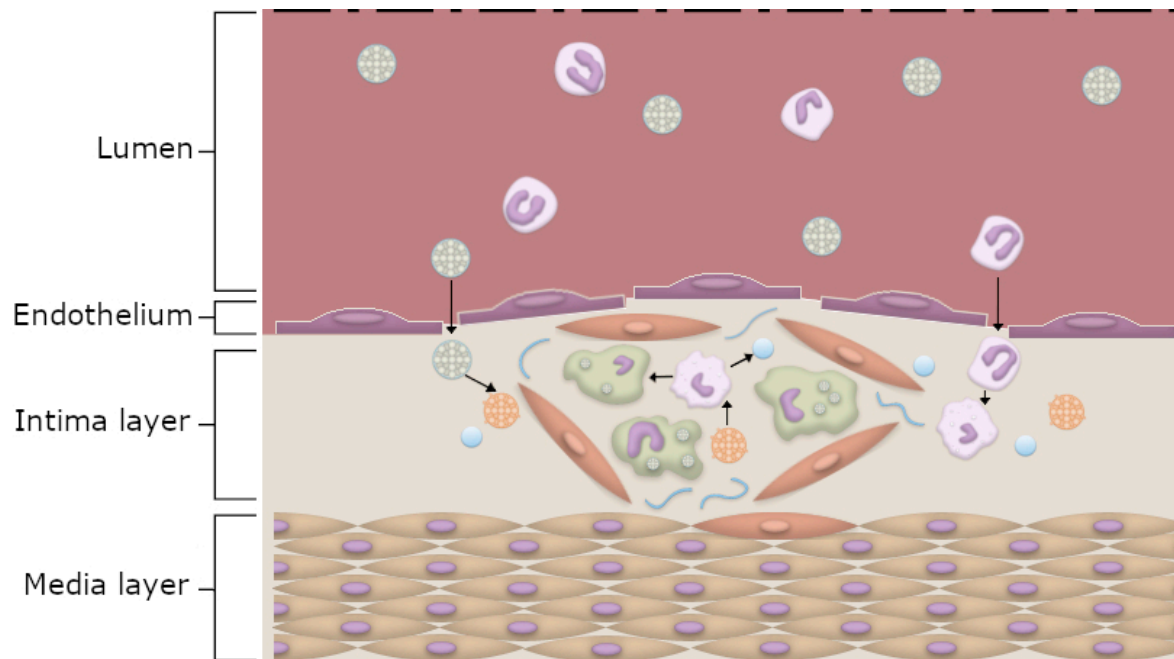


Figure 1.7: Process of atheroma plaques formation.

1.3.1 Composition of atheroma plaques

As commented, atheroma plaques are composed of a lipidic nucleus of foam cells and oxidised LDL surrounded by a fibrotic layer of synthetic smooth muscle cells and collagen fibres. The lipidic core provides volume to the plaque, while the fibrotic layer isolate the lipidic core. In addition, the fibrotic layer provides resistance to the plaque and thus, it is responsible of plaque stability.

1.3.2 Types of atheroma plaques

Atheroma plaques can be clasified attending to their type of growth and to their stability.

Attending to their type of growth, atheroma plaques can grow outwards from the arterial wall, without leading to a reduction in the diameter of the arterial lumen. These plaques are called plaques of positive remodelling, and they are dangerous due to that they are hardly detectable as they do not change the arterial lumen diameter. On the

contrary, plaques that grow towards the lumen are known as negative remodelling plaques. In addition, Glagov's model establish that, at the beginning of the process, atheroma plaques grow with positive remodelling and they continue to grow with negative remodelling (Glagov et al., 1978).

On the other hand, taking into account their stability, atheroma plaques can be classified as vulnerable and non-vulnerable plaques. There are multiple factors involved in the classification of atheroma plaques attending to their stability, like the mechanical stresses that they suffer and its composition. However, in this Thesis this classification is done attending only to their composition: Vulnerable plaques are those with a large lipidic nucleus and a thin fibrous layer, so they have a high risk of rupture that can lead to thrombus formation. In contrast, non-vulnerable plaques have a bigger fibrous layer so they do not have a huge risk of rupture. Due to this, they constantly increase their size, resulting in big narrowing of the arterial lumen.

The plaques developed in the computational models of this Thesis corresponds to vulnerable and non-vulnerable plaques with negative remodelling.

1.4 State of the art

In this Section, a review of the state of the art of computational models of atherosclerosis is included.

As explained before, atheroma plaques are developed as a consequence of an increase of the endothelial permeability of arteries. It is well accepted that this variation of permeability can be due to a change in the shape of endothelial cells depending on, among other causes, some mechanical stimuli caused by blood flow on the endothelial cells (Chien, 2008; Dai et al., 2004; Levesque et al., 1986). These mechanical stimuli can depend on several factors, such as the cardiac cycle, the geometry of the arteries, cyclic stretches, wall shear stresses and oscillatory shear stresses, among others (Alimohammadi et al., 2017; Ohayon et al., 2011; Sáez et al., 2015).

One of these mechanical stimuli is the wall shear stress (WSS) caused by blood flow in the endothelium, which has been widely used to predict location of plaques. However, it has the limitation of been calculated for stationary blood flow and not considering the cardiac cycle. It is well known that areas with physiological WSS promote endothelial cells to have an elongated shape, so the pores between them are small and limit the flow of substances across the endothelium. On the contrary, in areas of low WSS, endothelial cells are more circular, so pores are bigger and allow flow of substances between them, resulting in plaque apparition. The threshold of WSS below which plaques grow depends on the artery considered (Filipovic et al., 2013; Olgac et al., 2008). In the case of carotid arteries, areas with WSS lower than 2 Pa could be considered atheroprone, while areas of higher WSS are atheroprotective (Filipovic et al., 2013; Younis et al., 2004; Zhao et al., 2002).

To avoid the limitation of not consider transient blood flow, other studies use Time Averaged Wall Shear Stress (TAWSS) instead of WSS to take into account the cardiac cycle effects and to improve the accuracy of the prediction (Alimohammadi et al., 2017; Sáez et al., 2015). Another index that has also been used in some studies is Oscillatory Shear Index (OSI). There are some evidences about the influence of OSI on cells shape and, therefore, in the apparition of plaques, being areas of high OSI susceptible of plaques development (Alimohammadi et al., 2017). OSI also considers the complete cardiac cycle. However, most of these studies only take into account TAWSS or OSI to predict the location of plaques and do not consider the inflammatory process to reproduce the growth of plaques.

There are other indices that have been investigated recently such as Cross-flow index (Arshad et al., 2020), Transverse Wall Shear Stress (Peiffer et al., 2013) and Topological Shear Variation Index (Morbiducci et al., 2020), but their implementation in the computational models of this Thesis has not been possible due to that there are not enough experimental data correlating SI of endothelial cells with them.

In the literature, there are many models to study the growth of atheroma plaques in arteries. Depending on the framework in which they address the problem, these models are divided in two types: Continuum models and agent-based models (ABM). The main advantage of continuum models is that they allow the simulation of plaques development in real 3D geometries, which is hard in ABM due to the quantity of agents that would be needed to simulate. On the other hand, the main strength of ABM is that they can take into account the natural random behaviour of cells, which is not possible with continuum models.

In this Thesis, a continuous model will be developed, but some studies carried out with ABM are, for example, Olivares et al. (2016), Bhui and Hayenga (2017) and Corti et al. (2020). Olivares et al. (2016) developed a model for early-stage atherosclerosis, in which they consider substances as LDL, oxidised LDL, macrophages, foam cells, smooth muscle cells, endothelial cells and autoantibodies. However, due to the required computational cost, they can only model a section of $100 \times 100 \times 100 \mu m^3$ of the arterial wall. Bhui and Hayenga (2017) developed a three-dimensional idealised model of transendothelial migration during atherogenesis, in which they modelled endothelial cells, monocytes, macrophages, lymphocytes, neutrophils and foam cells. In addition, Corti et al. (2020) modelled atheroma plaque growth depending on WSS coupling a three dimensional computational fluid dynamics (CFD) problem with a two dimensional ABM. They considered a multilayered wall, composed of the intima, media, and adventitia layers, modelling also the internal and external elastic lamina considering the extracellular matrix, smooth muscle cells and foam cells.

Within the continuum models, their complexity depends on the different species that they consider. There are a huge quantity of models than have been developed in two-dimensional geometries. For example, Zohdi et al. (2004) used a cross-section of the artery to model the adhesion of monocytes to the endothelial surface. This adhesion is controlled by the intensity of the blood flow. Their model predicts a priori the time to plaque

rupture as a function of arterial geometry, diameter of the monocyte, adhesion stress, bulk modulus of the ruptured wall material, blood viscosity, flow rate and mass density of the monocytes. [Fok \(2012\)](#) proposed a mathematical model of intimal thickening, posed as a free boundary problem applied to a cross-section of the artery. Intimal thickening was driven by damage to the endothelium, resulting in the release of cytokines and migration of SMCs. More complex studies were presented by [Siogkas et al. \(2011\)](#), who reconstruct some cross-section segments of real coronary arteries from Intravascular Ultrasound images (IVUS) and used convection-diffusion-reaction equations to model oxidised LDL, macrophage and cytokine behaviour inside the arterial wall. They considered that all the LDL molecules and the monocytes were and differentiated, respectively, at the instant in which they pass through the endothelium. A similar study was presented by [Calvez et al. \(2009\)](#) from a mathematical point of view, but their study also includes foam cells and models a two dimensional geometry of a bifurcation of a carotid artery. Finally, [Bulelzaï and Dubbeldam \(2012\)](#) presented a qualitative mathematical model consisting of a number of ordinary differential equations for the concentrations of the most relevant constituents of the atherosclerotic plaque: macrophages, monocytes, foam cell and oxidised LDL.

[Olgac et al. \(2008\)](#) used a model applied to a coronary artery, using Kedem-Katchalsky equations ([Kedem and Katchalsky, 1958](#)) and the three-pore model to determine LDL flow across the endothelium, depending on WSS that blood produces in it. They also considered LDL behaviour in the arterial wall with a convection-diffusion-reaction equation, modelling its degradation. [Tomaso et al. \(2011\)](#) used a similar geometry and they were focused on the mechanical interactions of the different biological species that they considered. They modelled LDL and they also considered monocyte flow across the endothelium, assuming that all the monocytes in the arterial wall differentiate into macrophages.

[Cilla et al. \(2013\)](#) developed a mathematical model in the previous two-dimensional axisymmetric geometry presented by [Olgac et al. \(2008\)](#), with LDL and monocyte flows into the arterial wall depending on the WSS, including the three-pore model, and the interactions between all the substances commented before with convection-diffusion-reaction equations, also including smooth muscle cells and collagen fibres. They also simulated the growth of the plaque in the arterial wall.

There are some mechanobiological models applied to patient-specific geometries, like the one presented by [Filipovic et al. \(2013\)](#) who used Magnetic Resonance Imaging (MRI) to simulate their model in bifurcations of carotid arteries. They modelled LDL and monocyte flow across the endothelium depending on WSS, and also the behaviour of oxidised LDL, macrophages and cytokines in the arterial wall. However, they focused their study only in the location of plaques and not in their growth. [Alimohammadi et al. \(2017\)](#) and [Díaz-Zuccarini et al. \(2014\)](#) used the aortic bifurcation and the left femoral artery in their studies, respectively, and focused more on the location of plaques than on their growth. [Alimohammadi et al. \(2017\)](#) analysed the typical haemodynamical stimuli TAWSS or OSI and proposed a combined index, named HOLMES, to emphasize regions of highly oscillatory and low-magnitude WSS; however, they focused only on the location of calcifications.

All the commented studies consider the wall of the artery as a mono-layered wall, but real arteries have a multi-layered wall, as explained before in this chapter. Kenjereš and De Loor (2014) developed a computational model in a realistic geometry of a carotid artery bifurcation, in which they simulated LDL flow across the endothelium. The arterial wall in this study was composed by the intima and media layers, also considering the endothelium and the internal elastic lamina as membranes for the LDL flow.

There are also some studies focused on parameter influence, such as Tomaso et al. (2011), who analysed the influence of different LDL concentrations in blood to determine how it affects plaque growth. Cilla et al. (2015) analysed the effect of transmural transport properties on atheroma plaque formation, attending to LDL and oxidised LDL diffusion coefficient anisotropy. There are some studies that analyse the influence of parameters in agent-based models too. It is the case of Olivares et al. (2016), who analysed, in 8 cases the influence in the plaque of the oxidation rate of LDL, migration speed of agents, and auto-antibodies maximum concentration. Finally, Corti et al. (2020) made both, mono-parametric and multi-parametric sensitivity analyses to evaluate the changes in their results caused by changes in the parameters of an agent-based model of plaque growth.

Regarding fluid-structure interaction (FSI) models of atheroma plaques development, most of them are focused on the effect of FSI in the stresses that blood flow produces in the plaques, to study their stability, which is the case of Tang et al. (2008), Kock et al. (2008) and Gao et al. (2009). However, there are few models focused on the influence of FSI of blood flow and the growth of atheroma plaques, which are the most relevant for this Thesis. For example, in the two-dimensional model developed in Calvez et al. (2009), they model FSI using the mesh displacement due to the plaque formation and the blood flow. Chung and Vafai (2012) analysed the influence of FSI on LDL accumulation and on LDL flow across the endothelium. Finally, Deyranlou et al. (2015) analysed FSI on LDL accumulation in a carotid artery, modelling blood flow as a non-Newtonian fluid.

Table 1.1 is a summary of the principal continuum models of atherosclerosis formation, including the artery considered in each one of them, as well as the typology of the geometries. In addition, the haemodynamical stimuli and substances considered in each case are indicated. Finally, the type of modelling of the arterial wall in all the models is shown.

Article	Artery	Geometry	Haemodynamical stimuli	Substances	Arterial wall
Zhao et al. (2002)	Carotid bifurcation	3D	WSS	-	Mono-layered
Younis et al. (2004)	Carotid bifurcation	3D Cross-sections of MRI	TAWSS OSI Max. WSS temp. gradient	-	Mono-layered
Olgac et al. (2008)	Coronary	2D axisymmetric	WSS	LDL	Mono-layered
Calvez et al. (2009)	Carotid	2D	WSS	LDL oxLDL Macrophages Foam cells Cytokines Extracellular matrix	Intima layer
Siogkas et al. (2011)	Coronary	Cross-section segments	WSS	LDL Macrophages Cytokines	Intima layer
Tomaso et al. (2011)	-	2D axisymmetric	WSS	LDL Monocytes Macrophages	Mono-layered
Bulelzai and Dubbeldam (2012)	-	2D axisymmetric	WSS	Oxidised LDL Monocytes Macrophages Foam cells	Intima layer
Fok (2012)	-	Cross-section	-	Platelet derived growth factor SMCs	Multi-layered Intima Media

Article	Artery	Geometry	Haemodynamical stimuli	Substances	Arterial wall
Cilla et al. (2013)	Coronary	2D-axisymmetric	WSS	LDL	Mono-layered
				oxLDL	
				Monocytes	
				Macrophages Cytokines CSMCs SSMCs	
Collagen fibres					
Filipovic et al. (2013)	Carotid bifurcation	3D from MRI	WSS	Oxidised LDL	Mono-layered
				Macrophages Cytokines	
Díaz-Zuccarini et al. (2014)	Left femoral artery	3D from CT scans	WSS	LDL	Mono-layered
				Monocytes Macrophages	
Kenjereš and De Loor (2014)	Carotid bifurcation	3D	WSS	LDL	Multi-layered Intima Media
Sáez et al. (2015)	Carotid bifurcation	3D	TAWSS	-	-
			OSI		
Alimohammadi et al. (2017)	Aortic bifurcation	3D from CT scans	TAWSS	LDL	Mono-layered
			OSI		
			Highly Oscillatory, Low Mag. Shear		

Table 1.1: Summary of the atherosclerosis development models in the literature.

1.5 Objectives

The aim of this thesis is to study the pathology of atherosclerosis by developing advanced multiphysics models that allow to study the main processes of the disease, considering the haemodynamical changes as the main trigger of the process. This objective is to be achieved through the realisation of other more specific objectives:

- Analyse and improve the previous computational model of Cilla (2013), to enhance its biological accuracy and convergence.
- Carry out modifications in the improved computational model to predict the growth of vulnerable and non-vulnerable atheroma plaques.
- Application of the computational model to specific patient geometries of carotid artery bifurcations to perform its validation.
- Study the different haemodynamical stimuli commonly used in the literature and their implementation in the model.
- Perform a sensitivity analysis of the results obtained with the computational model to variations in the different parameters involved in the process, in order to determine their impact on the growth of the plaque.
- Application and analysis of the effects of FSI to the developed computational model, in order to determine its influence on plaque growth.

1.6 Thesis structure

This thesis is divided in several chapters, in which the problem of atherosclerosis is approached in a progressive way with the development of different computational models.

- Chapter 0 contains all the abbreviations and nomenclature used during all this Thesis.
- Chapter 1 presents an introduction to cardiovascular diseases and their globally effects. In addition, arteries and their components are explained, particularising for the case of the carotid arteries, in which the computational models studied in this Thesis are applied. In addition, the process of development of atherosclerosis is included, considering the substances and cells that are modelled in the computational models. In addition, the atherosclerosis models state of the art is analysed. Finally, the objectives and the structure of the Thesis are defined.
- Chapter 2 contains the reference mathematical model, which considers blood and substances flow along the arterial lumen, plasma and substances flow across the endothelium, the inflammatory process of the arterial wall, the mechanical model

used for the arterial wall, and the plaque growth. As commented, the computational model is based on the one proposed by Cilla (2013). Therefore, the improvements made in this model are explained as well.

- In Chapter 3, the reference computational model is explained, including the geometry and sensitivity analysis of the meshes of the lumen and arterial wall. The length of the geometry is also studied. The reference model corresponds to a vulnerable plaque model, whose results are analysed. Thus, some modifications in the mathematical model have been developed to achieve non-vulnerable plaques. In addition, the results obtained with the non-vulnerable plaques model are presented, including its validation. Finally, a sensitivity analysis of the model to variations in their parameters is developed.
- In Chapter 4, the reference model of vulnerable plaques is validated with pathological patient-specific geometries, whose repair process to obtain the respective healthy geometries is explained as well. The boundary conditions applied for the blood flow are also included, and some of the haemodynamical stimuli most commonly used to initiate atherosclerosis are defined, proposing a new one as a combination of them. Finally, the results and a discussion of them are included.
- Chapter 5 develops a methodology to include FSI in the computational model, considering two different cases: The first one in which endothelial repair due to the change of the haemodynamical stimuli is included, and the second one which considers that there is no endothelial repair.
- Finally, Chapters 6 and 7 include the general conclusions obtained during all the Thesis, in English and Spanish languages, respectively. The main contributions of the Thesis to the study of atherosclerosis and the future research lines are analysed. In addition, the publications and other contributions derived from this Thesis are included.
- The Thesis also has two different appendices. In Appendix A, the determination of the parameters of the model is included. Finally, in Appendix B the reason by which Darcy's law can be applied to plasma flow across the endothelium is explained.

Chapter 2

Mathematical modelling

Part of the contents of this Chapter can be found in:

- Hernández-López P., Cilla M., Martínez M. and Peña E.
Effects of the Haemodynamic Stimulus on the Location of Carotid Plaques
Based on a Patient-Specific Mechanobiological Plaque Atheroma Formation
Model.
Frontiers in Bioengineering and Biotechnology (2021). 9:690685.
<https://doi.org/10.3389/fbioe.2021.690685>
- Hernández-López, P.; Martínez, M.A.; Peña, E.; Cilla, M.
Understanding the Parameter Influence on Lesion Growth
for a Mechanobiology Model of Atherosclerosis.
Mathematics 2023, 11(4), 829.
<https://doi.org/10.3390/math11040829>

Chapter 2

2.1 General Overview

The computational model developed in this Thesis is based on the one proposed in the doctoral Thesis by Cilla (2013), explained in Section 1.4 of this Thesis, replacing some terms of the equations to improve their mathematical precision and convergence and also their biological accuracy. Some new improvements of the model will be presented in next chapters.

The computational model is a multiphysics continuum model of atheroma plaques growth in arteries. The model considers blood hemodynamics as the trigger of the process and to determine the location of plaques, and reproduce the behaviour of all the main substances involved in the process in the arterial wall.

First, an axisymmetric model has been developed, in which the lumen and the arterial wall are considered, assuming that the artery has as a mono-layered wall with homogeneous properties. It also considers the endothelium and the adventitia as membranes.

The mathematical model is computed in four different steps, as can be seen in Figure 2.1. These steps are, in order of execution, blood and substances flows along the arterial lumen, plasma flow across the endothelium (from the lumen into the arterial wall), the inflammatory process of the arterial wall due to the presence of different substances in it, and the growth of atheroma plaques.

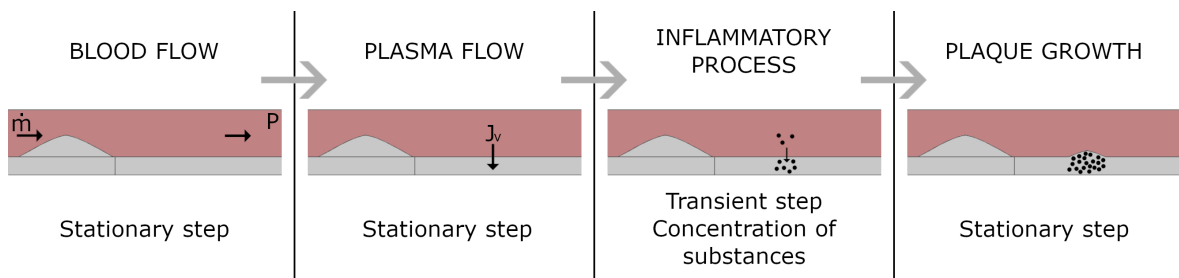


Figure 2.1: Workflow of the computational process for the base model.

The substances that are considered to be involved in the inflammatory process of the model include some molecules, like LDL and oxidised LDL, some cells, like monocytes,

macrophages, foam cells, contractile and synthetic smooth muscle cells, and cytokines and collagen fibres.

In this chapter, the mathematical model of atherosclerosis development is presented. First of all, the equations of the model are included in different sections, distinguishing into equations referred to blood flow in the lumen, plasma flow across the endothelium, substances flow along lumen, inflammatory process of the arterial wall, and plaque growth (Sections 2.2-2.7). All the boundary conditions applied for the simulation of these equations are in their respective sections, as well as the values of the parameters that have been employed. The determination of all these values of the parameters is explained with more detail in the Appendix A. After that, the changes in the equations of the previous model of Cilla (2013) are explained in Section 2.8 of this chapter.

2.2 Blood flow in the lumen

According to Caro et al. (1978) and Perktold et al. (1991), under physiological conditions and for vessels with diameter higher than 0.5 mm , blood is in the lineal zone of the curve of pseudoplastics fluids (Figure 2.2). It is the case of the arteries that usually develop atherosclerosis. Thus, blood is modelled as a Newtonian and incompressible fluid (due to its density remains constant).

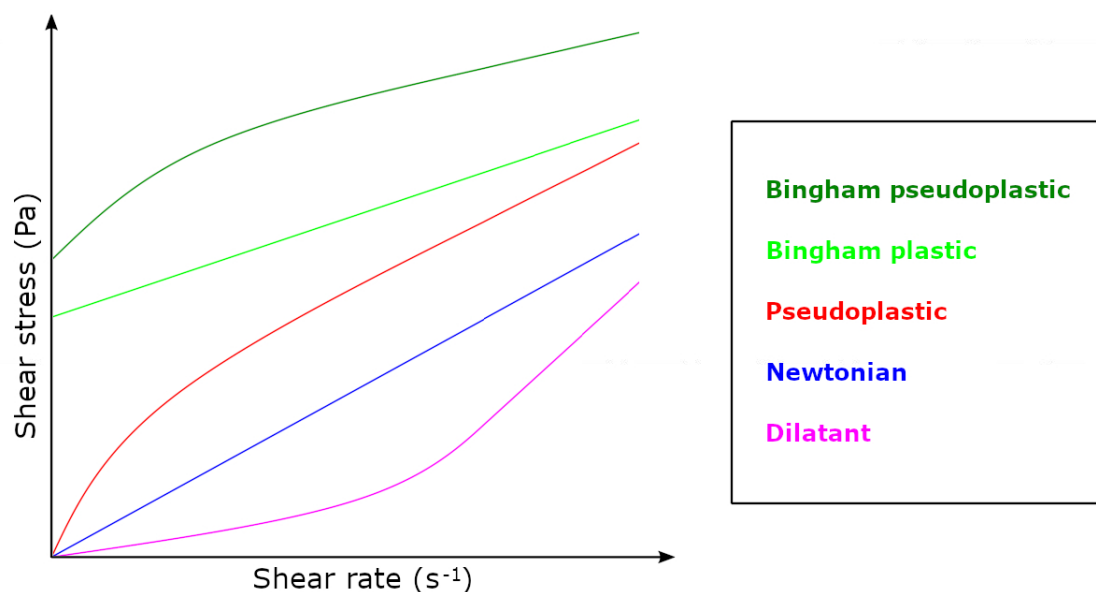


Figure 2.2: Fluid classification chart. Shear stress versus shear rate for different types of fluids (White, 1979).

Blood is basically composed by a liquid component, called plasma, and contains solid particles. Nevertheless, these particles are very small related to the lumen diameter of

arteries. Therefore, blood is considered as an homogeneous fluid (Caro et al., 1978). Additionally, blood flow is considered laminar due to Reynolds number in arteries under physiological conditions ($Re \approx 950$ for the case of carotid arteries, Malvè et al. (2014)).

Blood flow in lumen is governed by the Navier-Stokes and continuity equations:

$$\rho \frac{\partial \mathbf{u}_b}{\partial t} + \rho_b(\mathbf{u}_b \cdot \nabla) \mathbf{u}_b = \nabla \cdot [-P_b \mathbf{I} + \mu_b(\nabla \mathbf{u}_b + (\nabla \mathbf{u}_b)^T)] + \mathbf{F}_b \quad (2.1)$$

$$\rho_b \nabla \cdot \mathbf{u}_b = 0, \quad (2.2)$$

where the subscript b refers to blood so, parameters ρ_b and μ_b are, respectively, the density and dynamic viscosity of blood, while \mathbf{u}_b and P_b are the velocity and pressure of blood flow in the lumen. Finally, \mathbf{F}_b corresponds to internal forces of the blood, which are negligible in comparison with the friction between blood flow and the arterial wall (Cilla, 2013).

2.2.1 Boundary conditions

In addition, it is necessary to define some boundary conditions for blood flow in the lumen of the artery:

- No-slip condition of blood flow along the endothelium.
- Inlet velocity of blood flow.
- Outlet pressure of blood flow.

All the parameters that are necessary to calculate blood flow along the lumen are in Table 2.1.

Blood flow parameters

Parameter	Description	Value	Reference
μ_b	Blood dynamic viscosity	$0.0035 \text{ Pa} \cdot \text{s}$	Milnor (1989)
ρ_b	Blood density	$1050 \frac{\text{kg}}{\text{m}^3}$	Milnor (1989)

Table 2.1: List of the parameters needed to calculate blood flow in the arterial lumen.

2.3 Plasma flow across the arterial wall

The arterial wall is composed of different elements and cells with pores between them. All the layers that compose the arterial wall are permeable so the whole arterial wall is permeable as well (Caro et al., 1978). Due to this permeability, some elements contained in blood flow can cross the endothelium and get into the arterial wall. It is the case of plasma, which is the major component of blood. It consists mostly of water, but it also contains some mineral salts and proteins, among others (Mathew et al., 2022).

The plasma flow across the arterial wall can be modelled by Darcy's law, which is valid for cases of saturated and continuous media with Reynolds number lower than 10 which, as explained in the Appendix B of this Thesis, is the case of plasma flow in the arterial wall. Darcy's law (equation 2.3) represents a lineal relation between the velocity of plasma flow through the arterial wall, \mathbf{u}_p , and the pressure gradient in it, ∇P_p :

$$\mathbf{u}_p = -\frac{k_w}{\mu_p} \nabla P_p, \quad (2.3)$$

being k_w the Darcy permeability of the arterial wall, and μ_p the dynamic viscosity of plasma.

Furthermore, the continuity equation of plasma flow in the arterial wall has to be accomplished:

$$\frac{\partial(\epsilon_w \rho_p)}{\partial t} + \nabla \cdot (\rho_p \mathbf{u}_p) = J_v, \quad (2.4)$$

where ρ_p and ϵ_w are, respectively, the density of plasma and the porosity of the arterial wall. In addition, the term denoted as J_v represents plasma flow through the endothelium and it is calculated with Kedem-Katchalsky equations for flow through semi-permeable membranes considering the three pore model (Curry, 1974; Kedem and Katchalsky, 1958).

The endothelium is composed of cells, which are ordered to minimise the spaces between them. The three pore model considers that plasma flow through the endothelium is the result of the sum of various flows that have three different origins: Normal and leaky junctions between the endothelial cells, and vesicular pathways (Olgac et al., 2008). In Figure 2.3, a longitudinal section of the artery in a two-dimensional axisymmetric scheme is represented with its respective layers. The three pore model is also represented, by signalling normal and leaky junctions and vesicular pathways across the endothelium.

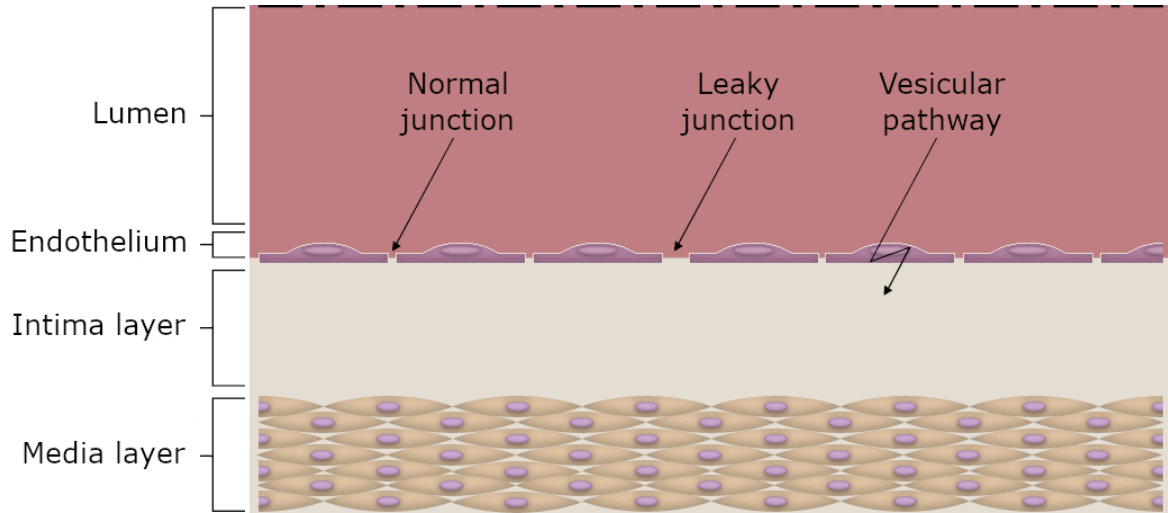


Figure 2.3: Structure of the arterial wall.

The first one of the flows has place when the endothelium is healthy, so endothelial cells have an elongated shape and the pores between them are small. In this case, all the junctions between cells are called "Normal Junctions". This plasma flow is denoted as Jv_{nj} .

On the other hand, when the endothelium is damaged or in some areas of flow recirculation, the cells that compose it are rounder. In this case, the pores between endothelial cells are bigger and allow more plasma flow. Therefore, there is an increase of the endothelial permeability in these areas. The largest junctions in these areas are called "Leaky Junctions", and plasma flow through leaky junctions is denoted as Jv_{lj} .

Finally, the third flow has place across the endothelial cells, and it occurs by "Vesicular Pathways". It is a way for molecules transport across membranes, in which a little plasma fraction can flow across the endothelium. This flow is represented as Jv_{vp} during all this Thesis. However, this plasma flow is very small related to the other two, so it is considered negligible (Olgac et al., 2008).

Therefore, plasma flow through the endothelium is due, in its totality, to convection and it can be expressed as:

$$J_v = Jv_{nj} + Jv_{lj} + \cancel{Jv_{vp}} \quad (2.5)$$

To completely determine plasma flow through the arterial wall, it is necessary to know the expressions corresponding to normal and leaky junctions flows. Plasma flow through normal junctions can be calculated as:

$$Jv_{nj} = Lp_{nj} \cdot (\Delta P_{End} - \cancel{\sigma_d} \Delta \Pi) \cdot (1 - \Phi_{lj}), \quad (2.6)$$

being Lp_{nj} the hydraulic conductivity of normal junctions. The value of Lp_{nj} depends on the thickness of the arterial wall (and, therefore, of the considered artery) and on the intraluminal pressure (Tedgui and Lever, 1984). ΔP_{End} is the pressure drop in the endothelium,

which depends on the intraluminal pressure, and takes values of 18 mmHg and 28 mmHg for intraluminal pressures of 70 mmHg and 180 mmHg , respectively (Tedgui and Lever, 1984). The term $\sigma_d \cdot \Delta\Pi$ is related to the osmotic pressure, being σ_d the osmotic reflection coefficient of plasma and $\Delta\Pi$ the osmotic pressure differential across the endothelium. However, according to Tedgui and Lever (1984), the influence of the osmotic term is small related to the one of the hydrostatic pressure, due to the osmotic pressure difference is approximately 10 mmHg , and the reflection coefficient cannot be higher than one. Therefore, the osmotic term is considered negligible (Tedgui and Lever, 1984). Finally, Φ_{lj} is the fraction of leaky junctions in the arterial wall (Huang et al., 1994; Huang and Tarbell, 1997; Weinbaum et al., 1985).

Nevertheless, the ratio Φ_{lj} is variable, but it is known experimentally that it is a function of the haemodynamics of blood flow, for example, of the wall shear stress (WSS) that blood flow produces in the endothelium, which can be calculated as:

$$WSS = \sqrt{\tau_x^2 + \tau_y^2 + \tau_z^2}, \quad (2.7)$$

where τ_x , τ_y and τ_z are the three components of the tangential stress vector in the different axes of the model for the lumen-wall interface of the model.

The ratio Φ_{lj} and WSS are related by experimental correlations based on the shape index of the endothelial cells (SI), that can be calculated as (Levesque et al., 1986):

$$SI = \frac{4\pi \cdot Area}{Perimeter^2}, \quad (2.8)$$

being *Area* and *Perimeter* those that corresponds to a unique endothelial cell so, SI takes a value of 1 for a circular cell and 0 for a linear cell.

Based on experimental data from Levesque et al. (1986), a relation between WSS of blood flow with the endothelium and the shape index of endothelial cells was proposed. In cases of low WSS, endothelial cells were circular, while with high WSS values they were more elongated.

To determine the behaviour of endothelial cells with WSS, a numerical correlation based in the experimental results of Levesque et al. (1986) is proposed. It was fitted using the software MATLAB (The MathWorks, Natick, Massachusetts, United States). This correlation is showed in Figure 2.4, obtaining that the endothelial shape index (SI) can be calculated as:

$$SI = 0.6296 \cdot e^{(-0.8709 \cdot WSS)} + 0.2145 \cdot e^{(-0.03938 \cdot WSS)} \quad (2.9)$$

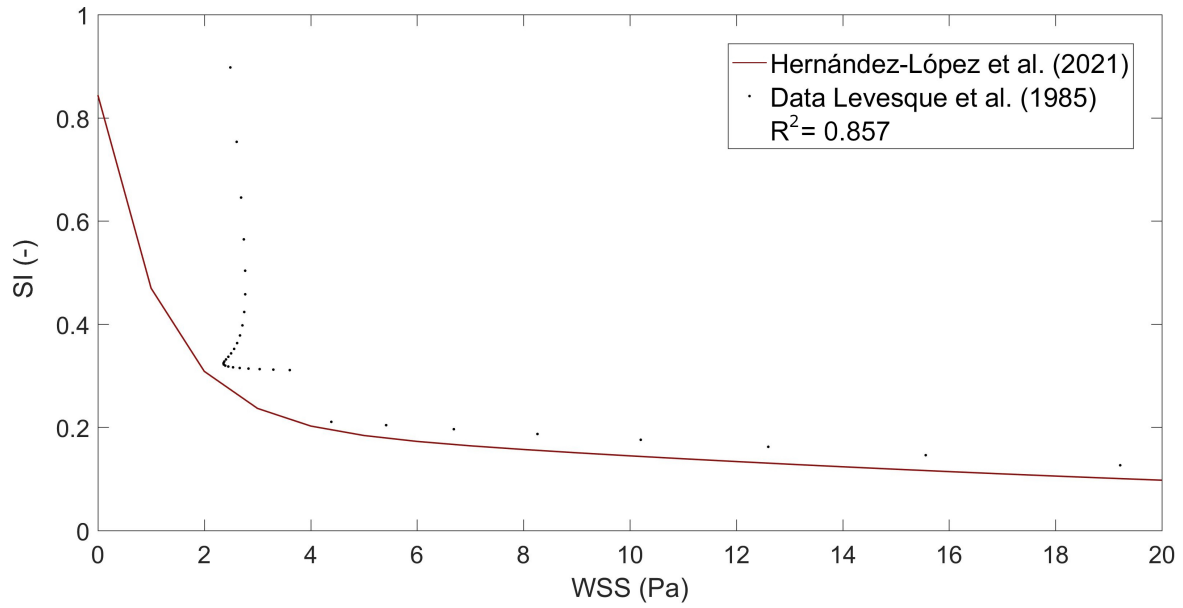


Figure 2.4: Correlation between Shape Index and Wall Shear Stress based on experimental data from [Levesque et al. \(1986\)](#). Dots of the graphic: Experimental data. Garnet line: Proposed correlation of WSS in function of SI.

It is well accepted that the areas of low WSS values are atheroprone, while the areas of high WSS values are atheroprotective. In particular, for carotid arteries, areas below 2 Pa are susceptible of atheroma plaques apparition ([Filipovic et al., 2013](#); [Younis et al., 2004](#); [Zhao et al., 2002](#)).

Cellular mitosis is a natural cellular division in which a cell gets divided into two new cells. In experimental studies of rat aortas, the number of endothelial mitotic cells (MC) in areas of known shape index was determined ([Chien, 2003](#)), so the next experimental correlation was developed for an unit area of 0.64 mm^2 ([Olgac et al., 2008](#)).

$$MC = 0.003797 \cdot e^{(14.75 \cdot SI)} \quad (2.10)$$

On the other hand, a leaky cell is an endothelial cell surrounded by a leaky junction and, therefore, substances and plasma can flow around it. Also basing in experimental studies, the next correlation relates the number of leaky cells (LC) and mitotic cells for the unit area of 0.64 mm^2 ([Lin et al., 1989](#); [Olgac et al., 2008](#)).

[Lin et al. \(1989\)](#) determined that the 45.3 % of areas of LDL leakage into the arterial wall are due to mitotic cells, and that, of the total mitotic cells, 80.5 % are leaky. In addition, [Olgac et al. \(2008\)](#), determined that the total number of leaky junctions due to non-mitotic cells was 30.7 %. Therefore, there are leaky cells associated to mitotic cells, but also to non-mitotic ones. The relation between the number of leaky and mitotic cells can be calculated as ([Olgac et al., 2008](#)):

$$LC = 0.307 + \frac{0.805 \cdot MC}{0.453} \quad (2.11)$$

Φ_{lj} is defined as the ratio between the area of leaky cells and the total area of the endothelium (Huang et al., 1994; Huang and Tarbell, 1997; Weinbaum et al., 1985). It can be calculated as:

$$\Phi_{lj} = \frac{LC \cdot \pi \cdot R_{cell}^2}{A_{unit}}, \quad (2.12)$$

taking as A_{unit} the unit area considered in all the anterior experimental correlations of 0.64 mm^2 . By using all the experimental correlations, it is possible now to obtain Φ_{lj} of Equation 2.6.

On the other hand, plasma flow through leaky junctions can be defined as:

$$Jv_{lj} = Lp_{lj} \cdot (\Delta P_{End} - \sigma_d \cdot \Delta \Pi), \quad (2.13)$$

where, as in normal junctions, ΔP_{End} , σ_d and $\Delta \Pi$ are, respectively, the pressure drop across the endothelium, the osmotic reflection coefficient and the osmotic pressure differential across the endothelium (negligible according to Tedgui and Lever (1984)). Finally, Lp_{lj} is the hydraulic conductivity of leaky junctions, that can be calculated with the equation 2.14:

$$Lp_{lj} = \frac{A_p}{S} \cdot Lp_{slj}, \quad (2.14)$$

where $\frac{A_p}{S}$ is the fraction of total area occupied by a leaky junction in relation to the total area available to it, and Lp_{slj} is the hydraulic conductivity of a single leaky junction.

To determine the value of these parameters, leaky junctions have been considered to have ring shape and to surround the leaky cells (Weinbaum et al., 1985; Yuan et al., 1991), as can be seen in Figure 2.5.

Leaky cells are assumed to be aleatory distributed with a distance between them of $2\varepsilon_{lj}$ (Weinbaum et al., 1985; Yuan et al., 1991). Therefore, circumferences of radius ε_{lj} can be traced periodically with a leaky cell in their respective centres.

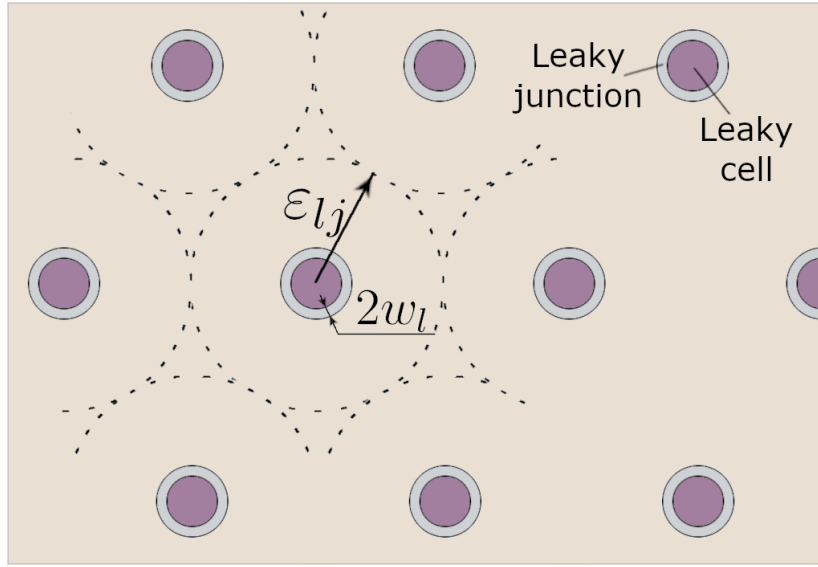


Figure 2.5: Distribution of leaky cells and leaky junctions in the endothelium. Leaky cells are represented in purple and leaky junctions in gray. Dashed circles represent the distribution between two leaky cells. Normal cells are located in the rest of areas and are represented with the background color.

According to Figure 2.5, the fraction of area occupied by a leaky junction versus the total area available to it can be defined as:

$$\frac{A_p}{S} = \frac{A_{slj}}{\pi \cdot \varepsilon_{lj}^2}, \quad (2.15)$$

where $\pi \cdot \varepsilon_{lj}^2$ is the total area available to a leaky junction (because they are separated a distance of $2 \cdot \varepsilon_{lj}$), and A_{slj} is the area of a single leaky junction, that can be calculated with the equation 2.16:

$$A_{slj} = \pi \cdot (R_{cell} + 2 \cdot w_l)^2 - \pi \cdot R_{cell}^2 = 2\pi \cdot R_{cell} \cdot 2w_l + w_l^2, \quad (2.16)$$

being R_{cell} the radius of endothelial cells, which takes a value of $15 \mu m$, and w_l the half-width of a leaky junction, $20 nm$ (Weinbaum et al., 1985). Assuming a simplification for reduced thickness which implies that the w_l^2 term can be neglected due to the small value of w_l in comparison to R_{cell} , the equation 2.16 can be rewritten as:

$$A_{slj} = 2\pi \cdot R_{cell} \cdot 2w_l \quad (2.17)$$

So, combining equations 2.15 and 2.17, $\frac{A_p}{S}$ can be written as:

$$\frac{A_p}{S} = \frac{4 \cdot R_{cell} \cdot w_l}{\varepsilon_{lj}^2} \quad (2.18)$$

As can be noticed, the value of ε_{lj} is still not known. However, the ratio between the area occupied by leaky cells an the experimental unit area, Φ_{lj} , can also be defined as the ratio between the area occupied by a leaky cell and the available area to it, so it can be rewritten as (Huang et al., 1994; Weinbaum et al., 1985):

$$\Phi_{lj} = \frac{R_{cell}^2}{\varepsilon_{lj}^2} \Rightarrow \varepsilon_{lj}^2 = \frac{R_{cell}^2}{\Phi_{lj}} \quad (2.19)$$

So, combining the equations 2.15, 2.16 and 2.19, the expression 2.20 can be obtained to calculate the area occupied by a leaky junction:

$$\frac{A_p}{S} = \frac{4w_l}{R_{cell}} \cdot \Phi_{lj} \Rightarrow \frac{A_p}{S} = \frac{4w_l \cdot \Phi_{lj}}{R_{cell}} \quad (2.20)$$

Therefore, the equation 2.14 can be written as:

$$Lp_{lj} = \frac{4w_l}{R_{cell}} \cdot \Phi_{lj} \cdot Lp_{slj} \quad (2.21)$$

Finally, attending to the equations 2.13 and 2.14, it can be observed that the hydraulic conductivity of a unique leaky junction, Lp_{slj} , is the only variable that rest to determine to have the flow of plasma through leaky junctions completely defined. This parameter can be defined as in Olgac et al. (2008):

$$Lp_{slj} = \frac{w_l^2}{3 \cdot \mu_p \cdot l_{lj}}, \quad (2.22)$$

being μ_p and w_l the dynamic viscosity of plasma, and the width of a leaky junction, respectively. Finally, l_{lj} represents the length of a leaky junction in the perpendicular plane to the endothelium membrane.

2.3.1 Boundary conditions

The boundary conditions that are imposed to calculate plasma flow from the lumen through the endothelium are:

- Normal inlet velocity of plasma into the arterial wall, at the endothelium. It is called J_v , and its calculation process has been already defined in this section of the Thesis.
- It is necessary to define the pressure at the adventitia, which takes a value of 17.5 mmHg (Olgac et al., 2008).

Table 2.2 shows all the parameters that are necessary to compute plasma flow through the endothelium.

Plasma flow parameters			
Parameter	Description	Value	Reference
<i>Physic properties</i>			
k_w	Darcy permeability	$1.2 \cdot 10^{-18} m^2$	Huang et al. (1994) Prosi et al. (2005)
$L_{p,nj}$	Normal junction conductivity	$1.984 \cdot 10^{-12} \frac{m}{s \cdot Pa}^{*,**}$	Tedgui and Lever (1984)
ϵ_w	Intima porosity	0.96	Ai and Vafai (2006)
μ_p	Plasma dynamic viscosity	$0.001 Pa \cdot s$	Milnor (1989)
ρ_p	Plasma density	$1050 \frac{kg}{m^3}$	Milnor (1989)
<i>Dimensions</i>			
A_{unit}	Unit area for the experimental correlations	$0.64 mm^2$	Lin et al. (1989) Olgac et al. (2008)
l_{lj}	Length of a leaky junction	$2 \mu m$	Weinbaum et al. (1985)
R_{cell}	Endothelial cell radius	$15 \mu m$	Weinbaum et al. (1985)
w_l	Half-width of a leaky junction	$20 nm$	Weinbaum et al. (1985)
<i>Pressures</i>			
P_{adv}	Pressure of the adventitia	$17.5 mmHg$	Olgac et al. (2008)
ΔP_{End}	Pressure drop in the endothelium	$20.727 mmHg^{**}$	Tedgui and Lever (1984)

Table 2.2: List of the parameters necessary to calculate plasma flow through the endothelium. * The value of the parameter is dependent of the considered artery (Table value for carotid arteries). ** The value of the parameter is dependent of the intraluminal pressure (Table value of $100 mmHg$).

2.4 Substances flow along the lumen

As commented before, blood contains several molecules and cells, such as LDL molecules and monocytes. LDL and monocytes are dragged across the arterial lumen by blood flow, and these movements are governed by convection-diffusion equations in the lumen:

$$\underbrace{\frac{\partial C_i}{\partial t}}_{Time} + \underbrace{\nabla \cdot (-D_i \nabla C_i)}_{Diffusion} + \underbrace{\mathbf{u}_b \cdot \nabla C_i}_{Convection} = 0 \quad (2.23)$$

The first term of the equation is related to temporal variations in the arterial lumen. The second term is due to the diffusion of the particles in blood, while the third one is due to their convection in blood. The variables C_i and D_i are the concentration and diffusion

coefficient of the considered substance in blood, and can be referred to LDL molecules or monocytes.

In addition, the flow of substances in the arterial lumen can be calculated as:

$$N_i = -D_i \nabla C_i + \mathbf{u}_b C_i, \quad (2.24)$$

where the first term is due to substances diffusion and the second one to their convection in the lumen.

2.4.1 Boundary conditions

The boundary conditions that are imposed for substances flows along the lumen are:

- Constant inlet concentrations of LDL molecules and monocytes. Normal values of LDL concentration in human blood are from 0.5 to 2 $\frac{mg_{LDL}}{ml}$ (Ai and Vafai, 2006) which, taking into account that the molecular mass of LDL is 386.65 $\frac{g}{mol_{LDL}}$ (Cilla, 2013), corresponds to 1.29 and 5.17 $\frac{mol_{LDL}}{m^3}$ respectively. The aim of this Thesis is to develop a computational model of atherosclerosis for pathological cases. Therefore, a high level of LDL concentration in blood equal to 2.7 $\frac{mg_{LDL}}{ml}$ is considered (Cilla, 2013), which corresponds to 6.98 $\frac{mol_{LDL}}{m^3}$. Moreover, a physiological monocyte inlet concentration in lumen of $550 \cdot 10^9 \frac{Monocyte}{m^3}$ is imposed as well (Khan, 2009).
- No LDL and monocyte flows through the endothelium. The aim of this step of the model is to obtain LDL and monocyte distributions in the lumen so, the solute flows through the endothelium are negligible compared to their concentrations in blood. Therefore, the loss of substances concentration in blood due to the transport into the arterial wall is considered to not affect concentrations in blood (Meyer et al., 1996).

Table 2.3 contains the parameters that are necessary for calculate LDL and monocyte flows along the lumen of arteries.

Substances flow in the lumen

Parameter	Description	Value	Reference
$C_{0,LDL,b}$	LDL concentration in blood	$6.98 \frac{mol_{LDL}}{m^3}$	Cilla (2013)
$C_{0,m,b}$	Monocyte concentration in blood	$550 \cdot 10^9 \frac{Monocyte}{m^3}$	Khan (2009)
$D_{LDL,b}$	LDL diffusion coefficient in blood	$5 \cdot 10^{-12} \frac{m^2}{s}$	Olgac et al. (2008)
$D_{m,b}$	Monocyte diffusion coefficient in blood	$1 \cdot 10^{-10} \frac{m^2}{s}$	Cilla et al. (2015)

Table 2.3: List of the parameters needed to calculate substances flow in lumen.

2.5 Inflammatory process of the arterial wall

There are many substances involved in the growth of atheroma plaques, among which low density lipoproteins (LDL), oxidised low density lipoproteins (oxLDL), monocytes (m), macrophages (M), cytokines (C), contractile and synthetic smooth muscle cells (CSMCs and SSMCs), foam cells (FC) and collagen fibres (Cg) are considered.

Behaviour of cells and substances in the arterial wall obeys convection-diffusion-reaction equations of the form:

$$\underbrace{\frac{\partial C_i}{\partial t}}_{Time} + \underbrace{\nabla \cdot (-D_i \nabla C_i)}_{Diffusion} + \underbrace{k_{lag,i} \cdot \mathbf{u}_p \cdot \nabla C_i}_{Convection} = \underbrace{f_{C_i}(\dots, C_i, \dots)}_{Source-sink} \quad (2.25)$$

The first term of the equation corresponds to temporal variations of the considered substance in the arterial wall, while the second and third terms are, respectively, diffusion and convection of the substance in it. Finally, reactive terms represent the interaction between substances in the arterial wall due to different phenomena e.g. chemotaxis, proliferation, differentiation, apoptosis, degradation or generation. Thus, the reactive terms are different for each of the considered substances.

In the Equation 2.25, C_i is the concentration of the considered substance and D_i its diffusion coefficient in the arterial wall. Due to the arterial wall layers and cells arrangement, the longitudinal and circumferential diffusions of substances in it are favoured over the radial ones, so diffusion of substances in the arterial wall has been considered anisotropic. According to Yuan et al. (1991), the ratio between the longitudinal and radial diffusion coefficients in the media layer of the arterial wall is approximately equal to 3. Due to the similar disposition of the arterial layers in the longitudinal and circumferential directions both, longitudinal and circumferential diffusion coefficients are considered equal. On the other hand, the convection of a substance in a free medium is not the same as in a porous one like the arterial wall. Thus, $k_{lag,i}$ limits the convection in the arterial wall related to the convection in a free medium, and it is named the solute lag coefficient of the considered substance in the arterial wall (Dabagh et al., 2009; Olgac et al., 2008; Sun et al., 2007).

The flow of substances across the arterial wall, N_i can be defined as:

$$\mathbf{N}_i = -D_i \nabla C_i + \mathbf{u}_p C_i, \quad (2.26)$$

in which the first and second terms are due to diffusion and convection of the considered substance, respectively.

In this Thesis, the only substance that has been considered to experience convection is LDL, due to its small size. Once that LDL gets oxidised, it has been considered that it does not experience convection. On the other hand, LDL, oxidised LDL, monocytes and macrophages have all been considered to experience diffusion in the arterial wall (Cilla et al., 2013).

All the parameters to calculate the inflammatory process in the arterial wall are collected in Table 2.5.

In the next subsections, a particularisation of the reactive terms is done for each one of the considered substances.

2.5.1 Evolution of LDL Concentration

Due to the small size of LDL molecules related to the arterial wall cells (LDL radius is approximately 11 nm (Tarbell, 2003) while endothelial cell radius is 15 μm (Weinbaum et al., 1985)), LDL molecules in the arterial are considered to experience convection. This convection is due to the plasma flow across the arterial wall and, due to the arterial wall pores, this convection is reduced by the $K_{lag,LDL}$ coefficient. LDL molecules additionally experience diffusion in the arterial wall (Filipovic, 2010; Prosi et al., 2005; Siogkas et al., 2011; Tomaso et al., 2011). On the other hand, once that a molecule of LDL is in the arterial wall, it gets oxidised (Libby, 2021; Libby et al., 2011). Therefore, the reactive term of LDL molecules represents their oxidation:

$$f_{C_{LDL,w}}(C_{LDL,w}) = \underbrace{-d_{LDL}C_{LDL,w}}_{\text{LDL oxidation}}, \quad (2.27)$$

where d_{LDL} and $C_{LDL,w}$ are, respectively, the oxidation ratio of LDL and its concentration at each time in the arterial wall.

In the same way as for plasma flow, LDL flow through the endothelium can be modelled with the three-pore model (Olgac et al., 2008). Molecules transport through the endothelium also occurs in different ways depending on their size: through normal and leaky junctions and vesicular pathways:

$$J_s = J_{s_{nj}} + J_{s_{lj}} + J_{s_{vp}} \quad (2.28)$$

LDL flow through each one of the possible ways in the endothelium can be calculated with the classical Kedem-Katchalsky equation (Kedem and Katchalsky, 1958):

$$J_{s,i} = C_{LDLdep} \cdot P_{app,i}, \quad (2.29)$$

being C_{LDLdep} the concentration of LDL molecules that are deposited in the arterial wall, and $P_{app,i}$ the coefficient of apparent permeability of the arterial wall, which can be referred to normal junctions, leaky junctions and vesicular pathways ($P_{app,nj}$, $P_{app,lj}$ and $P_{app,vp}$, respectively), according to the three pore model. For molecules with a size lower than 2 nm, transport is allowed through all the ways, but for greater molecules, which is the case of LDL, whose radius is approximately 11 nm (Tarbell, 2003), transport across normal junctions is not possible so, for this case, molecular transport through the endothelium only occurs by leaky junctions and vesicular pathways (Ogunrinade et al., 2002):

$$J_S = J_{S_{nj}} + J_{S_{lj}} + J_{S_{vp}} \quad (2.30)$$

According to [Cancel et al. \(2007\)](#), molecular transport of LDL through vesicular pathways corresponds to the 10 % of the flow through leaky junctions. Therefore:

$$P_{app,vp} = 0.1 \cdot P_{app,lj} \quad (2.31)$$

On the other hand, the apparent permeability of leaky junctions can be defined as ([Patlak et al., 1963](#); [Tarbell, 2003](#)):

$$P_{app,lj} = P_{lj} Z_{lj} + J_{v,lj} \cdot (1 - \sigma_{f,lj}), \quad (2.32)$$

where P_{lj} , Z_{lj} and $\sigma_{f,lj}$ are, respectively, the diffusive permeability of leaky junctions, a reduction factor of LDL concentration gradient at the entrance of the flow, and the solvent-drag coefficient of leaky junctions. So, combining equations 2.29, 2.31 and 2.32, LDL flow across the endothelium can be written as:

$$J_{S,LDL} = 1.1 \cdot C_{LDLdep} \cdot (P_{lj} Z_{lj} + J_{v,lj} (1 - \sigma_{f,lj})) \quad (2.33)$$

The diffusive permeability of leaky junctions is defined as ([Olgac et al., 2008](#)):

$$P_{lj} = \frac{A_p}{S} \chi P_{slj}, \quad (2.34)$$

where P_{slj} is the permeability of a single leaky junction, and χ is the difference between the total area of endothelial cells and the area of cells separated by leaky junctions:

$$\chi = 1 - \alpha_{lj}, \quad (2.35)$$

being α_{lj} the proportion of pore area occupied by substances transport which, for the case of LDL molecules, can be calculated as the ratio between the radius of an LDL molecule (R_{LDL}) and the half-width of a leaky junction (w_l) ([Olgac et al., 2008](#)):

$$\alpha_{lj} = \frac{R_{LDL}}{w_l} \quad (2.36)$$

On the other hand, P_{slj} can be calculated with the diffusion coefficient of LDL in a leaky junction (D_{lj}) and the length of a leaky junction (l_{lj}):

$$P_{slj} = \frac{D_{lj}}{l_{lj}} \quad (2.37)$$

The diffusion coefficient of LDL in a leaky junction is related to the LDL diffusion coefficient in the hole arterial wall with the next empirical correlation ([Renkin, 1954](#)):

$$\frac{D_{lj}}{D_l} = F(\alpha_{lj}) = 1 - 1.004\alpha_{lj} + 0.418\alpha_{lj}^3 - 0.16\alpha_{lj}^5 \quad (2.38)$$

On the other hand, the reduction factor of LDL concentration gradient, Z_{lj} , is a concentration reduction factor at the entrance of the pores of biological membranes, and it can be calculated as (Tarbell, 2003):

$$Z_{lj} = \frac{Pe_{lj}}{e^{(Pe_{lj})} - 1} \quad (2.39)$$

The reduction factor of LDL concentration depends on a modified Peclet number for membranes. This modified Peclet number relates convective and diffusive processes of the transport, and it is defined as (Tarbell, 2003):

$$Pe_{lj} = \frac{Jv, lj \cdot (1 - \sigma_{f, lj})}{P_{lj}} \quad (2.40)$$

For the cases of pure diffusion, Pe_{lj} tends to 0, so Z_{lj} tends to 1. In pure convective cases, Pe_{lj} tends to infinite and Z_{lj} to 0.

Finally, $\sigma_{f, lj}$ is the solvent-drag reflection coefficient of leaky junctions. It is a parameter to determine the selectivity of the endothelium to the entrance of substances into the arterial wall. Molecules with a reflection coefficient higher than one are excluded by the endothelium, and cannot cross into the arterial wall. It is given by the next equation Olgac et al. (2008):

$$\sigma_{f, lj} = 1 - \frac{2}{3}\alpha_{lj}^2(1 - \alpha_{lj}) \cdot F(\alpha_{lj}) - (1 - \alpha_{lj}) \left(\frac{2}{3} + \frac{2\alpha_{lj}}{3} - \frac{7\alpha_{lj}^2}{12} \right), \quad (2.41)$$

where the function $F(\alpha_{lj})$ has already been defined in Equation 2.38.

2.5.2 Evolution of Oxidised LDL Concentration

Once that a molecule of LDL gets into the arterial wall, it becomes oxidised. The hypothesis of, once that an LDL molecule is oxidised, it do not experience convection in the arterial wall has been done (Cilla et al., 2013).

However, oxidised LDL is considered to experience diffusion, due to its similar size to LDL (Oliveras et al., 2016). Thus, the oxidised LDL diffusion coefficient in the arterial wall is considered equal to the LDL ones. On the other hand, oxidised LDL molecules in the arterial wall are absorbed by macrophages. Therefore, oxidised LDL equation in the arterial wall has two reactive terms: The first one corresponds to LDL oxidation and the second one to the phagocytosis of oxidised LDL by macrophages.

$$f_{C_{oxLDL,w}}(C_{LDL,w}, C_{oxLDL,w}, C_{M,w}) = \underbrace{d_{LDL}C_{LDL,w}k_{(LDL-oxLDL)}}_{\text{LDL oxidation}} - \underbrace{LDL_{ox,r}C_{oxLDL,w}C_{M,w}}_{\text{OxLDL phagocytosed by macrophages}}, \quad (2.42)$$

where $C_{oxLDL,w}$ and $C_{M,w}$ are the oxidised LDL and macrophage concentrations at each point of the arterial wall. $LDL_{ox,r}$ is the ratio of the quantity of oxidised LDL that a single macrophage can absorb. Finally, $k_{(LDL-oxLDL)}$ is a parameter to make the unit conversion necessary to determine that, when an LDL molecule its oxidised, a new oxidised LDL molecule its formed.

2.5.3 Evolution of Monocyte Concentration

In a healthy artery, monocytes are present in the bloodstream. Due to the presence of oxidised LDL in the arterial wall of a pathological artery, there is a monocyte flow across the endothelium, from the lumen into the arterial wall. Due to this flow depends on the presence of oxidised LDL in the arterial wall, the monocyte flow across the endothelium depends also on the hemodynamical stimulus that has been considered for LDL flow into the arterial wall. For the case of WSS, it can be modelled with the next equation (Cilla et al., 2013).

$$J_{s,m}(WSS) = \frac{m_r}{\left(1 + \frac{WSS}{WSS_0}\right)} \cdot C_{oxLDL,w} C_{m,l}, \quad (2.43)$$

where m_r is the monocyte recruitment from the lumen into the endothelium. Monocyte flow across the endothelium is modelled as a sigmoid function, whose maximal and minimal values determine the areas of monocyte flow across the endothelium. Therefore, these values are dependent of the considered artery. In the case of a carotid artery, these values are equal to $2 Pa$ and $0 Pa$ (Filipovic et al., 2013; Younis et al., 2004; Zhao et al., 2002). To completely define the sigmoid, its average value called WSS_0 of $1 Pa$ is necessary.

Due to the large size of monocytes related to the arterial wall they do not have convection, but they experience diffusion in the arterial wall (Cilla et al., 2013). Once that a monocyte passes into the arterial wall, it can differentiate into a macrophage or, on the contrary, it can die due to apoptosis. Therefore, the monocyte equation in the arterial wall has two reactive terms: The first one corresponds to monocyte differentiation into macrophages and second one to their natural apoptosis:

$$f_{C_{m,w}}(C_{m,w}) = \underbrace{-d_m C_{m,w}}_{\text{Differentiation into macrophage}} - \underbrace{m_d C_{m,w}}_{\text{Monocyte apoptosis}}, \quad (2.44)$$

being $C_{m,w}$ the monocyte concentration in the arterial wall, d_m a parameter that represents the differentiation rate of monocytes into macrophages, and m_d the monocyte rate of apoptosis.

2.5.4 Evolution of Macrophage Concentration

Macrophages are cells so, in the arterial wall, they do not experience convection but they have diffusion (Cilla et al., 2013). Macrophages are formed in the arterial wall due to monocyte differentiation. In addition, once that they have phagocytosed as much of the oxidised LDL as they can, they become foam cells. Reactive terms of macrophages are, thus:

$$f_{C_{M,w}}(C_{M,w}, C_{m,w}, C_{oxLDL,w}) = \underbrace{d_m C_{m,w} k_{(m-M)}}_{\text{Monocyte differentiation}} - \underbrace{\frac{LDL_{ox,r}}{n_{FC}} \cdot C_{oxLDL,w} C_{M,w}}_{\text{Apoptosis to foam cells}}, \quad (2.45)$$

being the first term correspondent to monocyte differentiation into macrophages, and the second one relative to macrophage apoptosis.

$LDL_{ox,r}$ is the constant rate of oxidised LDL uptaken by macrophages and n_{FC} is the maximum amount of oxidised LDL that a single macrophage has to ingest to turn into a foam cell. To obtain the value of this parameter, it has been considered that macrophages are capable of ingest particles until 1.44 times their radius (Cannon and Swanson, 1992), taking into account that the density and molecular weight of LDL are $1063 \frac{kg}{m^3}$ (Ivanova et al., 2017) and $386.65 \frac{g}{mol}$ (Guarino et al., 2006), respectively. Finally, $k_{(m-M)}$ is a parameter to make the unit conversion that states that one monocyte differentiates into one macrophage.

2.5.5 Evolution of Cytokine Concentration

Cytokines are large size proteins so they do not experience convection in the arterial wall. In addition, cytokines are surrounded by macrophages so its diffusion can be considered negligible (Cilla et al., 2013). Cytokines are segregated by macrophages in the arterial wall due to the presence of oxidised LDL in it, and they also experience natural degradation. Therefore, the reactive terms of cytokines are due to their production by macrophages and to their natural degradation:

$$f_{C_{c,w}}(C_{c,w}, C_{oxLDL,w}, C_{M,w}) = \underbrace{C_r C_{oxLDL,w} C_{M,w}}_{\text{Production}} - \underbrace{d_c C_{c,w}}_{\text{Degradation}}, \quad (2.46)$$

where $C_{c,w}$ is the cytokine concentration in the arterial wall. C_r is the ratio of cytokine production by macrophages due to the presence of oxidised LDL in the arterial wall, and d_c is the cytokine degradation rate.

2.5.6 Evolution of Contractile Smooth Muscle Cell Concentration

Due to the big size of CSMCs the hypothesis that they have neither convection nor diffusion has been done. At the beginning of the inflammatory process, all the muscle cells in the arterial wall are of a contractile phenotype and, therefore, they can not move or interact with other cells or substances. However, the presence of cytokines in the arterial wall make the CSMCs change into a synthetic phenotype. Thus, CSMCs become SSMCs, which is represented by the reactive term:

$$f_{C_{SMC,w}}(C_{SMC,w}, C_{c,w}) = \underbrace{-C_{SMC,w} \cdot S_r \cdot \left(\frac{C_{c,w}}{k_c \cdot C_{c,w}^{th} + C_{c,w}} \right)}_{\text{Change of phenotype}} \quad (2.47)$$

$C_{SMC,w}$ is the CSMC concentration in the arterial wall. S_r represents CSMC rate of differentiation in SSMC due to the presence of cytokines and $C_{c,w}^{th}$ is a threshold of the maximum cytokine concentration allowed in the arterial wall. Finally, k_c is an adjustment parameter of the term whose determination is explained in more detail in Section 2.8.6.

2.5.7 Evolution of Synthetic Smooth Muscle Cell Concentration

Equally to CSMCs, SSMCs have neither convection nor diffusion. Once that a CSMC differentiates into a SSMC, it can proliferate or die due to apoptosis. Therefore, SSMC reactive terms in the arterial wall are, respectively, due to the differentiation of CSMCs into SSMCs and to SSMC proliferation and apoptosis:

$$\begin{aligned} f_{C_{SSMC,w}}(C_{SSMC,w}, C_{SMC,w}, C_{c,w}) = & \underbrace{C_{SMC,w} \cdot S_r \cdot \left(\frac{C_{c,w}}{k_c \cdot C_{c,w}^{th} + C_{c,w}} \right) \cdot k_{(SMC)}}_{\text{Change of phenotype}} + \\ & + \underbrace{\left(\frac{p_{ss} C_{c,w}}{C_{c,w}^{th}/2 + C_{c,w}} \right) C_{SSMC,w} \left(1 - \frac{C_{SSMC,w}}{C_{SSMC,w}^{th}} \right)}_{\text{Proliferation}} - \underbrace{r_{Apop} \cdot C_{SSMC,w}}_{\text{Apoptosis}} \end{aligned} \quad (2.48)$$

being $C_{SSMC,w}$ and $C_{SSMC,w}^{th}$ the concentration and a threshold of the maximum allowed concentration of SSMCs in the arterial wall. $k_{(SMC)}$ is a parameter to make the unit conversion that implies that one CSMC differentiates into one SSMC. Finally, p_{ss} and r_{Apop} are, respectively, the SSMC proliferation and apoptosis rates.

2.5.8 Evolution of Foam Cell Concentration

Foam cells have neither convection nor diffusion due to that they are dead cells. They are formed in the arterial wall once that a macrophage cannot ingest more quantity of

oxidised LDL. Foam cells compose the lipid core of atheroma plaques. Thus, their reactive term is:

$$f_{C_{FC,w}}(C_{oxLDL,w}, C_{M,w}) = \underbrace{\frac{LDL_{ox,r}}{n_{FC}} \cdot C_{oxLDL,w} C_{M,w} \cdot k_{(M-FC)}}_{\text{Macrophage apoptosis into foam cells}}, \quad (2.49)$$

where $k_{(M-FC)}$ is a parameter for unit conversion that represents that, when a macrophage has phagocytosed as much oxidised LDL as it can, it turns into a foam cell.

2.5.9 Evolution of Collagen Fibres

Finally, collagen fibres are molecules, so they can not move between the arterial wall pores. Therefore, collagen fibres in the arterial wall have neither convection nor diffusion. Collagen fibres are naturally present in the arterial wall. However, the aim of this mathematical model is to reproduce atheroma plaque formation and, thus, the natural collagen fibres production and degradation are not considered. Only non-equilibrium collagen fibres segregated by SSMCs due to atheroma plaque formation are considered. In addition, these collagen fibres can degrade. These are the two reactive terms of collagen considered in the process:

$$f_{C_{Cg,w}}(C_{Cg,w}, C_{SSMC,w}) = \underbrace{G_r \cdot C_{SSMC,w}}_{\text{Segregation}} - \underbrace{d_{Cg} \cdot C_{Cg,w}}_{\text{Degradation}}, \quad (2.50)$$

where G_r and d_{Cg} are the collagen secretion and degradation rates respectively, and $C_{Cg,w}$ its concentration in the arterial wall.

Table 2.4 contains a summary of the equations of the inflammatory process for all the considered substances.

Equations of the inflammatory process

Substance	Time	Diffusion	Convection	Source-sink
LDL	$\frac{\partial C_{LDL,w}}{\partial t}$	$\nabla \cdot (-D_{LDL,w} \nabla C_{LDL,w})$	$k_{lag,LDL} \cdot \mathbf{u}_p \cdot \nabla C_{LDL,w}$	$-d_{LDL} C_{LDL,w}$
Oxidised LDL	$\frac{\partial C_{oxLDL,w}}{\partial t}$	$\nabla \cdot (-D_{oxLDL,w} \nabla C_{oxLDL,w})$	—	$d_{LDL} C_{LDL,w} k_{LDL-oxLDL}$ $- LDL_{ox,r} C_{oxLDL,w} C_{M,w}$
Monocytes	$\frac{\partial C_{m,w}}{\partial t}$	$\nabla \cdot (-D_{m,w} \nabla C_{m,w})$	—	$-d_m C_{m,w}$ $-m_d C_{m,w}$
Macrophages	$\frac{\partial C_{M,w}}{\partial t}$	$\nabla \cdot (-D_{M,w} \nabla C_{M,w})$	—	$d_m C_{m,w} k_{(m-M)}$ $-\frac{LDL_{ox,r}}{n_{FC}} \cdot C_{oxLDL,w} C_{M,w}$
Cytokines	$\frac{\partial C_{c,w}}{\partial t}$	—	—	$C_r C_{oxLDL,w} C_{M,w}$ $-d_c C_{c,w}$
CSMCs	$\frac{\partial C_{CSMC,w}}{\partial t}$	—	—	$-C_{CSMC,w} \cdot S_r \cdot \left(\frac{C_{c,w}}{k_c \cdot C_{c,w}^{th} + C_{c,w}} \right)$
SSMCs	$\frac{\partial C_{SSMC,w}}{\partial t}$	—	—	$C_{CSMC,w} \cdot S_r \cdot \left(\frac{C_{c,w}}{k_c \cdot C_{c,w}^{th} + C_{c,w}} \right) \cdot k(SMC)$ $+ \left(\frac{p_{ss} C_{c,w}}{C_{c,w/2}^{th} + C_{c,w}} \right) C_{SSMC,w} \left(1 - \frac{C_{SSMC,w}}{C_{SSMC,w}^{th}} \right)$ $-T_{Apop} \cdot C_{SSMC,w}$
FCs	$\frac{\partial C_{FC,w}}{\partial t}$	—	—	$\frac{LDL_{ox,r}}{n_{FC}} \cdot C_{oxLDL,w} C_{M,w} \cdot k_{(M-FC)}$
Collagen	$\frac{\partial C_{Cg,w}}{\partial t}$	—	—	$G_r \cdot C_{SSMC,w}$ $-d_{Cg} \cdot C_{Cg,w}$

Table 2.4: Summary of the equations of the inflammatory process in the arterial wall.

2.5.10 Boundary conditions

The boundary conditions that are common to all the considered substances are:

- Substances transport across the endothelium is governed by plasma flow, which occurs in the normal direction to the longitudinal axis of the arterial lumen. Therefore, substances flows through both ends of the model are considered nulls.
- Adventitia is considered as an impermeable membrane so, there is no flow of substances through it.

In addition, there are some specific boundary conditions for some of the substances of the process:

- LDL convection velocity through the arterial wall corresponds to that of plasma flow in the arterial wall Section 2.3).
- LDL concentration in the adventitia, $C_{LDL,adv}$, has to be imposed following the experimental LDL distribution across the arterial wall of Meyer et al. (1996).
- At the beginning of the inflammatory process, the artery is considered as a healthy artery. Therefore, CSMCs are the only substance of the model that has initial concentration in the arterial wall (Yuan et al., 1991).
- The arterial wall is composed, among other substances, by collagen fibres. However, we consider that there is no initial concentration of collagen in the arterial wall. It is due to we model the collagen that is segregated due to the formation of atheroma plaques, but not the collagen that is naturally present in the arterial wall.
- Only LDL and monocytes can flow from the lumen into the arterial wall across the endothelium due to the rest of substances are not present in the bloodstream.

Table 2.5 includes all the parameters that are necessary to determine the inflammatory process of atheroma plaques formation in the arterial wall:

Inflammatory process parameters

Parameter	Description	Value	Reference
<i>Substances properties and dimensions</i>			
$D_{r,LDL,w}$ $D_{r,oxLDL,w}$	LDL and oxLDL diffusion coefficients in the radial direction of the arterial wall	$8 \cdot 10^{-13} \frac{m^2}{s}$	Prosi et al. (2005)
$D_{\theta,LDL,w}$ $D_{\theta,oxLDL,w}$	LDL and oxLDL diffusion coefficients in the circumferential direction of the arterial wall	$2.4 \cdot 10^{-12} \frac{m^2}{s}$	Prosi et al. (2005) Yuan et al. (1991)
$D_{z,LDL,w}$ $D_{z,oxLDL,w}$	LDL and oxLDL diffusion coefficients in the longitudinal direction of the arterial wall	$2.4 \cdot 10^{-12} \frac{m^2}{s}$	Prosi et al. (2005) Yuan et al. (1991)
$D_{r,m,w}$ $D_{r,M,w}$	Monocyte and macrophage diffusion coefficients in the radial direction of the arterial wall	$8 \cdot 10^{-15} \frac{m^2}{s}$	Cilla et al. (2013)
$D_{\theta,m,w}$ $D_{\theta,M,w}$	Monocyte and macrophage diffusion coefficients in the circumferential direction of the arterial wall	$2.4 \cdot 10^{-14} \frac{m^2}{s}$	Cilla et al. (2013) Yuan et al. (1991)
$D_{z,m,w}$ $D_{z,M,w}$	Monocyte and macrophage diffusion coefficients in the longitudinal direction of the arterial wall	$2.4 \cdot 10^{-14} \frac{m^2}{s}$	Cilla et al. (2013) Yuan et al. (1991)
$k_{lag,LDL}$	Solute lag coefficient of LDL	0.893	Dabagh et al. (2009)
l_{lj}	Length of a leaky junction	$2 \mu m$	Weinbaum et al. (1985)
Mw_{LDL}	LDL molecular weight	$386.65 \frac{g}{mol_{LDL}}$	Cilla (2013)
R_{LDL}	LDL radius	$11 nm$	Tarbell (2003)
w_l	Half-width of a leaky junction	$20 nm$	Weinbaum et al. (1985)
ρ_{LDL}	LDL density	$1063 \frac{kg}{m^3}$	Ivanova et al. (2017)
<i>Initial and threshold concentrations</i>			
$C_{0,CSMC}$	CSMC initial concentration	$3.16 \cdot 10^{13} \frac{CSMC}{m^3}$	Escuer et al. (2019)
$C_{c,w}^{th}$	Cytokine threshold	$1.235 \cdot 10^{13} \frac{mol_C}{m^3}^*$	Estimated
$C_{LDL,adv}$	LDL concentration at adventitia	$11.6, \%^{**} \cdot C_{LDLdep}$	Meyer et al. (1996)
$C_{SSMC,w}^{th}$	SSMC threshold	$4.764 \cdot 10^{13} \frac{SSMC}{m^3}$	Tracy (1997)
<i>Lumen-Arterial wall flow</i>			
C_{LDLdep}	LDL deposited at the endothelium	$10^{-2} \cdot C_{LDL,l}$	Meyer et al. (1996)
m_r	Monocyte recruitment	$6.636 \cdot 10^{-4} \frac{m^4}{mol_{oxLDL} \cdot d}^*$	Steinberg et al. (1997)
WSS_0	Reference WSS	$1 Pa^*$	Estimated

Table cont.

Inflammatory process parameters			
Parameter	Description	Value	Reference
<i>Parameters of reactive terms</i>			
C_r	Cytokine production	$3 \cdot 10^{-10} \frac{\text{mol}_C \cdot \text{m}^3}{\text{mol}_{oxLDL} \cdot \text{Macrophage} \cdot \text{s}}$	Cilla et al. (2013)
d_c	Cytokine degradation	$2.3148 \cdot 10^{-5} \text{ s}^{-1}$	Zhao et al. (2005)
d_{Cg}	Collagen degradation	$\frac{1}{30} \text{ d}^{-1}$	Humphrey (2002)
d_{LDL}	LDL oxidation frequency	$2.85 \cdot 10^{-4} \text{ s}^{-1}$	Ai and Vafai (2006)
d_m	Monocyte differentiation frequency	$1.15 \cdot 10^{-6} \text{ s}^{-1}$	Bulelzei and Dubbel-dam (2012)
G_r	Collagen production	$2.472 \cdot 10^{-21} \frac{\text{kg}_{Cg}}{\text{SSMC} \cdot \text{s}}$	Zahedmanesh et al. (2014)
k_c	Citokyne threshold factor	0.65093	Estimated
$LDL_{ox,r}$	Oxidised LDL uptake	$2.45 \cdot 10^{-23} \frac{\text{m}^3}{\text{Macrophage} \cdot \text{s}}$	Zhao et al. (2006)
m_d	Monocyte natural death frequency	$\frac{1}{60} \text{ d}^{-1}$	Krstic (1997)
n_{FC}	Maximum oxidised LDL uptake	$2.72 \cdot 10^{-11} \frac{\text{mol}_{oxLDL}}{\text{Macrophage}}$	Estimated
p_{ss}	SSMC proliferation	0.24 d^{-1}	Boyle et al. (2011)
r_{apop}	SSMC apoptosis rate	0.087 d^{-1}	Bennett et al. (1995)
S_r	SMC differentiation	0.0036 d^{-1}	Cilla et al. (2013)
<i>Conversion parameters</i>			
$k_{(LDL-oxLDL)}$	LDL oxidation into oxLDL	$1 \frac{\text{mol}_{oxLDL}}{\text{mol}_{LDL}}$	Estimated
$k_{(M-FC)}$	Macrophage death into SSMC	$1 \frac{\text{SSMC}}{\text{CSMC}}$	Estimated
$k_{(m-M)}$	Monocyte differentiation into macrophage	$1 \frac{\text{Macrophage}}{\text{Monocyte}}$	Estimated
$k_{(SMC)}$	CSMC differentiation into SSMC	$1 \frac{\text{SSMC}}{\text{CSMC}}$	Estimated

Table 2.5: List of the parameters that are needed to calculate the inflammatory process in arterial wall. * The values of these parameters are dependent of the considered artery (Table value for the case of carotid arteries). ** The value of the parameter is dependent of the intraluminal pressure (Table value for the case of 100 mmHg).

2.6 Arterial wall mechanical model

The arterial wall is modelled using the Yeoh's model for compressible, isotropic and hyperelastic materials, whose strain energy density function is (Yeoh, 1993):

$$\Psi = \sum_{i=1}^3 C_{Yeoh,i} \cdot [I_1 - 3]^i + \frac{1}{2} \cdot K_w (1 - J)^2, \quad (2.51)$$

where I_1 the first invariant of the right Cauchy-Green deformation tensor. $C_{Yeoh,i}$ are three material constants that were determined from experimental data. In addition, it is necessary to define the value of the initial compression modulus of the arterial wall, K_w . There are some studies in the literature, like Nolan and McGarry (2016) that shows that the arterial wall is not incompressible, and that it suffers a mean volumetric variation, J , of 9.31 %. K_w was fitted in order to find the value of initial compression of the arterial wall that corresponds to the experimental volumetric variation, obtaining a value of $4.46 \cdot 10^4 Pa$. This adjustment is included in Appendix A:

The constants used for the Yeoh's model can be seen in Table 2.6:

Parameter	Value (kPa)
$C_{Yeoh,1}$	17.005
$C_{Yeoh,2}$	- 73.424
$C_{Yeoh,3}$	414.952

Table 2.6: List of constants of the Yeoh's model in the arterial wall (Cebollero-Burgués, 2017).

2.6.1 Boundary conditions

To compute atheroma plaque mechanics wall it is necessary to define the next boundary conditions:

- Both ends of the model are fixed in the longitudinal axis of the artery (to avoid the movement of the artery as a rigid solid).
- Adventitia is fixed in the radial axis (to avoid its deformation occasioned by blood flow pressure).

2.7 Plaque initiation and growth

Finally, knowing the distribution of all the considered substances in the arterial wall, it is possible to compute the growth of atheroma plaques.

The arterial wall volumetric growth is due to the contribution of all the cells and substances that are present in the inflammatory process, but the influence of most of them is negligible due to their small sizes. Thus, only larger cells and collagen fibres are considered to contribute to plaque formation.

In addition, isotropic growth of plaques is considered so, the volumetric growth due to atheroma plaques formation can be written as:

$$\nabla \cdot v = \frac{\partial C_{FC,w}}{\partial t} \cdot v_{FC} + \frac{\partial C_{SSMC,w}}{\partial t} \cdot v_{SSMC} + \frac{\partial C_{Cg,w}}{\partial t} \cdot \frac{1}{\rho_{Cg}}, \quad (2.52)$$

where $C_{i,w}$ is the concentration of the considered substance in the arterial wall. v_{FC} and v_{SSMC} are, respectively, the volumes of a single FC and SSMC. Foam cells have been assumed to have spherical shapes whereas synthetic smooth muscle cells are modelled as ellipsoids, so their volumes can be calculated with Equations 2.53 and 2.54, respectively:

$$v_{FC} = \frac{4}{3}\pi R_{FC}^3 \quad (2.53)$$

$$v_{SSMC} = \frac{4}{3}\pi R_{SSMC}^2 \cdot l_{SSMC}, \quad (2.54)$$

being R_{FC} and R_{SSMC} the radius of a FC and a SSMC, respectively, and l_{SSMC} the length of a SSMC. Finally, ρ_{Cg} is the collagen density.

The parameters that are necessary to determine the growth of atheroma plaques in the arterial wall can be seen in Table 2.7.

Plaque growth parameters			
Parameter	Description	Value	Reference
l_{SSMC}	SSMC length	$115 \mu m$	Cilla et al. (2013)
R_{FC}	Foam cell radius	$15.264 \mu m$	Krombach et al. (1997) Cannon and Swanson (1992)
R_{SSMC}	SSMC radius	$3.75 \mu m$	Cilla et al. (2013)
ρ_{Cg}	Collagen density	$1000 \frac{kg}{m^3}$	Sáez et al. (2013)

Table 2.7: List of the parameters that are needed to calculate plaque growth in the arterial wall.

2.8 Summary of the improvements

As commented before, the mathematical model developed in this Thesis is based in the one proposed by Cilla et al. (2013).

Some changes in the equations of the previous model have been made in order to improve its convergence, as well as its biological meaning. These changes have been made in different terms of the equations, that are correspondent to the isotropy of diffusion coefficients of substances in the arterial wall, to plasma and LDL flows across the endothelium, and to changes in the reactive terms of some substances. In addition, it has been noticed that the convergence of the model is affected by the exponential terms, and the computational times of the model are bigger when exponential terms are considered. Therefore, all the exponentials in the reactive terms of the previous model have been replaced by others with fractional terms to improve the model convergence. Also, some conversion parameters have been added to the equations to improve the consistency of the units.

In this section, all the changes that have been made in the equations of the previous model are explained.

2.8.1 Substances diffusion coefficients

On the previous model, the diffusion coefficients in the arterial wall of LDL and monocytes were isotropic. In this Thesis, a change in these parameters has been done to improve their biological precision. According to layers and cells disposition in the arterial wall, the longitudinal and circumferential transports are favoured against the radial ones (Yuan et al., 1991).

Yuan et al. (1991) determined that the biological ratio between the longitudinal and radial diffusion coefficients of substances in the arterial wall is equal to 3. The diffusion coefficients of the substances that were considered in the previous model have been supposed to be the radial diffusion coefficients of the substances. Therefore, the longitudinal diffusion coefficients considered are the radial ones multiplied by 3. Due to the similar disposition of the arterial wall layers, the diffusion coefficients in the longitudinal and circumferential directions in the arterial are considered to be equals.

2.8.2 Plasma flow

In relation to the plasma flow across the endothelium, the equation to determine plasma flow through normal junctions has been changed. It previously was:

$$Jv_{nj} = Lp_{nj} \cdot (\Delta P - \sigma_d \cdot \Delta \Pi) \quad (2.55)$$

However, the equation 2.55 does not consider the decrease of the number of normal junctions that is produced when the number of leaky junctions increases (leaky junctions are not new junctions but they are normal junctions that turn into leaky junctions). Therefore, in the new equation 2.56, the decrease of normal junctions number due to leaky junctions apparition is considered by adding the parenthesis $(1 - \Phi_{lj})$:

$$Jv_{nj} = Lp_{nj} \cdot (\Delta P - \sigma_d \cdot \Delta \Pi) \cdot (1 - \Phi_{lj}), \quad (2.56)$$

where Φ_{lj} is the fraction of leaky junctions in the endothelium. This change in the equation is coherent with the equation of plasma flow across the leaky junctions (2.13), in which, as can be seen, the variable Lp_{lj} depends on Φ_{lj} too (equation 2.21).

2.8.3 LDL molecules

Two different changes have been made in the equations related to LDL molecules in the arterial wall:

- Change in LDL flow through the endothelium: The equation of LDL flow from the lumen into the arterial wall across the endothelium in the previous model was:

$$J_{S,LDL} = \frac{C_{LDL,l}}{1 + \frac{C_{LDL,l}}{C_{LDL,l}^{th}}} \cdot LDL_{dep} \cdot P_{app}, \quad (2.57)$$

where $C_{LDL,l}^{th}$ was a threshold of LDL concentration in the lumen, which had the value of the inlet LDL concentration in the lumen set as a boundary layer. As can be seen in the equation 2.57, there is a saturation term to limit LDL concentration in the arterial wall. However, the convection and diffusion terms of LDL in the arterial wall directly depend on the LDL concentration gradient. Therefore, LDL concentration in the arterial wall cannot be higher than LDL concentration in the lumen of the artery. Thus, this term of saturation is not necessary. In addition, a new variable named C_{LDLdep} has been defined as the concentration of LDL that is deposited into the arterial wall, and can be calculated as:

$$C_{LDLdep} = 10^{-2} \cdot C_{LDL,l} \quad (2.58)$$

Therefore, as can be seen in Section 2.5, the equation 2.57 has been changed, to:

$$J_{S,LDL} = C_{LDLdep} \cdot P_{app}, \quad (2.59)$$

- Consideration of the arterial wall pores in LDL molecules convection: The previous model considered the convection of LDL in the arterial wall in the same way than convection in a free medium. However, the arterial wall has a large quantity of pores due to its composition made of different cells. Therefore, substances convection in the arterial wall is affected by its pores and does not behave as in a free medium. It is the case of LDL molecules convection, which is the only substance that has been considered to experience convection in the arterial wall. To take into account the influence of the arterial wall pores in LDL convection, a parameter named solute lag

coefficient of LDL ($K_{lag,LDL}$) has been included in the correspondent term of LDL convection (equation 2.25). Therefore, $K_{lag,LDL}$ limits the LDL convection in the arterial wall due to the consideration of its pores and take the value of 0.893. More details about the determination of $K_{lag,LDL}$ are in Appendix A.

2.8.4 Monocyte

The reactive terms of monocytes in the arterial wall of the previous model are:

$$f_{C_{m,w}}(C_{m,w}) = \underbrace{-d_m C_{m,w}}_{\text{Differentiation into macrophages}} \underbrace{-m_d C_{m,w}}_{\text{Monocyte apoptosis}} + \underbrace{+ C_{m,w} C_{oxLDL,w} \cdot \exp\left(\frac{-C_{m,w}^2}{2C_{m,w}^{th2}}\right)}_{\text{Proliferation}} \quad (2.60)$$

As can be seen in the equations 2.44 and 2.60, in the previous model there was an additional reactive term of monocytes in the arterial wall that is not considered in this Thesis. This term was due to proliferation of monocytes in the arterial wall, and depends on monocyte and oxidised LDL concentrations in it. It also depends on a threshold of the maximum monocyte concentration in the arterial wall. It is an exponential term and it worsens the convergence of the model. Therefore, this term has been analysed to improve its unit consistency and convergence and, as can be seen in Figure 2.6, it has been noticed that this term provides very little concentration of monocytes compared to the other terms in the equation.

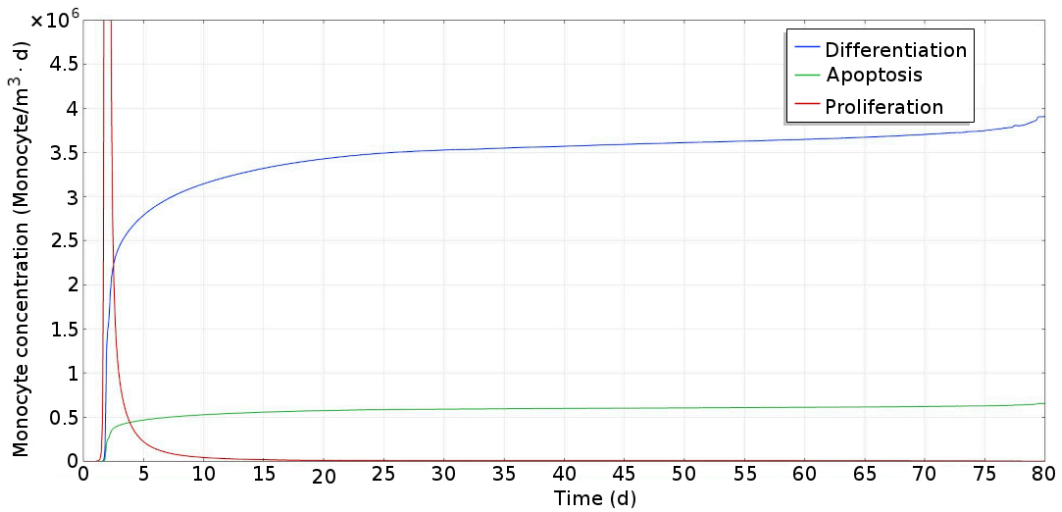


Figure 2.6: Evolution of monocyte concentration. Blue line represents the term of differentiation. Green line represents the term of apoptosis. Red line represents the term of proliferation (maximum concentration due to proliferation: $1.12 \cdot 10^8 \text{ Monocyte}/(\text{m}^3 \cdot \text{d})$).

Therefore, the term of monocyte proliferation of this equation has been neglected and, the reactive terms of monocytes in this thesis are, as can be seen in the equation 2.44, only due to monocyte differentiation into macrophages and to monocyte apoptosis.

2.8.5 Macrophage

Macrophage reactive terms are due to macrophages that are generated as a consequence of monocyte differentiation and to macrophage apoptosis into foam cells once that they cannot ingest more quantity of oxidised LDL.

The apoptosis of macrophages into foam cells in the previous model was:

$$-\frac{M_{r1}}{M_{r2}} \cdot LDL_{ox,r} C_{oxLDL,w} C_{M,w} \quad (2.61)$$

However, there is no unit consistency of this term of the equation and, also to improve its physical meaning, a new one has been developed in this Thesis:

$$-\frac{LDL_{ox,r}}{n_{FC}} \cdot C_{oxLDL,w} C_{M,w} \quad (2.62)$$

$LDL_{ox,r}$ is the quantity of oxidised LDL that a single macrophage can phagocyte in a day. Its value can be determined by knowing the rate of LDL quantity uptaken by a cell protein in a day and the quantity of macrophages that a cell protein contains, according to Zhao et al. (2006) and Steinman and Cohn (1972), respectively. In addition, n_{FC} represents the maximum quantity of oxidised LDL that a macrophage can phagocyte before turn into a foam cell, and can be calculated by knowing the volume of oxidised LDL that a macrophage can ingest, its density and its molecular weight, according to Krombach et al. (1997) and Cannon and Swanson (1992). The determination of the values of these parameters are explained in more detail in the appendix A.

2.8.6 Contractile Smooth Muscle Cells

The equations with exponential terms where optimised by replacing these terms with fractional ones. It is the case of the term referred to the change of phenotype of smooth muscle cells, which in the previous model was calculated as:

$$-C_{SMC,w} \cdot \left(1 - \exp\left(-\frac{S_r C_{c,w}}{C_{c,w}^{th}}\right)\right) \quad (2.63)$$

As can be seen in the equation 2.63, in addition, the unit of the exponential is inconsistent (it should be dimensionless).

The new developed term that has been used in this Thesis can be seen in the equation 2.64. To determine the value of the adjustment constant of the new term, k_c , a process of

minimisation by least squares was carried out so that the response of the new term was equivalent to the previous one. The value of k_c was then set to 0.65093.

$$-C_{CSMC,w} \cdot S_r \cdot \left(\frac{C_{c,w}}{k_c \cdot C_{c,w}^{th} + C_{c,w}} \right) \quad (2.64)$$

The behaviour of the two terms (the correspondent to the previous model and the developed here) can be seen in Figure 2.7, where it can be observed that the two different terms have similar behaviours:

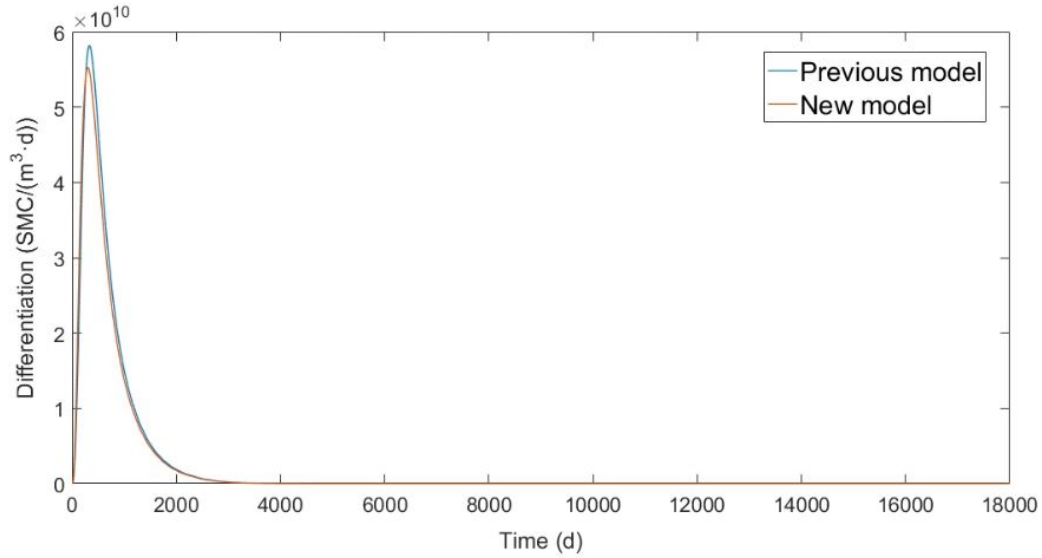


Figure 2.7: Evolution of the SMCs differentiation from the contractile phenotype into the synthetic one. Blue line represents the evolution in the previous model. Red line represents the evolution in the new model, without the exponential.

2.8.7 Synthetic Smooth Muscle Cells

A total of three changes have been made in the reactive terms of synthetic smooth muscle cells:

- The term correspondent to smooth muscle cells change of phenotype has been changed, according to the case of contractile smooth muscle cells term (2.8.6).
- The previous work modelled synthetic smooth muscle cell chemotaxis in the arterial wall. However, it represented proliferation instead of chemotaxis. The term used in the previous work was:

$$C_{SSMC,w} \frac{C_{c,w}}{C_{c,w}^{th}} m_{ss} \quad (2.65)$$

The value of the parameter m_{ss} was too small related to the literature values. Therefore, the value of this parameter was adjusted according to the literature (Boyle et al., 2011), and its name was changed to p_{ss} due to it is related to proliferation of synthetic smooth muscle cells. In addition, the saturation function of the term was changed to be of the form of all the new ones. Due to the new value of p_{ss} is very big related to the previous value of m_{ss} , the concentration of synthetic smooth muscle cells increases a lot. Therefore, a maximum concentration threshold was included, to limit the upper value of synthetic smooth muscle cells concentration in a biological range. Thus, the new term of proliferation of synthetic smooth muscle cells is:

$$\left(\frac{p_{ss} C_{c,w}}{C_{c,w/2}^{th} + C_{c,w}} \right) C_{SSMC,w} \left(1 - \frac{C_{SSMC,w}}{C_{SSMC,w}^{th}} \right) \quad (2.66)$$

- The apoptosis of synthetic smooth muscle cells has been added in this Thesis:

$$-r_{Apop} \cdot C_{SSMC,w}, \quad (2.67)$$

where r_{Apop} is the apoptosis rate of synthetic smooth muscle cells, and whose value determination is explained in the Appendix A of this tesis.

2.8.8 Foam Cells

The only reactive term of foam cells is the correspondent to macrophages that suffer apoptosis and turn into foam cells due to the phagocytosis of large quantities of oxidised LDL. This term is the same than in the equation of macrophages and, therefore, it has been modified. This change has been already explained in Section 2.8.5 of this chapter.

2.8.9 Conversion parameters

To finally achieve the unit consistency of all the equations of the model, some conversion parameters have been added to it. These conversion parameters are included in the reactive terms of the equations that appear in two difference substances, to model the change of a substance into another one, due to a physic process. It is the case of:

- $k_{(LDL \rightarrow oxLDL)}$: Conversion parameter that represents that a molecule of LDL gets oxidised and form another one of oxidised LDL.
- $k_{(m \rightarrow M)}$: Conversion parameter to represent the differentiation of a monocyte into a macrophage.
- $k_{(SMC)}$: Conversion parameter for the change of phenotype of a contractile smooth muscle cell into a synthetic one.

- $k_{(M-FC)}$: Conversion parameter to determine the death of a macrophage into a foam cell when it phagocytes the maximum quantity of oxidised LDL that is possible.

Chapter 3

Two-dimensional axisymmetric model

Part of the contents of this Chapter can be found in:

- Hernández-López, P.; Martínez, M.A.; Peña, E.; Cilla, M.
Understanding the Parameter Influence on Lesion Growth
for a Mechanobiology Model of Atherosclerosis.
Mathematics 2023, 11(4), 829.
<https://doi.org/10.3390/math11040829>

Chapter 3

3.1 General Overview

In this chapter, the reference axisymmetric computational model used in this Thesis is explained. In Section 3.2, the geometry used for all the two-dimensional models of this Thesis is introduced, which corresponds to a two-dimensional axisymmetric model of a carotid artery. In Section 3.3, the reference vulnerable model with stationary blood flow is analysed. In this section, the boundary conditions, the haemodynamical stimulus that is considered to initiate the process of atheroma plaques formation and the numerical methods are included. In addition, sensitivity analysis of the meshes of the lumen and the arterial wall are carried out. The results of the commented model are presented and analysed too.

In Section 3.4, some changes in the equations of the reference vulnerable model are developed to change the morphology of the obtained atheroma plaque, from a vulnerable plaque to a non-vulnerable one. In addition, the results obtained in this case are included. In Section 3.5, a comparison of the results of the vulnerable and non-vulnerable plaque models is done. Finally, in Section 3.6, a sensitivity analysis of the parameters of the model is developed as well.

3.2 Geometry

The reference model has been developed with a geometry of a carotid artery. This geometry is based on the model of Olgac et al. (2008) for coronary arteries, adapting the diameter of the lumen and the thickness of the arterial wall to the correspondent ones for carotid arteries. Carotid arteries have a bifurcation, which can be seen in Figure 1.4 of Chapter 1 of this Thesis.

However, the reference model of this Thesis has been developed in a two dimensional axisymmetric geometry, so it is not possible to model the bifurcation of the carotid arteries. It has been noticed that the area of carotid arteries that develops more quantity of plaques is the area of the bifurcation and, in particular, the area near the internal carotid artery (ICA) (Filipovic et al., 2013; Sáez et al., 2015; Younis et al., 2004; Zhao et al., 2002).

Therefore, the geometric parameters of the internal carotid artery in the area near the bifurcation have been chosen.

To determine the value of the lumen diameter, some patient-specific carotid images obtained with computed tomography scan (CT) provided by the Hospital Clínico Universitario Lozano Blesa in Zaragoza (Spain) have been used, according to ethics guidelines of the hospital. These clinical images are presented in more detail in Chapter 4 of this Thesis.

The diameter of the arterial lumen of the model has been determined with the value of the diameter of the internal carotid artery near the bifurcation from a healthy patient, and corresponds to a radius of 1.815 mm . The arterial wall of this reference model has been modelled as a mono-layered wall with homogeneous properties, and its thickness has been considered equal to 0.7 mm , according to Sommer et al. (2010), since only the arterial lumen is visible in CT images.

Figure 3.1 shows the considered geometry, which is composed of the lumen and the arterial wall with an obstacle that simulate a previous plaque disturbing the blood flow.

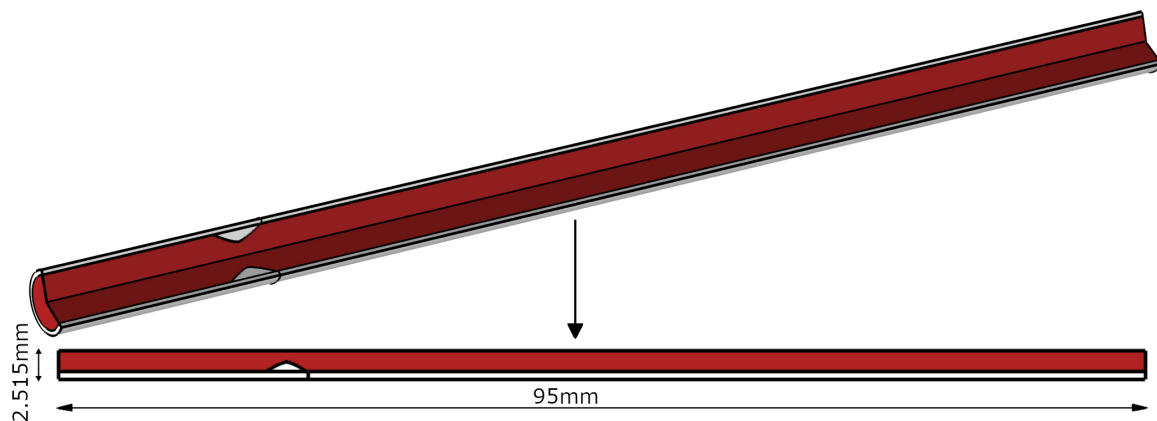


Figure 3.1: Two-dimensional axisymmetric geometry. Composed of lumen (in red color), arterial wall, and the previous plaque (both in white color).

As commented before in Chapter 2, atheroma plaques growth is related to some mechanical stimuli caused by blood flow. These mechanical stimuli produce a change in the shape index of the endothelial cells and, therefore, an increase in the endothelial permeability (Chien, 2008; Dai et al., 2004). Due to it, the obstacle plaque has been included in the geometry to reproduce a phenomenon that has been observed in real patients, called double stenosis: A first atheroma plaque emerge and disturbs blood flow downstream it, causing a recirculation and so, an increase of the permeability of the endothelium due to the change in the endothelial cells. Therefore, a new plaque is developed downstream the first one (De Bruyne et al., 2000; Pijls et al., 2000). The evolution of this second plaque is the one whose development is analysed in this Thesis.

To determine the geometry of the obstacle plaque for the case of the geometry of the carotid artery, it is necessary to define the stenosis ratio: a variable that is used to deter-

mine how much diameter of the lumen is occluded by the growth of an atheroma plaque. The stenosis ratio is defined as:

$$SR(\%) = \left(1 - \frac{\text{Area of lumen with plaque}}{\text{Area of healthy lumen}} \right) \cdot 100 \quad (3.1)$$

The stenosis ratio of the obstacle plaque in the geometry of coronary artery of [Olgac et al. \(2008\)](#) is equal to 64%. Therefore, to keep the same stenosis ratio in our geometry of carotid artery, the maximum height of the obstacle plaque has been set equal to 0.726 mm.

In addition, the length upstream of the obstacle plaque has been defined as five times the diameter of the artery to ensure that blood flow is completely developed before reach the obstacle plaque.

3.3 Reference vulnerable model

In this section, the case of the reference vulnerable model is analysed. The boundary conditions of blood flow in this case are explained in this section, as well as the haemodynamical stimulus considered to initiate the inflammatory process of the arterial wall. In addition, the sensitivity analysis of the lumen and the arterial wall meshes are included.

3.3.1 Governing equations

The governing equations of the vulnerable reference model and its parameters have been already explained in Chapter 2 of this Thesis, including the respective values that have been considered for all the parameters of the model.

3.3.2 Boundary conditions

The values of the inlet blood mass flow and outlet pressure in the internal carotid artery were taken from [Malvè et al. \(2014\)](#). They are applied as boundary conditions to determine blood flow along the arterial lumen. In that paper, they consider blood flow in a transitory way. Therefore, their values of blood mass flow and pressures are dependent on time, according to the cardiac cycle. However, in the reference model of this Thesis, blood flow is modelled as stationary. Thus, the average values of blood mass flow and pressure during a cardiac cycle are imposed as boundary conditions. In particular, the average inlet mass flow considered for the blood flow is equal to $5.3025 \cdot 10^{-3} \frac{kg}{s}$, and the average outlet pressure is 100 mmHg.

Table 3.1 contains the geometric parameters and boundary conditions of blood flow that are applied to the reference model.

	Parameter	Value
Geometrical parameters	Arterial lumen radius	1.815 mm
	Arterial wall thickness	0.7 mm
	Geometry lenght	95 mm
	SR of the obstacle plaque	64%
Blood flow parameters	Inlet blood flow	$5.3025 \cdot 10^{-3} \frac{\text{kg}}{\text{s}}$
	Outlet pressure	100 mmHg
Substance concentrations in the lumen	LDL	$6.98 \frac{\text{mol}_{LDL}}{\text{m}^3}$
	Monocytes	$550 \cdot 10^9 \frac{\text{Monocyte}}{\text{m}^3}$

Table 3.1: Values of the geometrical and blood flow parameters, and substance concentrations considered in the lumen for the reference model.

3.3.3 Haemodynamical stimulus

In the reference model, the considered mechanical stimulus to initiate the inflammatory process in the arterial wall is the Wall Shear Stress (WSS) of blood flow in the endothelium. It is an index that has been widely used to predict the location of atheroma plaques. However, the WSS has the limitation of being calculated for stationary blood flow and does not consider the cardiac cycle. It is well known that areas with physiological WSS promote endothelial cells to have an elongated shape, so pores between them are small and limit the flow of substances through the endothelium. In contrast, for areas with low WSS, the endothelial cells are more circular, so the pores between them are larger there and allow flow of substances across the endothelium, resulting in plaque emergence (Figure 1.5) (Chien, 2008; Dai et al., 2004). The threshold of WSS below which plaques can grow depends on the considered artery (Filipovic et al., 2013; Olgac et al., 2008). In the case of carotid arteries, areas with WSS lower than 2 Pa could be considered atheroprone, while areas of higher WSS are atheroprotective (Filipovic et al., 2013; Younis et al., 2004; Zhao et al., 2002).

3.3.4 Numerical methods

The software COMSOL Multiphysics (COMSOL AB, Burlington, MA, USA) has been used to solve the model. The numerical model has been solved using four consecutive steps, commented in Chapter 2 of this Thesis. First of all, the stationary blood and plasma flows have been computed in two consecutive stationary steps. In the third step, the inflammatory process of the arterial wall is calculated, for a total time of simulation equal to 10 years . Finally, the growth of the plaque in the year 10 is computed, in a last stationary step.

A direct solver (multi-frontal massively parallel sparse direct solver, MUMPS (MUMPS, 1999)) has been used to calculate all the steps of the model. In addition, the inflammatory process has been calculated using groups of segregated steps for the different substances.

The solution to the transient problems has been obtained using the Backwards differentiation formula (BDF) method (Curtiss and Hirschgelder, 1952; Gear, 1967), which is implicit, following Newton's method for non-linear problems.

The total number of degrees of freedom of the lumen can be determined by multiplying the components of the velocity of blood and the number of nodes in the lumen mesh. For the case of the arterial wall, the number of degrees of freedom would be equal to the multiplication of the components of the plasma flow velocity, the number of substance concentrations that we calculate and the number of nodes of the arterial wall mesh.

3.3.5 Sensitivity analysis of the mesh

A sensitivity analysis of the mesh has been done in both, the lumen and the arterial wall meshes, in order to determine which mesh is the more suitable one to solve the model with the minimal computational cost and providing accurate results. The domains of the model have been meshed using quadrilateral elements and, in the case of the mesh of the lumen, adding boundary layers near the endothelium to ensure the correct determination of the mechanical stimuli that blood flow produces in it. A discretisation of the geometry with P1-P1 elements has been made for the blood flow calculation, quadratic elements are used for the plasma flow through the endothelium, linear elements are used for the inflammatory process in the arterial wall, and quadratic Serendipity elements for the growth of the plaque.

The software COMSOL Multiphysics has some predefined options for meshing. In particular, for meshing a domain in which the physic to compute is fluid mechanics (the case of the lumen), the predefined meshes characteristics are shown in Table 3.2.

Mesh	Max. element size (mm)	Min. element size (mm)	Max. element growth rate	Resolution of curvature	Resolution of narrow regions
Extremely coarse	0.482	0.0153	1.4	1	0.9
Extra coarse	0.285	0.011	1.3	0.8	1
Coarser	0.191	0.00876	1.25	0.6	1
Coarse	0.147	0.00657	1.2	0.4	1
Normal	0.0986	0.00438	1.15	0.3	1
Fine	0.0767	0.00219	1.13	0.3	1
Finer	0.0613	$8.76 \cdot 10^{-4}$	1.1	0.25	1
Extra fine	0.0285	$3.29 \cdot 10^{-4}$	1.08	0.25	1
Extremely fine	0.0147	$4.38 \cdot 10^{-5}$	1.05	0.2	1

Table 3.2: Characteristics of the predefined meshes of COMSOL Multiphysics for domains with fluid mechanics.

To perform the sensitivity analysis of the mesh of the lumen, the extra coarse mesh has been selected in the first place, doing progressively a refinement of it to achieve finer meshes.

The procedure to determine which one of the meshes is the most appropriate consist in compare the results obtained with a mesh with the ones obtained with the immediately finer mesh, in order to observe the variation of their results. A variation in the results of less than 5% is considered acceptable. Therefore, if a result variation between two different meshes is higher than 5%, the coarse mesh will be automatically discarded. On the contrary, if none of the results achieved with two consecutive meshes vary more than a 5%, the coarser mesh will be considered as the most adequate mesh, and it will be the selected mesh.

To determine the most adequate mesh, the length of the endothelium with WSS lower than $2 Pa$ in analysed, as it has been observed that in carotid arteries the plaque grows when the WSS is less than $2 Pa$ (Filipovic et al., 2013; Younis et al., 2004; Zhao et al., 2002). In addition, the maximum velocities of blood flow in the hole lumen and in the section of the higher obstacle plaque height are analysed too.

As commented before, the mesh of the lumen will have some boundary layers to ensure the correct determination of the mechanical stimuli in the endothelium. Thus, the analysis of this mesh is developed in two different steps: On the first place, a mesh with a high number of boundary layers (specifically eight) will be analyse to determine the adequate element size. Then, knowing the element size adequate for the mesh, an analysis of the results obtained varying the number of boundary layers in the endothelium is done, to determine the quantity of boundary layers that are necessary.

In Table 3.3, the results obtained with different predefined meshes for the lumen are shown. The number of nodes of each one of the considered meshes and the computational time required to solve them are indicated as well. As can be seen, the difference of the computational time and of the number of nodes highly increase for the case of the finer mesh, but the results are similar than the ones obtained with the fine mesh.

Mesh	N. nodes of the mesh	Computational time	Length of WSS < $2 Pa$ (mm)	Max. blood velocity (m/s)	
				Lumen	Obstacle plaque area
Extra coarse	4455	14 s	30.85	1.7214	1.6888
Coarse	11420	26 s	31.61	1.7161	1.6696
Normal	22126	46 s	31.44	1.7296	1.6799
Fine	41660	57 s	32.30	1.7268	1.6796
Finer with max. elem. size 0.052 mm	80588	1 min 57 s	32.32	1.7255	1.6794

Table 3.3: Results obtained for the length of WSS lower than $2 Pa$ and maximum velocities in the hole lumen and in the area of the obstacle plaque depending on the mesh.

In Table 3.4, the variation of the results obtained with the different meshes is showed. As can be seen, the variation of the results obtained in all the cases is lower than 5 %.

Mesh comparison	Length of $WSS < 2 Pa$ variation (%)	Max. blood velocity variation (%)	
		Lumen	Obstacle plaque area
Coarse vs Extra coarse	2.4635	0.3079	1.1369
Normal vs Coarse	0.5378	0.7867	0.6169
Fine vs Normal	2.7354	0.1619	0.0179
Finer vs Fine	0.0619	0.0753	0.0119

Table 3.4: Variation (%) of the length of WSS lower than $2 Pa$ and of the maximum velocities in the hole lumen and in the area of the obstacle plaque depending on the mesh.

In Table 3.4, it can be notice a variation of more than 2 % in the length of endothelium with a WSS lower than $2 Pa$ for the extra coarse and normal meshes. Thus, these meshes can be discarded. The coarse mesh provides results that are similar to the ones of the normal mesh, but as the normal mesh has been discarded, the coarse mesh is discarded as well. On the contrary, for the cases of the fine and extra fine meshes, the results variation is small for all the parameters but, due to the difference of computational cost between these two meshes, the fine mesh is finally selected.

The next step on the sensitivity analysis of the mesh of the lumen is to determine the quantity of necessary boundary layers. For this purpose, the selected fine mesh is defined as the reference mesh, and its number of boundary layers has been varied, as can be seen in Table 3.5.

Boundary layers	N. nodes of the mesh	Computational time	Length of $WSS < 2 Pa$ (mm)	Max. blood velocity (m/s)	
				In the lumen	Obstacle plaque area
0	31700	51 s	31.82	1.7268	1.7898
1	32945	52 s	33.60	1.7268	1.6794
2	34190	55 s	32.93	1.7268	1.6796
3	35435	58 s	32.83	1.7268	1.6796
4	36680	56 s	32.45	1.7266	1.7896
5	37925	59 s	32.36	1.7266	1.7896
6	39170	54 s	32.31	1.7266	1.6794
7	40415	56 s	32.31	1.7266	1.6794
8	41660	57 s	32.30	1.7266	1.6794

Table 3.5: Results obtained for the length of WSS lower than $2 Pa$ and maximum velocities in the hole lumen and in the area of the obstacle plaque.

As can be seen in Table 3.5, the computational time required is similar in all the analysed cases, so it will not be a determinant factor in this analysis.

In Table 3.6, the variation of the analysed parameters is showed. These variations have been determined for each one of the boundary layers cases with the reference mesh of eight boundary layers.

Number of boundary layers comparison	Length of $WSS < 2 Pa$ variation (%)	Max. blood velocity variation (%)	
		Lumen	Obstacle plaque area
0 vs 8	1.4861	0.0116	6.5738
1 vs 8	4.0248	0.0116	0
2 vs 8	1.9505	0.0116	0.0119
3 vs 8	1.6409	0.0116	0.0119
4 vs 8	0.4644	0	6.5619
5 vs 8	0.1858	0	6.5619
6 vs 8	0.0310	0	0
7 vs 8	0.0310	0	0

Table 3.6: Variation (%) of the length of WSS lower than $2 Pa$ and of the maximum velocities in the hole lumen and in the area of the obstacle plaque depending on the number of boundary layers.

As can be seen in Table 3.6, the meshes with 0, 4 and 5 boundary layers have a variation in the maximum blood velocity in the area of the obstacle plaque higher than 5 %, so they can be discarded. All the meshes with 1, 2, 3, 6 and 7 boundary layers provide similar results than the reference mesh with 8 boundary layers, so the meshes with 2 and 3 boundary layers are considered enough. Of these two meshes, the one that differs less in the results of all the analysed parameters is the mesh with 3 boundary layers. So, the fine mesh with three boundary layers has been considered enough to discretise the lumen of the artery with the required accuracy, with a total of 35435 nodes.

As the arterial wall is meshed with quadrilateral elements and due to that the shape of the arterial wall in which the plaque is developed is rectangular, the mesh of the arterial wall is structured and, therefore, it is no necessary to define boundary layers to achieve more than one element in every section of the arterial wall.

To analyse the stability of the solution, the same criteria of the 5 % of variation is used. The results to analyse the stability in this case are the concentration of LDL in the area of the arterial wall that develops the maximum plaque, and the maximum growth of the plaque, regarding the displacement of the endothelium due to the plaque. Due to the computational cost, the time that has been calculated to analyse the sensitivity of the mesh is equal to one year.

A total of three meshes are analysed, whose number of nodes in the arterial wall and the maximum plaque growth can be seen in Table 3.7. As can be seen, the coarser mesh is the number one, while the finer is the number three:

Number of mesh	Number of nodes in the arterial wall	Wall thickness increase (mm)	Variation %
1	34055	0.8477	-
2	36001	0.8495	0.2123
3	36974	0.8534	0.4590

Table 3.7: Number of mesh, nodes and wall thickness increase for the analysed meshes in the arterial wall. Variation of the wall thickness increase between the considered and its immediate coarser meshes.

As can be seen in table 3.7, the variation of the wall thickness increase obtained with the three meshes is lower than 5 %. Therefore, the displacement of the endothelium due to the plaque growth will not be determinant to select the mesh, and the concentration of LDL in the section of maximum plaque development will be the criteria.

To determine the variation of concentration of LDL in each one of the meshes, a line perpendicular to the lumen has been traced across the arterial wall, from the endothelium to the adventitia, in the section of maximum plaque growth, to analyse the profile of LDL concentration in this line. Once that the profile of LDL concentration is known for a mesh, this concentration has been increased and reduced by a 5 %, obtaining a region in which the variation of LDL concentration is less than a 5 % from the obtained concentration.

In the next Figure, the region of LDL concentration variation of $\pm 5\%$ obtained for mesh 1 is represented, as well as the profile of LDL concentration obtained for mesh 2. As can be seen, the profile obtained with the second mesh in some points is outside of the defined region and, therefore, the variation of concentration is higher than a 5 %, so mesh 1 can be discarded.

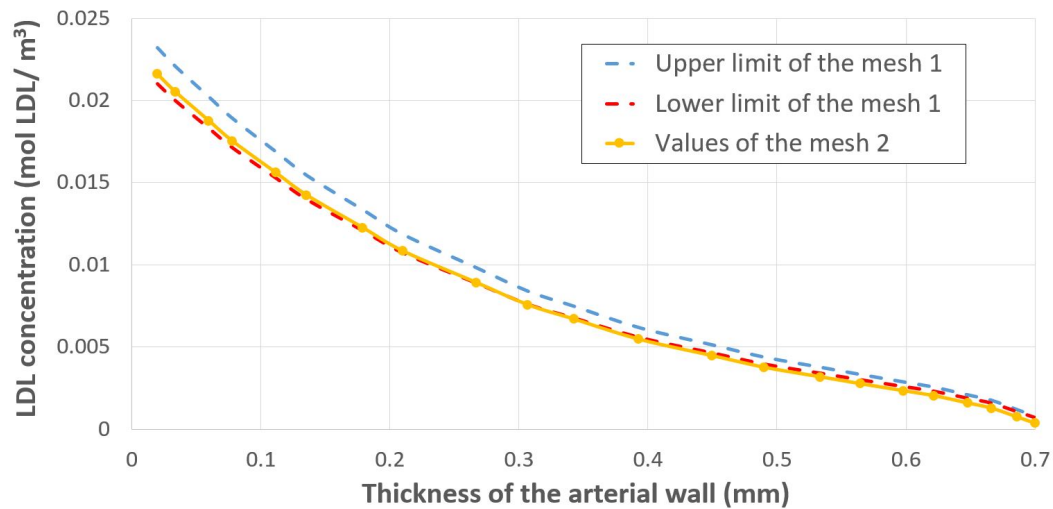


Figure 3.2: LDL concentration profile limits of the mesh 1 (Blue and red dashed lines for + 5 % and – 5 %, respectively), and LDL concentration profile for the mesh 2, in the section of maximum plaque development.

The process has been repeated with meshes 2 and 3, Figure 3.3:

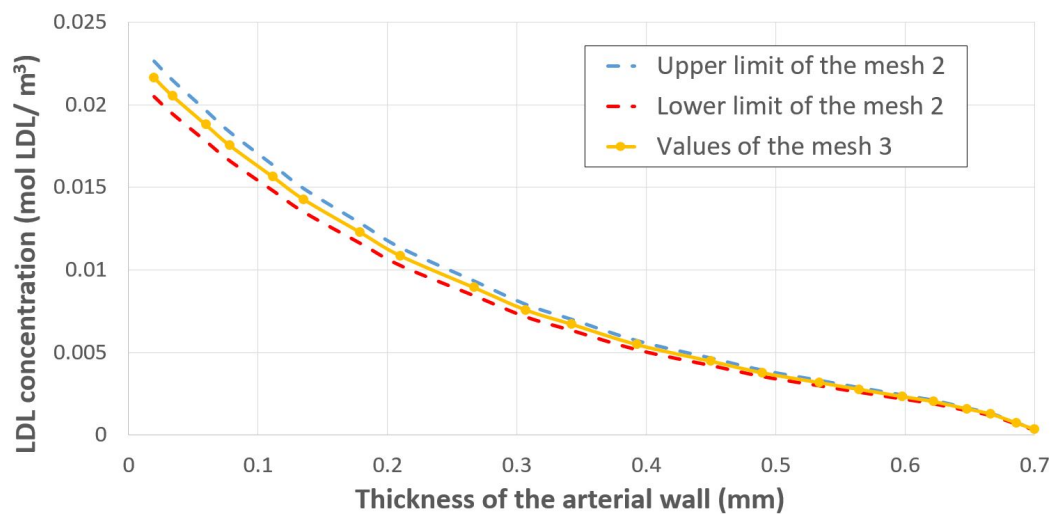


Figure 3.3: LDL concentration profile limits of the mesh 2 (Blue and red dashed lines for + 5 % and – 5 %, respectively), and LDL concentration profile for the mesh 3, in the section of maximum plaque development.

As can be seen in Figure 3.3, the variation of the profile of LDL concentration between the second and third meshes is less than a 5 % in all the LDL concentration profile. Therefore, the selected mesh for the arterial wall is the second one of Table 3.7.

The obstacle plaque and the area of the arterial wall upstream it do not need to be meshed due to no results are obtained for these areas.

The details of the second mesh of the arterial wall can be seen in Table 3.8:

Max. element size (mm)	Min. element size (mm)	Max. element growth rate	Resolution of curvature	Resolution of narrow regions
0.0195	0.00675	1.2	0.25	1

Table 3.8: Details of the selected mesh for the arterial wall.

Thus, the total number of nodes and boundary layers of the selected meshes of the lumen and the arterial wall are:

Mesh	Number of nodes	Number of boundary layers
Lumen	35435	3
Arterial wall	36001	0
Total mesh	70463	-

Table 3.9: Number of nodes and boundary layers of the selected meshes for the lumen and the arterial wall.

Two details of the selected meshes in the area of the obstacle plaque and downstream it can be seen in Figure 3.4, where the boundary layers of the mesh of the arterial lumen can be observed, attached to the endothelium. In addition, it can be seen that the mesh of the arterial wall is structured.

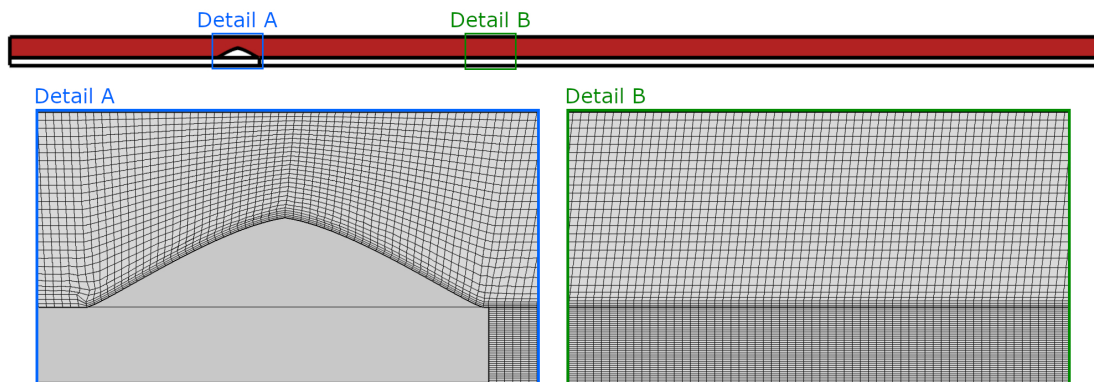


Figure 3.4: Details of the lumen and arterial wall meshes for the area of the obstacle plaque (Detail A) and for an example area downstream the obstacle plaque (Detail B).

3.3.6 Analysis of the geometry length

The length of the geometry before the obstacle plaque has been set equal to five times its diameter, to ensure the correct development of blood flow before reach the obstacle.

The model developed by [Olgac et al. \(2008\)](#) considers a total length of the artery equal to 111 *mm*. However, to reduce the computational cost of the model, an analysis of its necessary length was developed in the Master of Science in Biomedical Engineering final project made by Nicolás Laita Dieste ([Laita, 2019](#)), in which the author of this Thesis was co-director.

Three different total lengths were analysed: 65 *mm*, 95 *mm* and 115 *mm*, obtaining the results included in Table 3.10. This results are correspondent to the model for a coronary artery. However, it has been determined that the selected length is also valid for the case of the carotid model.

Analysed parameter	Total geometry length			Variation (%)	
	115 mm	95 mm	65 mm	95 vs 115 mm	65 vs 115 mm
Recirculation length (mm)	16.21	16.29	16.31	0.4935	0.6169
Máximum WSS (Pa)	63.01	63.17	63.18	0.2539	0.2697
Plaque position (mm)	20.95	20.93	20.92	0.0954	0.1431
Blood max. velocity (m/s)	0.96209	0.96209	0.96214	0	0.0051

Table 3.10: Results obtained for the three different total lengths analysed for the reference model ([Laita, 2019](#)).

As can be seen in Table 3.10, none of the results analysed with the different lengths varies more than a 5 % respect the considered length by [Olgac et al. \(2008\)](#), so all of them would be valid. To ensure that blood flow is completely developed at the end of the geometry, the case of length equal to 95 *mm* was selected. Thus, a total length of the geometry of 95 *mm* is used during all this Thesis.

3.3.7 Vulnerable plaque model results

In this section, the results obtained for the reference vulnerable model are shown.

In Figure 3.5, the velocity of blood flow along all the lumen is included, with two details of the velocity in the areas near the obstacle plaque and in the end of the geometry. It is possible to see how the blood flow is adapted to the shape of the geometry.

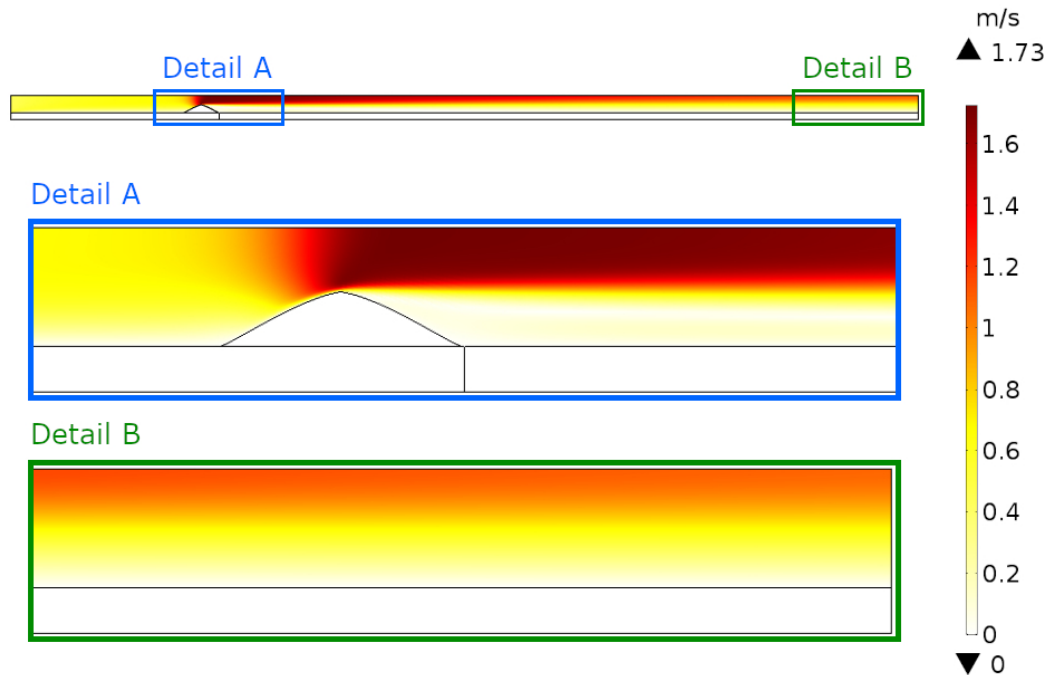


Figure 3.5: Velocity of the blood flow for the axisymmetric model in two dimensions. Details A and B show, respectively, details of the areas near the obstacle plaque and near the outlet of the geometry.

In Figure 3.5, it can be observed that the velocity of blood in the area of the obstacle plaque increases due to the decrease of the cross-section of the arterial lumen (due to the mass conservation equation). In addition, it can be seen that the blood flow is fully developed before reach the obstacle plaque and also at the end of the model, so the selected length for the geometry is adequate. As can be seen, the blood velocity in the area close to the endothelium is zero (due to the no-slip condition).

In addition, in Figure 3.5, it can be observed that the velocity of blood downstream the obstacle plaque is lower than in the other areas of the geometry. It is due to the recirculation that the obstacle plaque produces in the blood flow, which can be seen in Figure 3.6, in which the streamlines of blood flow can be observed:

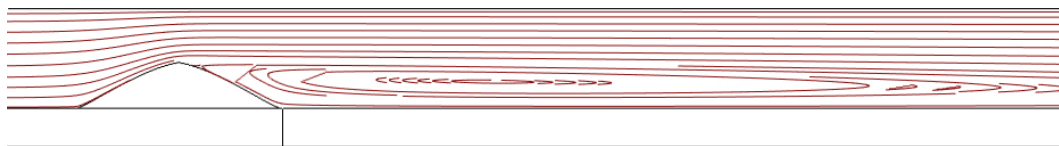


Figure 3.6: Streamlines of blood flow downstream the obstacle plaque in detail A.

In Figure 3.7 the profile of WSS along all the endothelium can be seen, from the inlet of the geometry to its outlet (which correspond to 0 mm and 95 mm in the horizontal axes of the graphic, respectively).

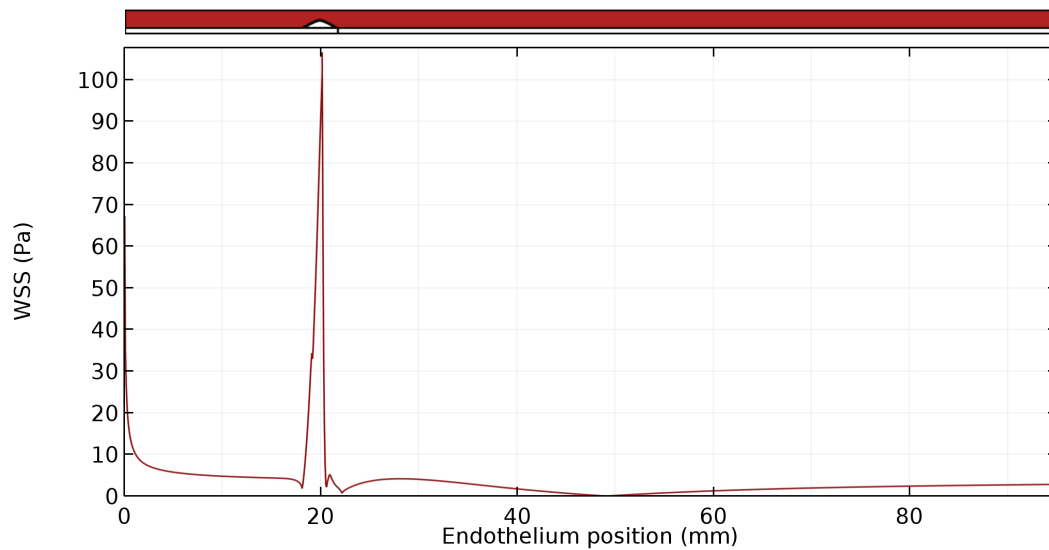


Figure 3.7: WSS profile along the hole geometry.

In Figure 3.7, it can be observed an increase of the values of WSS in the areas of the endothelium correspondent to the obstacle plaque, due to the increase of velocity that is produced there. In addition, the recirculation of blood present downstream the obstacle plaque causes a diminution in its velocity (Figure 3.5), that occasions a diminution in the WSS of this area. After that, the WSS increases again and reach a stable value which means that the blood flow is fully developed again.

The distribution of LDL and monocyte concentrations in the lumen are represented in Figure 3.8. As can be seen, both concentrations are constant in all the lumen. Therefore, the concentrations of LDL and monocytes in blood in the other models analysed in this Thesis have been considered as boundary conditions, by setting the inlet values of concentrations into the arterial wall.

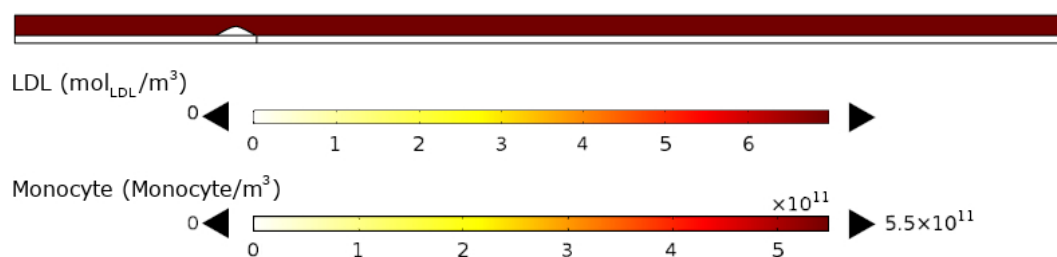


Figure 3.8: Distribution of LDL and monocyte concentrations in the lumen of the artery.

In Figure 3.9, the velocity of plasma flow across the arterial wall is represented. As can be seen, the plasma velocity is higher in the area that corresponds to the minimum WSS due to the end of the recirculation of blood flow occasioned by the obstacle plaque, which cause an increase of the endothelial permeability in this area.

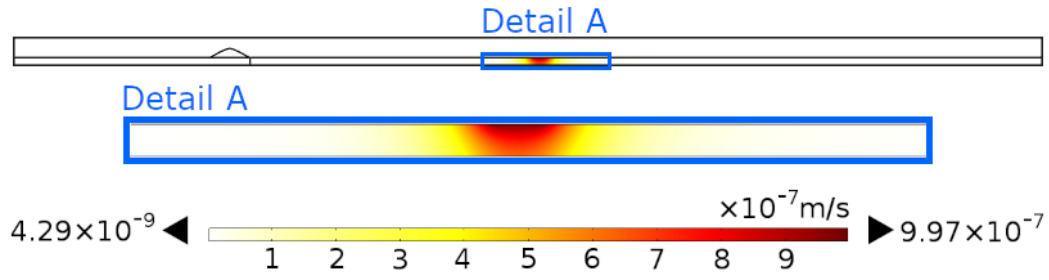


Figure 3.9: Velocity of plasma in the arterial wall.

The flows of LDL and monocytes from the lumen into the arterial wall, across the endothelium, are represented in Figure 3.10, in blue and garnet colors, respectively. As can be seen, these flows occur in the area of the geometry with low values of WSS, following Equations 2.33 and 2.43.

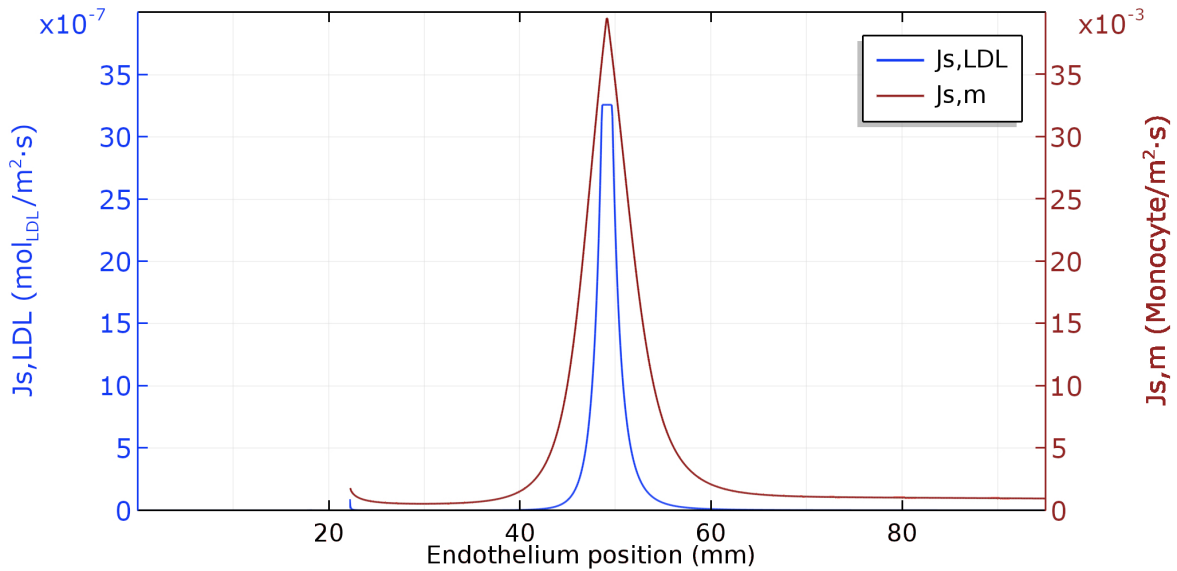


Figure 3.10: Flows of LDL and monocytes across the endothelium.

In addition, to verify that the experimental distribution of LDL concentration in the arterial wall obtained by Meyer et al. (1996) is accomplished, the relative concentration of LDL obtained with the model along the arterial wall is represented in Figure 3.11. This relative concentration is calculated as the ratio of the LDL concentration at each point of the arterial wall to the LDL that is deposited in the endothelium. The LDL distribution of Meyer et al. (1996) in the arterial wall is true for a healthy artery. Therefore, the distribution of LDL in the model is verified near the end of the model. For that, a line has been traced in the arterial wall, perpendicular to the lumen, whose points 0 and 0.7 mm are referred to the endothelium and the adventitia, respectively. The points of this line are represented in the horizontal axis of the Figure.

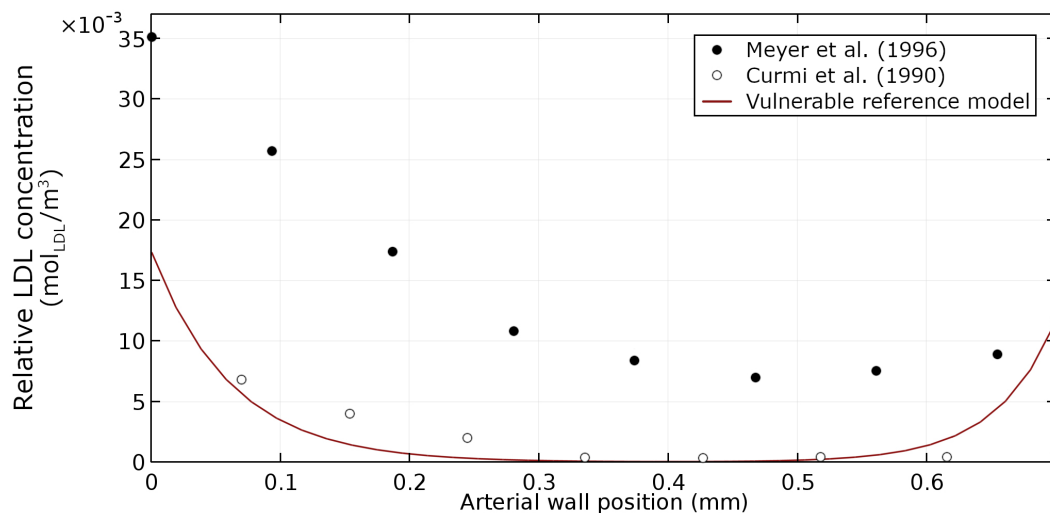


Figure 3.11: LDL distribution obtained in a healthy area of the geometry.

As can be seen in Figure 3.11, the highest value of relative LDL concentration is located in the endothelium due to the LDL flow across it. This value decreases for the intermediate points of the arterial wall, and increases again near the adventitia. This increase of LDL is due to that the adventitia is a membrane that causes the accumulation of LDL near it.

In Figure 3.12, the results of the inflammatory process and the growth of the plaque are represented, for a time of simulation equal to 10 years. First of all, a global view of the growth of the plaque in the model is represented. As can be seen, the plaque grows in the area of low WSS obtained before due to the recirculation occasioned by the obstacle plaque, and produces a maximum increase of the arterial wall thickness equal to 0.85 mm , which corresponds to a 71.73 % of stenosis ratio.

In addition, in Figure 3.12, the concentrations of the nine substances that are involved in the inflammatory process are represented in the area close to the new plaque.

There is a high concentration of LDL in the area of the arterial wall with plaque growth, due to the increase in the endothelial permeability in this area. Due to the convective effects in the LDL in the arterial wall, it moves into the adventitia, so its oxidation takes place along the entire thickness of the arterial wall, resulting in oxidised LDL throughout the arterial wall.

On the contrary, the response of monocytes is the opposite because when they enter into the arterial wall they differentiate into macrophages due to the presence of oxidised LDL, so there is only a high concentration of monocytes in the area of the wall close to the endothelium. On the other hand, macrophages also have diffusion, so they spread throughout the area of the arterial wall where oxidised LDL is present.

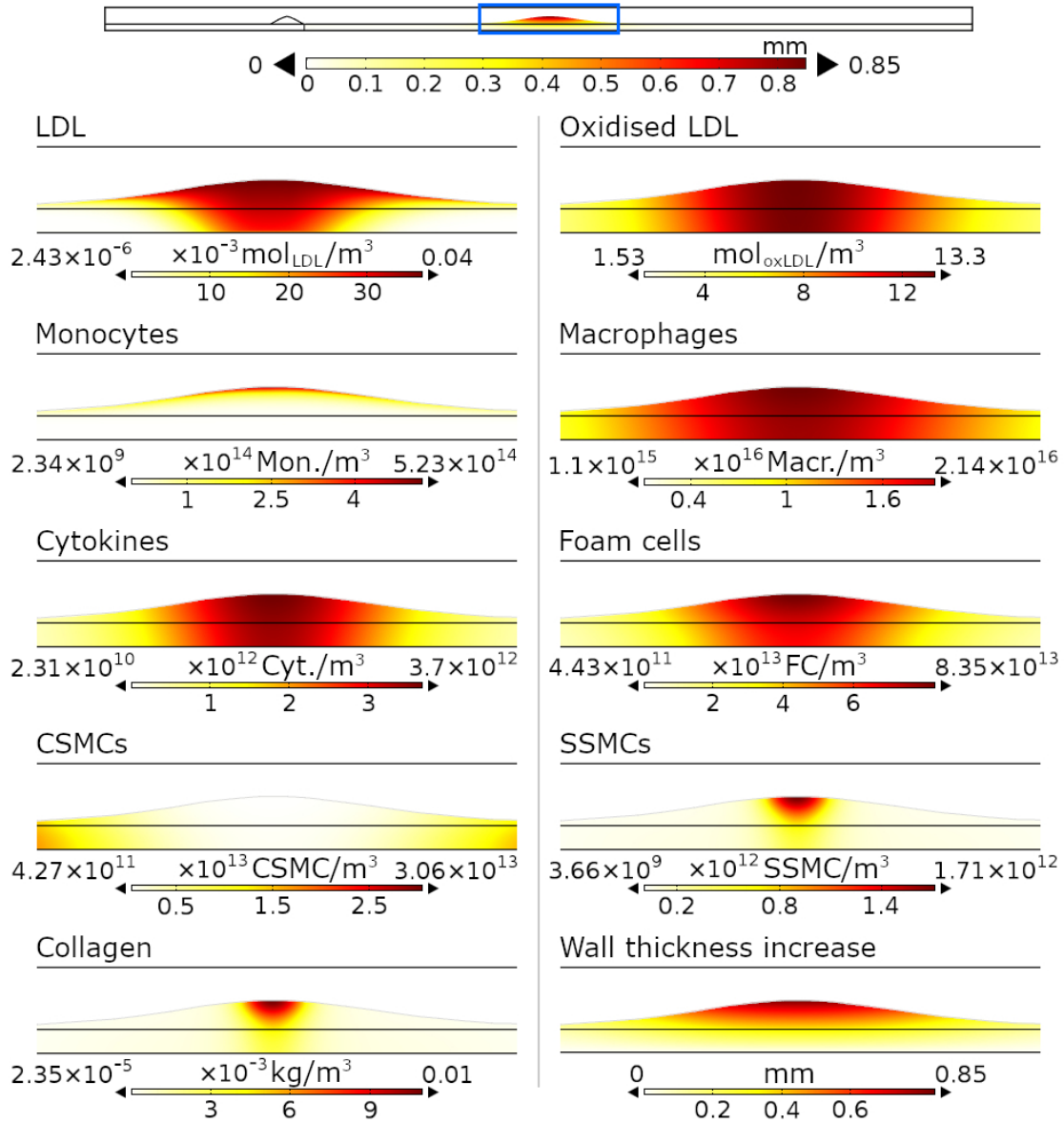


Figure 3.12: Arterial wall thickness increase and concentrations of all substances obtained for a simulation time of 10 years.

Cytokines are secreted by macrophages when they phagocytose oxidised LDL, so there is a high concentration of cytokines in the same areas as oxidised LDL and macrophages. The same occurs in the case of foam cells, where a higher amount can be seen in the area close to the endothelium.

As can be seen, there is an accumulation of all the substances in the area that develops the atheroma plaque, except in the case of CSMCs, whose concentration decreases there. It is due to that the contractile muscle cells in the arterial wall change their phenotype due to the presence of cytokines and, therefore, the number of CSMCs is reduced in the area of growth.

The distributions of SSMCs and collagen are the same due to collagen fibres are secreted by SSMCs. Both are concentrated in the area of the wall with oxidised LDL close to the endothelium, and form the fibrotic layer of the plaque.

Finally, in Figure 3.12, there is also a detail of the thickness increase of the arterial wall in the area of plaque growth. Based on the maximum wall thickness increase in Figure 3.12, it can be determined that the stenosis ratio in of the new plaque is 71.73 %.

In Figure 3.13, the volumetric growth of the plaque developed with the reference model due to each one of the substances that contribute to plaque volume for a total time of 10 years can be seen (Equation 2.52):

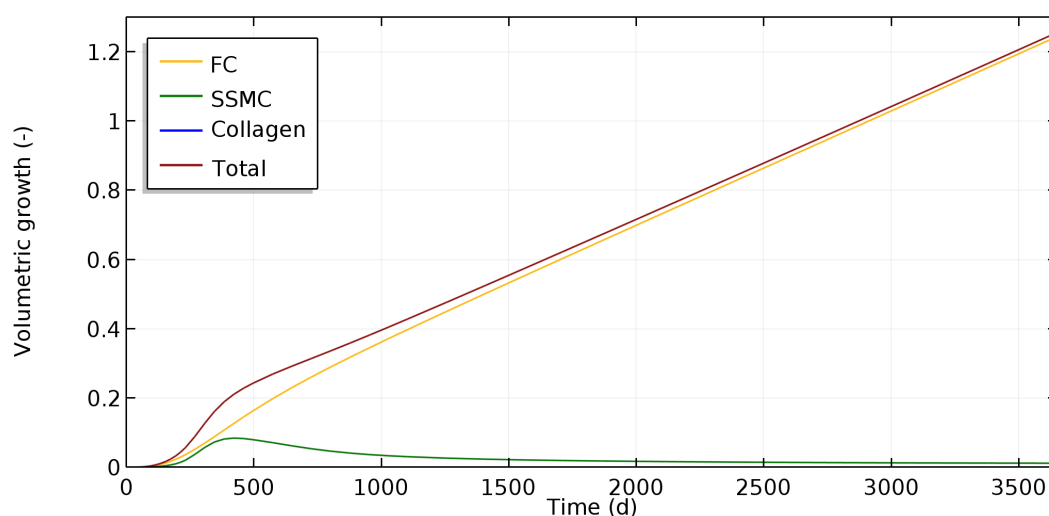


Figure 3.13: Volumetric growth of the plaque due to FCs, CSMCs, collagen fibres and total (yellow, green, blue and garnet lines), for a total time of 10 years.

As can be observed in Figure 3.13, the volumetric growths of the plaque due to FCs, SSMCs and collagen fibres are 1.25 , 0.01 and $1.1 \cdot 10^{-5}$, respectively, which corresponds to a total volumetric growth of the plaque of 1.26 . Therefore, the 99.20 % of the plaque growth is due to FCs, which corresponds to a vulnerable atheroma plaque (Fuster et al., 2005; Le Floc'h et al., 2009) with a large lipidic nucleus and a thin fibrous layer which can break and realease the lipidic nucleus into the bloodstream, causing a thrombus that obstructs the blood flow Libby and Theroux (2005).

The validation of this mechanobiological model is developed for patient-specific geometries of bifurcations of carotid arteries in Chapter 4 of this Thesis.

3.4 Mathematical modelling for non-vulnerable plaques

In the results of Section 3.3 it has been concluded that the plaque obtained with the reference model corresponds to a vulnerable atheroma plaque (Fuster et al., 2005; Le Floc'h et al., 2009). This type of plaque is the most studied because, in case of rupture, it is the most dangerous. However, non-vulnerable atheroma plaques are also important as they lead to very large reductions in the lumen of the arteries in which they are located. Therefore, a model of non-vulnerable plaque growth has been developed from the reference model, modifying some of the reactive terms of the substances involved in the process.

The vulnerability of a plaque is dependent on multiple factors, such as its size or stresses caused by blood flow in it, but it is also dependent on its composition. There is a high risk of rupture of plaque with a large lipidic nucleus (composed of FCs) and a thin fibrous cap (composed of SSMCs and collagen fibres) (Fuster et al., 2005; Le Floc'h et al., 2009). Therefore, a high quantity of foam cells and a small amount of synthetic smooth muscle cells and collagen fibres will be indicators of plaque with a high risk of rupture than one with a large quantity of synthetic smooth muscle cells and collagen (Fuster et al., 2005; Le Floc'h et al., 2009; Pan et al., 2021; Virmani et al., 2006).

Therefore, in order to obtain the non-vulnerable plaque model, some of the reactive terms of the substances that compose the fibrous layer of the plaque (SSMCs and collagen) have been modified to achieve a higher quantity of them, which would imply a bigger fibrous cap and a lower risk of rupture. These changes are explained in the next section.

3.4.1 Governing equations

The governing equations for the non-vulnerable reference model and the values of the parameters involved in the process are correspondent to the ones of the vulnerable reference model, already been explained in Chapter 2, with some modifications on the Equations referred to SSMCs and collagen fibres.

As previously commented, the reason why the reference model corresponds to a vulnerable plaque model is the fibrotic layer of the plaque, which is thin due that the threshold of SSMCs in the proliferation term of Equation 2.48 limits their proliferation and, in turn, their apoptosis term is very high. Therefore, once that there is no more differentiation of CSMCs into SSMCs, the concentration of SSMCs ceases to increase.

Thus, to achieve the non-vulnerable plaque reference model, the parenthesis of SSMCs threshold has been removed, and the values of the parameters of proliferation and apoptosis rates of SSMCs (p_{ss} and r_{apop}) have been adjusted by iterating within the literature ranges, to provide a higher concentration of SSMCs. The selected values after the iterative process for the parameters p_{ss} and r_{apop} are, respectively $0.0202 d^{-1}$ (Budu-Grajdeanu et al., 2008) and $8.011 \cdot 10^{-8} s^{-1}$ (Kockx et al., 1996).

The volumetric growths of the plaque due to FCs, SSMCs and collagen fibres with these changes are shown in Figure 3.14:

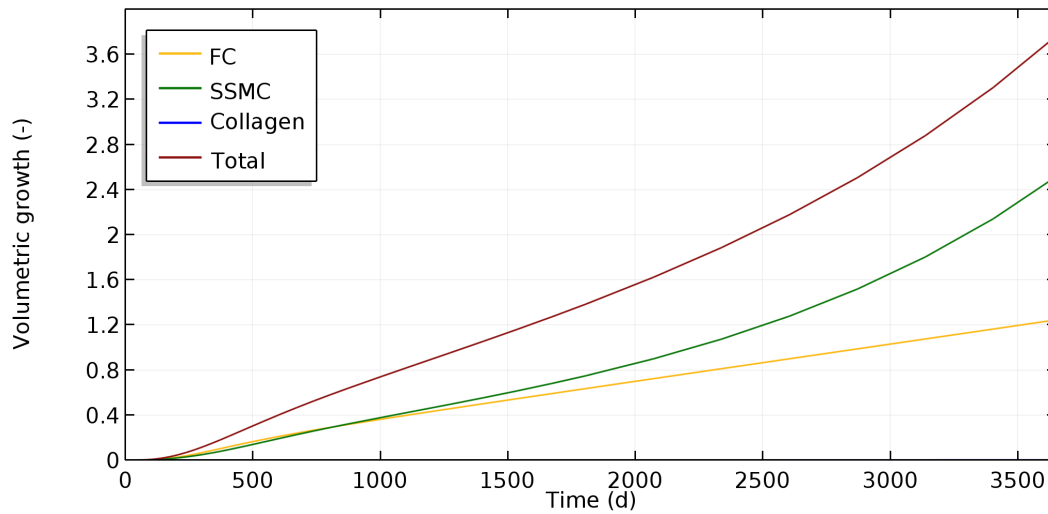


Figure 3.14: Reference model without threshold of SSMCs and reducing p_{ss} to $0.0202 d^{-1}$ and r_{apop} to $8.011 \cdot 10^{-8} s^{-1}$: Volumetric growth of the plaque due to FCs, CSMCs and collagen fibres (yellow, green and blue lines), and total volumetric growth of the plaque (garnet line), for a total time of 10 years.

As can be seen in Figure 3.14, the volumetric growth for a time of 10 years of simulation due to FCs, SSMCs and collagen is equal to 1.25 , 2.54 and $2.3 \cdot 10^{-3}$, respectively. This means that the 32.96 % of the plaque is composed of FCs, while the 66.97 % is composed of SSMCs. As can be seen, the growth of the plaque in this case is due to FC and SSMCs. However, there is no growth related to collagen fibres.

The segregation of collagen fibres directly depends on SSMCs (Equation 2.50). Due to the natural production of collagen in the arterial wall is not modelled, the natural degradation rate of collagen has been eliminated as well in this model, obtaining the results of Figure 3.15.

As can be seen, with this variations in the reference vulnerable model, the plaque is composed now by FCs, SSMCs and collagen, with respective volumetric growths of 1.25 , 2.54 and 0.10 , and a total volumetric growth of 3.90 . Thus, the volumetric composition of the growth of the plaque is 32.13 % of FCs, 65.29 % of SSMCs and 2.57 % of collagen fibres. Therefore, the plaque obtained with this variations of the reference vulnerable model equations is a non-vulnerable plaque with a greater fibrotic layer than obtained with the reference vulnerable model one.

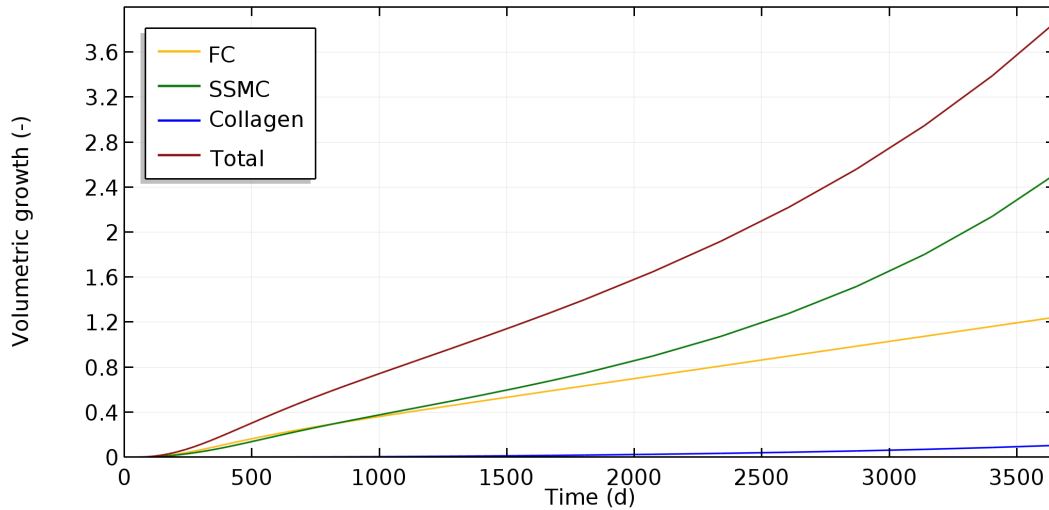


Figure 3.15: Reference model without threshold of SSMCs and reducing p_{ss} to $0.0202 d^{-1}$ and r_{apop} to $8.011 \cdot 10^{-8} s^{-1}$, without natural degradation of collagen: Volumetric growth of the plaque due to FCs, CSMCs and collagen fibres (yellow, green and blue lines), and total volumetric growth of the plaque (garnet line), for a total time of 10 years.

To summarise these changes, in Table 3.11 are included the changes in the equations of SSMCs and collagen, and the selected values of the parameters that have been modified to achieve the non-vulnerable plaque model.

Equation	Suppressed	Resultant term
2.48	Proliferation threshold parenthesis	$\left(\frac{p_{ss} C_{c,w}}{C_{c,w/2}^{th} + C_{c,w}} \right) \cdot C_{SSMC,w}$
2.50	Degradation term	—
Parameter	Value	Reference
p_{ss}	$0.0202 d^{-1}$	(Budu-Grajdeanu et al., 2008)
r_{apop}	$8.011 \cdot 10^{-8} s^{-1}$	(Kockx et al., 1996)

Table 3.11: Changes in the equations and parameters for the non-vulnerable reference model.

3.4.2 Non-vulnerable plaque model results

The results of concentrations of all the substances and the wall thickness increase after 10 years of inflammatory process are included in Figure 3.16. As can be seen, a global view of the wall thickness increase is represented at the top of the Figure. Additionally, details of the individual substances in the area of the plaque growth and the wall thickness increase

in that area are shown as well. The maximum increase on the thickness of the arterial wall due to the plaque growth is equal to 1.34 mm .

As in the case of the vulnerable model, there is accumulation of all substances in the plaque growth area, except for the case of CSMCs. As commented before for the case of the vulnerable plaques, this is due to the CSMCs in the area of plaque growth change their phenotype to a synthetic one, so their number decreases in this area.

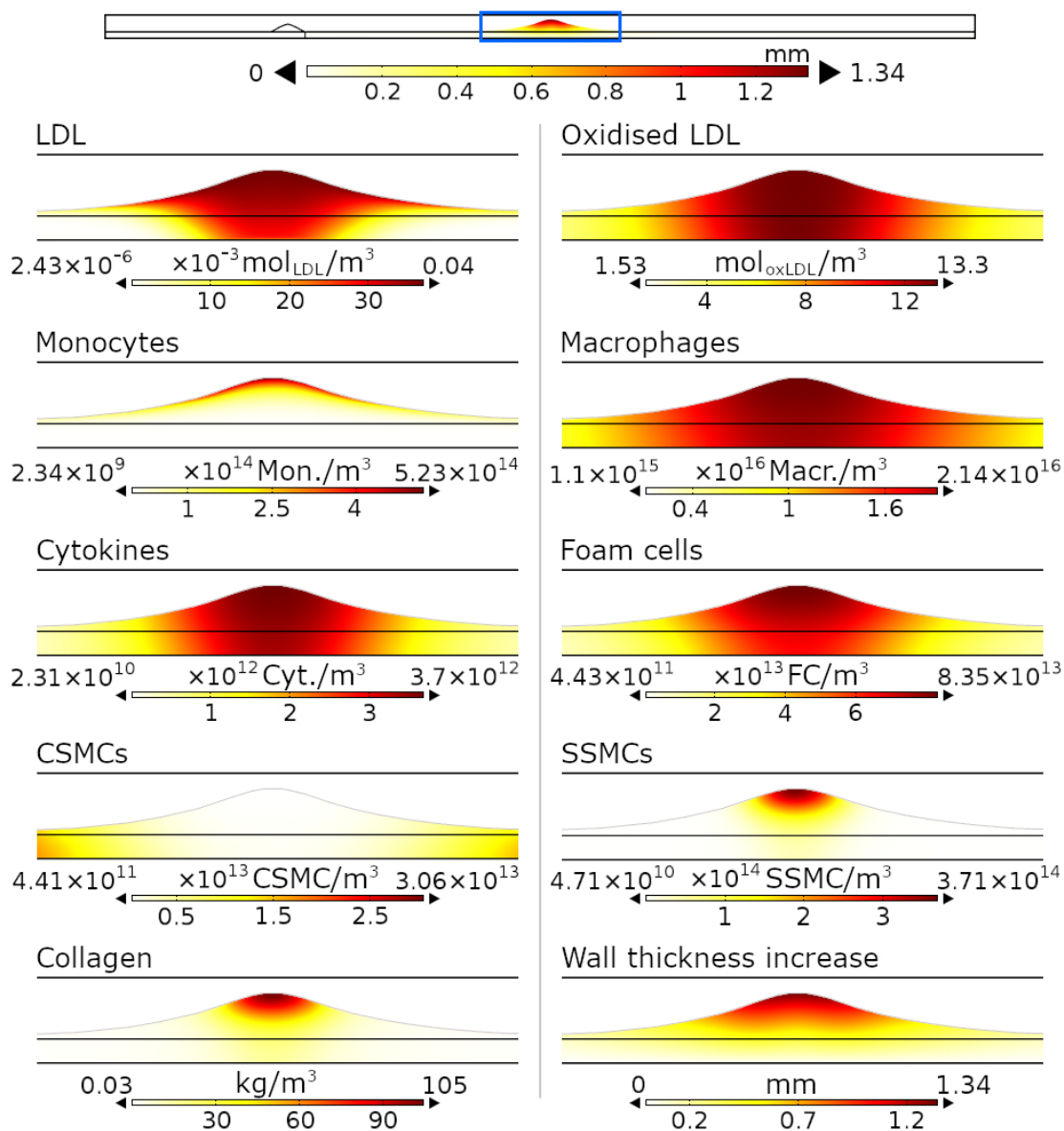


Figure 3.16: Arterial wall thickness increase and concentrations of all substances obtained for a simulation time of 10 years with the model of non-vulnerable plaques.

In Figure 3.16, it can be seen that, as happened for the case of the vulnerable plaque model, there is a high concentration of LDL, oxidised LDL, macrophages, cytokines and

foam cells throughout the thickness of the arterial wall in the area of plaque growth. Also, it can be observed that foam cells are again more concentrated in all the area of plaque growth. On the contrary, monocytes, SSMCs and collagen are accumulated in the area of plaque growth closest to the endothelium. For the case of monocytes, it is due to their differentiation into macrophages in the arterial wall while, for the case of SSMCs and collagen it is due to that the presence of cytokines is higher near the endothelium.

Finally, as the maximum increase of the arterial wall thickness is 1.34 mm , the stenosis ratio of the model of the non-vulnerable plaque corresponds to 93.15 %.

3.4.3 Validation of the non-vulnerable model

To validate the model of non-vulnerable plaques, clinical images by [Le Floc'h et al. \(2009\)](#) are used. These images, which correspond to intravascular ultrasound (IVUS) images of coronary arteries, were used in that paper to determine the morphology and vulnerability of the plaques based on parameters such as mechanical stresses on them due to blood flow and their composition.

In this Thesis, the IVUS images are only used to contrast the composition of the plaques, with the limitation of not considering their mechanical stresses. Attending to their composition and the results presented in [Le Floc'h et al. \(2009\)](#), all the considered plaques in the paper correspond to non-vulnerable plaques due to their fibrous cap thickness and lipidic area.

In [Le Floc'h et al. \(2009\)](#), a total of 7 clinical images are analysed. For the case of the first image, they computationally vary the thickness of the fibrous cap, obtaining their models 2 and 3, which are not considered here due to that they do not correspond to clinical images. Therefore, the images 1, 4, 5, 6 and 7 of their article are used to validate the model of non-vulnerable plaques. In addition, the image 5 has two different plaques that are near to each other so only the one that is closest to the arterial lumen is considered in this Thesis. In the case of the image 7, it also has presence of two plaques, but both of them are near to the lumen and so both of them are considered here.

In Table 3.12, the areas of the lipidic core and fibrous layer for all the considered plaques are included. The area of the lipidic core has been obtained directly from [Le Floc'h et al. \(2009\)](#), while the area of the fibrous layer has been manually measured with the software ImageJ (NIH, Bethesda, MD, USA). In addition, the average values of both areas are included at the end of the table.

Attending to the average values on Table 3.12, it is possible to determine the mean percentage of the plaques occupied by the lipidic nucleus and by the fibrous layer, which correspond, respectively, to 67.31 % and 32.69 %.

	Lipidic nucleus area (mm^2)	Fibrous layer area (mm^2)
Plaque 1	1.604	1.206
Plaque 4	5.557	1.118
Plaque 5.1	0.505	0.381
Plaque 6	1.996	1.409
Plaque 7.1	2.151	1.421
Plaque 7.2	0.701	0.560
Average values	2.08	1.01

Table 3.12: Areas of the lipidic nucleus and of the fibrous layer of the plaques included on Le Floc'h et al. (2009).

For the case of the non-vulnerable plaque model developed in this Thesis, if the wall thickness increase due to foam cells, SSMCs and collagen fibres are analysed separately, we obtain growths of 0.85 mm , 0.47 mm and 0.02 mm , respectively. Therefore, the 63.43 % of the plaque obtained with the non-vulnerable model corresponds to the lipidic core and the 36.57 % corresponds to the fibrous layer.

As can be seen by contrasting both results, the fibrous layer obtained with the non-vulnerable model is close to the mean value of the IVUS images and, therefore, it can be concluded that the plaques developed with the model effectively correspond to non-vulnerable plaques.

3.5 Vulnerable vs non-vulnerable plaque models

As can be observed in Sections 3.3 and 3.4, the plaque size and its stenosis ratio are higher in the case of the non-vulnerable model. There is a total wall thickness increase of 0.85 mm obtained with the vulnerable model versus 1.34 mm obtained with the non-vulnerable one. This produces a higher stenosis ratio in the case of the vulnerable model than in the non-vulnerable one (71.73 % and 93.15 %, respectively).

It is due to that the variations in the equations to obtain the non-vulnerable model do not affect the FCs, so the growth due to FCs is the same in both, the cases of the vulnerable and non-vulnerable models. However, the growth due to SSMCs and collagen increases in the case of the non-vulnerable plaques due to an increase in the fibrous layer of the plaque, which results in a higher total plaque growth in this case.

In Figure 3.17, the temporal evolution of all the substances concentrations are represented for the vulnerable and non-vulnerable models (garnet and green colors, respectively). The evolution of the concentrations is represented in two points of the section of maximum plaque growth that corresponds to Points 1 and 2 which are located, respectively, in one and two thirds of the wall thickness. The results obtained in Points 1 and 2 are

represented, respectively, in continuum and dotted lines. For the cases of LDL, oxidised LDL, monocytes, macrophages, cytokines, foam cells and CSMCs, the concentration profiles are the same in the cases of the vulnerable and non-vulnerable models due to their equations in both models are the same.

As can be seen in Figure 3.17, the LDL concentration profile is constant over time, due to the flow of LDL from the lumen into the arterial wall is also constant. Additionally, Point 1 has a higher LDL concentration than Point 2 because it is closer to the endothelium.

In the case of oxidised LDL, the concentration in the arterial wall increases until it reaches a maximum, after which it decreases until it reaches approximately an equilibrium situation. This decrease is due to an increase of macrophages in the arterial wall, which phagocytose the oxidised LDL, and the equilibrium situation is due to an equilibrium of the LDL that gets oxidised and the oxidised LDL phagocytosed by macrophages.

The case of monocytes is similar to that of oxidised LDL, although their decrease is due to their differentiation into macrophages and to their natural degradation. The equilibrium of monocytes is due to the equilibrium between these two phenomena and the monocytes that pass through the endothelium.

On the other hand, in the case of macrophages, its concentration only increases. These increase is higher at the beginning of the process due to the higher monocyte concentration in the arterial wall. However, the decrease of monocyte over time produces a reduction in the differentiation and therefore, in the velocity in which macrophages are produced in the arterial wall.

As can be seen, the cytokine concentration increases until it reaches a maximum value, after which it decreases until it reaches stability. This stability is due to the stabilisation of the oxidised LDL concentration profile.

For the case of foam cells, its concentration increases over time. It is due to that they are constantly produced when macrophages can not ingest more quantity of oxidised LDL and to that they accumulate in the arterial wall.

The concentration profiles of CSMCs and SSMCs are closely related due to the CSMCs can only differentiate into SSMCs. CSMCs decrease over time due to the apparition of oxidised LDL and cytokines in the arterial wall and this is the reason why SSMCs increase at the same time. The SSMCs profiles obtained for the vulnerable and non-vulnerable models are different due to in the non-vulnerable one, its proliferation and apoptosis are respectively increased and decreased. This is the reason why the non-vulnerable model has a higher concentration of SSMCs in the arterial wall.

In the case of collagen, its concentration increases over time due to the increase of SSMCs in the arterial wall. Additionally, it can be observed that there is a higher concentration of collagen in the case of the non-vulnerable plaque because, in this case, there is also a higher concentration of SSMCs.

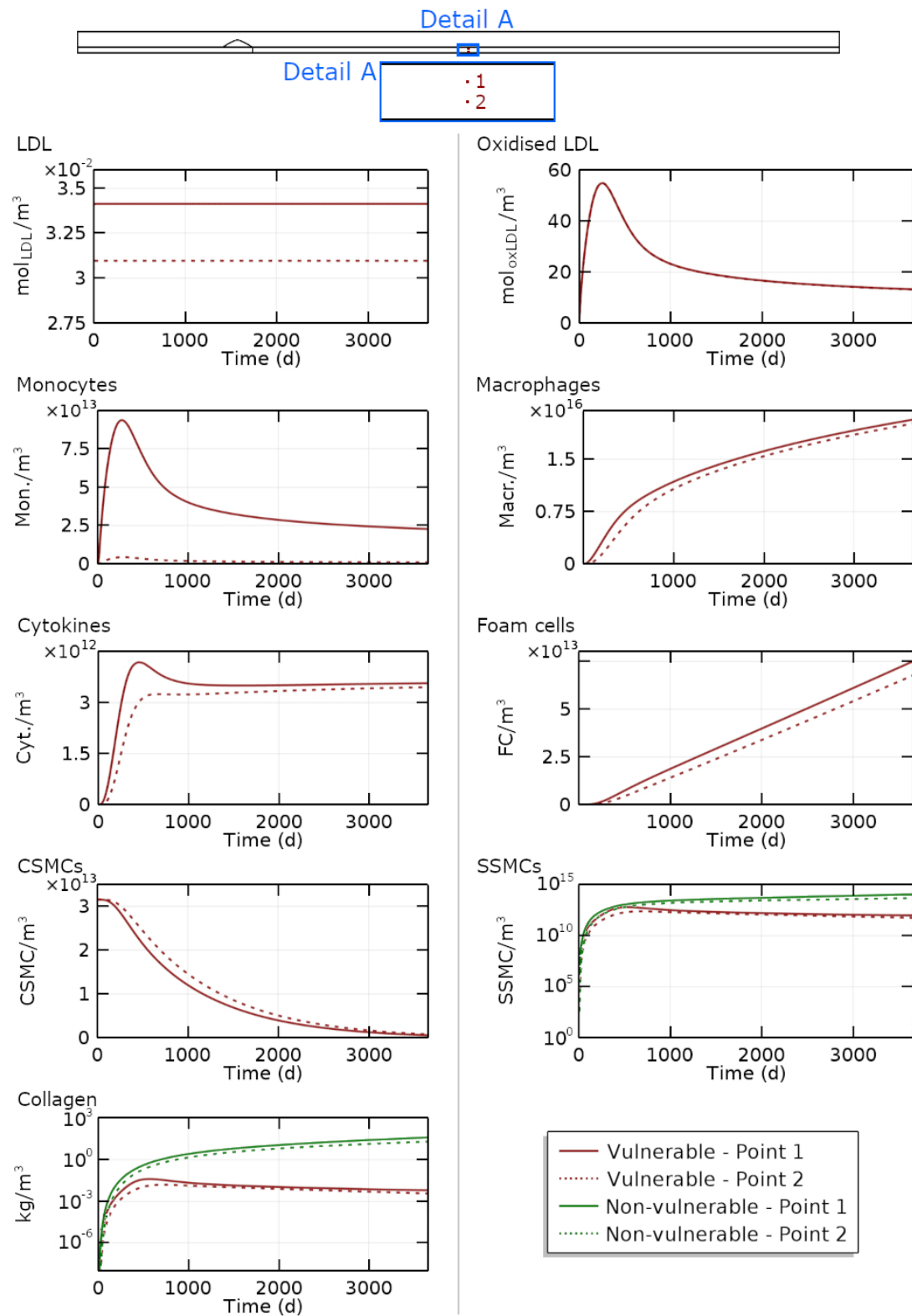


Figure 3.17: Evolution of substances concentration for a total time of 10 *years* for the vulnerable and non-vulnerable models (garnet and green colors, respectively).

3.6 Sensitivity analysis of the parameters of the model

In this section, we develop a sensitivity analysis of the results of the model, depending on its parameters, to determine the effect of these parameters in the growth and composition of atheroma plaques. This analysis has been done for the case of the non-vulnerable plaques model (Section 3.4), but the influence of the parameters in the reference vulnerable model would be analogue due to its parameters and equations are the same (the threshold of SSMCs is eliminated in the non-vulnerable plaques model, but this produces an increase on the concentration of SSMCs, so its effect on the plaque is already known). This influence of the parameters would be the same in the case of other arteries or geometries as well.

The mathematical model used has a total of 52 parameters, which come from different studies and that can be related to experimental or computational analysis. Among the experimental ones, there are some differences between the analysis conditions. For example, some of the parameters have been determined from in vitro tests, while others are from in vivo ones. Moreover, they come from studies of different species and from different arteries (coronary, carotid or aorta). Finally, some of them have been estimated based on computational results. Therefore, the values of the parameters can have a large variation, so it is relevant to perform a sensitivity analysis of the parameters of the model, which can help to understand the role of every parameter in the generated plaque.

The objective of this study is to analyse plaque growth and its composition. To do so, a previous selection of the parameters to analyse was made. Therefore, geometric parameters, initial concentrations, material properties, flow properties, and other factors that are well known have not been considered in the analysis because their influence on the model seems to be clear (for example, an increase in the radius of foam cells would result in an increase in the stenosis ratio due to an increase in the volume of the plaque). Thus, in this study, only the parameters related to the reactive terms of the convection-diffusion-reaction equations of the inflammatory process are analysed, as well as the diffusion coefficients of substances in the arterial wall.

The analysed parameters have been increased and reduced by 25 % and 10 % in 61 different simulations in a mono-variant sensitivity analysis. The values of the parameters for all the cases are included in Table 3.13.

The percentage of change in the volume of the plaque due to each of the substances involved in the growth (foam cells that compose the lipidic core of the plaque, and synthetic smooth muscle cells and collagen fibre, which correspond to the fibrous layer of the plaque) has been analysed, as well as the variation in the stenosis ratio

Tables 3.14 and 3.15 show the results obtained by increasing and decreasing the selected parameters by 25% and 10%, respectively.

Parameter	Description	Value−25%	Value −10%	Mean value	Value +10%	Value +25%
$D_{LDL,w} = D_{LDLox,w} \left(\frac{m^2}{s} \right)$	LDL and oxLDL diff. coeff.	$6 \cdot 10^{-13}$	$7.2 \cdot 10^{-13}$	$8 \cdot 10^{-13}$	$8.8 \cdot 10^{-13}$	$1 \cdot 10^{-12}$
$D_{m,w} = D_{M,w} \left(\frac{m^2}{s} \right)$	Mon. and macr. diff. coeff.	$6 \cdot 10^{-15}$	$7.2 \cdot 10^{-15}$	$8 \cdot 10^{-15}$	$8.8 \cdot 10^{-15}$	$1 \cdot 10^{-14}$
$d_{LDL} (s^{-1})$	LDL oxidation	$2.1375 \cdot 10^{-4}$	$2.565 \cdot 10^{-4}$	$2.85 \cdot 10^{-4}$	$3.135 \cdot 10^{-4}$	$3.5625 \cdot 10^{-4}$
$d_m (s^{-1})$	Monocyte differentiation	$8.625 \cdot 10^{-7}$	$1.035 \cdot 10^{-6}$	$1.15 \cdot 10^{-6}$	$1.265 \cdot 10^{-6}$	$1.4375 \cdot 10^{-6}$
$m_d (d^{-1})$	Monocyte death	0.012	0.0144	0.016	0.0176	0.02
$LDL_{ox,r} \left(\frac{m^3}{Macrophage \cdot s} \right)$	OxLDL uptake	$1.8375 \cdot 10^{-23}$	$2.205 \cdot 10^{-23}$	$2.45 \cdot 10^{-23}$	$2.695 \cdot 10^{-23}$	$3.0625 \cdot 10^{-23}$
$n_{FC} \left(\frac{mol_{oxLDL}}{Macrophage} \right)$	Max. oxLDL uptake	$2.04 \cdot 10^{-11}$	$2.448 \cdot 10^{-11}$	$2.72 \cdot 10^{-11}$	$2.992 \cdot 10^{-11}$	$3.4 \cdot 10^{-11}$
$C_r \left(\frac{mol_{oxLDL} \cdot mol_C \cdot m^3}{mol_C \cdot m^3 \cdot Macrophage \cdot s} \right)$	Cytokine production	$2.25 \cdot 10^{-10}$	$2.7 \cdot 10^{-10}$	$3 \cdot 10^{-10}$	$3.3 \cdot 10^{-10}$	$3.75 \cdot 10^{-10}$
$d_c (s^{-1})$	Cytokine degradation	$1.7355 \cdot 10^{-5}$	$2.082 \cdot 10^{-5}$	$2.314 \cdot 10^{-5}$	$2.545 \cdot 10^{-5}$	$2.8925 \cdot 10^{-5}$
$S_r (d^{-1})$	SMC differentiation	$2.7 \cdot 10^{-3}$	$3.24 \cdot 10^{-3}$	$3.6 \cdot 10^{-3}$	$3.96 \cdot 10^{-3}$	$4.5 \cdot 10^{-3}$
$p_{ss} (d^{-1})$	SSMC proliferation	0.0152	0.0182	0.0202	0.022	0.0253
$G_r \left(\frac{kg_C}{SSMC \cdot s} \right)$	Collagen production	$1.8675 \cdot 10^{-21}$	$2.241 \cdot 10^{-21}$	$2.49 \cdot 10^{-21}$	$2.739 \cdot 10^{-21}$	$3.1125 \cdot 10^{-21}$
$C_{c,w}^{th} \left(\frac{mol_C}{m^3} \right)$	Cytokine threshold	$9.2625 \cdot 10^{12}$	$1.111 \cdot 10^{13}$	$1.235 \cdot 10^{13}$	$1.358 \cdot 10^{13}$	$1.5437 \cdot 10^{13}$
$n_r \left(\frac{mol_{oxLDL} \cdot day}{m^4} \right)$	Monocyte recruitment	$4.977 \cdot 10^{-4}$	$5.972 \cdot 10^{-4}$	$6.636 \cdot 10^{-4}$	$7.299 \cdot 10^{-4}$	$8.295 \cdot 10^{-4}$
$r_{apop} (s^{-1})$	SSMC apoptosis rate	$6.008 \cdot 10^{-8}$	$7.209 \cdot 10^{-8}$	$8.011 \cdot 10^{-8}$	$8.812 \cdot 10^{-8}$	$1.001 \cdot 10^{-7}$

Table 3.13: Analysed parameters and their respective values for the cases of increase and decrease them by 25 % and 10 %.

Parameter	FC volume variation (%)		SSMC volume variation (%)		Cg volume variation (%)		SR variation (%)	
	− 25 %	+25 %	− 25 %	+25 %	− 25 %	+25 %	− 25 %	+25 %
$D_{LDL,w}$	7.35	− 5.65	> 100	− 92.81	> 100	− 74.38	-	− 36.61
$D_{oxLDL,w}$								
$D_{m,w}$	4.82	− 4.07	> 100	− 43.43	> 100	− 39.57	-	− 19.71
$D_{M,w}$								
d_{LDL}	− 20.29	18.51	− 99.89	> 100	− 93.98	> 100	− 82.68	-
d_m	− 0.98	0.63	− 42.43	21.00	− 31.32	15.33	− 7.28	4.69
m_d	0.23	− 1.09	15.32	− 34.09	12.95	− 29.32	7.90	− 8.16
$LDL_{ox,r}$	− 3.73	2.90	> 100	− 99.89	> 100	− 93.27	-	− 12.99
n_{FC}	48.43	− 36.00	− 0.21	0.13	− 0.10	0.24	> 100	− 77.22
C_r	0	0	− 99.89	> 100	− 95.52	> 100	− 22.05	-
d_c	0	0	> 100	− 99.89	> 100	− 94.14	-	− 21.95
S_r	0	0	− 5.50	6.46	− 7.48	7.71	− 0.64	0.032
p_{ss}	0	0	− 99.89	> 100	− 96.88	> 100	− 22.17	-
G_r	0	0	0	0	− 24.54	48.32	− 1.08	2.09
$C_{c,w}^{th}$	0	0	> 100	− 99.89	> 100	− 94.14	-	− 21.96
m_r	− 3.77	3.75	− 41.23	> 100	− 35.02	> 100	− 20.83	-
r_{apop}	0	0	> 100	− 99.91	> 100	− 96.72	-	− 22.19

Table 3.14: Foam cells, synthetic smooth muscle cells, and collagen volume variations (second, third, and fourth columns, respectively), and stenosis ratio variation (fifth column), by reducing and increasing the values of the parameters by 25%.

Parameter	FC volume variation (%)		SSMC volume variation (%)		Cg volume variation (%)		SR variation (%)	
	− 10 %	+10 %	− 10 %	+10 %	− 10 %	+10 %	− 10 %	+10 %
$D_{LDL,w}$	2.69	− 2.42	> 100	− 67.85	> 100	− 48.60	-	− 21.31
$D_{oxLDL,w}$								
$D_{m,w}$	2.32	− 1.32	> 100	− 13.45	> 100	− 9.32	-	− 11.23
$D_{M,w}$								
d_{LDL}	− 7.89	7.60	− 97.67	> 100	− 81.81	> 100	− 45.91	-
d_m	− 0.54	0.32	− 25.54	12.55	− 19.89	8.35	− 2.67	2.10
m_d	0.05	− 0.43	7.65	− 25.43	4.56	− 20.88	3.91	− 3.06
$LDL_{ox,r}$	− 1.36	1.23	> 100	− 97.85	> 100	− 82.55	-	− 9.61
n_{FC}	15.50	− 11.52	− 0.07	0.04	− 0.03	0.08	57.57	− 26.82
C_r	0	0	− 99.13	> 100	− 86.56	> 100	− 21.31	-
d_c	0	0	> 100	− 98.69	> 100	− 84.93	-	− 21.16
S_r	0	0	− 1.17	1.38	− 1.59	1.64	− 0.13	0.007
p_{ss}	0	0	− 99.89	> 100	− 91.40	> 100	− 21.75	-
G_r	0	0	0	0	− 4.50	8.77	− 0.19	0.36
$C_{c,w}^{th}$	0	0	> 100	− 98.69	> 100	− 84.93	-	− 21.15
m_r	− 0.26	0.26	− 2.89	> 100	− 2.45	67.59	− 1.49	-
r_{apop}	0	0	> 100	− 99.90	> 100	− 91.14	-	− 21.77

Table 3.15: Foam cells, synthetic smooth muscle cells, and collagen volume variations (second, third, and fourth columns, respectively), and variation in the stenosis ratio (fifth column), reducing and increasing the values of the parameters by 10%.

The first column of Tables 3.14 and 3.15 represents the parameter whose influence is being analysed. The second, third, and fourth double columns are, respectively, changes in the volume of foam cells, synthetic smooth muscle cells, and collagen fibres in the plaque, caused by the considered parameter variation. Finally, the last double column is the change in the stenosis ratio of the artery due to the change in the considered parameter.

As can be seen in Tables 3.14 and 3.15, the trend of the results is the same in the cases of variation of 25% and 10% parameters variation. Therefore, the results will be discussed only with reference to the 10% variation table (Table 3.15), and can be extrapolated for the 25% variation table (Table 3.14).

As can be seen in Tables 3.14 and 3.15, the variation of the substances was limited to a maximum of 100%, signalled in both Tables in garnet. Therefore, in cases where the variation in the percentage of a substance was greater than 100%, the stenosis ratio was not calculated.

When considering the parameters that influence the change in the volume of foam cells in the plaque (Table 3.15), these are, in order of influence, n_{FC} , d_{LDL} , $D_{LDL,w} = D_{LDLox,w}$ and $D_{m,w} = D_{M,w}$, which are related to foam cells, LDL, and the diffusion properties of substances in the arterial wall, respectively. As can be seen, none of the variations produces a change in the volume of foam cells greater than 100%.

The parameters that cause a higher change in the volume of synthetic smooth muscle cells are, in order of influence: d_{LDL} , C_r , p_{ss} , m_r , r_{apop} , d_c , $C_{c,w}^{th}$ and $LDLox,r$, when increased (the first four produce a change greater than 100%). When their values decrease, the most influential are, in order: $D_{LDL,w} = D_{LDLox,w}$, $D_{m,w} = D_{M,w}$, $LDLox,r$, d_c , $C_{c,w}^{th}$, r_{apop} , p_{ss} , C_r , and d_{LDL} , the first six of which cause changes greater than 100%. Therefore, for the change in the volume of synthetic smooth muscle cells volume in the plaque, the parameters d_{LDL} , C_r , p_{ss} , r_{apop} , d_c , $C_{c,w}^{th}$ and $LDLox,r$ have huge influences, regardless if their values are increased or decreased.

For the variation of collagen volume in the plaque, the most influential parameters are, when increased: d_{LDL} , C_r , p_{ss} , r_{apop} , d_c , $C_{c,w}^{th}$ and $LDLox,r$, while when decreased: $D_{LDL,w} = D_{LDLox,w}$, $D_{m,w} = D_{M,w}$, $LDLox,r$, d_c , $C_{c,w}^{th}$, and r_{apop} .

In Figure 3.18, the variation in the volume of foam cells, synthetic smooth muscle cells, and collagen fibres is represented in a graph of parallel bars for variations of $\pm 10\%$. In cases of parameters that cause a volume variation higher than 100 % in any of the considered substances, the bar of this substance is represented in red, i.e., the cases of the diffusion coefficients d_{LDL} , $LDLox,r$, C_r , d_c , p_{ss} , $C_{c,w}^{th}$, m_r , and r_{apop} .

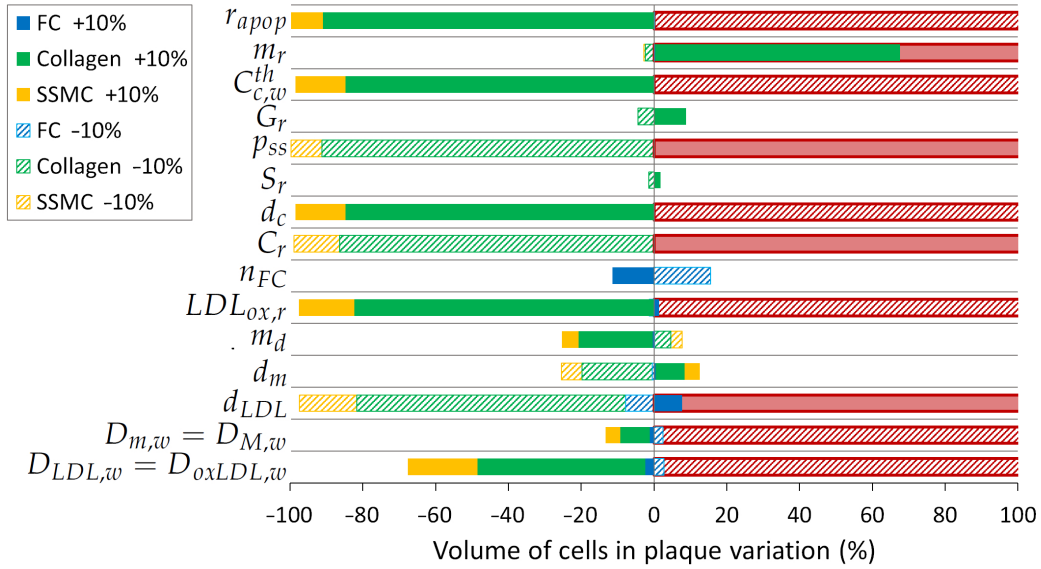


Figure 3.18: Variation of the volume of FC, SSMC and collagen (blue, yellow and green colours) when increasing and decreasing the parameters by 10 % (solid and striped colors, respectively). Bars in red represent a variation of one of the substances higher than 100 %.

Figure 3.19 represents the change in the stenosis ratio due to the variation of the considered parameters when varied $\pm 10\%$. The red bars refer to cases in which at least one of the substances that adds volume to the plaque has a volume variation greater than 100 %.

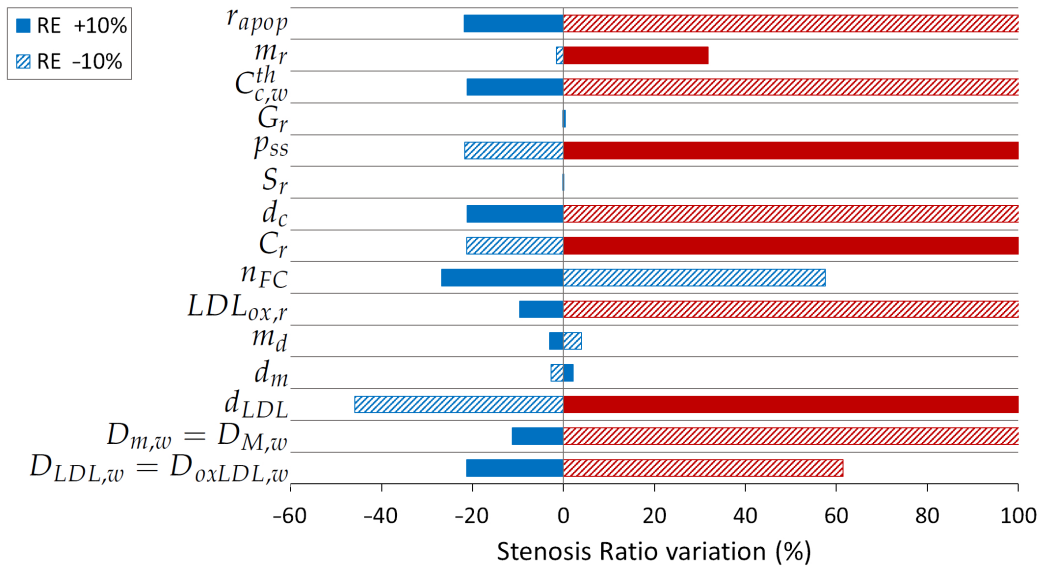


Figure 3.19: Variation of the stenosis ratio (blue color) when increasing and decreasing the parameters by 10 % (solid and striped colors, respectively). Bars in red represent a variation of one of the substances higher than 100 %.

As can be seen in the results, on the one hand, the parameters whose variations are directly proportional to the stenosis ratio are the degradation rate of LDL (d_{LDL}), the monocyte differentiation rate (d_m), the parameters referring to the production and degradation of cytokines (C_r and S_r), the proliferation rate of synthetic smooth muscle cells (p_{ss}), the segregation rate of collagen (G_r) and the parameter related to the amount of monocyte recruited by the endothelium (m_r). On the other hand, some of the analysed parameters are inversely proportional to the growth of the plaque, and an increase in their values will cause a decrease in the volume of the plaque and, therefore, in the stenosis ratio. It is the case of the diffusion parameters of substances on the arterial wall ($D_{LDL,w} = D_{LDLox,w}$ and $D_{m,w} = D_{M,w}$), the rate of death of monocytes (m_d), the rate of oxidised LDL that is uptaken by macrophages, and the maximum amount of oxidised LDL that a macrophage can ingest ($LDLox,r$ and n_{FC}), the cytokine degradation rate, its threshold in the arterial wall (d_c and $C_{c,w}^{th}$), and the rate of apoptosis of synthetic smooth muscle cells (r_{apop}).

As can be noticed, the parameters that influence the change in the volume of synthetic smooth muscle cells also influence the change in the volume of collagen. It is due to the segregation of collagen fibre by SSMC, so collagen depends directly on them.

The less influential parameters in the volume change of substances in the plaque are: d_m , m_d , S_r , and G_r . It should be noted that d_m and m_d are parameters referring to monocytes, which act at the beginning of the process. Therefore, a great influence on them could be expected. However, monocytes highly affect the results with the parameter m_r , which is the monocytes recruitment from the lumen, and its variation has a huge influence on the volume of FC in the plaque and, therefore, in the stenosis ratio.

As can be seen in Figure 3.18, r_{apop} has a large influence on the variation of volume of synthetic smooth muscle cells and collagen for both cases, when increasing and decreasing its value by 10%. The smaller the r_{apop} value, the more plaque is generated, as it is an apoptosis factor of synthetic smooth muscle cells. However, its influence on the variation of the stenosis ratio is greater in the case of increasing its value than in the case of decreasing it. As it is a parameter related to the apoptosis ratio of synthetic smooth muscle cells, its change does not cause variation in the results of foam cells (Figure 3.19).

m_r has more influence in both concentrations and stenosis ratio variation when increased (Figures 3.18 and 3.19). This is because, when its value is decreased, the amount of monocytes deposited in the arterial wall is reduced.

$C_{c,w}^{th}$ has a large influence in the variations of the results, having more influence when increased (the change of volume and stenosis ratio are greater than 100% in this case, as can be seen in Figures 3.18 and 3.19). It is a parameter involved in the differentiation of contractile smooth muscle cells into synthetic ones due to the presence of cytokines in the arterial wall. Thus, it does not influence the volume of foam cells.

As G_r is a parameter of collagen fibre segregation, it only has influence on the change of the volume of collagen in the plaque (Figure 3.18). Therefore, its influence on the stenosis ratio is limited (Figure 3.19).

p_{ss} is related to the proliferation of synthetic smooth muscle cells, so it does not influence the results of foam cells. On the contrary, as can be seen in Figure 3.18, increasing it by 10% produces a change greater than 100% in the variation of synthetic smooth muscle cells and collagen fibres.

S_r changes do not cause a large variation in the volume of any substance or the plaque stenosis ratio (Figure 3.19).

d_c is a parameter that also has a large influence on the volume variations (Figure 3.18). This parameter represents the cytokine degradation; thus, the higher it is, the more cytokines are degraded and, thus, the volume and the ratio of stenosis are lower (Figure 3.19). The same occurs with C_r , which represents the cytokine production.

n_{FC} represents the maximum amount of oxidised LDL that a macrophage can ingest before becoming a foam cell. Therefore, an increase in its value produces a reduction in the volume of foam cells and the stenosis ratio (Figures 3.18 and 3.19). Its influence on the variation of the volume of the substances is not very large, but it produces an important variation in the stenosis ratio. When these results are contrasted with those of a substance that produces a large variation in synthetic smooth muscle cells and collagen volumes (for example, d_c), it can be observed that a smaller change in the volume of foam cells produces a larger change in the stenosis ratio. It can be explained by attending to Equation 2.52: The volume of a foam cell is equal to $1.489 \cdot 10^{-14} m^3$, while the volume of a synthetic smooth muscle cell is equal to $6.774 \cdot 10^{-15} m^3$. Therefore, due to their size difference, less change in foam cell volume is needed to produce a similar stenosis ratio variation.

$LDL_{ox,r}$ is related to the oxidised LDL uptaken by macrophages, so it affects the volume of each of the considered substances. An increase in its value produces a reduction in the volume of substances (Figure 3.18) and therefore of the stenosis ratio (Figure 3.19).

d_m and m_d are both parameters referring to monocytes. The first one is related to their differentiation, while the second one refers to their apoptosis. Therefore, their influences are opposite. Their influence is more notable for synthetic smooth muscle cells and collagen volumes (Figure 3.18) but, as commented before, they are two of the less influential parameters.

d_{LDL} is the degradation rate of LDL, so it has an influence on foam cells, synthetic smooth muscle cells, and collagen fibres and, therefore, in the stenosis ratio of the plaque (Figures 3.18 and 3.19). So, it is one of the most influential parameters of the model and the most influential in the stenosis ratio when it is reduced.

$D_{LDL,w} = D_{LDLox,w}$ and $D_{m,w} = D_{M,w}$ are related to the diffusion of substances in the arterial wall, so they affect all the processes. Therefore, they influence the results of all the substances, and are some of the most important parameters in the model (Figures 3.18 and 3.19).

With all of this information, knowing the influence of all the parameters, they could be adjusted to achieve more or less vulnerable atheroma plaques, according to the percentage volume of foam cells, synthetic smooth muscle cells, and collagen fibres **Le Floc'h**

et al. (2009); Pan et al. (2021). Therefore, reducing the maximum amount of oxidised LDL that a macrophage can ingest and the ratio of oxidation of LDL (n_{FC}) will cause plaque with bigger lipid nuclei, which can develop into more unstable plaque. However, as can be seen, it has no influence on SSMC and collagen volumes in the plaque. Conversely, increasing the apoptosis ratio of SSMCs, the cytokine threshold in the arterial wall and its degradation rate, and the rate of oxidised LDL uptaken by macrophages (r_{apop} , $c_{c,w}^{th}$, d_c and $LDL_{ox,r}$, respectively), and reducing SSMC proliferation, cytokine production, and the oxidation LDL ratio (p_{ss} , C_r , and $d_L LDL$, respectively) will produce plaque with less fibrotic layer and, thus, a high risk of rupture.

The findings of this study should be interpreted in the context of its limitations. For example, the study of the influence of parameters was done only in the geometry of the carotid artery. However, the behaviour of the mathematical model would be the same for other geometrical configurations and arteries, for example, coronary or aorta arteries, adapting the values of the corresponding parameters if necessary. Another limitation of the study is that it was done with a 2D-axisymmetric model instead of a real geometry. In addition, blood flow and the inflammatory process are not coupled, which could influence the shape and stenosis ratio of the developed plaque. In this study, we also do not consider the influence of the mechanics of the arterial wall in the development of the plaque (such as tortuosity or changes in the permeability of the arterial wall due to the thickness variation of it with the cardiac cycle).

3.7 Conclusions

This chapter includes the reference model of atheroma plaque growth developed in this Thesis. For this purpose, a two-dimensional geometry of a coronary artery model (Olgac et al., 2008) has been adapted to the correspondent for carotid artery. Additionally, a sensitivity analysis of the meshes used for the lumen and for the arterial wall has been carried out, as well as an analysis of the length required for the geometry.

The plaque growth in the model depends on a mechanical stimulus of blood flow with the arterial wall (WSS) due to recirculation that the obstacle plaque of the geometry originates in the blood flow.

Among the results obtained for the reference vulnerable model, it can be observed (Figure 3.8), that the concentrations of LDL and monocytes along the arterial lumen are constant. This is the reason why, in the rest of this Thesis, the LDL and monocyte flows in the lumen will not be simulated. Thus, LDL and monocyte concentrations in the lumen will be included as boundary conditions at the endothelium.

The stenosis ratio obtained with the reference model is equal to 71.73 % and, as can be seen, a 99.20 % of the volumetric growth of the plaque is due to foam cells. Therefore, it can be concluded that the reference model corresponds to a model of vulnerable plaques.

In addition, a model of non-vulnerable plaques has been done, increasing the growth of the plaque due to SSMCs and collagen. This model has been validated with real IVUS images (Le Floc'h et al., 2009). The stenosis ratio of the plaque in the non-vulnerable model is 93.15 %, which is higher than in the vulnerable case.

Both models, the vulnerable and the non-vulnerable plaque models have been computed considering the inflammatory process of the arterial wall and the growth of the plaque as uncoupled processes, which is a limitation of the models.

Substances concentrations over time for the vulnerable and non-vulnerable models is also analysed, obtaining the same results for both cases except for SSMCs and collagen, which have a greater concentration in the non-vulnerable plaque model.

Finally, an analysis of the influence of some parameters of the non-vulnerable plaques model for the geometry in two-dimensions axisymmetric of carotid artery has been done. The mathematical model has a large number of parameters that can affect the growth of the plaque. However, some of them are considered well-known due to, for example, corresponding to geometrical properties of arteries or substances. Therefore, the parameters whose influence on plaque growth was analysed are related to the reactive terms of the equations referred to substances in the arterial wall. These parameters have been modified by increasing and decreasing their value in different cases by 25% and 10% and, to determine how they affect plaque growth, variations in the volume of substances that add volume to the plaque have been analysed (foam cells, synthetic smooth muscle cells, and collagen fibres). In addition, the variation in the plaque stenosis ratio was analysed.

As can be seen in Section 3.6, the variation of the selected parameters carries important variations on the results. d_{LDL} , d_m , C_r , S_r , p_{ss} , G_r , and m_r are directly proportional to the change of substances volume (FC, SSMC, and collagen) and to the stenosis ratio, while $D_{LDL,w} = D_{LDLox,w}$, $D_{m,w} = D_{M,w}$, m_d , $LDLox,r$, n_{FC} , d_c , $C_{c,w}^{th}$, and r_{apop} are inversely proportional.

In addition, it was noticed that a variation in foam cell volume results in more of a change in the plaque stenosis ratio than in the volume of synthetic smooth muscle cells or collagen, due to their larger volume.

For all of this, it could be interesting to study the vulnerability of plaque by changing the analysed parameters, knowing how each one of them affects the volume of foam cells, synthetic smooth muscle cells, and collagen fibres in the plaque.

Due to vulnerable plaques are more dangerous than non-vulnerable ones, in all the next chapters of this Thesis, only the vulnerable model is analysed.

Chapter 4

Effect of haemodynamical stimuli in patient-specific geometries

Part of the contents of this Chapter can be found in:

- Hernández-López P, Cilla M., Martínez M. and Peña E.
Effects of the Haemodynamic Stimulus on the Location of Carotid Plaques
Based on a Patient-Specific Mechanobiological Plaque Atheroma Formation
Model.
Frontiers in Bioengineering and Biotechnology (2021). 9:690685.
<https://doi.org/10.3389/fbioe.2021.690685>

Chapter 4

4.1 General Overview

The aim of this chapter is to analyse the predictability of the different haemodynamical stimuli used in the literature to estimate the location of atheroma plaques, improving the base model developed under axisymmetric hypothesis (Chapter 3).

In this chapter, 3D pathological patient-specific geometries of carotid arteries with different degrees of atheroma plaques are used to fictitiously reconstruct healthy arteries. In addition, a healthy geometry is computed as well. Then, the inflammatory process of apparition of plaques is computationally developed in the healthy geometries.

The reference model (Chapters 2 and 3) has been improved by the introduction of transient blood flow and new mechanical stimuli. The endothelium is modelled as a thin layer of endothelial cells, which change their shape as a function of the haemodynamical stimulus by becoming rounder or elongated according to the stimulus and thus allowing more or less substance transport along the endothelium. The haemodynamical stimuli considered in this chapter are the time average wall shear stress of blood flow with the arterial wall (TAWSS), the oscillatory shear index of blood flow (OSI) and a new variable combination of them (NV). The arterial wall is modelled as a single layer (intima-media) with a permeable membrane (endothelium).

Finally, the plaques predicted using the computational mechanobiological model are compared with the real plaques located on the clinical images taken from the patients, in order to determine which hemodynamical stimulus can better predict location and size of plaques.

In Section 4.2 the clinical images of the carotid arteries used in this chapter are presented. Their reconstructions and healthy computational geometries developed are included as well. The boundary conditions that are applied to each one of the geometries and their determination are explained in Section 4.3.

The different haemodynamical stimuli considered in this chapter (TAWSS, OSI and NV) are included in Section 4.4, while the numerical methods and the sensitivity analysis of the meshes are, respectively, in Sections 4.5 and 4.6. In Section 4.7, the total number of cardiac cycles that are compute is determined.

Finally, the results obtained for all the patient-specific geometries with all the analysed mechanical stimuli and the conclusions are presented in Sections 4.8 and 4.9, respectively.

4.2 Geometries

Clinical images of four different male patients with atherosclerosis and one healthy volunteer have been segmented using the software Materialise Mimics (Materialise N. V., Leuven, Belgium) to obtain eight different patient-specific geometries of carotid artery bifurcations, including common, internal and external carotid arteries (CCA, ICA and ECA, respectively).

The clinical CT images were provided by the Hospital Clinico Universitario Lozano Blesa in Zaragoza, Spain, according to the ethics guidelines of the hospital. One geometry corresponds to a healthy volunteer without pathology, and the others correspond to four patients with developed atheroma disease.

An example of the clinical images is shown in Figure 4.1. The bifurcation of the carotid artery can be seen in the central zone of the left figure. The part of the artery that is visible in the image corresponds to the lumen of the artery, while the arterial wall cannot be appreciate. As can be seen, there is a discontinuity in the arterial lumen correspondent to the presence of an atheroma plaque, which cannot be seen in the clinical images. It can be also noticed a white coloured area in the discontinuity (white arrows), which corresponds to a calcification of the plaque. In the right view of the Figure, the section of the calcification is shown.

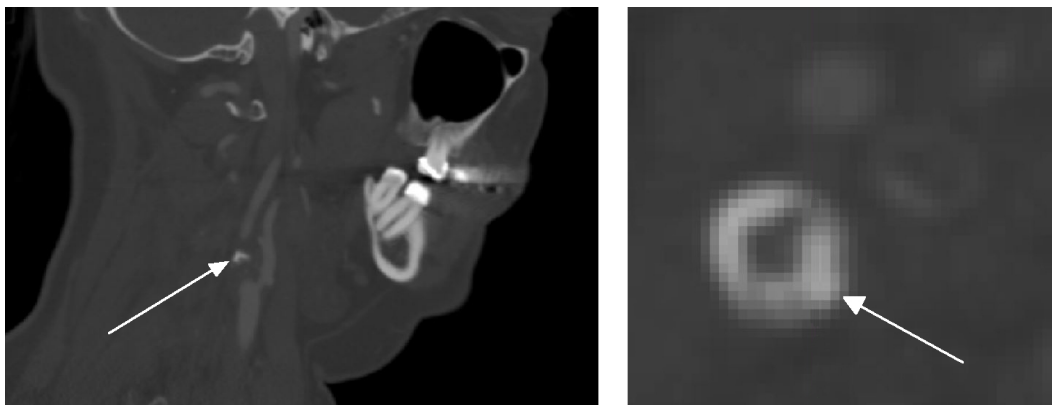


Figure 4.1: Example of an image of a bifurcation of carotid artery (white arrows signal the calcification).

A thresholding segmentation technique has been used to computationally reconstruct the lumen of the vessel from the clinical images, as can be seen in Figure 4.2, in which the resultant mask is represented in green colour.

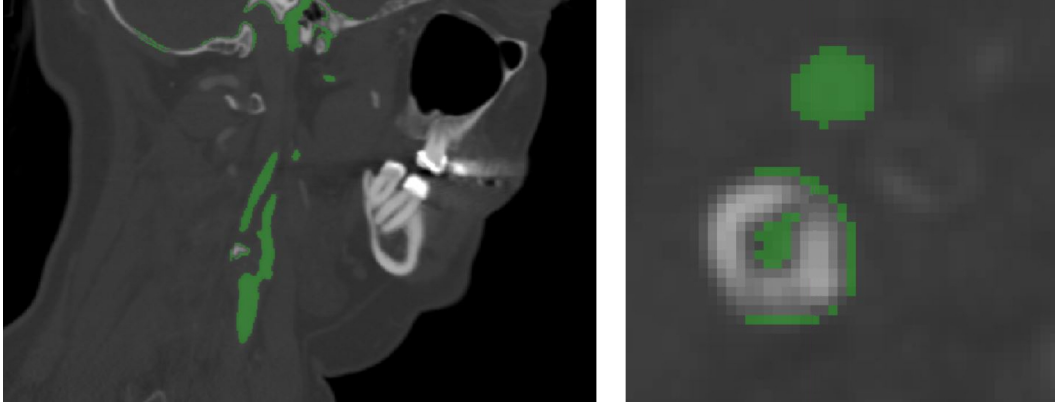


Figure 4.2: Example of the thresholding of an image of a bifurcation of carotid artery.

In addition, it is possible to obtain a 3D image of the artery of the real patient from the mask generated by the segmentation, Figure 4.3, where the reduction of the lumen caused by the atheroma plaque as well as the calcification can be seen. In addition, other small vessels that supply the brain and the face with blood can be observed in the ICA and ECA.

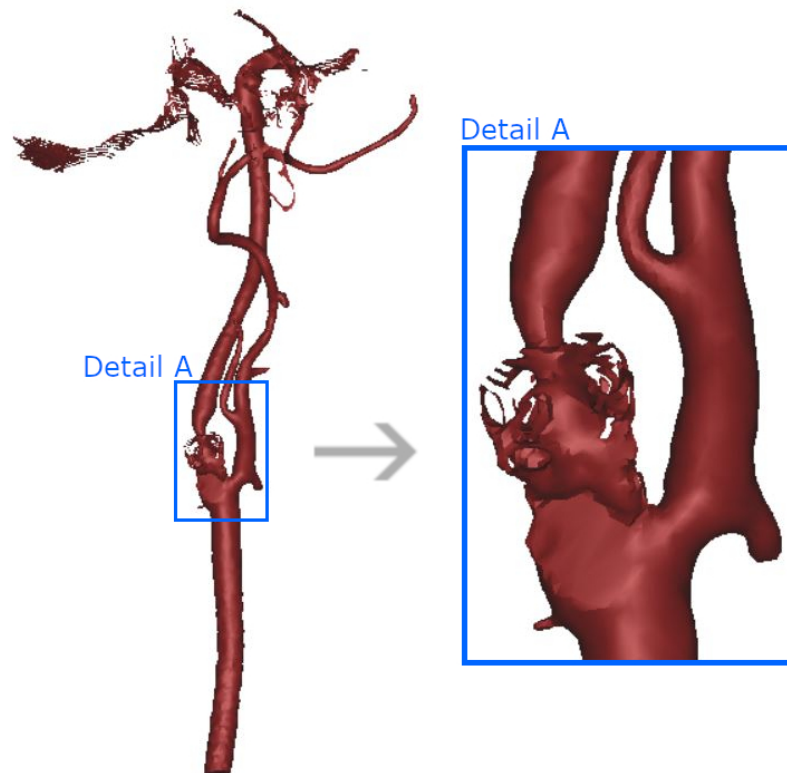


Figure 4.3: Geometry in 3D of the artery of the real patient with a detail of the area near the atheroma plaque and the calcification.

Once that the segmentation of the images has been done, the plaques of the carotids can be located, and they have been digitally removed to obtain the geometries that are considered as the healthy arteries previous to the development of the pathology.

Finally, the arterial wall has been extruded with the software Rhinoceros (Robert McNeel & Associates, Seattle, WA, United States) to obtain a 3D geometry of the arterial wall with variable thickness, imposing a thickness of 0.7mm for the CCA and 0.53mm to the ICA and ECA (Sommer et al., 2010). In addition, the thickness in the area close to the bifurcation has been progressively reduced when advancing from the CCA to de ICA and ECA, according to their respective thickness.

In Figure 4.4, the reconstructed lumen of the example is included in the left, as well as the complete geometry with the arterial wall in the middle and a detail of the area of the bifurcation, in the right.

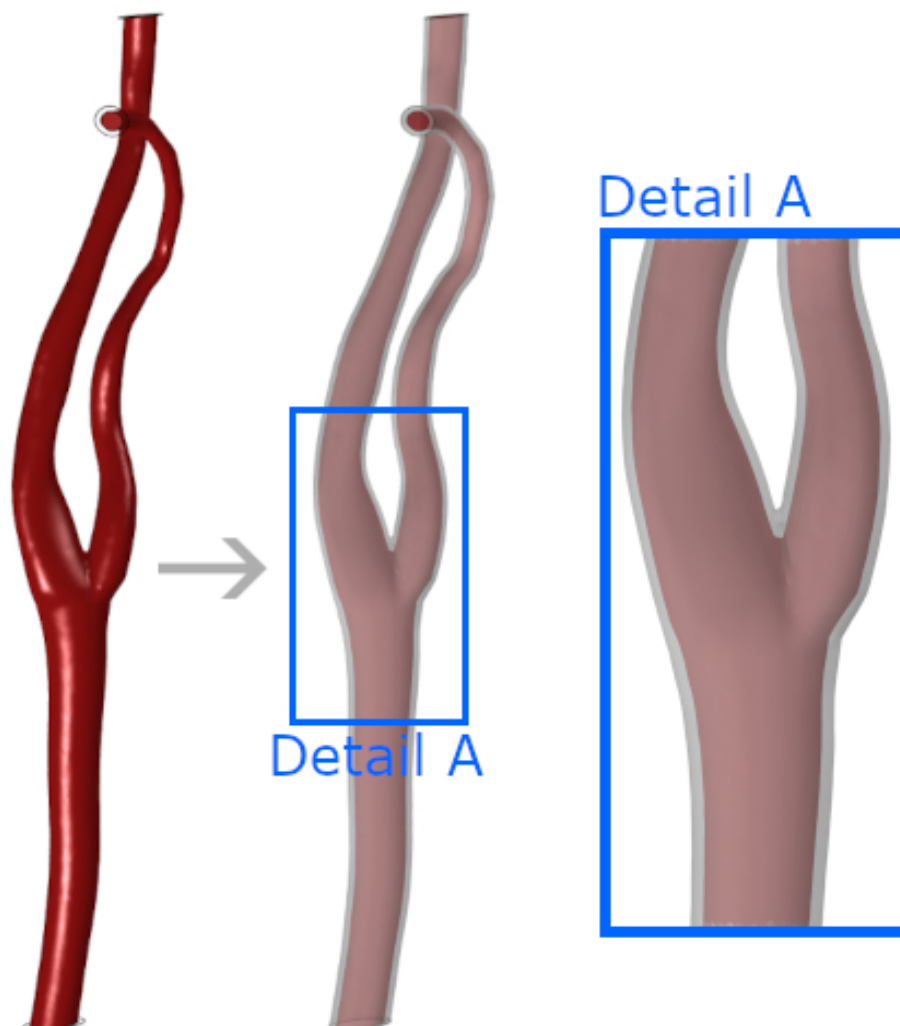


Figure 4.4: Reconstructed geometry of the real patient with a detail of the area near the bifurcation.

The different geometries are coded from "A" to "H". Table 4.1 shows the correspondence between patients and geometries, as well as if a geometry corresponds to a right or a left carotid artery.

	Patient	Geometries	Carotid
Pathological	1	A	Left
		B	Right
	2	-	Left - Completely occluded
		C	Right
	3	D	Left
		E	Right
	4	F	Left
		G	Right
Healthy	5	H	Left

Table 4.1: Correspondence between patients and each one of the computed geometries.

As can be seen in Table 4.1, there is a total of five patients, four of which corresponds to pathological patients that present atheroma plaques. The other patient corresponds to a healthy patient. Two different geometries have been reconstructed from each one of the patients, with the exception of patient "2", whose left carotid artery had the ICA completely occluded by a plaque. Therefore, the lumen of the ICA cannot be seen in his clinical image and thus the complete carotid bifurcation cannot be repaired. In addition, in the case of the healthy patient, only the left carotid artery was provided. Thus, there is only one healthy geometry.

All the geometries of the real carotids with atheroma plaques are shown in Figure 4.5, where the plaques are indicated by arrows. In addition, the healthy geometry is included as well.

All the geometries, with the exception of "E", have large atheroma plaques at both, the CCA close to the bifurcation and at the ICA. On the contrary, geometry "E" presents an unique plaque in the ICA.

In addition, Figure 4.6 shows details of the bifurcation area of the computed geometries of all the carotid arteries. The geometry "H", correspondent to the healthy geometry, has not been modified.

By comparing Figures 4.5 and 4.6, some differences can be noticed, in addition to the reconstruction of the plaques. These differences are due to the simplifications that are necessary to compute the model, e.g. the small side branches of the carotids have been eliminated in the computed geometry to simplify the model and it could have some influence on the blood flow distribution.

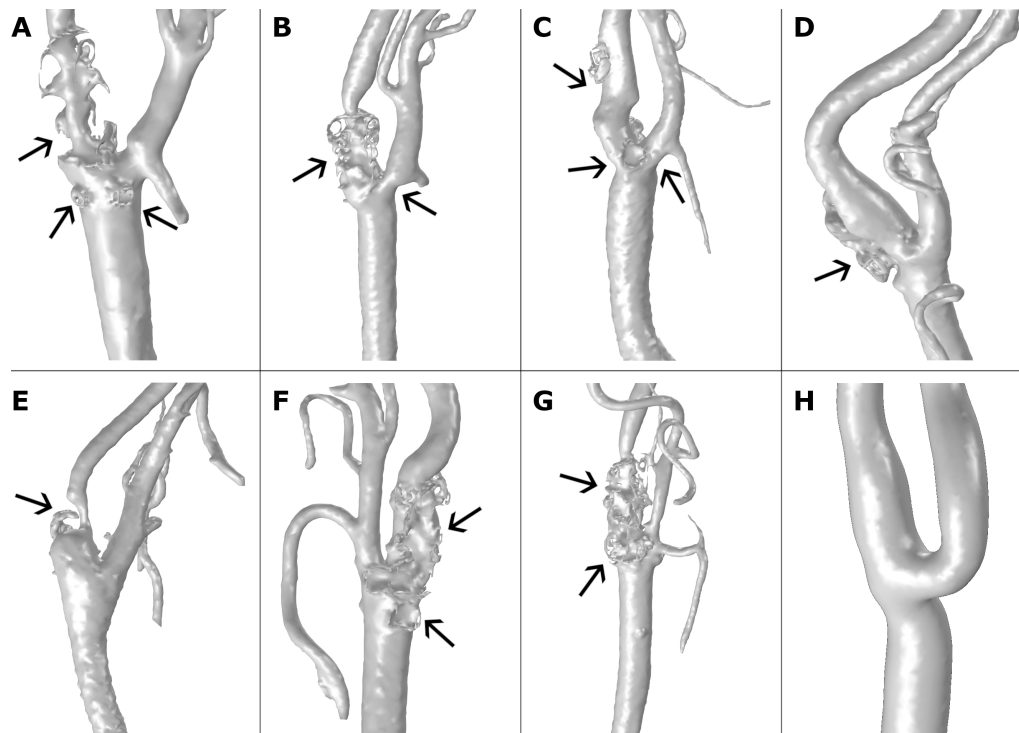


Figure 4.5: Details of the bifurcation area of all the patients with atheroma plaque ("A"–"G") and the healthy volunteer ("H"). Black arrows signal the plaques.

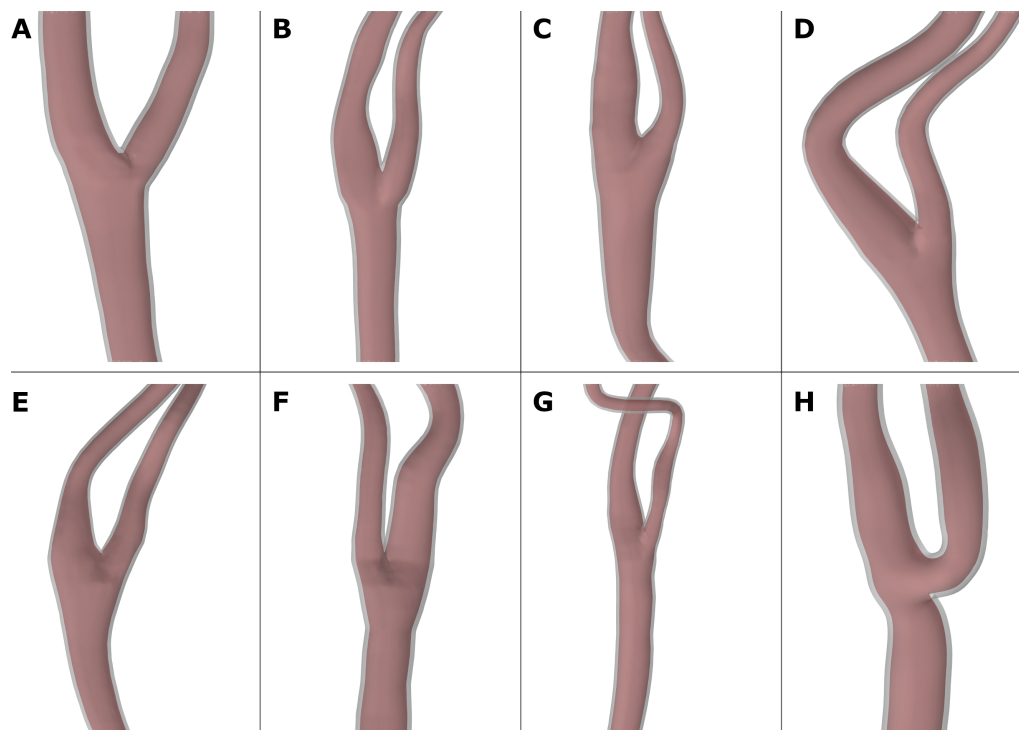


Figure 4.6: Details of the bifurcation area of all the reconstructed geometries.

The patient-specific geometry "A" has been used to estimate the parameters not found in the literature to computationally reproduce the location and size of the real plaque. Once done these estimations, these parameters have been used for the other geometries. The healthy volunteer, named "H", has been used to demonstrate that the mechanobiology model can also predict a healthy case without pathological plaques.

4.3 Boundary conditions

Due to the influence of haemodynamic stimuli on the growth model, blood flow in this chapter is modelled in transient mode. Mass flow and pressure of blood in arteries change throughout the cardiac cycle, depending on the movements of the heart. In particular, a heartbeat is composed of ventricular systole and diastole. During the ventricular systole, the heart contracts and ejects blood into the aorta, increasing then the pressure and velocity of blood flow in all the arteries of the human body. On the contrary, during ventricular diastole, the heart relaxes and, therefore, the pressure and velocity of blood flow in arteries decrease (Fung, 1997). In addition, a non-slip condition is imposed at the endothelium.

4.3.1 Murray's law

At the inlet of the lumen of the geometries, transient mass flow is imposed. In the same way, transient pressures are imposed at the two outlets of the lumen as boundary conditions. There is no specific data of the patients to define the boundary conditions corresponding to each geometry. Therefore, the transient flow and pressures during a cardiac cycle imposed as boundary conditions for the different patients have been determined according to the literature.

The transient inlet blood flow during a cardiac cycle of Malvè et al. (2014) has been defined as the inlet mass flow for all the geometries. In addition, Murray's law has been applied to establish the correct division of blood flow in the bifurcations of all the geometries (Equation 4.1). For that, the mean inlet mass flow in the CCA during a cardiac cycle (\dot{m}_{CCA}), has been extracted from Malvè et al. (2014) and the mean values of the outlet mass flows in the ICA and ECA of all the geometries have been determined:

$$\dot{m}_{outlet,i} = \frac{\dot{m}_{CCA} \cdot D_{outlet,i}^3}{\sum_{i=1}^n D_{outlet,i}^3}, \quad (4.1)$$

where the subscript i makes reference to all the outlet branches of the bifurcation, in this case, ICA and ECA. Therefore, $\dot{m}_{outlet,i}$ is the outlet mass flow of the ICA or ECA in each case, while $D_{outlet,i}$ is its diameter near the bifurcation. The divisor term of the equation is equal to the sum of the diameters of the ICA and ECA near the bifurcation of all the carotid arteries. Then, the outlet mass flows in each artery have been determined with Equation 4.1.

Once that the values of the mean outlet mass flows of the ICA and ECA are known for all the carotid geometries, the relation of the outlet pressures of the ICA and ECA that produce these flows have been determined by iterating with the Software COMSOL Multiphysics, obtaining the results included in Table 4.2:

Geometry	D_{ICA} (mm)	D_{ECA} (mm)	Mass flow ICA (kg/s)	Mass flow ECA (kg/s)	Relation P_{ECA} and P_{ICA} (mmHg)
A	6.41	4.61	$6.04 \cdot 10^{-3}$	$2.26 \cdot 10^{-3}$	$P_{ECA} = P_{ICA} - 1.02$
B	5.63	4.64	$5.32 \cdot 10^{-3}$	$2.98 \cdot 10^{-3}$	$P_{ECA} = P_{ICA} - 11.77$
C	7.55	4.32	$7.00 \cdot 10^{-3}$	$1.31 \cdot 10^{-3}$	$P_{ECA} = P_{ICA} - 1.77$
D	8.39	4.64	$7.10 \cdot 10^{-3}$	$1.21 \cdot 10^{-3}$	$P_{ECA} = P_{ICA}$
E	6.84	5.39	$5.58 \cdot 10^{-3}$	$2.73 \cdot 10^{-3}$	$P_{ECA} = P_{ICA} + 1$
F	6.6	3.92	$6.87 \cdot 10^{-3}$	$1.44 \cdot 10^{-3}$	$P_{ECA} = P_{ICA} - 0.5$
G	6.76	2.93	$7.68 \cdot 10^{-3}$	$6.25 \cdot 10^{-4}$	$P_{ECA} = P_{ICA} - 2$
H	3.55	2.83	$5.51 \cdot 10^{-3}$	$2.79 \cdot 10^{-3}$	$P_{ECA} = P_{ICA} - 1$

Table 4.2: Results of Murray's law in all the carotid arteries. Diameters and outlet mass flows of the ICAs and ECAs, and relations of pressures at the outlet of the ECAs and ICAs.

Knowing the relation between the outlet pressures of the ICA and ECA for all the geometries, their values during a complete cardiac cycle have been determined. For that, an average pressure of 100 mmHg has been defined at the outlet of the ICA during the cardiac cycle, maintaining the proportional profile for pressures over a complete cardiac cycle of Malvè et al. (2014). In Figure 4.7, the blood flow at the inlet of the CCA and pressures at the outlets of the ICA and ECA imposed for the case of the geometry "A" are represented.

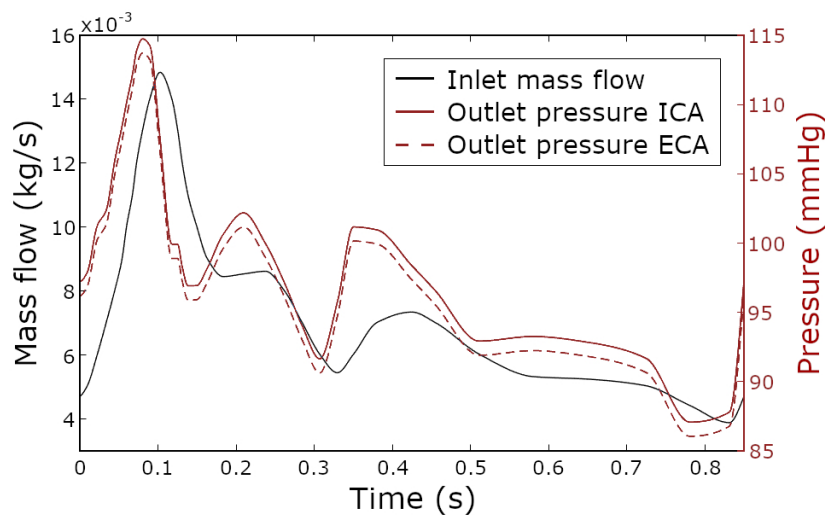


Figure 4.7: Blood mass flow at the inlet of the CCA of the geometry "A" and pressure at the outlets of the ICA and ECA (Malvè et al., 2014).

4.3.2 LDL and monocyte concentration in lumen

According to the results of Chapter 3, the concentrations of LDL and monocytes in the lumen are imposed as boundary conditions of the model. The patients were supposed to have a high level of hypercholesterolemia with an LDL concentration in blood of $6.98 \frac{\text{mol}}{\text{m}^3}$, equivalent to $270 \frac{\text{mg}}{\text{dL}}$ (Cilla, 2013).

A concentration of monocytes equal to $550 \cdot 10^9 \frac{\text{Monocyte}}{\text{m}^3}$ is also imposed (Khan, 2009).

4.4 Haemodynamical stimuli

Three different mechanical stimuli are analysed in this chapter as potential triggers for the inflammatory process and predictors to foresee the position and growth of atheroma plaques: TAWSS, OSI, which are commonly used in the literature (Alimohammadi et al., 2017; Sáez et al., 2015), and a combination of them that is proposed in this Thesis as a new stimulus (NV).

A total of three cardiac cycles have been simulated, to ensure that the blood flow is developed (Section 4.7) and thus, the values of the third cardiac cycle are considered to determine the distribution of the haemodynamical variables in the endothelium of the artery that initiates the plaque growth.

The first one of this haemodynamical stimuli is TAWSS, which can be defined as:

$$TAWSS = \frac{1}{T} \int_0^T |\tau(t)| \cdot dt, \quad (4.2)$$

where T is the period of a cardiac cycle and $|\tau(t)|$ the magnitude of WSS dependent of time, being WSS already defined in Equation 2.7.

Analogously to the case of WSS, the shape index of the endothelial cells directly depends of TAWSS, being proximal to 1 in case of low TAWSS -meaning that endothelial cells are almost circular-. To determine the behaviour of endothelial cells with TAWSS, this behaviour is assumed to be the same than in the case of WSS and, therefore, the numerical correlation based in the experimental results of Levesque et al. (1986) (Figure 2.4 of Chapter 2) applied to TAWSS is used:

$$SI = k_1 \cdot e^{(k_2 \cdot TAWSS)} + k_3 \cdot e^{(k_4 \cdot TAWSS)} \quad (4.3)$$

The values of the parameters k_1 , k_2 , k_3 and k_4 are included in Table 4.3.

It is well accepted that areas of low TAWSS are atheroprone. In particular, for carotid arteries, areas below 2 Pa are usually considered susceptible of apparition of atheroma plaques (Filipovic et al., 2013; Younis et al., 2004; Zhao et al., 2002).

The second mechanical stimulus considered in this chapter is OSI, which is defined as:

$$OSI = 0.5 \cdot \left(1 - \frac{|\frac{1}{T} \int_0^T \tau(t) \cdot dt|}{TAWSS} \right) \quad (4.4)$$

SI can be considered to depend directly of OSI so, to determine this behaviour, the next correlation is proposed, obtained from pseudo-experimental data of Sáez et al. (2015) with the Software MATLAB, Figure 4.8.

The endothelial shape index in the case of OSI can be calculated as:

$$SI = k_5 \cdot OSI^2 + k_6 \cdot OSI + k_7 \quad (4.5)$$

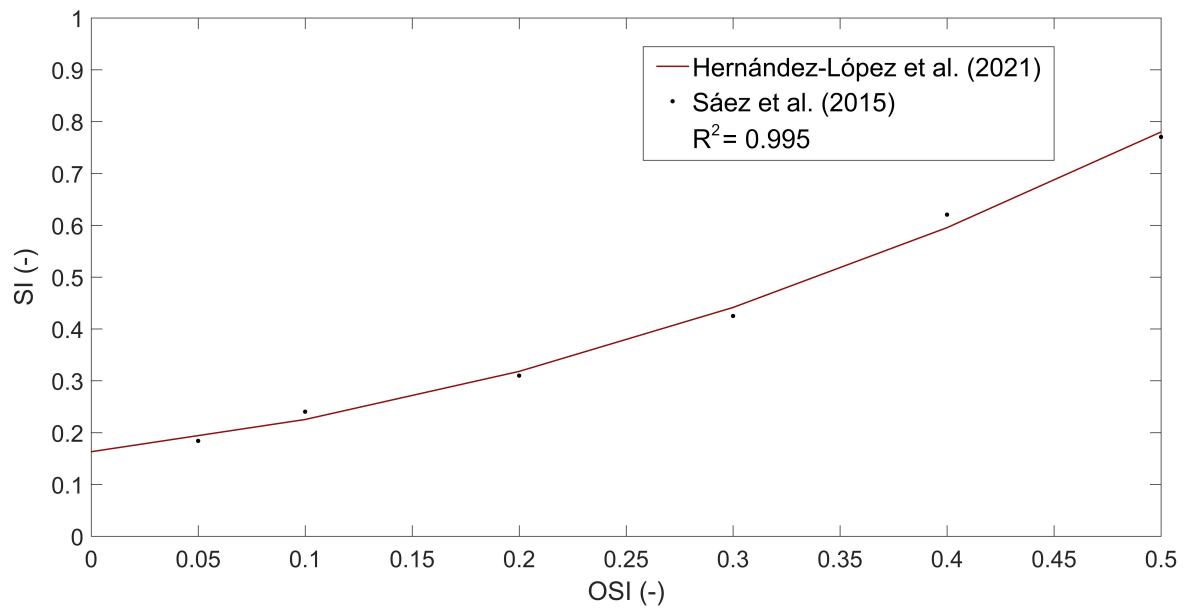


Figure 4.8: Correlation between shape index and oscillatory shear index based on pseudo-experimental data from Sáez et al. (2015) (Dots of the graphic). Garnet line: Proposed correlation of OSI in function of SI.

Areas with high OSI are atheroprone, so atheroma plaques are more likely to appear there (Sáez et al., 2015). To estimate the OSI threshold, the value of SI corresponding to a value of TAWSS of $2Pa$ (Equation 4.3) is calculated ($SI = 0.3085$) assuming that, for this value of SI, the LDL molecules can pass through the endothelium. Therefore, by replacing this SI value of 0.3085 on Equation 4.5, it can be estimated that atheroma plaques will grow up in areas of OSI higher than 0.1910. The values of the parameters k_5 , k_6 and k_7 are included in Table 4.3.

Finally, we propose a new index to calculate the growth of plaques as a combination of TAWSS and OSI, with the aim of take into account the effect of both stimuli. For that, pseudo-experimental data from Sáez et al. (2015) is used to approximate the variable SI as a function of TAWSS and OSI with the software MATLAB, obtaining:

$$SI = k_8 \cdot e^{k_9 \cdot OSI} + k_{10} \cdot e^{k_{11} \cdot (\frac{TAWSS}{TAWSS_0})^2}, \quad (4.6)$$

To determine areas of plaques growth with this new index, the values of the thresholds obtained before for TAWSS and OSI are used. All the adjustment parameters used in the analysis k_8 , k_9 , k_{10} and k_{11} , are in Table 4.3. The approximation surface is showed in Figure 4.9.

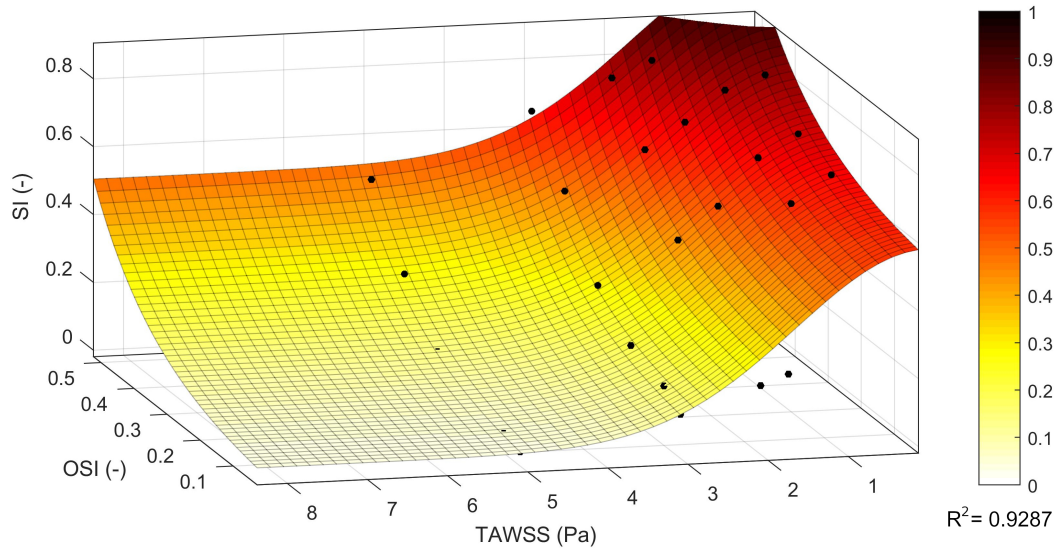


Figure 4.9: Correlation surface among the shape index, time average wall shear stress and oscillatory shear index based on data from Sáez et al. (2015).

The adjustment parameters for all the considered mechanical stimuli are:

Mechanical stimulus	Parameter	Value
TAWSS Threshold = 2 Pa	k_1	0.6296
	k_2	-0.8709
	k_3	0.2145
	k_4	-0.03938
OSI Threshold = 0.1910	k_5	1.53
	k_6	0.4688
	k_7	0.1631
NV TAWSS threshold = 2 Pa OSI threshold = 0.1910	k_8	0.0264
	k_9	5.647
	k_{10}	0.5513
	k_{11}	-0.1815

Table 4.3: Adjustment parameters for the correlation of SI as a function of TAWSS, OSI and NV.

Monocyte flow from the lumen into the arterial wall through the endothelium also depends on the hemodynamical stimulus that is considered. For the case of TAWSS, it can be modelled with Kedem-Katchalsky equation as (Gijssen et al., 2008; Malek and Alper, 1999):

$$J_{s,m}(TAWSS) = \frac{m_r}{\left(1 + \frac{TAWSS}{TAWSS_0}\right)} \cdot C_{LDL,ox,w} C_{m,l}, \quad (4.7)$$

where m_r is monocyte recruitment from the lumen to the endothelium. TAWSS is modelled as a sigmoid function with maximal and minimal values equal to 2 and 0 Pa to allow LDL flow across the endothelium. To completely define the sigmoid, an average value called $TAWSS_0$ of 1 Pa is necessary.

On the other hand, there is no function in the literature of the monocyte flow across the endothelium depending on OSI. Therefore, a new equation has been developed so that the monocyte flow in the case of OSI is analogous to that of TAWSS.

The monocyte flow depends, in addition of the haemodynamical stimulus, on the parameter of monocyte recruitment and the concentrations of oxidised LDL in the arterial wall and monocyte in the lumen (Equation 4.7), which are the same independently of the considered haemodynamical stimulus. For this purpose, the part of the equation dependent on TAWSS has been considered equal to the function of OSI that has to be approximated, and named as multiplying function:

$$\frac{1}{1 + \frac{TAWSS}{TAWSS_0}} = f(OSI) \quad (4.8)$$

Due to that plaques are developed in areas of low TAWSS and high OSI, the multiplying function in this cases has to be the same for both haemodynamical stimuli. For example, the maximum value of the multiplying function (equal to 1) corresponds to the case of TAWSS equal to 0 Pa, and to the case of OSI equal to 0.5. Table 4.4 shows the known values of the multiplying function depending on TAWSS and its corresponding values of OSI:

TAWSS (Pa)	OSI (-)	Multiplying function (-)
2	0.1910	$\frac{1}{3}$
1	0.3455	$\frac{1}{2}$
0	0.5	1

Table 4.4: Multiplying function values respective to the considered cases of TAWSS and OSI.

Subsequently, these points have been approximated with the software MATLAB with an exponential function, obtaining that the monocyte flow in the case of OSI is:

$$J_{s,m}(OSI) = m_r \cdot (8.503 \cdot OSI^2 - 3.741 \cdot OSI + 0.7449) \cdot C_{LDL,ox,w} C_{m,l}, \quad (4.9)$$

The approximate function is included in Figure 4.10:

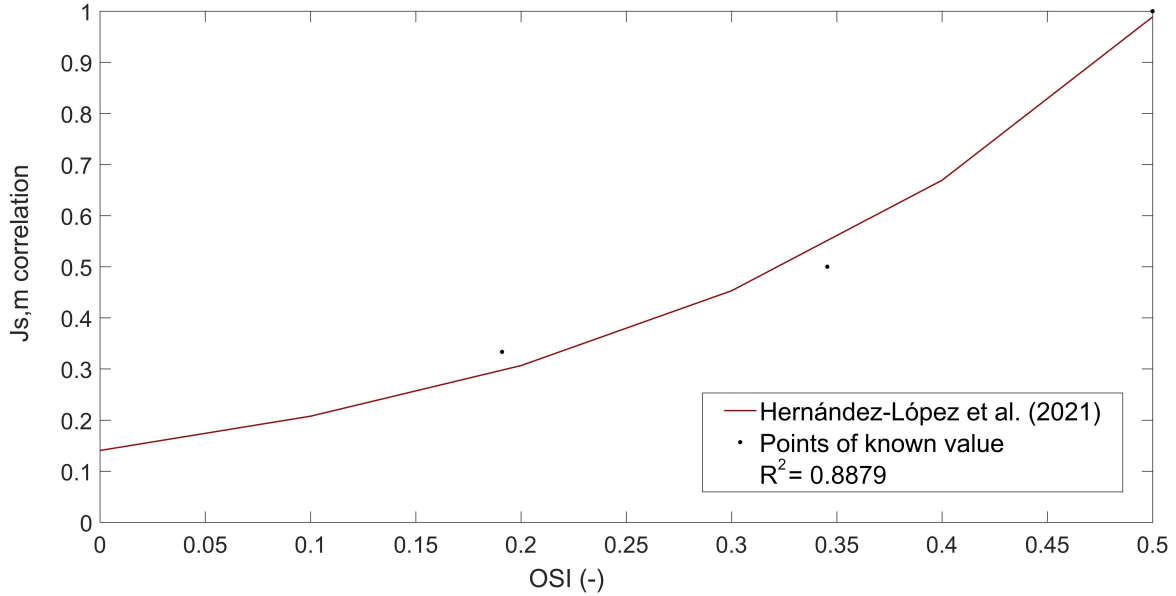


Figure 4.10: Correlation between the flow of monocytes across the endothelium and OSI. Garnet line: Proposed correlation of monocyte flow in function of SI.

The analogue procedure has been done for the NV, in which the multiplying function is a combination of TAWSS and OSI. To define the multiplying function depending on NV, three different cases of knowing values have been analysed: The first one considers low values of both, TAWSS and OSI, and thus, monocyte flow across the endothelium is only due to TAWSS. The second is the opposite case, in which there are high values of TAWSS and OSI and the monocyte flow is only due to the effect of OSI. Finally, the third case considers the effect of low values of TAWSS and high values of OSI and, therefore, the monocyte flow in this case is due to both haemodynamical stimuli. For this purpose, we assume that when TAWSS is equal to 0 Pa or OSI is equal to 0.5, the endothelial pores are completely saturated and no more monocyte influx is possible, so in this case the maximum monocyte flow is the same as in the cases of maximum flow due to only TAWSS or OSI. The resultant multiplying function for the case of NV is:

$$J_{s,m}(TAWSS, OSI) = m_r \cdot (0.8588 \cdot e^{-0.6301 \cdot \frac{TAWSS}{TAWSS_0}} + 0.1295 \cdot e^{3.963 \cdot OSI}) \cdot C_{LDL,ox,w} C_{m,l} \quad (4.10)$$

The correlation surface is shown in Figure 4.11:

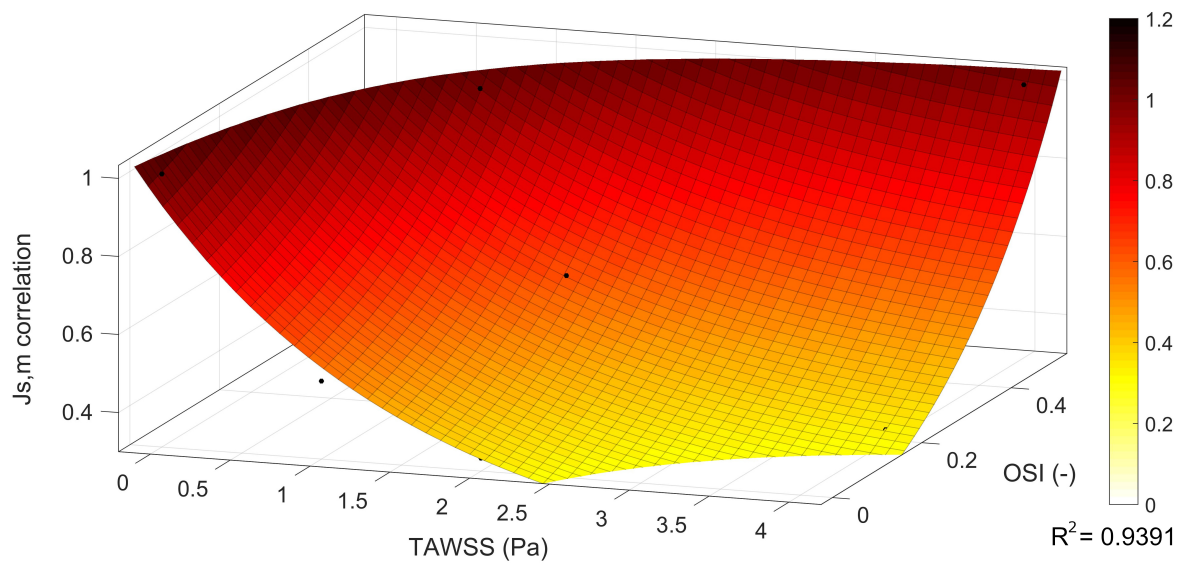


Figure 4.11: Correlation surface among the flow of monocytes across the endothelium, TAWSS and OSI.

4.5 Numerical methods

The total time of the numerical simulations implemented is 30 years (Insull, 2009). The software COMSOL Multiphysics (COMSOL AB, Burlington, MA, USA) has been used to computationally solve the model. A first transient step has been used to simulate the blood flow along three cardiac cycles. Then, a second step under stationary hypothesis has been performed to solve the plasma flow across the endothelium. Afterwards, a third step has been computed in transient mode to calculate the concentrations of all the substances in all the arterial wall during thirty years, and finally, a fourth and last stationary step has been made to compute the growth of the plaques from the concentration of all the substances at thirty years. In Figure 4.12 there is a scheme with the followed workflow.

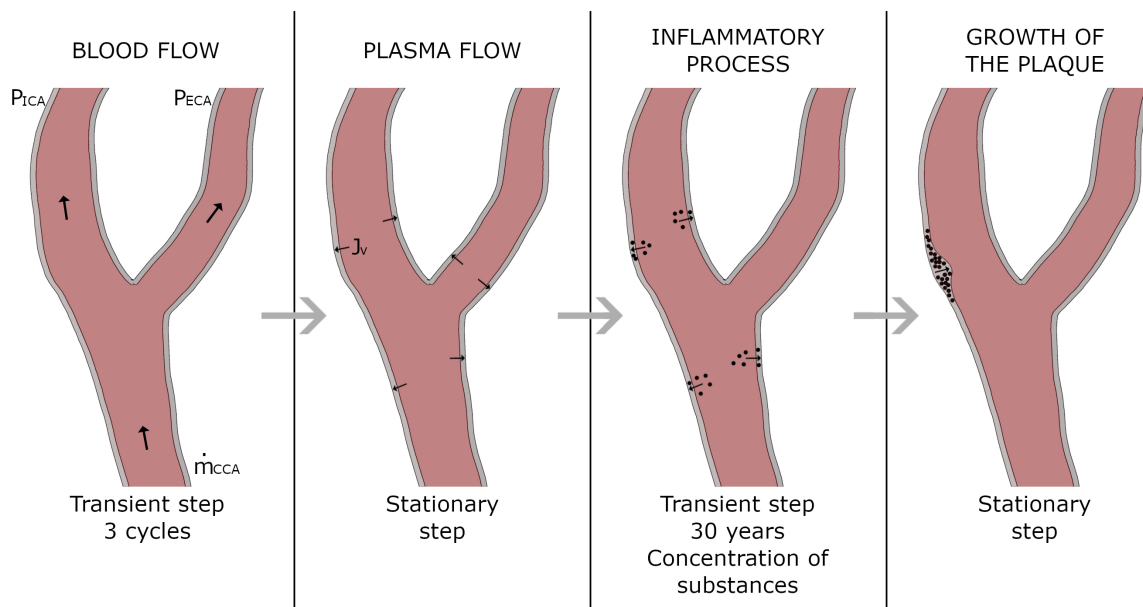


Figure 4.12: Workflow of the computational process.

A direct linear solver (parallel direct sparse solver, PARDISO, (PARDISO, 2007)) has been used to solve the transient blood flow along the lumen. The direct linear solver (MUMPS, (MUMPS, 1999)) has been employed to compute the plasma flow through the endothelium. The inflammatory process of all the substances has been computed with an iterative solver (Generalized Minimum Residual method, GMRES (Saad and Schultz, 1986)), using different segregated steps for groups of substances. Finally the growth of the plaques has been computed with the linear solver MUMPS and the Newton's method. In addition, the transient blood flow and the inflammatory process in the arterial wall has been solved using the BDF implicit method (Curtiss and Hirschfelder, 1952; Gear, 1967) and Newton's method for non-linear problems.

4.6 Mesh sensitivity analysis

The geometries are meshed using triangular elements. A discretisation with P1-P1 elements has been made for the blood flow. Quadratic elements are used to the plasma flow across the endothelium, while linear and Serendipity quadratic elements are used for the inflammatory process and the plaque growth, respectively. Mesh sensitivity analysis has been performed for both, the lumen and the arterial wall, to determine optimal meshes to finally compute the whole process. With this sensitivity analysis, the characteristics of the meshes are determined, and the total number of elements of each mesh depends on the geometry. All the selected meshes have two boundary layers in the lumen (near the endothelium) and, also, two couples of boundary layers in the arterial wall (near the endothelium and near the adventitia), to ensure the correct determination of flows across the arterial wall. The number of boundary layers of the mesh of the lumen has been analysed as well.

Two details of the selected mesh for the case of the geometry "A" are shown in Figure 4.13.

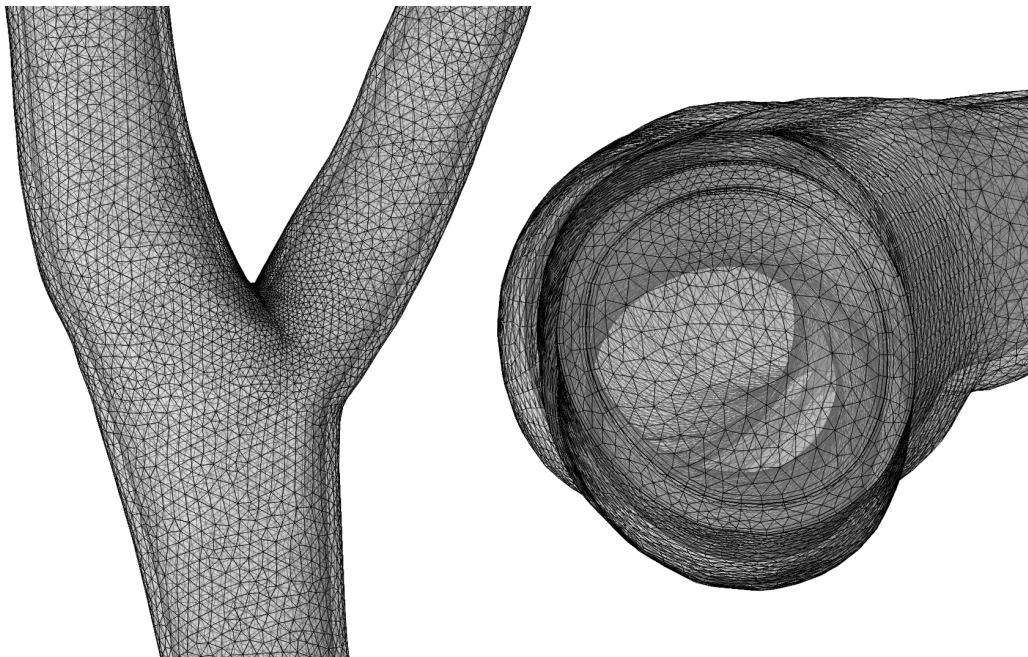


Figure 4.13: Details of the selected mesh for patient "A" in the areas of the bifurcation (left) and in the inlet of the geometry (right).

To determine the optimal meshes for the lumen and the arterial wall, the criteria of less than 5% variation in results explained in Chapter 3 has been chosen.

For the sensitivity analysis, the geometry "A" has been used to determine the optimal characteristics of the meshes of the lumen and the arterial wall. Due to that all the geome-

tries have similar sizes, these characteristics have been applied then to all the geometries, to generate their meshes.

As commented in Section 4.5, the mesh of the lumen has boundary layers near the endothelium. Therefore, the sensitivity analysis of the mesh of the arterial lumen has been done in two different steps. In the first step, the size of the elements is analysed while, in the second one, the number of boundary layers near the endothelium is determined.

In order to determine the appropriate size for the lumen elements, an analysis of the results obtained with three different meshes has been carried out. The characteristics of the three meshes are the same, with the exception of the maximum element size. The common characteristics of all meshes are included in Table 4.5.

Min. element size (mm)	Max. element growth rate	Resolution of curvature	Resolution of narrow regions
0.119	1.1	0.4	0.9

Table 4.5: Characteristics of the analysed meshes for the lumen.

Three different maximum element sizes are analysed, with respective values of 0.5, 0.47 and 0.4 mm, which result in three meshes for the lumen of the geometry "A" with a total of 145940, 170748 and 264485 nodes, respectively. All these meshes have 2 boundary layers in the area of the lumen close to the endothelium.

The results of TAWSS and OSI in the geometry "A" obtained with the three analysed meshes are shown in Figure 4.14. In the case of TAWSS, the results are showed with the maximum threshold of 2 Pa, due to it is the area in which plaques growth.

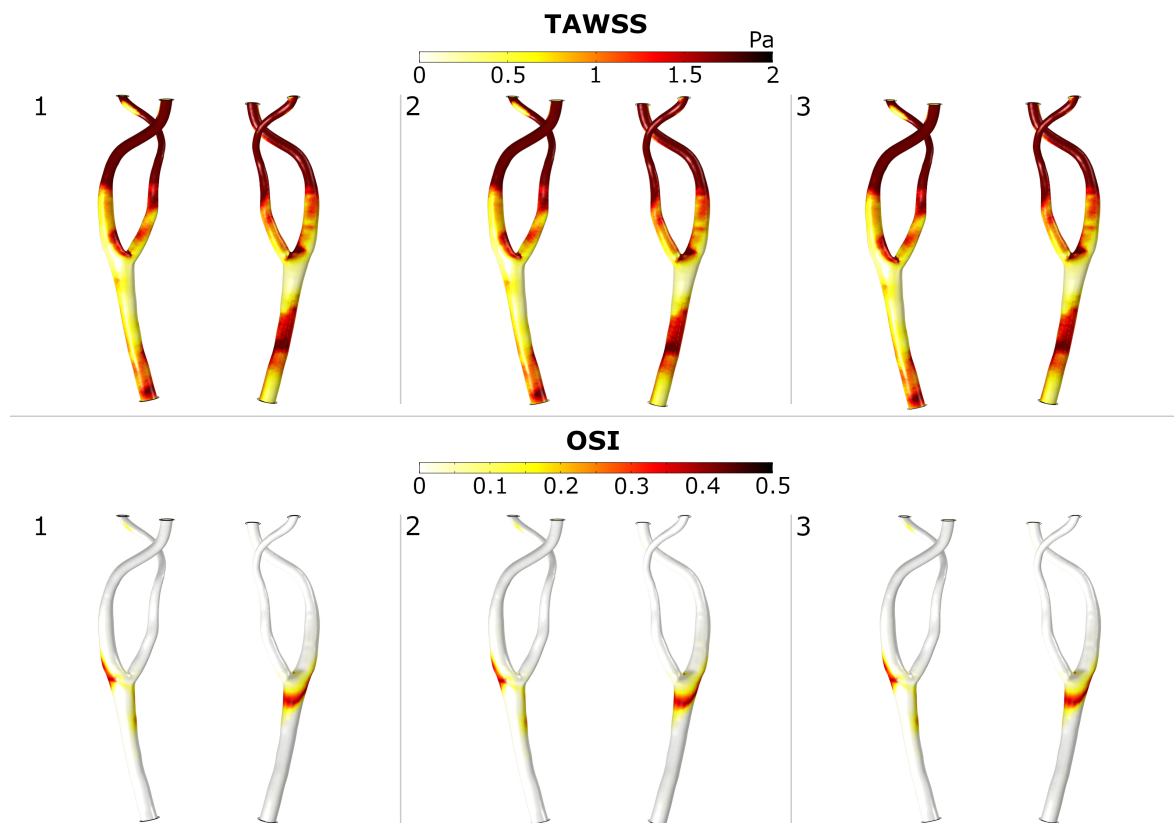


Figure 4.14: Mesh sensibility for the lumen of geometry "A", depending on the element size. The first row corresponds to the distribution of TAWSS with a threshold of 2 Pa while the second row correlates with OSI. Numbers 1, 2 and 3 correspond to maximum element sizes of 0.5, 0.47 and 0.40 mm, respectively.

As can be seen in Figure 4.14, there are no appreciable differences between the results of any of the analysed meshes, neither for TAWSS nor for OSI. Therefore, the surfaces on which the plaques can grow obtained with each of the meshes have been analysed.

As can be observed in Table 4.6, the differences between the variation of the areas with TAWSS lower than 2 Pa obtained with the meshes of 0.5 mm and 0.47 mm of maximum elements sizes and with the meshes of 0.47 mm and 0.4 mm are, respectively, 3.16 % and 2.74 %. However, the difference of these areas obtained with the meshes of 0.5 mm and 0.4 mm of maximum element sizes is 5.81 %, which is higher of 5 %. In addition, the variation of the area of OSI higher than 0.1910 is lower than 5 % in all the cases. Therefore, the mesh of the maximum elements size equal to 0.5 mm is discarded, and the selected mesh for the lumen of the arteries is that of maximum element size equal to 0.47 mm which, in the case of the geometry "A", corresponds to a total of 170748 nodes.

Maximum element size	Area of $TAWSS < 2 Pa$		Area of $OSI > 0.1910$	
	(mm^2)	Variation (%)	(mm^2)	Variation (%)
0.5 mm	2148.7	-	197.30	-
0.47 mm	2080.8	3.16	201.17	1.96
0.4 mm	2023.7	2.74	199.05	1.05

Table 4.6: Results of the areas of geometry "A" with $TAWSS < 2 Pa$ and $OSI > 0.1910$, obtained with the three different analysed element sizes for the meshes of the lumen.

In addition, the number of boundary layers of the lumen mesh near the endothelium has also been analysed, for the cases of two, three and four boundary layers in the geometry "A". In Figure 4.15, the results of TAWSS lower than $2 Pa$ and OSI are also included.

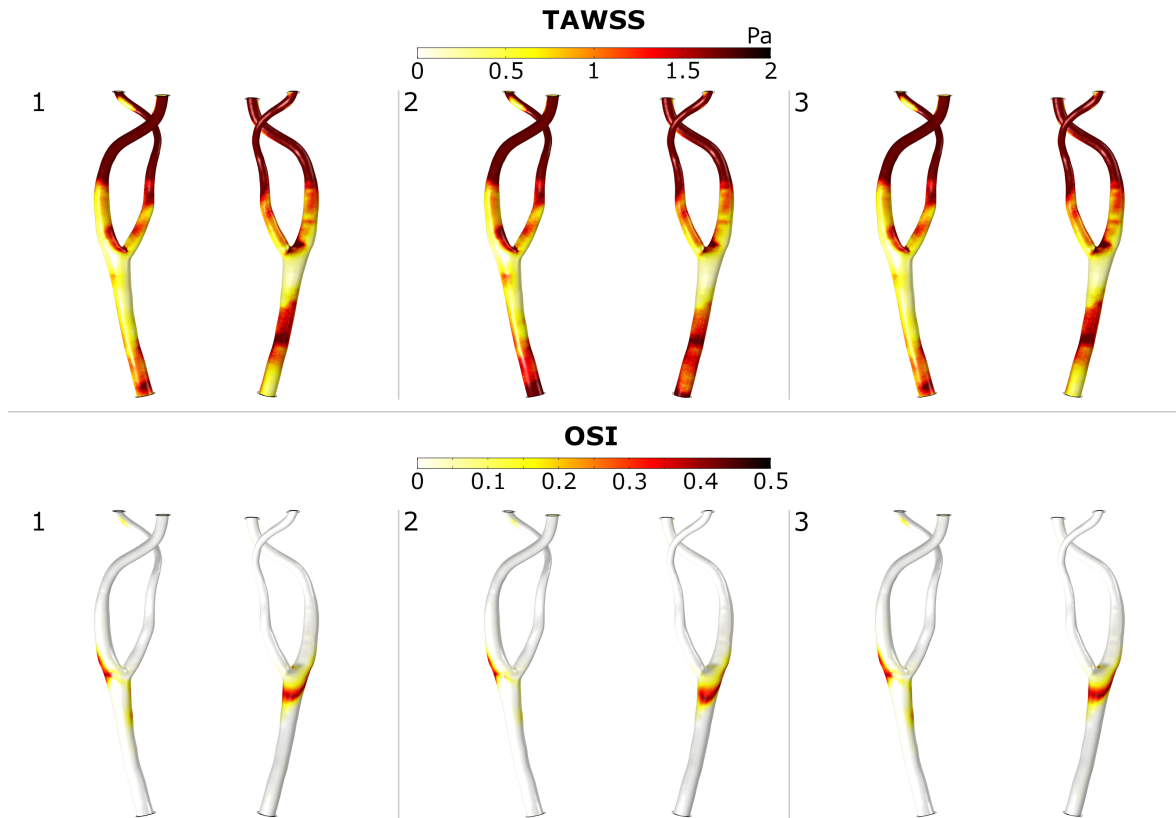


Figure 4.15: Mesh sensibility for the lumen of geometry "A", depending on the number of boundary layers. The first row corresponds to the distribution of TAWSS with a threshold of $2 Pa$ while the second row correlates with OSI. Numbers 1, 2 and 3 correspond to 2, 3 and 4 boundary layers, respectively.

As can be seen in Figure 4.15, there are no appreciable differences between the results obtained with different number of boundary layers. For this reason, the areas susceptible

of apparition of plaque in these cases are analysed:

Number of boundary layers	Area of $TAWSS < 2 Pa$		Area of $OSI > 0.1910$	
	(mm^2)	Variation (%)	(mm^2)	Variation (%)
2	2080.8	-	201.17	-
3	2092.6	0.56	204.70	1.75
4	2154.8	2.97	204.64	0.02

Table 4.7: Results of the areas of geometry "A" with $TAWSS < 2 Pa$ and $OSI > 0.1910$, with the different number of boundary layers analysed for the meshes of the lumen.

According to Table 4.7, the differences between the area with TAWSS lower than 2 Pa are 0.56 % between two and three layers, 2.97 % between three and four layers and 3.55 % between two and four layers. The differences in the area of OSI higher than 0.1910 are, in all the cases, lower than 1.75 %. Thus, the mesh with two boundary layers has been selected to optimise the computational time.

In addition, a sensitivity analysis of the mesh of the arterial wall has been done. In all the analysed cases, two boundary layers in the area near the endothelium and other two in the area near the adventitia have been included, to ensure that they are more than one node in the thickness of all the arterial wall (specially in the area near the bifurcation), due to that it is necessary to compute convection and diffusion across the arterial wall.

As in the case of the meshes of the lumen, the characteristics of all the arterial wall analysed meshes are the same, with the exception of the maximum element size, which has been determined as 0.85, 0.73 and 0.39 mm for the three analysed meshes.

The three analysed meshes, as well as the results of maximum LDL concentration and the maximum increase of the wall thickness due to the plaque growth for the geometry "A" are included in Table 4.8. Results of both variables for all the meshes are shown for the cases of considering TAWSS and OSI as the main mechanical stimulus.

The variation of the maximum LDL concentration in the arterial wall for all the cases is lower than 5 %. However, the variation of the maximum wall thickness increase obtained between the first and second meshes is 66 % and 57 % for the cases of considering TAWSS and OSI, respectively. Thus, the mesh of maximum element size equal to 0.85 mm has been discarded. On the contrary, the second and third meshes give the same results for the case of maximum wall thickness increase and, therefore, the characteristics of the second mesh are selected to compute all the geometries.

Max. element size (mm)	Mechanical Stimulus	$C_{LDL,max,w}$ ($\frac{mol_{LDL}}{m^3}$)	Wall thickness increase (mm)
0.85	TAWSS	0.036	0.069
	OSI	0.036	0.007
0.73	TAWSS	0.037	0.023
	OSI	0.037	0.003
0.39	TAWSS	0.036	0.023
	OSI	0.036	0.003

Table 4.8: Results of maximum LDL concentration in the arterial wall and maximum wall thickness increase, obtained with the different meshes analysed for the arterial wall with TAWSS and OSI as main mechanical stimuli.

The selected characteristics for the meshes are included in Table 4.9:

Max. element size (mm)	Min. element size (mm)	Max. element growth rate	Resolution of curvature	Resolution of narrow regions
0.73	0.49	1.08	0.3	0.95

Table 4.9: Characteristics of the mesh selected for the arterial wall.

Finally, the number of nodes of the lumen and the arterial wall meshes for all the geometries are included in Table 4.10.

Geometry	Number of nodes of the mesh	
	Lumen	Arterial wall
A	170748	174699
B	171050	169864
C	159709	164193
D	160870	174465
E	170304	163234
F	170482	161836
G	170326	161643
H	123581	144494

Table 4.10: Number of nodes of the lumen and the arterial wall meshes of all the geometries.

4.7 Analysis of the number of cardiac cycles

An analysis of the number of cardiac cycles necessary to model the blood flow along the lumen has been performed. For that, a total of five cardiac cycles have been computed in the geometry "A" obtaining the results of Table 4.11.

Cardiac cycle	TAWSS max. (Pa)	Area of $TAWSS < 2 Pa$ (mm^2)	Variation (%)	OSI max. (Pa)	Area of $OSI < 0.1910$ (mm^2)	Variation (%)
1	18.34	2081.9	-	0.49	202.0	-
2	18.32	2079.7	0.10	0.49	203.8	0.89
3	18.30	2080.8	0.05	0.49	201.2	1.27
4	18.29	2080.1	0.03	0.49	201.9	0.34
5	18.29	2080.4	0.01	0.49	201.1	0.39

Table 4.11: Results of TAWSS and OSI obtained for five cardiac cycles in the geometry "A".

As can be seen, the maximum values of TAWSS and OSI and the areas considered as atheroprone resultant for each one of the cardiac cycles are analysed (areas of TAWSS lower than $2 Pa$ and OSI higher than 0.1910). The variation of the results has been calculated for the cases of the atheroprone areas depending on TAWSS and OSI, and it has been determined between the analysed number of cardiac cycles in each case and the immediately previous one. These variations are lower than 5 % for all the analysed cycles and, therefore, all the solutions provided by any of the analysed number of cardiac cycles would be valid.

However, to minimise possible local errors in some instants of blood flow along the cardiac cycle due to the initiation of the process, a total number of three cycles has been chosen to ensure that the blood flow is completely developed. Therefore, the results of flow obtained for the third cardiac cycle are selected to calculate the plasma flow and the inflammatory process of the arterial wall.

4.8 Results

As can be seen, although the geometries are patient-specific, the parameters are based in literature due to the impossibility of determining their value for each patient. Therefore, there is some variability in them, which has been checked to see how it can affect to the model (Chapter 3). The parameters of the model have been calibrated with the patient "A" and used later for the rest of geometries. In the case of the parameters referred to size of cells, an average value of the parameters given in literature has been taken.

Regarding measurable parameters for each patient, the most important parameters whose variation would suppose a different behaviour of the model are LDL and monocyte

concentration in blood, as well as the arterial pressure of the patient since there are studies that correlate changes in the endothelial permeability as a function of the arterial pressure (Tedgui and Lever, 1984), and other factors, e.g. if the patients are taking medication or not.

In the case of different vascular regions with the same arterial pressure, the parameters that could vary are the hydraulic conductivity of the normal junctions, $L_{p,nj}$ (Tedgui and Lever, 1984), the monocyte recruitment, m_r (Steinberg et al. 1985), as well as the thickness of the arterial wall (Olgac et al. 2008, Sommer et al. 2010).

4.8.1 Healthy geometry results

First, the results obtained for the healthy geometry, "H", are analysed. The results of SI and maximum increase of the wall thickness due to the growth of plaques, computed with TAWSS, OSI and the new proposed variable for the healthy geometry are presented in Figure 4.16.

As could be expected, small areas with high SI -usually accepted as atheroprone- presents in the healthy geometry are small and, thus, the corresponding wall thickness increase due to plaque formation is reduced. In particular, in the case of OSI, negligible growth is presented.

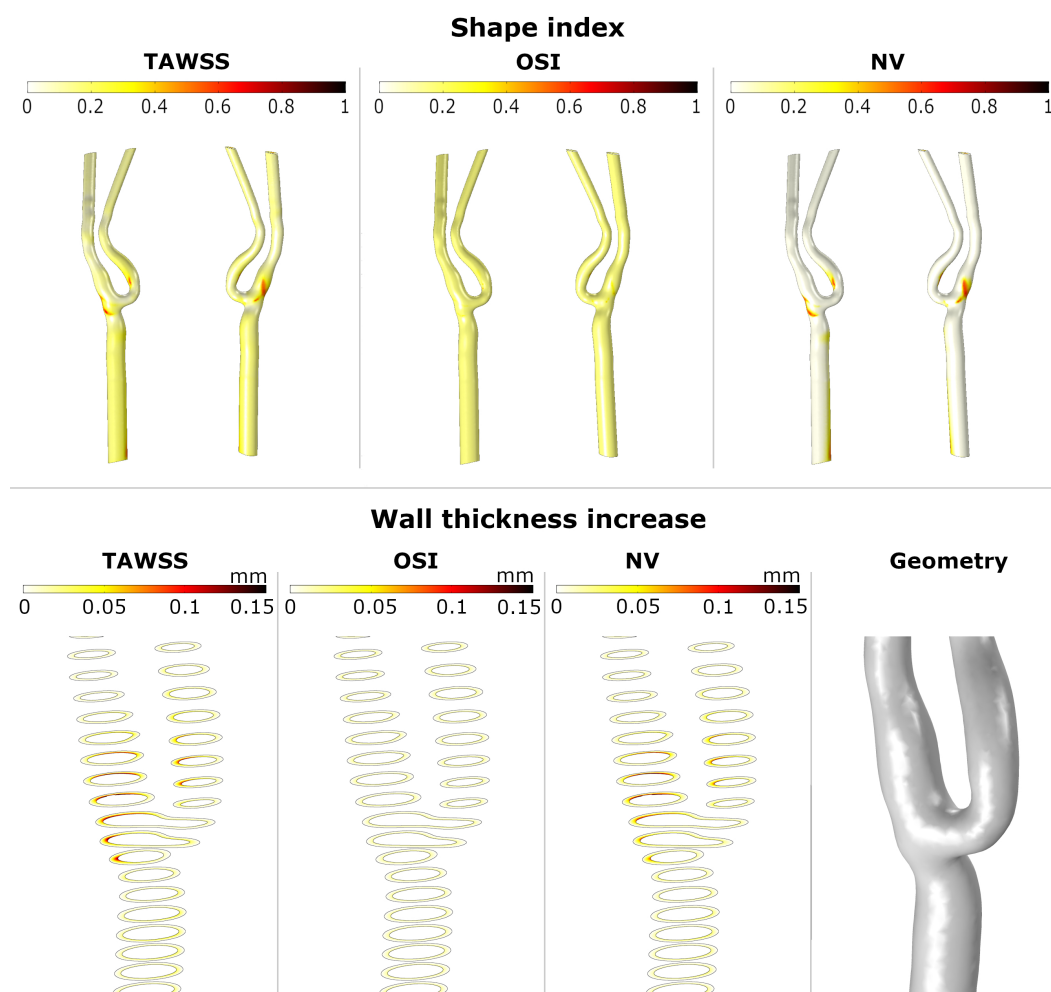


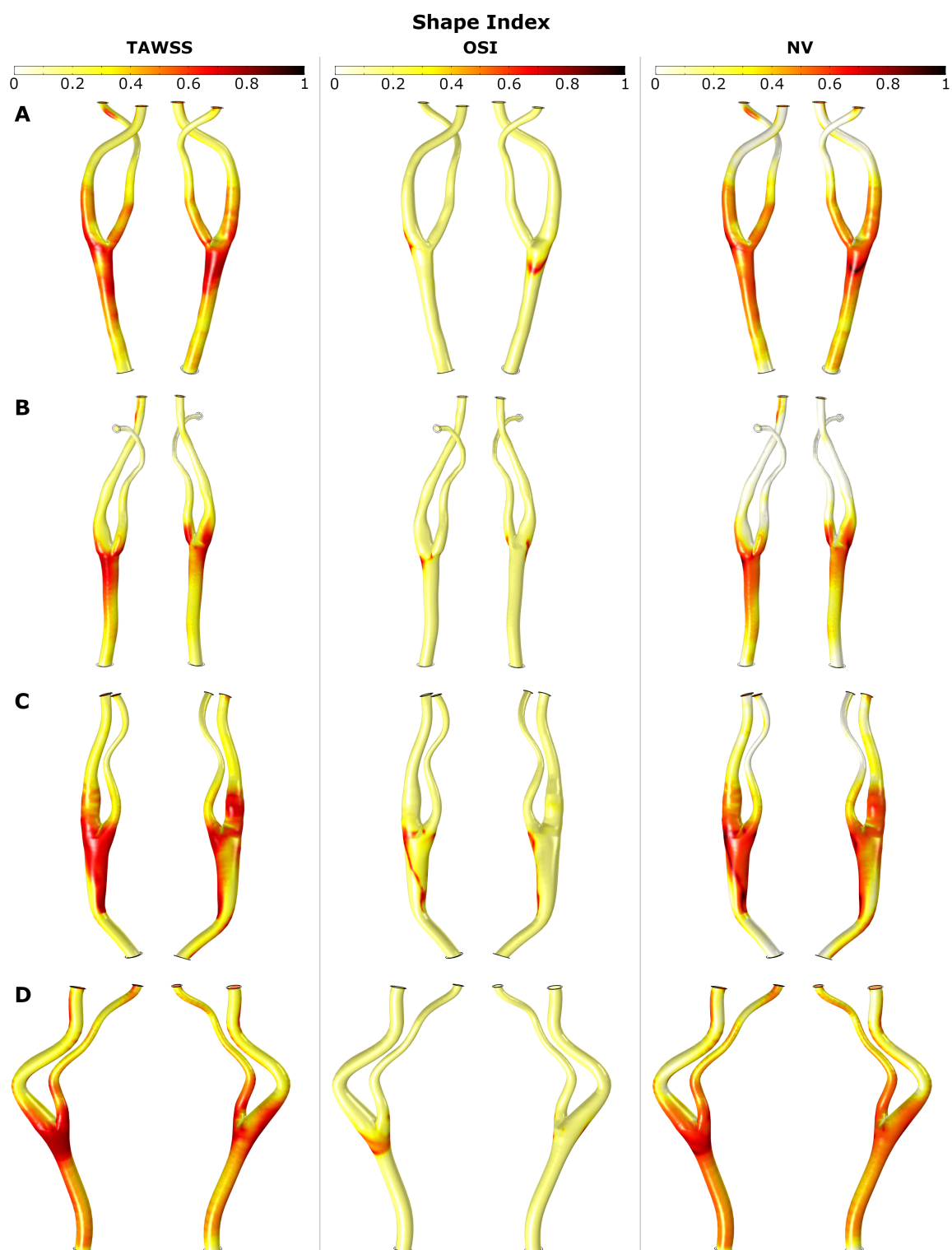
Figure 4.16: Shape index distribution (first row) and a detail of the wall thickness increase in the bifurcation area (second row) in the healthy geometry ("H").

Therefore, with the results obtained for the healthy geometry "H", it can be concluded that, in cases of healthy arteries, the computational model does not result in atheroma plaques growth.

4.8.2 Pathological geometries results

The SI distributions obtained with TAWSS, OSI and the new variable are represented for all the pathological carotid bifurcations in Figure 4.17.

As can be seen, OSI predicts the areas of high SI values near the bifurcation but with smaller areas than TAWSS, which also predicts areas of high SI in the CCA close to the bifurcation as well as in some areas of ICA and ECA. Finally, the new index also predicts high SI in these areas but in a more localised way than TAWSS. Note that for "E" geometry, none of the stimuli predicts the location of the plaque.



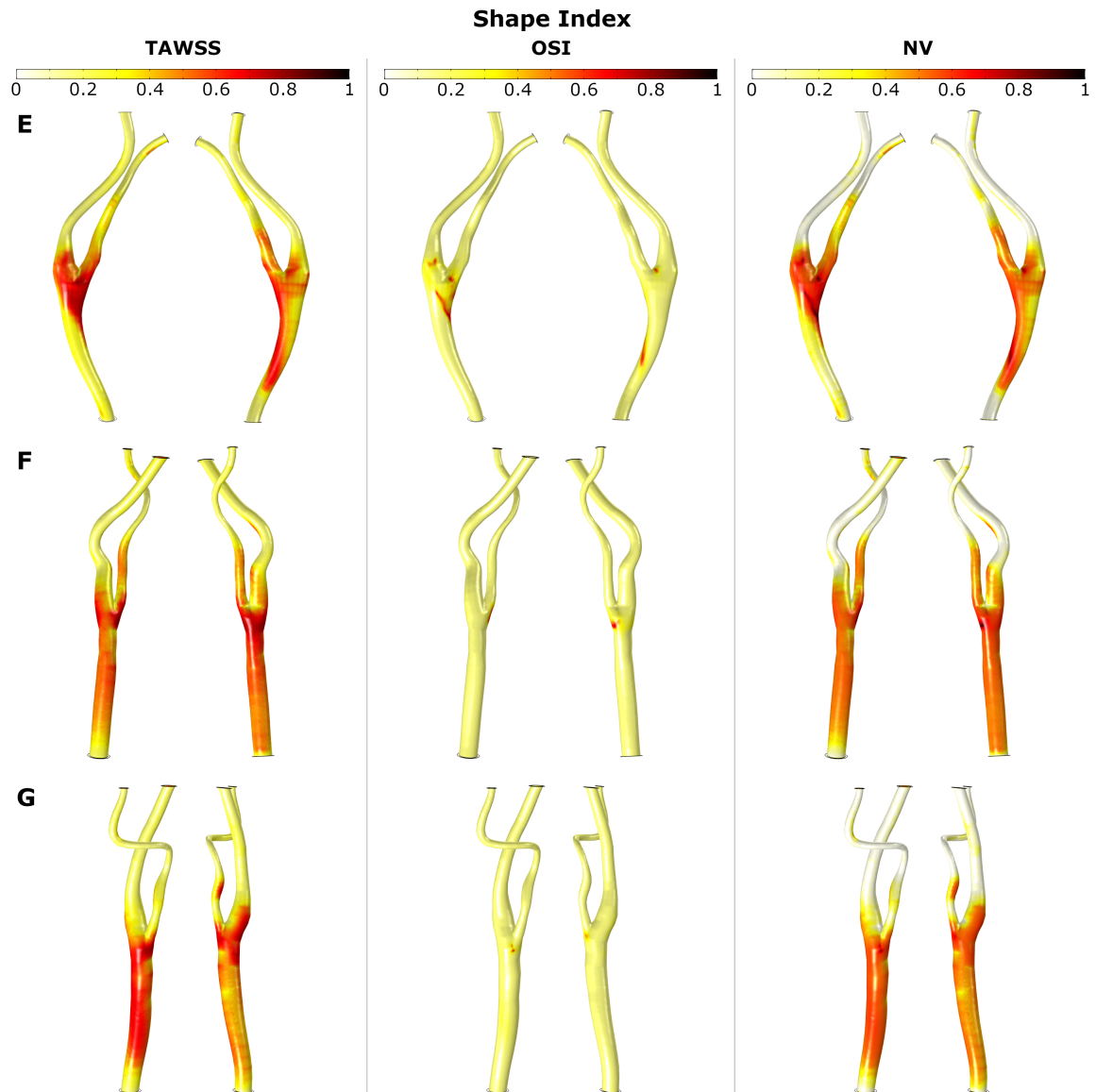


Figure 4.17: Shape index distribution in all the geometries ("A"–"G") with the different mechanical stimuli studied. The first column depicts the use of TAWSS, the second column the OSI and last column the proposed combination of TAWSS and OSI.

Figure 4.18, shows the results of concentrations of LDL, oxidised LDL and monocytes for all the considered haemodynamical stimuli, for the patient "A", after 30 years of inflammatory process. As can be seen, for all the stimuli, there is a high LDL concentration in the areas of high SI (Figure 4.17, row A) and, therefore, these areas also have elevated concentrations of oxidised LDL and monocytes.

As in Chapter 3, there is LDL and oxidised LDL concentration in all the arterial wall thickness due to the effect of LDL convection. On the contrary, there is only monocyte concentration in the areas near the endothelium due to their differentiation into macrophages.

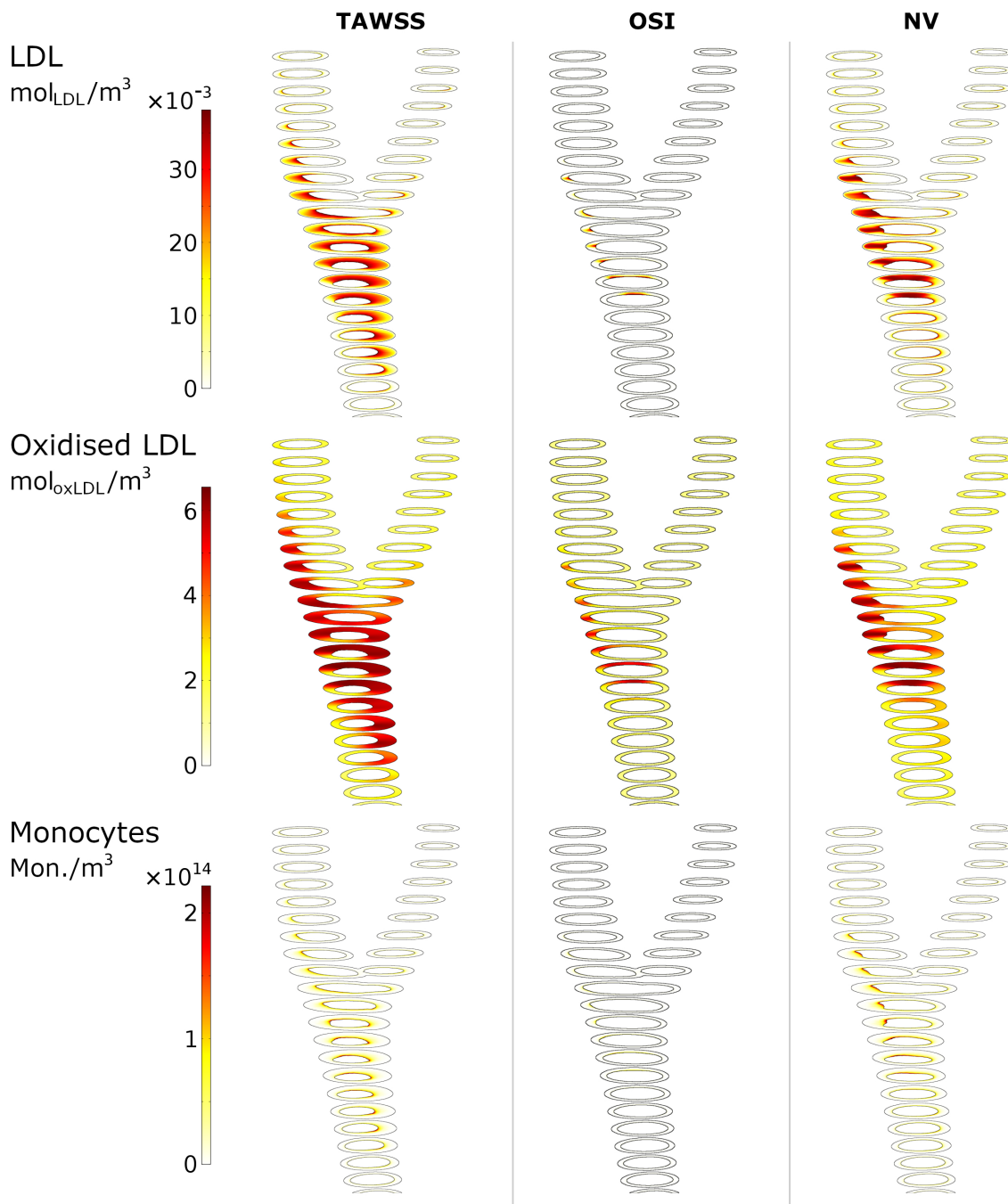


Figure 4.18: LDL, oxidised LDL and monocyte concentration for the patient "A" considering TAWSS, OSI and NV (first, second and third columns, respectively), after 30 years of inflammatory process.

In Figure 4.19, the resultant concentrations of macrophages, cytokines and foam cells are included. As can be seen, their distributions are similar due to all of them depends on monocyte and oxidised LDL (Equations 2.4). In addition, their concentrations are distributed through all the wall thickness due to the diffusion of macrophages.

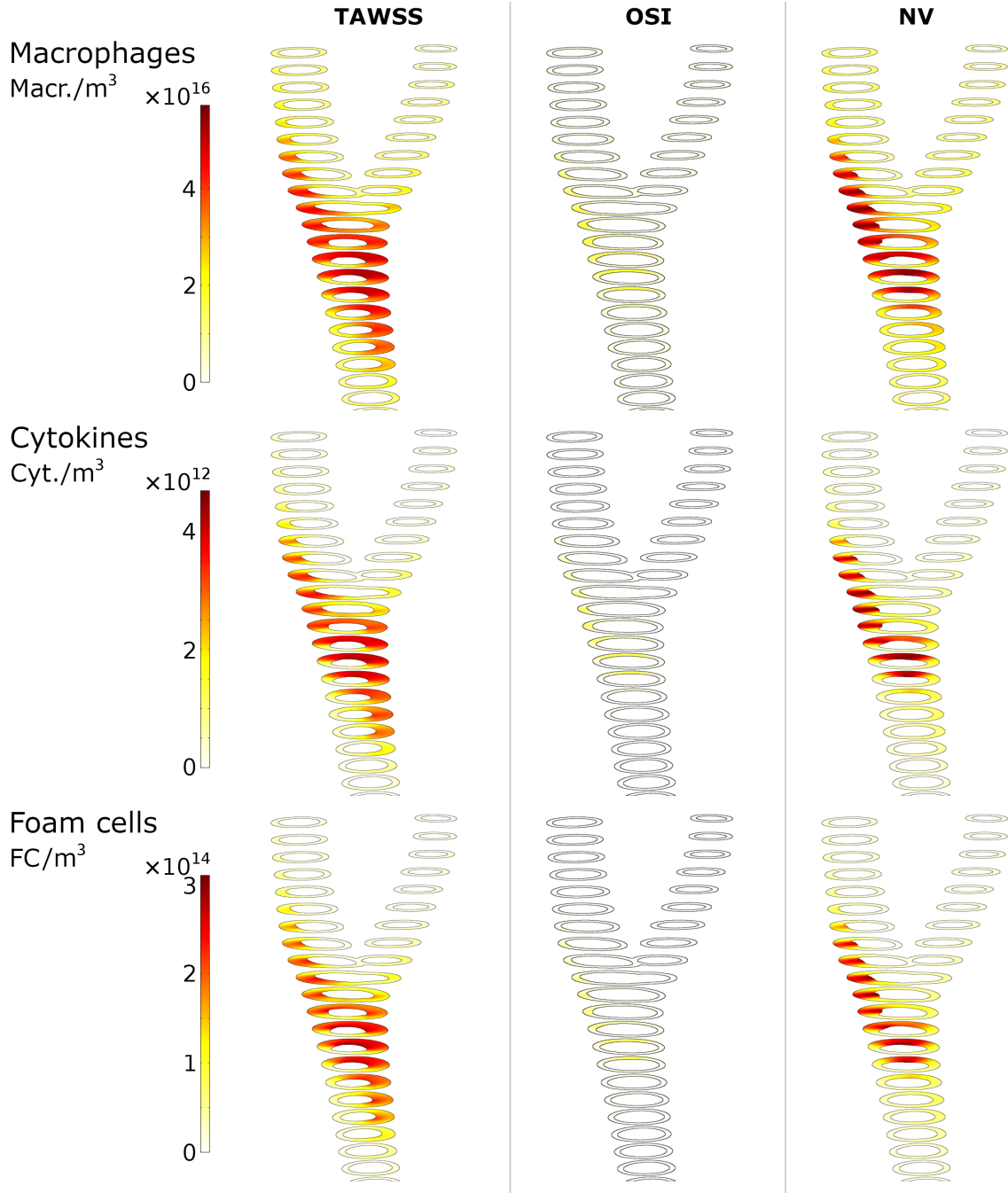


Figure 4.19: Macrophage, cytokine and foam cells concentration for the patient "A" considering TAWSS, OSI and NV (first, second and third columns, respectively), after 30 years of inflammatory process.

Finally, the concentrations of CSMCs, SSMCs, and collagen after 30 years for the patient "A" are included in Figure 4.20. As can be seen, there is a diminution of CSMCs concentration in the areas of high SI for the case of the three mechanical stimuli while, on the contrary, these areas have a high concentration of SSMCs and collagen.

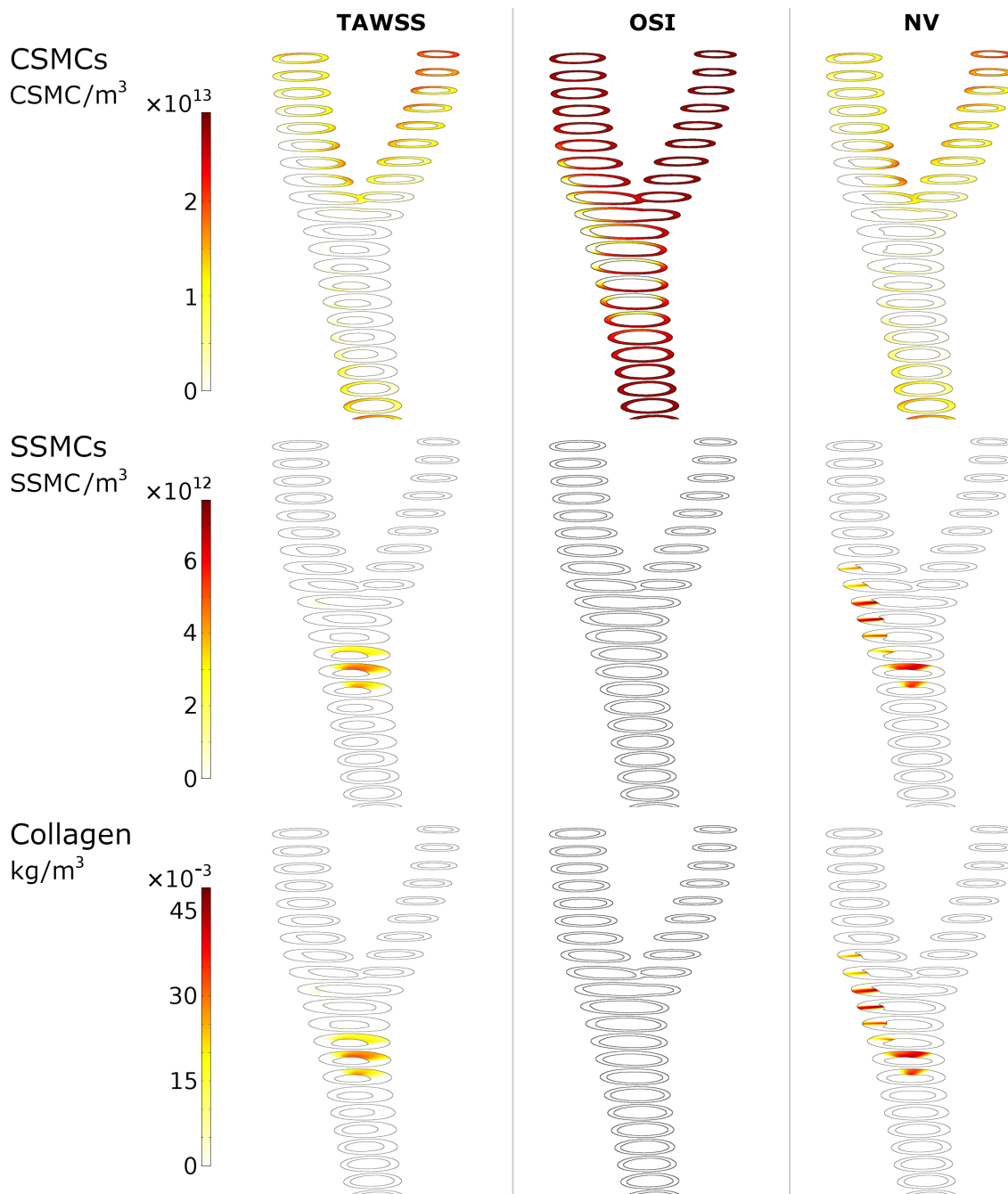


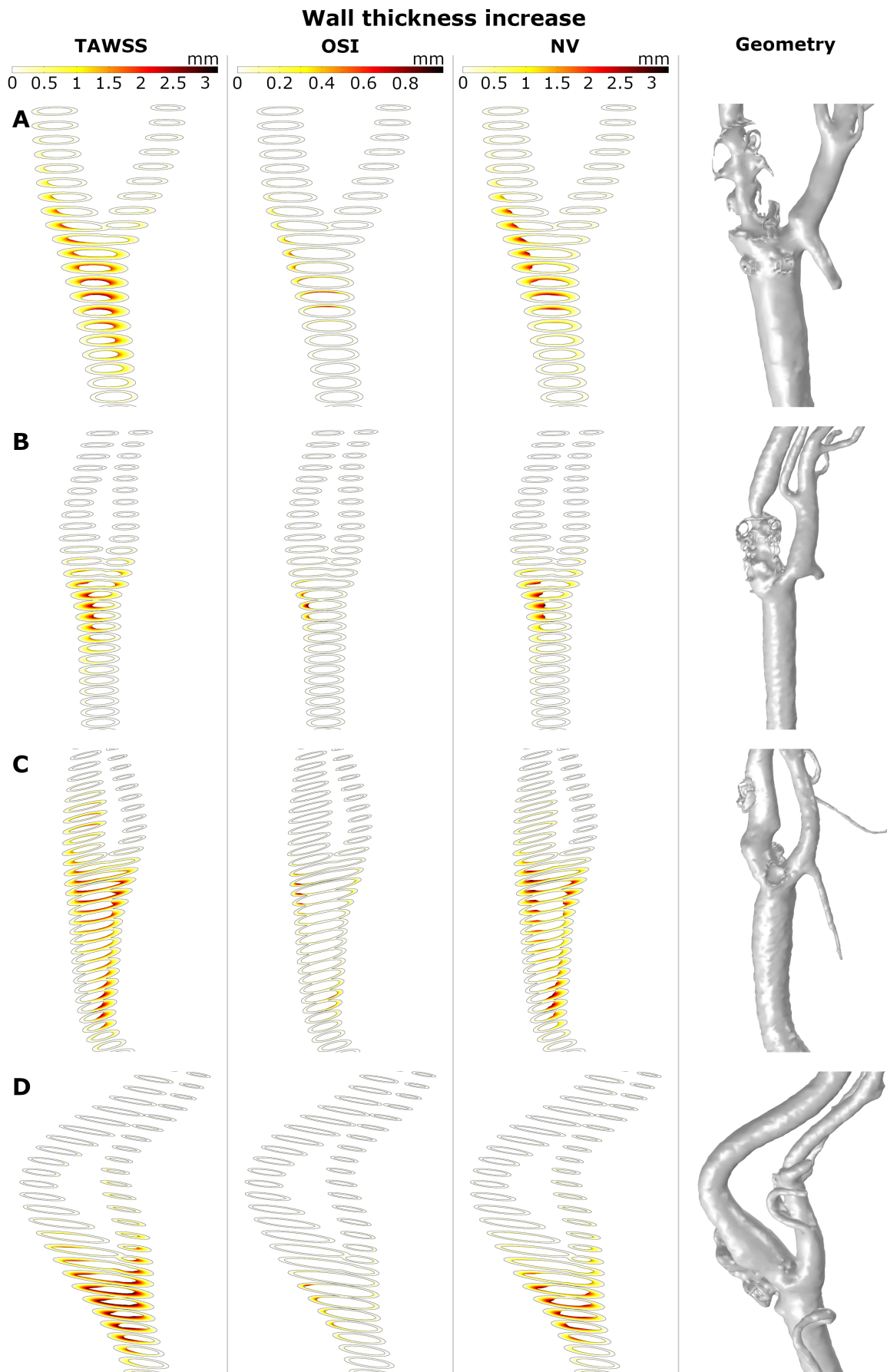
Figure 4.20: CSMC, SSMC and collagen concentration for the patient "A" considering TAWSS, OSI and NV (first, second and third columns, respectively), after 30 years of inflammatory process.

In addition, as can be seen in Figures 4.18, 4.19 and 4.20, the substances concentrations obtained for the case of OSI are smaller than the obtained with TAWSS and NV, and the areas of high concentrations are smaller too. It is due to that the area of high SI obtained for the case of OSI is smaller than the other two. However, the areas of high concentrations

obtained with TAWSS are bigger than in the case of NV, obtaining high substances concentration in the CCA, where the patient has no plaque (Figure 4.5). On the contrary, the CCA has no high concentration in the case of considering NV due to the influence of OSI on it. In addition, with NV there is a high substances concentration in the ICA which is not achieved with TAWSS, in the area in which the real patient has presence of plaque.

Finally, in Figure 4.21, the increase in the wall thickness due to the apparition of plaques after 30 years of the inflammatory process is represented for all the geometries, considering the different haemodynamical stimuli. Generally, the location of plaques is better estimated using the new proposed stimulus. For all the cases, OSI underestimates the area of the plaques and shows the worst prediction of the location. TAWSS predicts non-physiological growth on the CCA due to the very low values of WSS in this area.

Figure 4.21 shows that, for the patients "A", "C" and "D", the location of the plaque matches the clinical evidence using only the new stimulus and the prediction fails for TAWSS and OSI. For patient "B", the new index predicts the location of the plaque of the ICA but fails on the length of the disease. For patient "C", the new stimulus matches the location of the plaques on ICA and ECA; however, it predicts plaque on CCA that it is not presented on the clinical images, likely due to an excessive influence of TAWSS in this area. Plaques on the ICA were not predicted by any of the stimuli for patients "E" and "G".



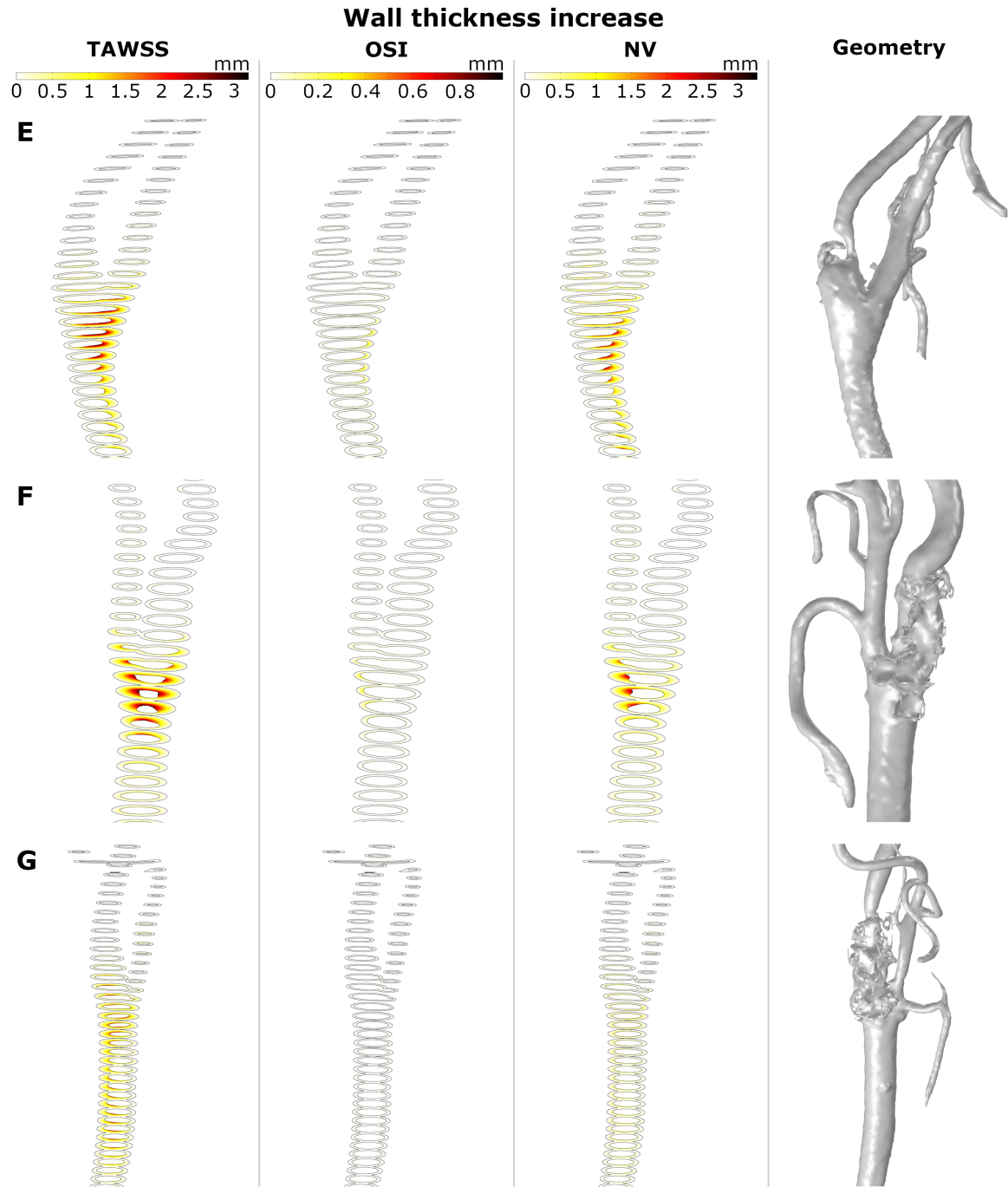


Figure 4.21: Wall thickness increase due to plaques apparition in all the geometries ("A"–"G") with the different mechanical stimuli studied. The first column depicts the use of TAWSS, the second column the OSI, the third column the proposed combination of TAWSS and OSI and the last column the real plaques of the patients.

In Tables 4.12-4.18, the measures of the area of the lumen for all the plaques that are predicted with the computational model and the area of the lumen with the real plaques are shown. In addition, the area of the healthy areas in the zones of the predicted plaques and their stenosis ratio are included.

As can be seen, the model predicts two plaques for the geometries "A", "B", "C" and "G", in their CCA and ICA. For the cases of the geometries "D", "E" and "F", only one plaque is predicted in the area of the CCA.

		Geometry "A"		
		Area of lumen with plaque (mm^2)	Area of healthy lumen (mm^2)	SR (%)
Plaque near the CCA	TAWSS	21.62	53.49	59.58
	OSI	50.01	53.49	6.51
	NV	32.43	53.49	39.37
	Real	46.09	53.49	13.83
Plaque near the ICA	TAWSS	24.73	35.59	30.51
	OSI	34.59	35.59	2.81
	NV	26.59	35.59	25.29
	Real	10.51	35.59	70.47

Table 4.12: Results obtained for the two plaques of the geometry "A".

		Geometry "B"		
		Area of lumen with plaque (mm^2)	Area of healthy lumen (mm^2)	SR (%)
Plaque near the CCA	TAWSS	33.08	62.92	47.43
	OSI	61.04	62.92	2.99
	NV	40.19	62.92	36.13
	Real	51.34	62.92	18.40
Plaque near the ICA	TAWSS	27.53	38.32	28.16
	OSI	37.58	38.32	1.93
	NV	30.57	38.32	20.22
	Real	23.16	38.32	39.56

Table 4.13: Results obtained for the two plaques of the geometry "B".

		Geometry "C"		
		Area of lumen with plaque (mm^2)	Area of healthy lumen (mm^2)	SR (%)
Plaque near the CCA	TAWSS	63.98	120.96	47.11
	OSI	108.48	120.96	10.32
	NV	57.27	120.96	52.65
	Real	46.99	120.96	61.15
Plaque near the ICA	TAWSS	33.99	53.53	36.50
	OSI	52.82	53.53	1.33
	NV	41.37	53.53	22.72
	Real	35.91	53.53	32.92

Table 4.14: Results obtained for the two plaques of the geometry "C".

		Geometry "D"		
		Area of lumen with plaque (mm^2)	Area of healthy lumen (mm^2)	SR (%)
Plaque near the CCA	TAWSS	40.70	110.09	63.03
	OSI	100.61	110.09	8.61
	NV	58.29	110.09	47.05
	Real	52.41	110.09	52.39

Table 4.15: Results obtained for the plaque of the geometry "D".

		Geometry "E"		
		Area of lumen with plaque (mm^2)	Area of healthy lumen (mm^2)	SR (%)
Plaque near the CCA	TAWSS	23.56	30.85	23.63
	OSI	30.29	30.85	1.82
	NV	25.96	30.85	15.85
	Real	24.80	30.85	19.61

Table 4.16: Results obtained for the plaque of the geometry "E".

		Geometry "F"		
		Area of lumen with plaque (mm^2)	Area of healthy lumen (mm^2)	SR (%)
Plaque near the CCA	TAWSS	25.52	70.03	63.56
	OSI	68.32	70.03	2.44
	NV	44.62	70.03	36.28
	Real	46.56	70.03	33.51

Table 4.17: Results obtained for the plaque of the geometry "F".

		Geometry "G"		
		Area of lumen with plaque (mm^2)	Area of healthy lumen (mm^2)	SR (%)
Plaque near the CCA	TAWSS	37.45	64.74	42.15
	OSI	64.72	64.74	0.03
	NV	50.85	64.74	21.45
	Real	58.55	64.74	9.56
Plaque near the ICA	TAWSS	40.81	55.49	26.45
	OSI	54.19	55.49	2.34
	NV	48.31	55.49	12.94
	Real	30.06	55.49	45.83

Table 4.18: Results obtained for the two plaques of the geometry "G".

Finally, Table 4.19 shows the computational stenosis ratio obtained for all the plaques of the geometries with the different mechanical stimuli considered and compared them with the real ones taken from the clinical images, calculating the stenosis difference of the results in each case.

		Real	TAWSS		OSI		NV	
Geometry		SR (%)	SR (%)	Stenosis difference (-)	SR (%)	Stenosis difference (-)	SR (%)	Stenosis difference (-)
"A"	CCA	13.83	59.58	45.75	6.51	-7.32	39.37	25.54
	ICA	70.47	30.51	-39.96	2.81	-67.66	25.29	-45.18
"B"	CCA	18.40	47.43	29.03	2.99	-15.41	36.13	17.73
	ICA	39.56	28.16	-11.40	1.93	-37.63	20.22	-19.34
"C"	CCA	61.15	47.11	-14.04	10.32	-50.83	52.65	-8.50
	ICA	32.92	36.50	3.58	1.33	-31.59	22.72	-10.20
"D"	CCA	52.39	63.03	10.64	8.61	-43.78	47.05	-15.98
"E"	CCA	19.61	23.63	4.02	1.82	-17.79	15.85	-3.76
"F"	CCA	33.51	63.56	30.05	2.44	-31.07	36.28	-27.28
"G"	CCA	9.56	42.15	32.59	0.03	-9.53	21.45	14.89
	ICA	45.83	26.45	-19.38	2.34	-43.49	12.94	-32.89

Table 4.19: Stenosis ratio of all the real plaques, the plaques predicted with the computational model for the different mechanical stimuli and stenosis difference between them.

It can be observed that the stenosis ratio after 30 years is better predicted using the new variable for the seven studied arteries. In general, for all the geometries, the new variable has values of maximal and minimal stenosis differences with respect to the real arteries of 32.89 and 3.76, respectively. TAWSS generally overestimates the stenosis ratio with a maximal and minimal stenosis differences of 45.7 and 3.58 with respect to the real plaques, respectively. In contrast, OSI underpredicts the stenosis ratio in all the cases, with maximal and minimal stenosis differences of 67.66 % and 7.35 %, respectively.

As can be seen, although there are some plaques that are better predicted with TAWSS or OSI than with the NV, there is no clear evidence of any particularity of the geometries by which it can be concluded that certain plaques will be better predicted in the case of considering TAWSS or OSI. Therefore, it is not possible to predict which one of them would be better at predicting plaques based on a carotid characteristics. Additionally, in cases where a geometry develops two plaques, only one of them is correctly predicted using, for example, TAWSS, while the other is better predicted using OSI. Therefore, the combination of the effects of both stimuli in the NV leads to the prediction of all plaques. It can be noticed by calculating the mean values of the stenosis differences of all the computed

plaques with respect the real ones for the cases of TAWSS, OSI and NV, which corresponds to 21.86, 32.32 and 16.65, respectively.

The growth model fails to predict the location and size when haemodynamics cannot predict high SI on the location of the plaques. Although most of the plaques predicted with the model correspond to the ones clinically observed, there are a few plaques that cannot be explained with this model. For patients "E" and "G", the stenosis appears in a zone where no haemodynamical disturbance is observed; therefore in these patients, haemodynamics are not the main trigger of the disease and could be due to other systemic or genetic conditions of the patient in this location, e.g., external lesion or pathological weakness of the intimal layer.

As seen, the location of plaques is better predicted than the stenosis ratio, which has been predicted with stenosis differences with respect the real plaques between 3.76 and 32.89 for the case of NV, depending on the analysed geometry. This could be because the location of plaques only depends on haemodynamics, while the stenosis ratio also depends on specific parameters of the patients that are unknown, such as real concentration of LDL in the blood and the time that they have had high LDL levels. Moreover, it is also dependent on specific parameters of the inflammatory model. It could obviously rely on other factors not taken into account in the model that could affect plaque growth, e.g., age, gender, blood pressure level or genetic conditions. However, in general, the model using the new haemodynamic stimulus should predict the location and the growth of the plaques.

4.8.3 Plaque growth updating the geometry

Even though the model correctly predicts the plaques appearing in the specific bifurcation and the ECA, some plaques presented at the ICA are not very well predicted by any mechanical stimulus studied in this work. We hypothesized that it could be due to the uncoupled form between haemodynamics and plaque growth, where fluid is computed at the beginning of the process and it is not updated with the plaque growth. First, plaques appear at the CCA branch, and then they cause a change of the blood flow downstream and the variable stimuli -TAWSS, OSI and NV- could be affected at an area behind them and a new plaque is likely to appear in the ICA. To validate this hypothesis, the growth of geometry "B" has been computed until 15 years, and then the geometry has been actualised and computed again. Figure 4.22 shows the different results obtained that represent the wall thickness increases for a total of 30 years and for only half of the time (15 years), the updated geometry of the bifurcation including the stenosis for 15 years and the wall thickness increase for 30 years with the updated geometry. The clinical image is represented as well. It can be observed that the plaque in the ICA for the case of updating the geometry better matches the real plaque. Due to the high computational cost of the 3D version of the mechanobiological model, full FSI for 3D real carotid images is not available.

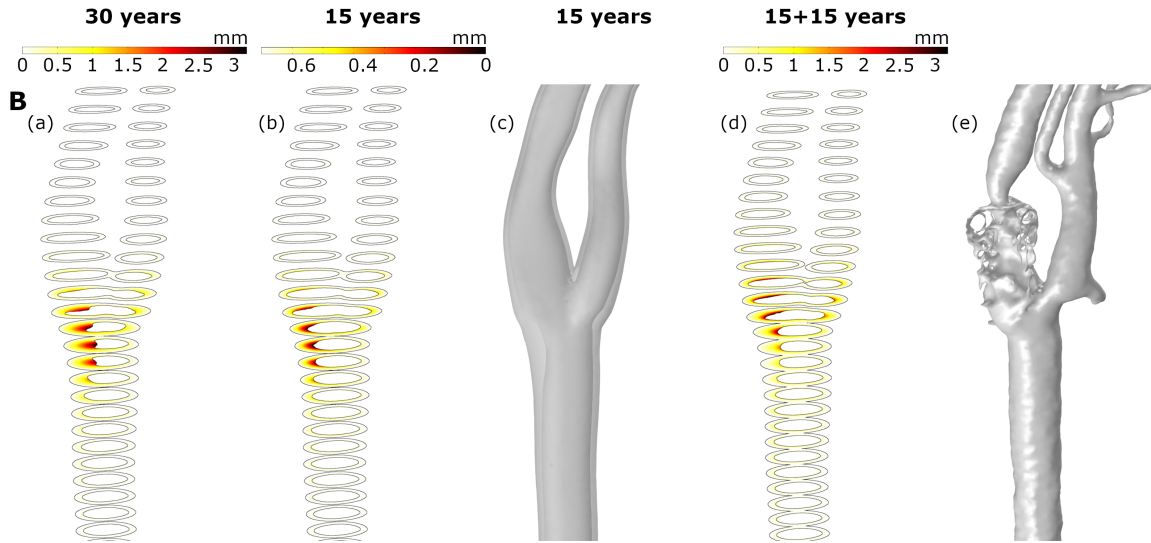


Figure 4.22: Results for wall thickness increase due to the apparition of plaques in patient B with 30 and 15 years of continuous process (a and b, respectively), the updated geometry after 15 years of the growth process (c), the wall thickness increase after 30 years in the updated geometry (d) and the real plaque of the patient (e).

4.9 Conclusions

This work extends the mechanobiological model developed in Chapter 3 from an axisymmetric to a 3D model and is essential as a prior step to its application to patient-specific images. It is worth highlighting that atheroma plaques are usually eccentric, and this feature cannot be captured with 2D axisymmetric models. However, the computational cost is higher, and some simplifications are necessary. Another improvement of this model is the computation of blood flow in the transient mode.

This transient mode for the blood flow allows us to analyse and compare some of the most common mechanical stimuli that are normally used for predicting atheroma plaque locations, TAWSS and OSI. A new mechanical stimulus as a combination of TAWSS and OSI is also proposed to better predict the location of plaques. The model has been used to check which mechanical stimulus is more appropriate to predict the location of atheroma plaques on carotid geometries.

The model has been computed in a healthy geometry without significant plaque in which there is no relevant haemodynamical stimuli to develop atheroma plaques to verify that the model is stable and plaques only grow when there is an atheroprone stimulus. Additionally, atheroma plaque growth has been computed in different geometries obtained from pathological patient-specific images in order to obtain the equivalent healthy geometries to validate the results of the model.

As can be seen in Figure 4.21, plaques predicted with different haemodynamical stimuli growth in different locations and present different stenosis ratio; thus, the choice of the haemodynamical stimulus to predict the location of plaque results crucial. TAWSS predicts excessively large plaques in the CCA branch of the carotids, far from the bifurcation, that do not match with the real ones. On the other hand, TAWSS adequately predicts the size of plaques appearing in its own bifurcation location compared with the real geometries. In contrast, OSI locates plaques with a better precision than TAWSS, but the growth ratio is very low in comparison to the actual ones. Finally, NV proposed in this study combines the results achieved with TAWSS and OSI, predicting in a more adequate way the location of atheroma plaques as in OSI - limiting the growth in areas of the CCA far from the bifurcation- and its growth is similar to the real one observed in the clinical images, similar to TAWSS.

However, there are some plaques in the ICA of the geometries that cannot be predicted with any of the haemodynamical stimuli. This can be explained with the results obtained for the case of geometry "B" updating the geometry after the first 15 years of inflammatory process, where the predicted plaque in the ICA is more similar to the real one of the patient than in the uncoupled case. Thus, FSI would have influence in the geometries of the plaques obtained, but it is not available due to the high computational cost that it entails.

The findings of this study should be interpreted within the context of its limitations. For example, the model would be improved by implementing a fluid-structure interaction to better approximate the real pathology. The haemodynamics are considered the main trigger of atherosclerosis initiation. Thus, the cyclic stretch effects of vessel compliance or curvature were disregarded. Another limitation of the model is that the real geometries without plaques are unknown. It is a limitation because the real healthy geometries can have some differences with the reconstructed ones and it can have an influence in the obtained results. There is no real plaque growths monitoring to see plaque geometry evolution, and, in the same way, there is no real data from each patient, e.g., blood pressure and flow, LDL levels and number of years with high LDL levels and other pathologies that they may have, so patient-specific parameters are not used to solve the problem. A total of 30 years has been considered for the analysis, based in the literature (Insull, 2009). In addition, there are no experimental data about OSI and TAWSS and OSI combination influences on SI. In addition, a simplified model has been used, in which only the more important substances for plaque growth are considered and that do not consider different kinds of cytokines (IL-4, IL-10, IL-13 or TFG beta) or T-cells or free radicals that oxidize LDL. Adjusted parameters come from different species and vessels in which the studies were developed, and they were not all human carotids. Other processes that may have an important role in atherosclerosis, such as mechanotaxis, are not considered. This model assumes that the substances can move from the lumen to the arterial wall, but not in the reverse direction, and the transport properties are set as constant, but in fact, they are very likely to change during plaque formation.

In conclusion, despite the limitations, the model can predict the location and the growth of plaques in the main cases. The results show that prediction of plaques is better, in most cases, using the new mechanical stimulus proposed in this study than using TAWSS or OSI, with a maximal stenosis difference between the computed plaques and the real ones of 32.89. Based on the results, it can be concluded that the functional regulation of the endothelium by local haemodynamic shear stress provides a model for understanding the focal propensity of atherosclerosis in the setting of systemic factors and this may help to guide future therapeutic strategies.

In the future, the model could be used to predict if a patient is susceptible to develop atheroma plaques and if so, to determine the places where plaques are likely to appear. In this way, it would be possible to take the necessary treatment to prevent atheroma plaque development and all the consequences derived from atherosclerosis.

Chapter 5

Fluid-Structure Interaction analysis

Part of the contents of this Chapter will be included in:

- Hernández-López P., Cilla M., Martínez M., Peña E. and Malvè M.
Fluid-structure interaction influence on a mechanobiological model of
atheroma plaques growth.

Chapter 5

5.1 General Overview

In the previous chapters of this Thesis, the haemodynamics of blood flow, the inflammatory process of the arterial wall, and the growth of atheroma plaques have been computed in an uncoupled way: The growth of the plaque has been computed at the end of the inflammatory process, only taking into consideration the final substance concentration in the arterial wall. However, in a real patient, these process are coupled: the plaque growth happens at the same time than the inflammatory process, and causes changes in blood haemodynamics that can affect the shape index of the endothelial cells and, therefore, the endothelial permeability and the evolution of the plaque.

The effects of Fluid-Structure Interaction (FSI) have been analysed at the end of Chapter 4, being one of its main conclusions: FSI can have an important influence on the atheroma plaques predicted with the model, and can lead to changes in the shape of the atheroma plaques that are produced. However, these conclusions have been depicted with an approximate way to compute FSI, in which the computational model is still calculated in an uncoupled way, but actualising the geometry and the blood flow in the middle of the inflammatory process (*15 years*).

Therefore, an improved FSI model is developed and computed in this chapter, with the aim of validate the hypothesis of Chapter 4, and analyse how the FSI can affect the growth of plaques, by comparing the plaque obtained with the uncoupled and FSI models. A total time of 10 years have been computed for the inflammatory process and the growth of the plaques of all the models presented in this chapter, due to the computational cost of the model and that it has been considered enough time to analyse the variations in the results provided by the uncoupled and FSI models.

In addition, due to the computational cost that the real geometries of Chapter 4 require, the FSI analysis has been done in the reference 2D axisymmetric model of vulnerable atheroma plaques (Chapter 3). Note that the reference model included in Section 3.3 has the limitation of calculate blood flow as stationary, assuming WSS as the main mechanical stimulus to initiate atheroma plaques growth. However, since the aim of this chapter is to compare the results obtained with the uncoupled and the FSI models, the reference model in this case is computed considering transient blood flow as well.

The considered geometry, the boundary conditions that are applied in this chapter and the considered haemodynamical stimulus are included in Sections 5.2, 5.3 and 5.4, respectively. The uncoupled base model with transient blood flow is explained in Section 5.5, including the numerical methods that have been used, the sensitivity analysis of the mesh and the obtained results.

Due to that there is no clear evidence of the endothelial behaviour attending to its reparation when the haemodynamical stimuli change, two different models of FSI have been developed and included in Section 5.6. The first one of the models considers endothelial repair while, the second one, considers that the endothelium remains permanently damaged and thus, there is no endothelial repair. The numerical methods used for both FSI models and the obtained results for each one are included in this section as well.

Finally, a comparison of the results obtained with the uncoupled and FSI models with and without endothelial repair is presented in Section 5.7, and the obtained conclusions are explained in Section 5.8.

5.2 Geometry

Due to the high computational cost of the real geometries models and of the FSI technique caused by the moving mesh, the geometry used for all the developed cases in this chapter is the same than in the reference model, and can be seen in Figure 3.1. It corresponds to the two-dimensional axisymmetric model of an internal carotid artery with an obstacle plaque which disturbs blood flow. This obstacle occasions an increase in the endothelium permeability of the area downstream it, causing the emergence of a new plaque there. As commented in Chapter 3, it is a phenomenon that has been observed in real patients, called double stenosis (De Bruyne et al., 2000; Pijls et al., 2000).

5.3 Boundary conditions of transient blood flow

As commented, the main objective of this chapter is to compare the results obtained with the uncoupled and FSI models. Thus, due to that in the FSI model the blood has to be modelled as transient, it needs to be modelled in transient mode for the uncoupled model as well.

Therefore, the boundary conditions applied for blood flow in this chapter are those correspondent to the data of the ICA of Malvè et al. (2014). The transient blood mass flow and its pressure during a cardiac cycle are applied in the inlet and outlet of the geometry, respectively, and are shown in Figure 5.1.

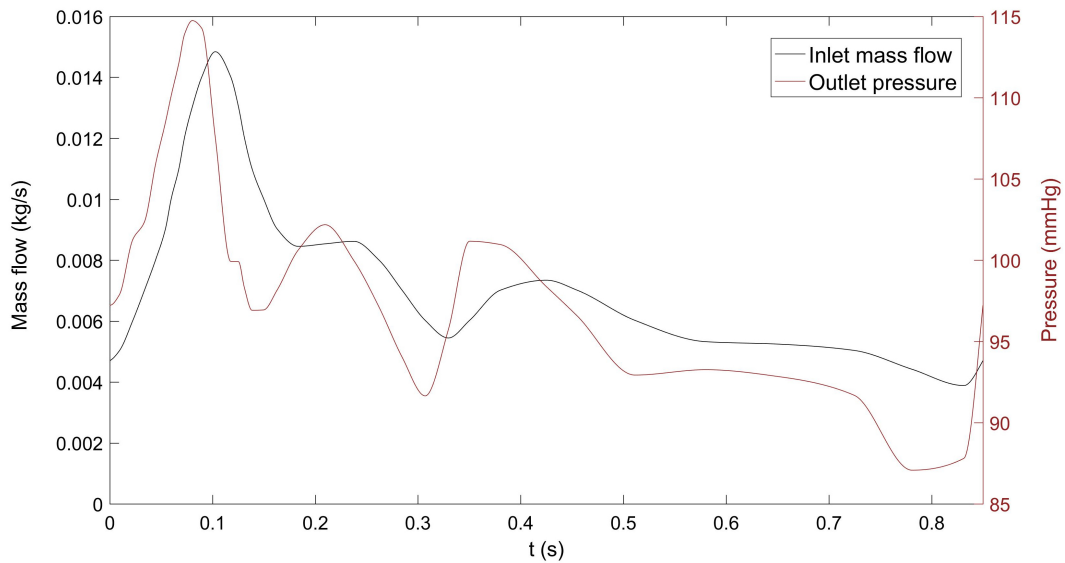


Figure 5.1: Blood mass flow at the inlet and pressure imposed at the inlet and outlet of the geometry, respectively (Malvè et al., 2014).

Following the results of Chapter 4 regarding the number of cardiac cycles that are necessary to ensure that the blood flow is fully developed, a total of three cardiac cycles are computed. Thus, the values obtained for the third cardiac cycle are considered to determine the haemodynamical stimulus in each case.

5.4 Haemodynamical stimulus

The haemodynamical stimulus considered in the FSI computations as trigger of atheroma plaques growth is NV. This stimuli was developed in Chapter 4 for the patient-specific geometries of carotid arteries, which depends on TAWSS and OSI during a cardiac cycle. NV has been chosen due to that it has been concluded that it predicts the growth of plaques better than only use TAWSS or OSI. NV and the equations for the SI of the endothelial cells and the monocyte flow across the endothelium applied with it are explained in Chapter 4.

5.5 Reference model with transient blood flow

The uncoupled reference model of vulnerable plaques with the geometry in 2D-axisymmetric and considering transient blood flow, as well and its results are presented in this section.

5.5.1 Numerical methods

Blood flow in this case changes according to the cardiac cycle and, therefore, is dependent on time. Thus, it is necessary to calculate blood flow in a transient step, previous to the stationary step of plasma flow, as can be seen in Figure 5.2, in which the workflow of the process is included.

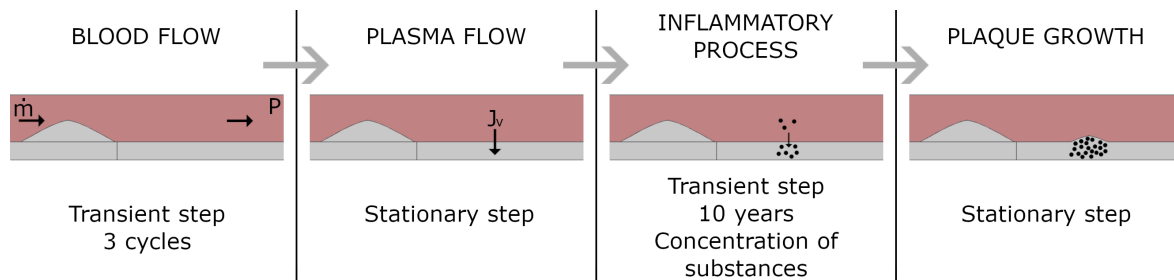


Figure 5.2: Workflow of the computational process for the 2D axisymmetric model with transient blood flow.

The software COMSOL Multiphysics (COMSOL AB, Burlington, MA, USA) is used to computationally solve the model. Due to that the geometry and the mathematical model are the same than in Chapter 3, the numerical methods used for this case are the same as well. In addition, as blood flow is modelled in a transient step in this case, the BDF with Newton's method has been used to solve it, as well as the inflammatory process of the arterial wall.

5.5.2 Sensitivity analysis of the mesh

As commented before, the boundary conditions of the blood flow in Chapter 3 and in this chapter are different due to, in Chapter 3, blood flow is modelled in a stationary step while, in the FSI case, it is modelled as transient. Thus, the sensitivity analysis of the mesh of the arterial lumen of Chapter 3 could not be valid here.

To analyse the convergence of the mesh, the lengths of endothelial SI greater than 0.3085 considering NV as the haemodynamical stimulus (combination of TAWSS and OSI) are studied. In addition, the maximum blood velocity in the lumen and in the area of the obstacle plaque are analysed too.

As in the case of the stationary blood flow (Chapter 3), the number of nodes of the mesh and its quantity of boundary layers need to be analysed. The number of nodes has been analysed, using 5 boundary layers in the endothelium. The analysed meshes, including the number of nodes and the computational time required to solve the model are included in Table 5.1.

Mesh	N. nodes of the mesh	Computational time
Extra coarse	3564	1 min35 s
Coarse	9707	3 min6 s
Normal	19573	6 min38 s
Fine	37925	10 min20 s
Finer with max. elem. size 0.052 mm	75275	15 min17 s

Table 5.1: Number of nodes and computational time of the lumen meshes analysed for the case of transient blood flow.

As can be seen in Tables 5.1, the computational time in of the transient model is higher than the stationary blood flow one (Table 3.3) , and has more variability between different meshes. The results obtained for the analysed meshes are shown in Table 5.2. Blood velocity varies according to the cardiac cycle so, the results of maximum blood velocity included in Table 5.2 are the correspondent to the maximum blood velocity in the hole lumen for the time of higher inlet blood flow velocity imposed during the cardiac cycle (Figure 5.1):

Mesh	NV: Length of SI > 0.3085 (mm)	Max. blood velocity (m/s)	
		Lumen	Obstacle plaque area
Extra coarse	30.1003	2.5064	2.4453
Coarse	30.8413	2.5061	2.4589
Normal	30.1087	2.5184	2.4569
Fine	30.0765	2.5219	2.4732
Finer with max. element size 0.052mm	30.4550	2.5128	2.4659

Table 5.2: Results obtained, attending to the considered mesh, for the length of SI higher than 0.3085 for NV as haemodynamical stimulus, and maximum velocities of transient blood flow in the hole lumen and in the area of the obstacle plaque.

The variations of the results obtained with the different analysed meshes are shown in Table 5.3:

Mesh comparison	NV: Length of SI > 0.3085 variation (%)	Max. blood velocity variation (%)	
		Lumen	Obstacle plaque area
Coarse vs Extra coarse	2.4618	0.0120	0.5502
Normal vs Coarse	2.3754	0.4908	0.0813
Fine vs Normal	0.1069	0.1390	0.6634
Finer vs Fine	1.2585	0.3608	0.2952

Table 5.3: Variation (%), attending to the considered mesh, of the length of SI higher than 0.3085 for the case of consider NV as haemodynamical stimulus, and of the maximum velocities of transient blood flow in the hole lumen and in the area of the obstacle plaque.

All the considered meshes in Table 5.3 are valid, due to all their results present variations lower than 5 %. Therefore, to be consistent with the mesh selected for the case of stationary blood flow, the fine mesh has been chosen as well to discretise the lumen for the case of transient blood flow.

In addition, the number of boundary layers of the selected fine mesh, near the endothelium, have been analysed. The results obtained are included in Table 5.4:

Boundary layers	NV: Length of SI > 0.3085 (mm)	Max. blood velocity (m/s)	
		Lumen	Obstacle plaque area
0	34.0266	2.5237	2.4751
1	34.2729	2.5244	2.4758
2	33.0650	2.5216	2.4729
3	30.8716	2.5219	2.4732
4	30.6311	2.5219	2.4732
5	30.0765	2.5239	2.4753
6	30.5011	2.5230	2.4746
7	30.2219	2.5216	2.4729

Table 5.4: Results obtained, attending to the number of boundary layers, for the length of SI higher than 0.3085 for NV as haemodynamical stimulus, and maximum velocities of transient blood flow in the hole lumen and in the area of the obstacle plaque.

Finally, the results variation between the different boundary layers number are shown in Table 5.5, taking as the reference mesh the mesh with 7 boundary layers due to its results should be more precise.

Mesh comparison	NV: Length of SI > 0.3085 variation (%)	Max. blood velocity variation (%)	
		Lumen	Obstacle plaque area
0 vs 7	12.5892	0.0833	0.0890
1 vs 7	13.4042	0.1110	0.1173
2 vs 7	9.4074	0	0
3 vs 7	2.1498	0.0119	0.0121
4 vs 7	1.3540	0.0119	0.0121
5 vs 7	0.4811	0.0912	0.0971
6 vs 7	0.9238	0.0555	0.0687

Table 5.5: Variation (%), attending to the number of boundary layers, of the length of SI higher than 0.3085 for the case of consider NV as haemodynamical stimulus, and of the maximum velocities of transient blood flow in the hole lumen and in the area of the obstacle plaque.

As can be seen in Table 5.5, the meshes with 0, 1 and 2 boundary layers provide results with a variation higher than 5 %. Therefore, these meshes can be discarded. The variations obtained between the rest of the meshes are acceptable. Thus, due to that the mesh of 3 boundary layers would suppose a lower computational cost and, in addition, this mesh has been selected for the case of considering stationary blood flow, this mesh has been chosen again for the case of transient blood flow.

In reference to the arterial wall mesh, the conditions of the inflammatory process of the arterial wall and the conditions of the growth of the plaque are the same in this case than in the reference vulnerable plaques model of Chapter 3. Therefore, the mesh for the arterial wall in the cases of stationary and transient blood flow will be the same, and it is no necessary to perform a new sensitivity of the arterial wall mesh.

Finally, in Table 5.6, the total number of nodes and boundary layers of the meshes for the lumen and the arterial wall in the case of considering transient blood flow are included and, as can be seen, they are the same than for the case of stationary blood flow (Table 3.9).

Mesh	Number of nodes	Number of boundary layers
Lumen	35435	3
Arterial wall	36001	0
Total mesh	70463	-

Table 5.6: Number of nodes and boundary layers of the selected meshes for the lumen and the arterial wall in the case of transient blood flow.

5.5.3 Results

Due to the aim of this chapter is to analyse the differences of the developed plaques with the different computed models, only the arterial wall thickness increase is analysed. Figure 5.3 shows the increase of the arterial wall thickness in the uncoupled model, considering NV as the main haemodynamical stimulus, after a total of 10 *years* of inflammatory process.

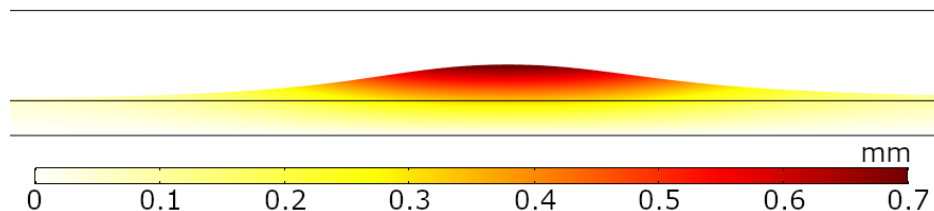


Figure 5.3: Arterial wall thickness increase for the uncoupled model with NV, for a time of simulation of 10 years.

As can be seen, the maximum wall thickness increase is equal to 0.70 *mm*, which corresponds to a stenosis ratio of 62.58 %.

5.6 Fluid-Structure Interaction

As commented, due to changes in blood flow caused by the growth of a plaque, the SI of the endothelial cells changes over time. Some areas considered as atheroprone at the beginning of the process (due to have an elevated SI), can turn into areas considered as atheroprotective later (with a low SI value). Thus, in these areas, the permeability of the endothelium is lower than at the beginning of the process and, therefore, it can be considered as an endothelial repair produced by changes on the haemodynamics.

There are some studies that mention endothelial repair (Fok, 2012). However, there is no clear evidence about endothelial repair or the way in which it occurs. Due to that there are no studies with numerical results about endothelial repair due to changes in haemodynamics, two different FSI models have been performed, considering the two extreme cases. The first one considers that, once that the endothelium is no longer under the levels of the haemodynamic stimulus that cause plaque growth, the endothelial permeability of that area decreases and, therefore, the endothelium is repaired. In contrast, the second model considers that, even if the haemodynamic stimulus that leads to plaque growth ceases, the endothelial permeability remains high due to that the endothelium has been permanently damaged, and therefore, it does not consider endothelial repair.

5.6.1 Numerical methods

The software COMSOL Multiphysics (COMSOL AB, Burlington, MA, USA) has been used to solve both models of FSI developed in this chapter.

There is a huge time scale difference between the durations of a cardiac cycle and of the inflammatory process that leads to the growth of an atheroma plaque. The cardiac cycle lasts some ms (Malvè et al., 2014), while the inflammatory process takes place over several years (Insull, 2009). To solve the problem that this time scale difference produces and the computational cost that it would imply, a semi-coupled model has been developed.

First, the blood flow of the healthy geometry is calculated and then, using the results of the third cardiac cycle, the inflammatory process is calculated with the NV, coupled to the plaque growth using a moving mesh that allows the geometry to change as the plaque grows. Subsequently, an updated of the geometry after that time of plaque growth is done and blood flow is recalculated, so that the TAWSS and OSI obtained are different from the initial ones due to the adaptation of blood flow to the new geometry. Therefore, the NV results of the third cardiac cycle are applied to the deformed geometry, in which the previously calculated concentration values are imposed as initial concentrations for each substance. This process is repeated several times, until reach the desired simulation time of 10 years.

Due to the semi-coupled process, the intervals in which the geometry is updated may lead to different results, so that the shorter the update interval, the more similar the results will be to those that would be obtained by a full FSI analysis, and thus the more similar the process will be to what happened in real patients. However, for the shorter update time, the necessary number of geometry updates is higher and, therefore, the calculation number and computational time will be greater. Thus, in order to analyse how the geometry update frequency affects the results, calculations have been performed with update periods of 10, 5, 2.5 and 1.25 years for both models (considering and not considering endothelial repair). The workflow of the semi-coupled model is included in Figure 5.4.

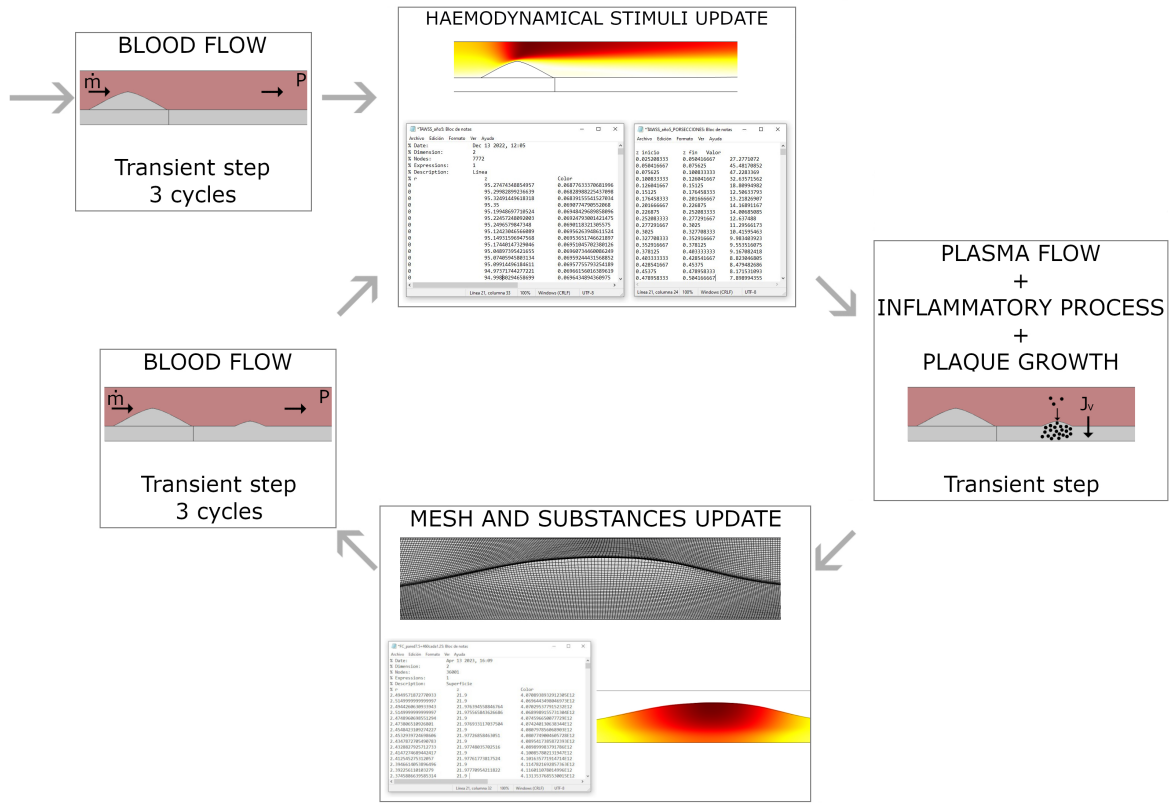


Figure 5.4: Workflow of the computational process for the FSI models.

To update the geometry in each temporal interval, the resultant mesh from the calculation of the previous interval is imported.

In addition, the concentrations obtained at the end of the interval before the geometry update remain in the arterial wall. Because of this, the concentration results obtained for all substances before the geometry update are exported in text files, in which the concentration of each substance at each node of the arterial wall mesh is available, depending on its radial and longitudinal coordinates. Subsequently, these concentrations are imported as the initial concentrations of each substance in the arterial wall at the beginning of the new time interval, after the geometry update.

To compute the FSI model, it is necessary to define the mesh as a moving mesh that changes with the growth of the plaque. The smooth method selected to compute the deformation of the moving mesh is Laplace smoothing, by which the next equations are solved in all the nodes of the mesh:

$$\frac{\partial^2}{\partial X^2} \frac{\partial x}{\partial t} + \frac{\partial^2}{\partial Y^2} \frac{\partial x}{\partial t} = 0 \quad (5.1)$$

$$\frac{\partial^2}{\partial X^2} \frac{\partial y}{\partial t} + \frac{\partial^2}{\partial Y^2} \frac{\partial y}{\partial t} = 0 \quad (5.2)$$

being x and y the coordinates of the nodes in the deformed mesh, and X and Y the coordinates of the nodes in the reference mesh.

The main strength of Laplace smoothing is that requires little computational cost due to, as can be seen in Equations 5.1 and 5.2, the displacement of each node in one direction is not coupled with the one of the other direction. It has the disadvantage of not prevent inversion of the elements of the mesh. However, due to that the mesh of the arterial wall is composed of quadrilateral elements and that it is an structured mesh (Chapter 3), the displacement of the mesh in each one of the temporal steps is small related to the size of the geometry and no one of the mesh elements gets inverted.

The direct solver MUMPS has been used for both temporal steps, using the implicit BDF method to solve them, with the Newton's method for non-linear problems. In addition, the inflammatory process of the arterial wall, the plaque growth and the moving mesh are computed dividing them in different groups of segregated steps.

5.6.2 Model with endothelial repair

In this section, the model considering endothelial repair and its results are presented. As explained in Chapter 4, NV depends on TAWSS and OSI during a cardiac cycle. Therefore, the values of the third one of the computed cardiac cycles in every geometry update are considered to initiate the inflammatory process in all the intermediate steps.

It is important to note that, in this model, only the value of the haemodynamic stimuli obtained in the update of the geometry under consideration is taken into account. In addition, it should be noted that the nodes in which TAWSS and OSI are known will suffer a change of coordinates due to the deformation of the mesh caused by the plaque growth. The largest displacement of the mesh nodes will occur in the radial direction, since this is the predominant direction in which growth occurs, as can be seen in the results obtained for the uncoupled model (Figure 5.3).

In Figures 5.5 and 5.6, the results of plaque area and stenosis ratio obtained for the uncoupled model and for all the analysed time intervals of updating the geometry in the case of FSI considering endothelial repair are compared. The area of the plaque has been calculated as the total area of the plaque in the longitudinal section of the axisymmetric model. The full FSI model cannot be calculated due to its high computational requirements.

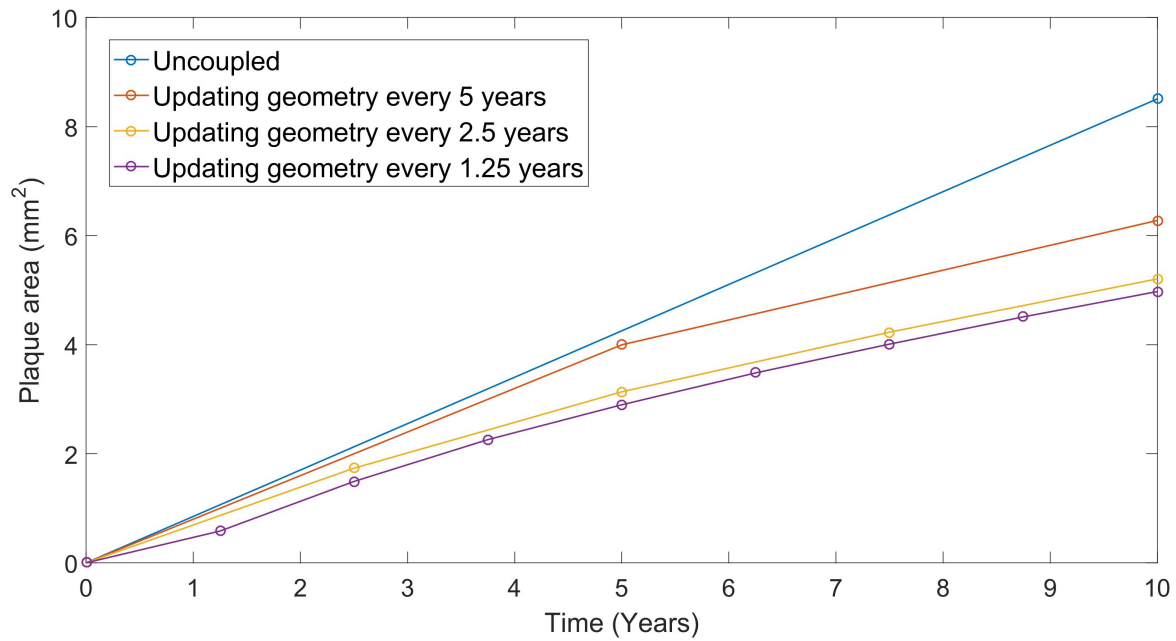


Figure 5.5: Plaque area obtained for the uncoupled and FSI with endothelial repair models, for all the temporal intervals of geometry updating.

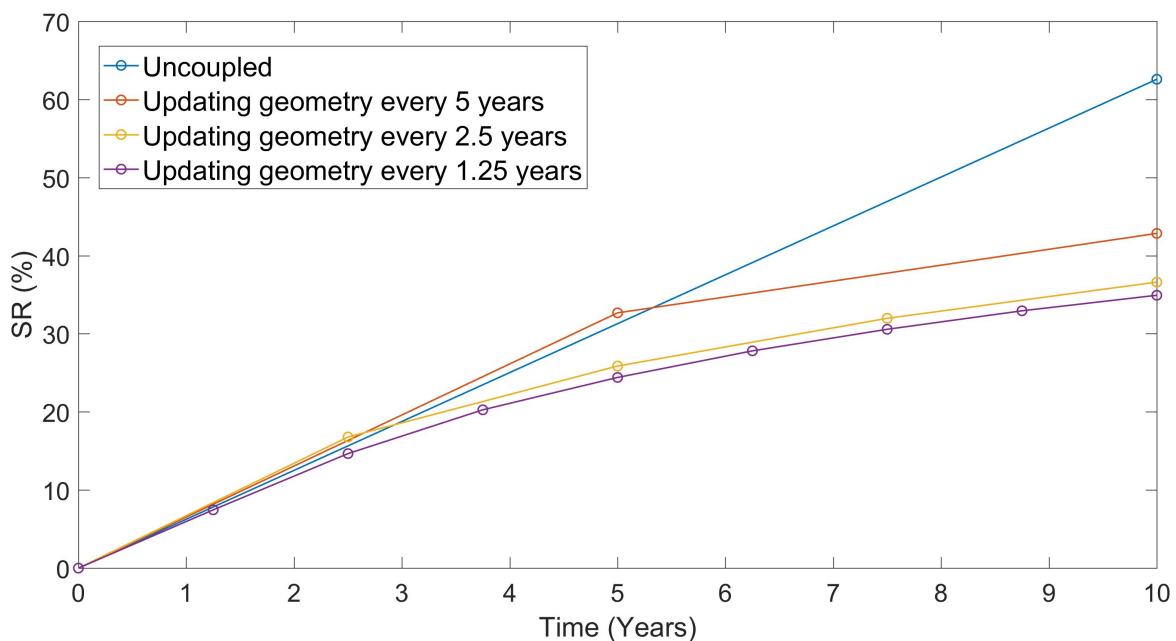


Figure 5.6: Stenosis ratio obtained for the uncoupled and FSI with endothelial repair models, for all the temporal intervals of geometry updating.

As can be seen, the plaque area and the stenosis ratio are higher in the uncoupled model than in the FSI model with endothelial repair. Furthermore, for the case of the FSI

with endothelial repair, the area of the plaque and the stenosis ratio decrease as the time between geometry updates decreases, with convergence being reached in the case of geometry update every 2.5 years.

It can also be seen how performing a calculation with an FSI model with endothelial repair instead of the uncoupled one has a great influence on the resulting plaque. Thus, fluid-structure interaction is an important element to take into account in the process of atheroma plaque formation.

Since it has been observed that the convergence in the results obtained is achieved in the case of updating the geometry every 2.5 and 1.25 years, the resulting geometry for all the mesh update intervals in this case are shown in Figure 5.7. Additionally, the location of the maximum increase of the arterial wall thickness in each case is signalled with a red dot, and its corresponding value is also included.

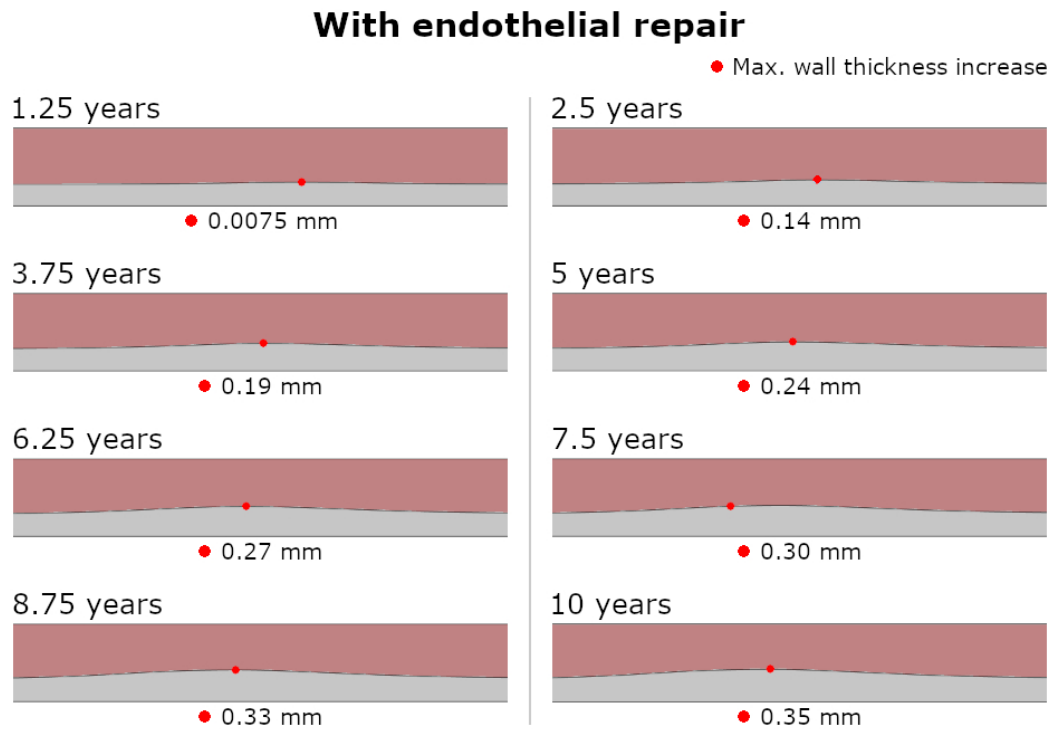


Figure 5.7: Geometry and maximum wall thickness increase for all the time intervals of geometry updating every 1.25 years, for the case of FSI considering endothelial repair.

As can be seen, the position of the point of maximum wall thickness increase changes over time, which is due to the effect of the geometry update and NV in each case. Because of this, the plaque that is produced considering this model has a lower stenosis ratio than the one of the uncoupled model, due to the change of the area of the endothelium in which substances can flow from the lumen into the arterial wall. Therefore, the generated plaque in this case has a more longitudinal and less radial shape than the plaque

obtained with the uncoupled model. The maximum arterial wall thickness increase due to the plaque growth in this FSI model is equal to 0.35 mm , which corresponds to a 34.92 % of stenosis ratio.

As can be seen, the plaque growth obtained for the 10 years of simulation is small due to the endothelium is considered to be automatically repaired at every instant, which could not be real. Therefore, there would be evidence that endothelial repair should occur more gradually.

5.6.3 Model without endothelial repair

In this section, the model considering that the endothelium is not repaired when the haemodynamical stimulus changes is developed.

The process to determine the haemodynamical stimuli in the endothelium is the same than in the case of considering endothelial repair (Section 5.6.2). However, it is necessary to compare all the historical results of TAWSS and OSI in each geometry update, in order to maintain those that correspond to the higher endothelial permeability in each one of the longitudinal sections of the geometry. Thus, due to the areas of low TAWSS and high OSI are considered atheroprone (Chapter 4), the minimal and maximal historical values of TAWSS and OSI, respectively, are considered.

Figures 5.8 and 5.9 show the evolution of the area of the resultant plaque and its stenosis ratio obtained for the uncoupled model and for the model with FSI in which endothelial repair is not considered.

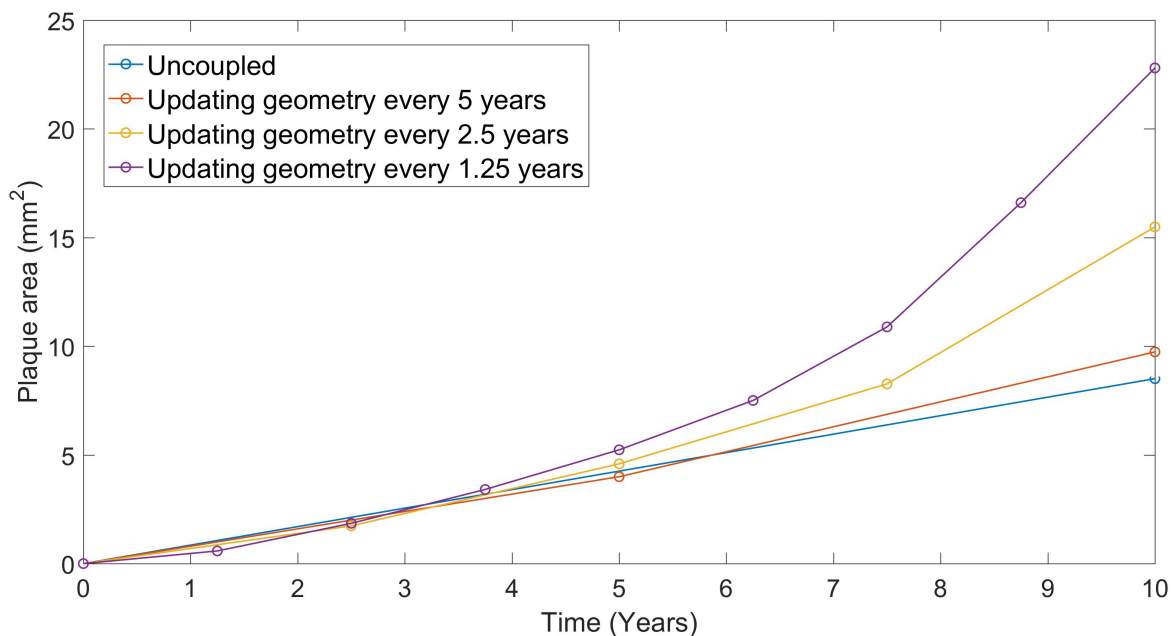


Figure 5.8: Plaque area obtained for the uncoupled and FSI without endothelial repair models, for all the temporal intervals of geometry updating.

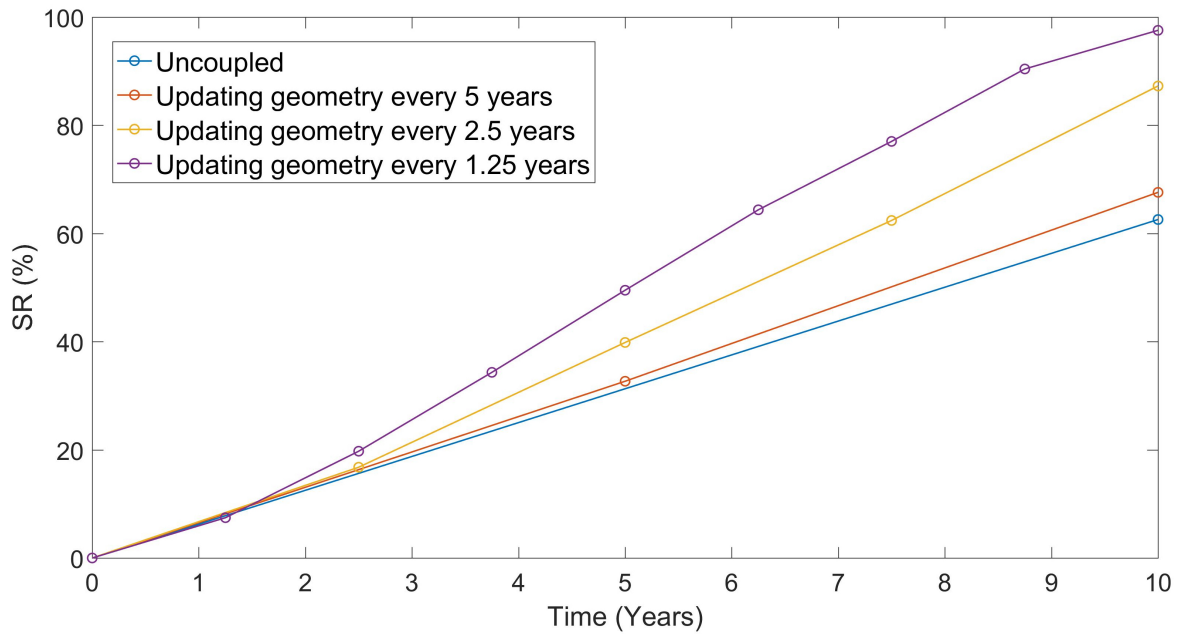


Figure 5.9: Stenosis ratio obtained for the uncoupled and FSI without endothelial repair models, for all the temporal intervals of geometry updating.

As can be seen, the plaque area and the stenosis ratio obtained for the case of FSI without endothelial repair are larger than those obtained in the uncoupled model, in contrast to the obtained for the case of FSI with endothelial repair. This is due to the fact that, since in this case the endothelium is not repaired, the area of substances flow through the endothelium is enlarged with each geometry update, due to the changes in the haemodynamical stimuli. In addition, this explains the reason why the plaque is larger the more frequently the geometry is updated, as can be seen in the image: More quantity of geometry updates is related to a greater area of substances flow across the endothelium.

It can be seen that the stenosis ratio of the plaque increases with increasing the frequency of geometry updating. In the case of updating the geometry every 1.25 years, the obtained stenosis ratio for the year 10 is almost 100%. Thus, if the geometry update frequency is increased further, the value of 100% would be reached in a period of less than 10 years, as there is a larger area of substances flow across the endothelium.

On the other hand, the area of the plaque increases continuously with increasing the geometry update frequency and, since the plaque expands longitudinally, a stable value of plaque area value is not reached. This implies that, in this case, a fully coupled FSI model would be necessary to determine the final geometry of the plaque.

Figure 5.10 shows the geometry evolution in the case of the FSI without considering endothelial repair, for a geometry update period of 1.25 years. The point of higher increase in the arterial wall thickness at each time interval is marked with a red dot.

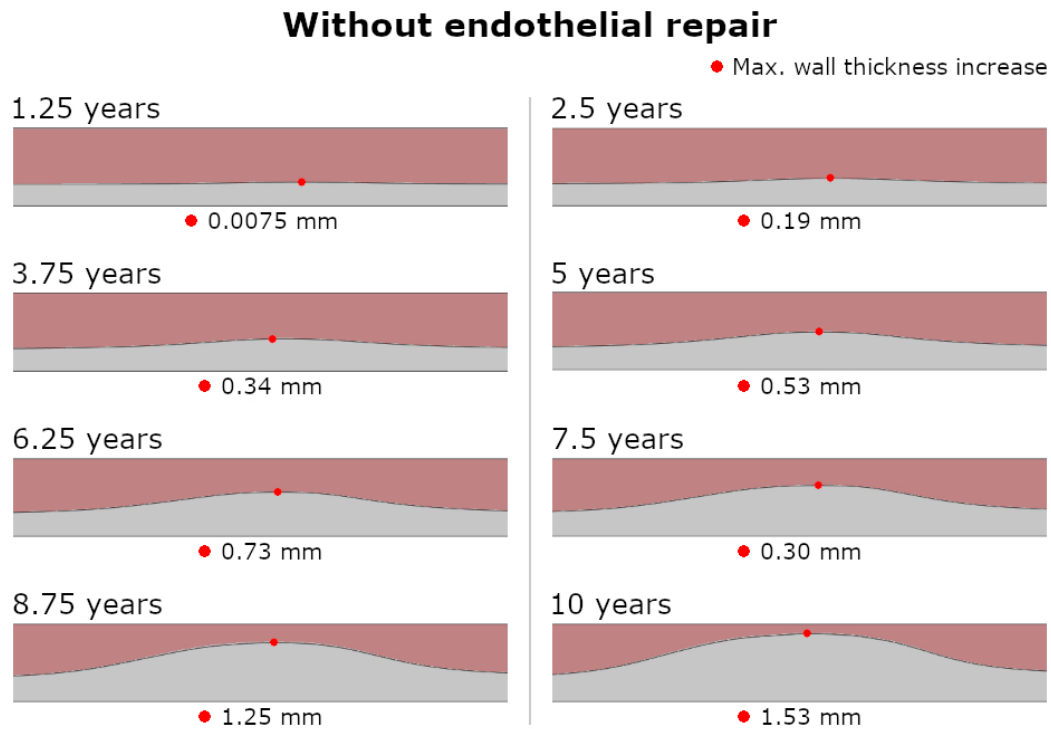


Figure 5.10: Geometry and maximum wall thickness increase for all the time intervals of geometry updating every 1.25 years, for the case of FSI without considering endothelial repair.

Figure 5.10 shows that, as in the case of FSI considering endothelial repair, the point of maximum wall thickness increase due to plaque formation is displaced horizontally. However, in this case, this horizontal displacement is smaller than in the model with endothelial repair. This fact is due to, although the change in haemodynamic stimulus leads to plaque growth in new areas, it also continues to grow in the same areas of the beginning. Therefore, the maximum increase in the arterial wall thickness due to the formation of the atheroma plaque will be located in the initial area of plaque growth.

Additionally, it can be seen that the shape of the plaque developed in this case is different from that obtained in the case of the uncoupled model since in this case, the plaque grows more longitudinally.

Due to this high value of the stenosis ratio in only 10 years of simulation, it can be deduced that this model does not perfectly reproduce the real behaviour of the atheroma plaques, which can take even *30 years* (Insull, 2009). Thus, the total growth provided with this FSI model is very high due to it assumes that the endothelium is not repaired at any time during the simulation and remains permanently damaged.

5.7 Comparison of the results

This section presents an analysis of the comparison of the results obtained in the three different models: Uncoupled and FSI with and without endothelial repair. As can be seen in Figures 5.5 and 5.8, the area of the developed plaques is bigger for the case of the FSI model without endothelial repair, followed by the uncoupled model and, finally, by the FSI model with endothelial repair. As commented, it is due to that in the case of the model without endothelial repair, the areas of substance flow through the endothelium are accumulated with each geometry update. In contrast, in the case of the model that considers endothelial repair, the area of substance entry into the arterial wall is reduced. The uncoupled case is finally an intermediate case. It can also be seen in Figure 5.11, in which the concentration of the substances that contribute to the plaque volume are represented, for the simulation time of 10 years, in each one of the models.

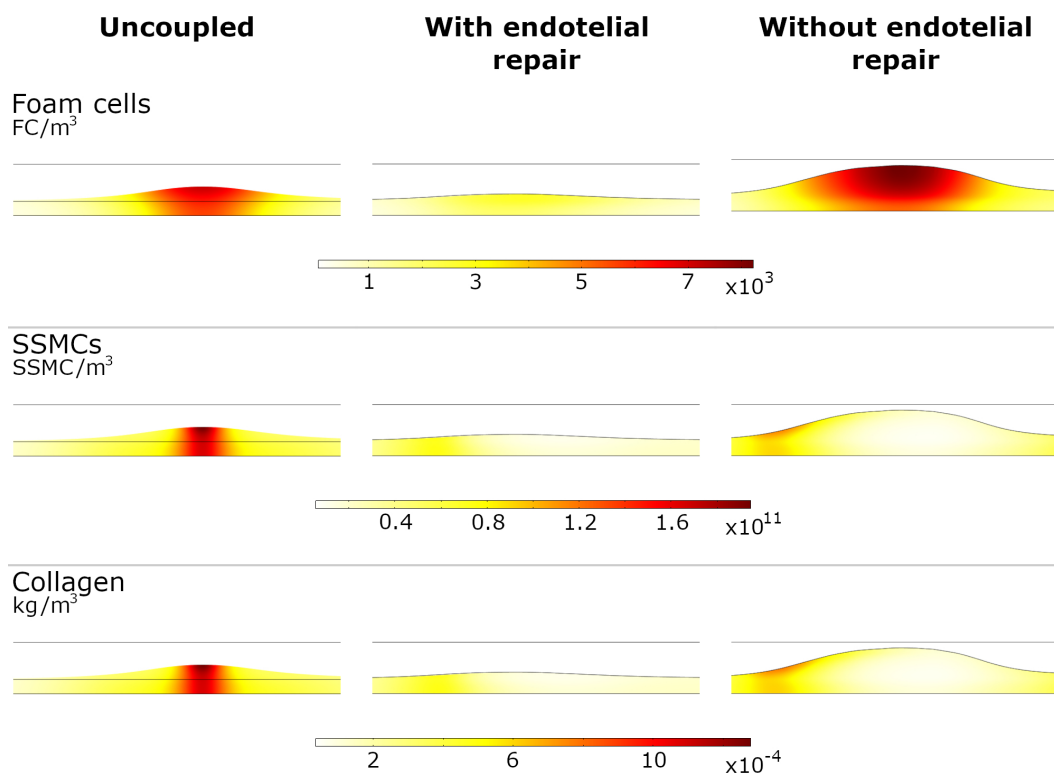


Figure 5.11: Concentration of foam cells, SSMCs and collagen after 10 *years* of simulation for the uncoupled and the two FSI developed models.

The first thing to mention about Figure 5.11 is the change in the shape of the plaques generated with each one of the models, which has already been discussed. As can be seen, the highest concentration of FCs corresponds to the FSI model without endothelial repair due to, as mentioned, the accumulation of areas of substances flow from the lumen into

the arterial wall. On the other hand, due to the analogue reason, the model with FSI that considers endothelial repair is the model with the lowest concentration of FCs.

The distribution of SSMCs concentration is the same than the distribution of collagen fibres in all the analysed models due to that the reactive terms of the collagen equation directly depend on the concentration of SSMCs (Equation 2.50). Therefore, only the concentration of SSMCs is analysed, being the case of collagen analogous.

As can be seen, the highest concentration of SSMCs in year 10 is found for the uncoupled model, whereas it would be logical to expect the highest concentration in the case of the FSI model without endothelial repair, as happened in the case of FCs. However, it should be remembered that the computational model that is being simulated is the vulnerable plaque model developed in Chapter 3. Therefore, the fibrotic layer of the atheroma plaque, which is composed of SSMCs and collagen, is very small. Thus, SSMCs do not proliferate as much as in the non-vulnerable model so that, when the maximum concentration of SSMCs due to the change of phenotype of CSMCs is reached, the concentration of SSMCs starts to decrease due to their apoptosis (Figure 3.13). Due to this and to the larger area of substance flow through the endothelium in the case of the FSI model without endothelial repair, the maximum concentration of SSMCs is reached earlier in this model than in the uncoupled one, so that the concentration of SSMCs in year 10 is lower in this case than in the uncoupled model. It can also be seen that, due to this phenomenon, the concentration of SSMCs in the FSI models is lower in the centre of the plaque than in its outer areas and, therefore, the fibrous cap of the plaque can be observed, which is not possible with the uncoupled model. The thickness of the fibrous cap obtained is lower than $100\ \mu\text{m}$, which actually corresponds to vulnerable plaques (Cilla, 2013).

In Figure 5.12, the LDL concentration obtained for the three computed models after 10 years of simulation is shown.

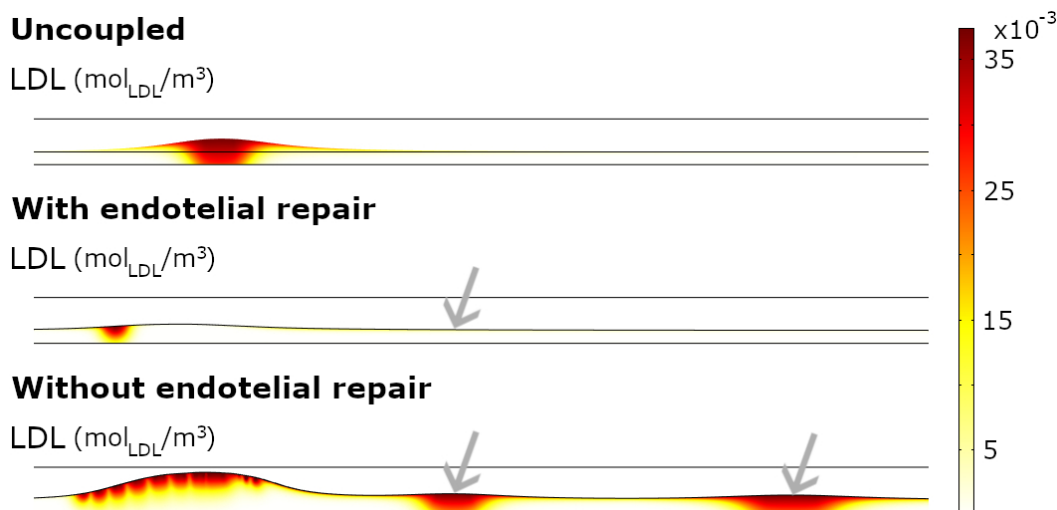


Figure 5.12: LDL concentration after 10 *years* of simulation for the uncoupled and the two FSI developed models.

As can be seen, due to the influence of the FSI, there are some areas downstream the analysed plaques in which LDL flow is allowed in both FSI models, which does not exist in the uncoupled model. It is more noticeable in the case of the FSI model which does not consider endothelial repair. This LDL flow is due to the fact that, updating the haemodynamics of blood considering the changes in the geometry due to the formation of the plaque, derives in the apparition of new areas with low WSS and high OSI downstream the first plaque, which produces new plaques downstream the first one that can also be seen in the Figure. It is a phenomenon called double stenosis that has been observed in real patients (De Bruyne et al., 2000; Pijls et al., 2000) and that has been used to develop the reference model of this Thesis (Chapter 3) and the FSI models of this chapter.

As can be seen in all the results obtained in this chapter, the FSI has an important influence in the results obtained with the model, causing changes in the shape of the developed plaque, in its area and in its stenosis ratio. In addition, the endothelial repair also affects the resultant plaque, being bigger in the case of not considering it. The real behaviour of the endothelium repair should be in an intermediate model between the two models of FSI developed in this Thesis, in which the endothelial cells could repair but not immediately. However, the real behaviour is not known, so this intermediate scenario could not be done at the moment.

5.8 Conclusions

In this chapter, a fluid-structure interaction model for atheroma plaque growth has been developed to validate the hypothesis put forward in Chapter 4, which stated that some of the real plaques were not correctly predicted with the computational model due to that the influence of the FSI was not taken in consideration.

However, due to the high computational cost of the patient-specific models, the FSI has been applied to the two-dimensional axisymmetric reference model developed in Chapter 3. For that, the new haemodynamic variable (NV) developed in Chapter 4, has been used as the main haemodynamical stimulus due to it has been concluded that it is the one that predicts better the real plaques.

Additionally, due to the difference in time scales between the cardiac cycle and the inflammatory process of the arterial wall, a simplification has been done: a semi-coupled FSI model has been developed, in which a total of 10 years of inflammatory process have been calculated by updating the geometry and the haemodynamical stimulus for periods of 5, 2.5 and 1.25 years.

Two different models of FSI have been performed. The first one of the models considers endothelial repair when the haemodynamic stimulus changes due to plaque growth in the arterial wall. On the contrary, the second FSI model considers that, once that the endothelial permeability increases, it remains elevated even if the haemodynamic stimulus that causes the increase changes and, therefore, it is a model that is considered with-

out endothelial repair. That is once that the endothelium has been damaged, it remains permanently damaged. The plaque growth obtained with these two models is different, and it suggests that that what actually happens is that the properties of endothelial repair would be between the two considered cases. However, these properties are not known and, therefore, this intermediate scenario could not be modelled.

Since the model has been performed in a semi-coupled way, an analysis of the variation of the results obtained with geometry update periods of 5, 2.5 and 1.25 years has been performed in both cases, with and without endothelial repair. It has been obtained that, in the case of considering endothelial repair, the convergence in the results is reached for geometry update periods of 1.25 years. In the case of the model without endothelial repair, such convergence is not achieved because, as the update period decreases, more areas of substance flow through the endothelium appear, which lead to more plaque growth. In addition, for an update period of 1.25 years, a stenosis ratio close to 100% is obtained, while the plaque area continues to increase due to this phenomenon.

Large differences are observed in the shape of the plaques obtained with the uncoupled and both FSI models, as well as in the stenosis ratio. In the cases of the FSI models, the developed plaques are more longitudinal than the plaques obtained with the uncoupled model, which has also been observed in the clinical images of Chapter 4.

In addition, it has been observed that, in both FSI models, some new plaque naturally grow downstream of the first one, which is the one that is analysed. It has been observed in clinical practice real patients (De Bruyne et al., 2000; Pijls et al., 2000). However, these new plaques do not appear in the case of the uncoupled model.

Therefore, despite the limitations of the model, from the results obtained in this Chapter it can be concluded that fluid-structure interaction has a major influence on the process of atheroma plaques formation and should not be neglected. However, the model has a high computational cost and requires very long computational times. The calculation time of the plaque growth at each geometry update varies depending on the model and the period of update. For example, in the case of the model that does not consider endothelial repair, the calculation time was more than 8 days for the last geometry update with periods of 1.25 years. Therefore, it is not feasible to apply it to the 3D models.



Chapter 6

Conclusions

Chapter 6

6.1 General overview

A summary of the main conclusions obtained in all this Thesis is presented on this Conclusion Chapter. In addition, the principal contributions of this Thesis are included, as well as the proposed future research lines and the limitations of the developed models. Finally, the publications of scientific articles in journals and oral communications in scientific conferences that have been derived from the work of this Thesis are also included.

6.2 General conclusions

As explained before, atherosclerosis is one of the leading causes of mortality worldwide nowadays. It is a pathology which produces the narrowing of the arterial lumen, resulting in important consequences such as heart attacks, strokes or ischemia. However, the process of atheroma plaques formation is still not completely known and, therefore, all the efforts focused on a better understanding of this pathology can result as crucial to early detect and even prevent its development.

In this Thesis, a computational model to reproduce atheroma plaques formation in arteries has been developed, improving the previous model by [Cilla \(2013\)](#). The computational model has been applied to carotid arteries geometries. However, it can be also applied to other arteries, adapting the geometry and parameters of the model to them. In this model, blood and substances flow in the arterial lumen are considered. In addition, plasma and substances flow from the lumen into the arterial wall, across the endothelium, are modelled as well. These flows are determined considering the three pore model ([Olgac et al., 2008](#)) and, therefore, the substance flows across the endothelium are dependent of the haemodynamics of blood. The inflammatory process in the arterial wall is a complex process in which many substances are involved. Some of them, which are considered as some of the most important substances in this process, are included in the mathematical model, which considers LDL and oxidised LDL molecules, monocytes, macrophages, cytokines, foam cells, CSMCs and SSMCs and collagen fibres. Finally, the plaque growth is also modelled by knowing the concentration of all the considered substances in the arterial wall after the inflammatory process.

In Chapter 3, the two reference models of this Thesis have been developed for the case of a two-dimensional axisymmetric geometry of a carotid artery. This geometry uses the phenomenon of the double stenosis to disturb the blood flow and produce an area of the endothelium with the necessary conditions to develop increased endothelial permeability. This phenomenon has been observed in real patients (De Bruyne et al., 2000; Pijls et al., 2000). Therefore, the atherosclerosis process in the model is initiated considering WSS as the main haemodynamical stimulus. The results obtained show that LDL and monocyte concentrations in the arterial lumen are constant and thus, to reduce the computational cost of the model, they have been imposed as boundary conditions for the other models developed in this Thesis.

In addition, attending to the analysis of the volumetric growth of the resultant plaque, it has been concluded that the reference model corresponds to a model of vulnerable atheroma plaques, with a large lipidic nucleus and a small fibrotic layer. Therefore, some modifications in the equations and in the parameters of SSMCs and collagen fibres (substances which compose the fibrotic layer of the plaque) have been done within the range of the literature values, to develop a reference model of non-vulnerable plaques. The vulnerable model has been validated in Chapter 4 with patient-specific geometries of carotid arteries, while the non-vulnerable one has been validated using real IVUS images of Le Floc'h et al. (2009), obtaining good results.

Due to the large variability of the parameters involved in the process found in the literature, which can affect the plaques growth, a sensitivity analysis of some selected parameters has been carried out. These parameters are those referred to the reactive terms of the substances in the arterial wall, and have been varied by increasing and decreasing their values in a 25 % and in a 10 %. It has been concluded that some of the parameters variations produce variation greater than 100 % in the results obtained and, therefore, the variation of these parameters can have important variations in the results. Of the analysed parameters, d_{LDL} , d_m , C_r , S_r , p_{ss} , G_r , and m_r are directly proportional to the stenosis ratio variation, while $D_{LDL,w} = D_{LDLox,w}$, $D_{m,w} = D_{M,w}$, m_d , $LDLox,r$, n_{FC} , d_c , $C_{c,w}^{th}$, and r_{apop} are inversely proportional to it.

Due to that the vulnerable plaques are more dangerous than the non-vulnerable ones (they can lead to thrombus occasioned by their rupture), the computational models analysed in Chapters 4 and 5 of this Thesis have been developed using the mathematical model of the vulnerable plaques. As commented, the mathematical vulnerable model has been validated with patient-specific geometries of carotid arteries bifurcations in Chapter 4. The clinical images were provided by the Hospital Clínico Universitario Lozano Blesa in Zaragoza (Spain), and corresponds to four different pathological patients and a healthy volunteer. To validate the computational model, the geometries of the pathological images have been reconstructed to obtain their respective healthy geometries, in which the computational model of vulnerable plaques have been computed. Finally, the plaques resultant of the simulations have been contrast with the plaques of the patients. However, a limitation of this procedure is that the real healthy geometries of the pathological arteries

are not known, due to there is no data of the patients before they developed atherosclerosis.

In addition, and with the aim of determine which one of the haemodynamical stimuli commonly used in literature (Alimohammadi et al., 2017; Sáez et al., 2015) is more adequate to calculate the areas of increased endothelial permeability that leads to plaque growth, the blood flow has been modelled in a transient step depending on the cardiac cycle (Malvè et al., 2014). The haemodynamical stimuli that have been considered are TAWSS, OSI and NV, which is a combination of them proposed in this Thesis. For that, numerical correlations that relate these haemodynamical stimuli with endothelial SI, based on experimental data for the case of TAWSS (Levesque et al., 1986) and in pseudo-experimental data for OSI and NV (Sáez et al., 2015), have been developed. In addition, numerical expressions to determine the monocyte flow across the endothelium for the cases of OSI and NV have been developed, by knowing the respective values of monocyte flow for the case of TAWSS. The number of cardiac cycles that are necessary to ensure the correct development of blood flow has also been studied, determining that a total of three cardiac cycles is enough.

In the case of the healthy volunteer, the model does not reproduce plaque growth, which is significant due to that it allows to verify that the model only predicts plaque growth in the pathological cases. For the cases of the pathological geometries, it has been noticed that the use of different haemodynamical stimuli produces the prediction of plaques in different locations of the geometries, and with different stenosis ratio. Therefore, the choice of the haemodynamical stimulus results crucial for the resultant plaques.

Regarding the localisation of the plaques, TAWSS predicts large plaques located in the CCA of the geometries, which are not present in the real arteries. On the contrary, OSI predicts plaque location with a better precision. On the other hand, taking into account the stenosis ratio of plaques, TAWSS is more precise than OSI, which produces plaques with lower stenosis ratio than the real ones in all the cases. Due to that NV is a combination of TAWSS and OSI, it predicts the location of plaques better than TAWSS, due to the influence of OSI, and it also predicts the stenosis ratio better than OSI, due to the results of stenosis ratio obtained with TAWSS. Therefore, of the analysed haemodynamical stimuli, NV is the one that better predicts the plaques in most of the cases.

However, some plaques in the area of the ICA of the real arteries have not been predicted with the computational model with any of the considered haemodynamical stimuli. It is due to that the model is calculated in an uncoupled way, and not taking into account the influence of FSI, as has been studied for the case of geometry "B". In the case of updating the geometry after 15 years of inflammatory process and recompute the blood flow with the new geometry, the haemodynamical stimuli change, and the final predicted plaque is different than the one obtained with the uncoupled case: with this geometry update, the plaque of the ICA is better predicted.

Thus, due to this effect, at the end of Chapter 4 it has been concluded that the haemodynamical update could have an important influence on the plaques obtained with the

computational model. Therefore, the influence of the haemodynamic stimuli update in atherosclerosis has been studied in Chapter 5 with a FSI model. Due to the computational cost of the real geometries, the study of the haemodynamics update influence has been performed in the geometry in two-dimensions axisymmetric, presented before in Chapter 3.

First of all, the two-dimensional model has been improved by including transient blood flow with the simulation of the cardiac cycle. Due to that one of the conclusions of Chapter 4 is that NV predicts the plaques better than only use TAWSS or OSI, NV has been chosen as the main haemodynamical stimulus to initiate atherosclerosis in the model with FSI.

To analyse the influence of the haemodynamical updating in the resultant plaque, the uncoupled model with NV is computed first. In addition, due to that the properties of endothelial repair occasioned by haemodynamical changes are not clear, two different FSI models have been developed: One of them considers endothelial repair while the other one considers that, once that the endothelium has been damaged, it remains permanently damaged.

Due to the time scale differences between the cardiac cycle and the inflammatory process, a semi-coupled model (updating the geometry every few years) has been developed instead of a fully FSI one (updating the geometry at every instant of time). Therefore, an analysis of the geometry update frequency has been done, with updating periods of 5, 2.5 and 1.25 years for both models, with and without endothelial repair. In the case that considers endothelial repair, the results convergence is reached for the updating period of 1.25 years. On the contrary, in the case that does not consider endothelial repair, the convergence is not reached due to the creation of new areas of substance flow across the endothelium with every geometry update.

A large influence of haemodynamics update in the resultant plaques has been noticed in both, plaques geometry and stenosis ratio. The plaques obtained with both FSI models are more longitudinal than the ones obtained with the uncoupled model. In addition, the resultant plaques are bigger in the case of not considering endothelial repair due to the accumulation of inlet substance flows with the geometry updating, which does not appear in the uncoupled or FSI with endothelial repair models. Due to the differences of plaques predicted with FSI considering endothelial repair and not considering it, it can be concluded that the real behaviour of the endothelial cells would be an intermediate case between them. However, due to that this real behaviour is not known, this intermediate case could not be calculated, being this a limitation of the model.

In the FSI models new plaques are naturally developed downstream the first one, which also validates the phenomenon of the double stenosis used to produce the recirculation that leads to the growth of a new plaque in the two-dimensional axisymmetric models of this Thesis.

Despite the limitations of the models developed during this Thesis, we can conclude that the growth model can be used to predict vulnerable and non-vulnerable atheroma

plaques formation in arteries, and they can be also applied to patient-specific geometries with good accuracy. In addition, it can be concluded that FSI has a large influence on the achieved plaques and should not be depicted.

6.3 Thesis contributions

The main contribution of this Thesis is the development of a computational model of atherosclerosis capable of reproduce and, therefore, prevent the apparition of atheroma plaques in arteries. Other important contributions of the Thesis are:

- The improvements that have been done in the formulation and the convergence of the previous mathematical model by, for example, replacing the exponential terms on the equations of the inflammatory process in the arterial wall, among other changes.
- It has been checked that the reference model corresponds to a vulnerable plaques model, attending to the plaque composition.
- A non-vulnerable reference model has been developed from the vulnerable one, with modifications of SSMCs and collagen equations and their respective parameters within the range of the literature. This model has also been validated with real IVUS images from [Le Floc'h et al. \(2009\)](#).
- A sensitivity analysis of the parameters of the model has been performed, due to the huge range of values found in the literature, determining how would variations in these parameters values affect the growth of the plaque.
- Temporal blood flow calculation has been developed using a transient step depending on the cardiac cycle, for the two-dimensional axisymmetric and patient-specific geometries.
- The vulnerable reference model has been validated with its application to patient-specific geometries of carotid arteries. In addition, it has been validated that the model does not produce atheroma plaques in the case of healthy geometries.
- Different haemodynamical stimuli have been analysed in patient-specific geometries to determine their influence on the resultant plaques. These haemodynamical stimuli are TAWSS, OSI and NV, which depends on them. It has been concluded that NV, which has been proposed in this Thesis, better predicts the plaques of the real-patients in the most of the analysed cases, due to that it combines the main strengths of use TAWSS and OSI individually.
- A previous simplified FSI analysis has been developed for one of the real carotids, which has been used to check that including haemodynamics update better predicts

some of the plaques that are present in the real patients, and which are not predicted with the uncoupled model.

- Two different models considering FSI have been applied to the two-dimensional model of vulnerable plaques (due to the computational cost that would be required to apply them to the patient-specific geometries), to analyse the influence of the haemodynamics update in the simulated plaques. The main conclusion is that the influence of the haemodynamics update in the resultant plaques is important in their stenosis ratio and geometries, and should not be depicted.
- The importance of endothelial repair in FSI models has been analysed, concluding that it has a high influence in the resultant plaques. The real behaviour of the endothelial cells should be in an intermediate case between the two analysed models.

6.4 Future research lines

The future planned research lines are intended to improve the developed model, focusing on its limitations:

- An study of the influence of the mechanics of the arterial wall in atheroma plaque formation is being developed. For that, three different computational models are being analysed: The first one considers the effects of the tortuosity of the arterial wall in the developed plaques. The second takes into account the effects of the arterial wall porosity in the plaques. Finally, the third one of the models combines the effects of the two previously commented.
- A multilayered wall model more similar to the real arterial wall is being developed to overcome the limitation of the monolayered wall of all the models included in this Thesis. It has been developed considering the intima, media and adventitia layers, with the endothelium, internal and external elastic lamina modelled as membranes. In addition, the effect of chemotaxis has been included in the multilayered wall model, due to CSMCs change of phenotype in the arterial media is produced by the presence of cytokines in the intima layer. However, the chemotaxis velocity is still being adjusted in the model, using experimental data from the literature.
- Include the mechanotaxis taking into account the effect of the arterial wall stresses due to its deformation.
- The influence of hypertension in the developed plaques should be analysed due to that there are evidences of hypertension increases the risk of atheroma plaque formation.
- To take into account the changes in the transport properties of the arterial wall due to the apparition of the plaques which, in this Thesis, have been considered as constant during the whole process.

- The influence of other factors in the resultant plaques, like changes in the patient conditions due to drug administration or variations of LDL and monocyte concentrations in the bloodstream, should be studied to achieve a more realistic model.
- The vulnerable and non-vulnerable plaque models have been validated only attending to the plaque composition. However, there are many factors involved in these definitions, as the mechanical stresses that plaques suffer, which can be included in the model in a future line.
- To analyse the real behaviour of endothelial cells repair with the changes on the haemodynamical stimuli, to posteriori reproduce this real behaviour of cells in the computational FSI model.
- Some other substances involved in the process of atherosclerosis can be included in the model, like high-density lipoproteins, different kinds of cytokines, T-cells, free oxygen radicals that oxidise LDL and metalloproteinases that are responsible of collagen degradation.
- The developed computational model is a continuum model which, as commented, allows the simulation of real geometries due to not consider individual cells. However, this model cannot reproduce the natural random behaviour of cells, which is the main advantage of agent-based models. Therefore, a future line is to develop a methodology to couple the continuum model with an agent-based model, combining the advantages of both types of model.

6.5 Publications and other contributions

In this section, the scientific articles and the oral communications in scientific conferences derived from the work developed during this Thesis are included.

6.5.1 Journal contributions

- Hernández-López, P., Cilla, M., Martínez, M.A. and Peña, E.
Effects of the haemodynamic stimulus on the location of carotid plaques based on a patient-specific mechanobiological plaque atheroma formation model.
Frontiers in Bioengineering and Biotechnology, 2021, 9, 690685.
IF: 6.064 Q1. DOI: 10.3389/fbioe.2021.690685
- Hernández-López, P., Martínez, M.A., Peña, E. and Cilla, M.
Understanding the parameter influence on lesion growth for a mechanobiology model of atherosclerosis.
Mathematics, 2023, 11, 829.
IF: 2.542 Q1. DOI: 10.3390/math11040829

- Hernández-López, P., Cilla, M., Martínez, M.A., Peña, E. and Malvè, M.
Fluid-structure interaction influence on a mechanobiological model of atheroma plaques growth.
In preparation.
- Another article about the influence of the arterial wall mechanics will be developed:
Hernández-López, P., Laita-Dieste, N., Cilla, M., Martínez, M.A. and Peña, E.
Arterial wall mechanics influence on a model of atherosclerosis.

6.5.2 Communications in scientific conferences

International

- Authors: **Hernández-López, P.**, Cilla,M., Martínez, M. A. y Peña, E.
Title: On modelling patient-specific carotid atherosclerotic plaque formation.
Format: Poster and flash presentation.
Conference: Virtual Physiological Human Conference 2018 (VPH2018).
Place: Zaragoza, Spain.
Date: 5-7th of September, 2018.
- Authors: Hernández-López, P., **Cilla,M.**, Martínez, M. A. y Peña, E.
Title: Mechanobiological modeling of atheroma plaque formation in carotid patient-specific geometries.
Format: Presentation.
Conference: XIV Conference de Métodos Numéricos en la Ingeniería.
Lugar celebración: Guimarães, Portugal.
Date: 1st-3rd of July, 2019.
- Authors: **Hernández-López, P.**, Cilla,M.,Martínez, M. A. y Peña, E.
Title: Mechanobiological modelling of atheroma plaque formation in carotid patient-specific geometries.
Format: Presentation.
Conference: Congress of the European Society of Biomechanics 2019 (ESB2019).
Place: Vienna, Austria.
Date: 7-10th of July, 2019.
- Authors: Laita-Dieste, N., Hernández-López, P., Cilla,M., Mena, A., Martínez, M. A. y **Peña, E.**
Title: Effect of Mechanics On Atheroma Plaque Formation and Development: Mechanobiological Model Coupled with Wall Expansion and FSI.
Format: Presentation.
Conference: 25th Congress of the European Society of Biomechanics.
Lugar celebración: Vienna, Austria.
Date: 7-10th of July, 2019.

- Authors: **Hernández-López, P.**, Cilla,M.,Martínez, M. A. y Peña, E.
Title: Patient-specific atheroma plaque growth depending on the mechanical stimulus.
Format: Poster
Conference: 5th Barcelona VPH Summer School.
Place: Barcelona, Spain.
Date: 7-11th of June, 2021.
Additional information: Award to the best Hands-on.
- Authors: **Hernández-López, P.**, Cilla,M.,Martínez, M. A. y Peña, E.
Title: Analysis of the influence of different mechanical stimuli in atheroma plaques in patient-specific carotids.
Format: Presentation.
Conference: European Society of Biomechanics (ESB2021).
Place: Online.
Date: 11-14th of July, 2021.
- Authors: **Hernández-López, P.**, Cilla,M.,Martínez, M. A. y Peña, E.
Title: Analysis of the influence of the arterial wall mechanics in a mechanobiological model of atherosclerosis.
Format: Poster.
Conference: European Society of Biomechanics (ESB2022).
Place: Porto, Portugal.
Date: 26-29th of June, 2022.
- Authors: **Hernández-López, P.**, Cilla,M.,Martínez, M. A., Peña, E. y Malvè, M.
Title: Mechanobiological model of atheroma plaque growth based on fluid-structure interaction.
Format: Presentation.
Conference: European Solid Mechanics Conference (ESMC2022).
Place: Galway, Ireland.
Date: 4-8th of July, 2022.

National

- Authors: **Hernández-López, P.**, Cilla,M., Martínez, M. A. y Peña, E.
Title: Modelado mecanobiológico del crecimiento de placa de atheroma en arteria carótida.
Format: Presentation.
Conference: VIII Reunión del Capítulo Español de la Sociedad Europea de Biomecánica (ESB).
Place: Castellón de la Plana, Spain.
Date: 22nd and 23rd of November, 2018.

- Authors: **Hernández-López, P.**, Cilla,M., Martínez, M. A. y Peña, E.
Title: Modelo mecanobiológico de la formación de placa de ateroma en arteria carótida de paciente específico.
Format: Poster.
Conference: VIII Jornada de Jóvenes Investigadores del Instituto e Investigación en Ingeniería de Aragón (I3A).
Place: Zaragoza, Spain.
Date: 6th of June, 2019.
- Authors: Hernández-López, P., Laita,N., Cilla,M., Martínez, M. A. y **Peña, E.**
Title: Effect of wall expansion and hypertension on ateroma plaque formation and development: mecanobiological model.
Format: Presentation.
Conference: IX Reunión del Capítulo Español de la Sociedad Europea de Biomecánica.
Place: Las Palmas de Gran Canaria, Spain.
Date: 24th and 25th of October, 2019.
- Authors: **Hernández-López, P.**, Cilla,M., Martínez, M. A. y Peña, E.
Title: Crecimiento de placa de ateroma en arteria carótida de paciente específico según diferentes estímulos mecánicos.
Format: Poster.
Conference: IX Jornada de Jóvenes Investigadores del I3A.
Place: Zaragoza, Spain.
Date: 11th of December, 2020.
Información adicional: Obtención del premio a la Mejor Contribución Científica en la División de Ingeniería Biomédica.
- Authors: **Hernández-López, P.**, Cilla,M., Martínez, M. A. y Peña, E.
Title: Influencia del estímulo mecánico empleado en el crecimiento de placa de ateroma en arterias carótidas de paciente específico.
Format: Presentation.
Conference: VII Jornadas del Programa de Doctorado de Ingeniería Mecánica.
Place: Zaragoza, Spain.
Date: 17th and 18th of December, 2020.
- Authors **Hernández-López, P.**, Cilla,M., Martínez, M. A., Peña, E.y Malvè M.
Title: Modelo de crecimiento de placa de ateroma con interacción fluido-estructura.
Format: Poster.
Conference: X Jornada de Jóvenes Investigadores del I3A.
Place: Zaragoza, Spain.
Date: 21st of October, 2021.
- Authors: **Hernández-López, P.**, Cilla,M., Martínez, M. A. y Peña, E.
Title: Análisis de la influencia de diferentes estímulos mecánicos en el crecimiento de

placa de ateroma en arterias carótidas de paciente específico.

Format: Presentation.

Conference: X Reunión Anual del Capítulo Nacional Español de la Sociedad Europea de Biomecánica.

Place: Granada, Spain.

Spain Date: 25th and 26th of October, 2021.

- Authors: **Hernández-López, P.**, Cilla,M., Martínez, M. A., Peña, E.y Malvè M.
Title: Modelo mecanobiológico del crecimiento de placa de ateroma con interacción fluido-estructura.
Format: Presentation.
Conference: VIII Jornadas del Programa de Doctorado de Ingeniería mecánica.
Place: Zaragoza, Spain.
Date: 12th of November, 2021.
- Authors: Hernández-López, P., Laita, N., Cilla,M., Martínez, M. A. y **Peña, E.**
Title: Effect of mechanics in a mechanobiological model of atherosclerosis.
Format: Presentation.
Second Colloquium of the Spanish Theoretical and Applied Mechanics Society.
Place: Sevilla, Spain.
Date: 28th and 29th of March, 2022.
- Authors: **Hernández-López, P.**, Laita, N., Cilla,M., Martínez, M. A. y Peña, E.
Title: Influencia de la mecánica de la pared arterial en el crecimiento de placa de ateroma.
Format: Presentation.
Conference: XI Jornada de Jóvenes Investigadores del I3A.
Place: Zaragoza, Spain.
Date: 16th of July, 2022.
- Authors: **Hernández-López, P.**, Laita,N., Cilla,M., Martínez, M. A. y Peña, E.
Title: Modelo mecanobiológico de crecimiento de placa de ateroma en arteria: Influencia de la mecánica de la pared arterial.
Format: Presentation.
Conference: XI Reunión Anual del Capítulo Nacional Español de la Sociedad Europea de Biomecánica.
Place: Zaragoza, Spain.
Date: 24th and 25th of October, 2022.



Chapter 7

Conclusiones

Chapter 7

7.1 Introducción

En este capítulo se incluye un resumen de las principales conclusiones obtenidas a lo largo de la presente Tesis Doctoral. Además, se analizan las principales contribuciones de la Tesis y se proponen algunas líneas de trabajo futuras a partir de los resultados obtenidos y de las limitaciones que presentan los modelos computacionales desarrollados. Finalmente, se incluyen las publicaciones en revistas científicas derivadas del trabajo realizado, así como participaciones en congresos científicos.

7.2 Conclusiones finales

Como se explica en el capítulo de introducción de esta Tesis, actualmente la aterosclerosis es una de las principales causas de mortalidad en tMechanics and thermodynamics of transcapillary exchange F. Curry, C. Michel, E. M. Renkin Published 1984 Chemistryodo el mundo. Es una patología que produce la disminución del diámetro del lumen de las arterias, pudiendo derivar en consecuencias graves con una elevada mortalidad, tales como infartos o isquemias. Sin embargo, el proceso de formación de las placas de ateroma todavía no se conoce completamente y, por lo tanto, todos los esfuerzos que se enfoquen en una mejor comprensión de esta patología pueden resultar cruciales para detectar su aparición en una etapa temprana e incluso para prevenir su desarrollo.

En esta Tesis se ha desarrollado un modelo computacional capaz de reproducir el crecimiento de placas de ateroma en arterias, mejorando el modelo previo de Cilla (2013), y ha sido aplicado a geometrías de arterias carótidas. Aunque también puede ser aplicado a otras arterias mediante la respectiva adaptación de la geometría y de los parámetros necesarios. En este modelo se consideran en primer lugar el flujo sanguíneo y de sustancias en el lumen de la arteria, se modelan los flujos de plasma y de sustancias que tienen lugar a través del endotelio, desde el lumen hacia el interior de la pared arterial. Dichos flujos se determinan mediante la implementación del modelo de los tres poros (Olgac et al., 2008) y, por lo tanto, los flujos de sustancias y plasma a través del endotelio son dependientes de la hemodinámica del flujo sanguíneo. El proceso inflamatorio que tiene lugar en la pared arterial es un proceso complejo, en el cual están involucradas una gran cantidad de sustancias. Algunas de dichas sustancias, consideradas como las más importantes

del proceso, se incluyen en el modelo matemático, el cual considera moléculas de LDL y LDL oxidado, monocitos, macrófagos, citoquinas, células espumosas, células musculares de fenotipos contráctil y sintético y fibras de colágeno. Finalmente, se modela el crecimiento de la placa una vez conocidas las concentraciones en la pared arterial de todas las sustancias consideradas en el proceso inflamatorio.

En el Capítulo 3, se han desarrollado los dos modelos considerados de referencia para una geometría de arteria carótida. Se trata de dos modelos axisimétricos cuya geometría se basa en el fenómeno bien conocido de la doble estenosis para generar una recirculación en el flujo sanguíneo y ocasionar un área en el endotelio con las condiciones necesarias para desarrollar un incremento de su permeabilidad, y que ha sido observado en pacientes reales (De Bruyne et al., 2000; Pijls et al., 2000). Por lo tanto, el proceso de aterosclerosis en el modelo se inicia considerando el WSS como el principal estímulo hemodinámico.

Adicionalmente, atendiendo al análisis del crecimiento volumétrico de la placa resultante, se ha concluido que el modelo de referencia corresponde a un modelo de placas de atheroma vulnerables, con un gran núcleo lipídico y una capa fibrótica pequeña. Para obtener lo que se denomina una placa no vulnerable (capa fibrótica grande y núcleo lipídico pequeño), se han realizado algunas modificaciones en las ecuaciones y parámetros de las SSMCs y de las fibras de colágeno, dentro de los rangos encontrados en literatura, las cuales son las sustancias que componen la capa fibrótica de la placa. El modelo de placa vulnerable ha sido validado en el Capítulo 4 mediante geometrías de arterias carótidas de paciente específico, mientras que el modelo no vulnerable se ha validado empleando imágenes IVUS reales de pacientes de Le Floch et al. (2009), con las que se determinó la no vulnerabilidad de las mismas.

Debido a la gran variabilidad de los parámetros involucrados en el proceso que se ha encontrado en la literatura, la cual puede afectar al crecimiento y morfología de las placas obtenidas, se ha realizado un análisis de sensibilidad de algunos de los parámetros del modelo. Dichos parámetros son los relacionados con los términos reactivos de las sustancias en la pared arterial, los cuales se han modificado incrementando y reduciendo sus valores en un 25 % y en un 10 %. Se ha concluido que las variaciones de algunos de los parámetros producen cambios en los resultados obtenidos mayores al 100 % y, por tanto, una variación en los valores de dichos parámetros podría suponer grandes cambios en los resultados obtenidos. De todos los parámetros analizados, d_{LDL} , d_m , C_r , S_r , p_{ss} , G_r , y m_r son directamente proporcionales a la variación del ratio de estenosis, mientras que $D_{LDL,w} = D_{LDL_{ox,w}}$, $D_{m,w} = D_{M,w}$, m_d , $LDL_{ox,r}$, n_{FC} , d_c , $C_{c,w}^{th}$ y r_{apop} son inversamente proporcionales a él.

Debido a que las placas vulnerables resultan más peligrosas que las no vulnerables (pueden derivar en trombos ocasionados por su ruptura), los modelos computacionales analizados en los Capítulos 4 y 5 de esta Tesis se han desarrollado empleando el modelo matemático de placas vulnerables.

Como se ha comentado previamente, el modelo matemático de placa vulnerable se ha validado en el Capítulo 4 con geometrías de bifurcaciones de arterias carótidas de pa-

ciente específico. Las imágenes clínicas fueron proporcionadas por el Hospital Clínico Universitario Lozano Blesa en Zaragoza, y corresponden a cuatro pacientes patológicos y a un voluntario sano. Para realizar la validación del modelo, las geometrías obtenidas de las imágenes patológicas se han modificado removiendo las placas, obteniendo así sus respectivas geometrías sanas, en las cuales se ha calculado el modelo computacional de placa vulnerable. Finalmente, las placas obtenidas mediante las simulaciones se han comparado con las placas reales que presentan los pacientes. Sin embargo, una limitación de este proceso es que no se dispone de las geometrías sanas reales de los pacientes, debido a que no se tienen datos de ellos previos al desarrollo de la aterosclerosis.

Con el objetivo de determinar cuál de los estímulos hemodinámicos empleados habitualmente en la literatura (Alimohammadi et al., 2017; Sáez et al., 2015) es más adecuado para calcular las áreas con aumento de permeabilidad endotelial en las cuales se produce crecimiento de placa, el flujo sanguíneo en las geometrías de paciente específico se ha modelado en estado transitorio y dependiente del ciclo cardíaco (Malvè et al., 2014). Los estímulos hemodinámicos considerados son los conocidos TAWSS, OSI y NV, la cual es una combinación de TAWSS y OSI propuesta en esta Tesis. Para ello, se han desarrollado correlaciones numéricas que relacionan dichos estímulos mecánicos con el SI de las células endoteliales, basadas en datos experimentales para el caso del TAWSS (Levesque et al., 1986) y en datos pseudo-experimentales para los casos del OSI y NV (Sáez et al., 2015). Adicionalmente, conociendo los valores correspondientes de flujo de monocitos para el caso del TAWSS se han desarrollado expresiones numéricas para determinar el flujo de monocitos a través del endotelio para los casos del OSI y de NV. Se ha estudiado también el número de ciclos cardíacos que son necesarios simular para asegurar el completo desarrollo del flujo sanguíneo, determinando que un total de tres ciclos cardíacos es suficiente.

En el caso del voluntario sano, el modelo no reproduce crecimiento de placa, lo cual es una validación muy importante debido a que permite comprobar que el modelo únicamente predice crecimiento de placa en los casos patológicos, demostrando la estabilidad del modelo. Por otra parte, para las geometrías patológicas, se ha observado que el uso de los diferentes estímulos hemodinámicos en el modelo produce cambios tanto en las posiciones de las placas como en sus ratios de estenosis. Por ello, la elección del estímulo hemodinámico a emplear resulta crucial.

Atendiendo a la posición de las placas, TAWSS predice grandes placas en la CCA que no están presentes en las arterias reales. Por el contrario, OSI predice la posición de las placas con una mayor precisión. Por otra parte, atendiendo al ratio de estenosis de las placas, TAWSS es más preciso que OSI, el cual calcula placas con un ratio de estenosis menor al real para todos los casos analizados. Debido a que NV es una combinación de TAWSS y OSI, predice mejor la posición de las placas que el TAWSS, debido a la influencia del OSI y, adicionalmente, predice el ratio de estenosis mejor que el OSI debido a los resultados obtenidos con el TAWSS. Por ello, de los tres estímulos hemodinámicos analizados, NV es el que predice mejor las placas en la mayoría de los casos.

Sin embargo, algunas de las placas presentes en la ICA de las arterias reales no se han

podido predecir con ninguno de los estímulos hemodinámicos empleados. Una de las posibles explicaciones de estos malos resultados puede ser que el modelo se ha calculado de una manera desacoplada, sin tener en cuenta la influencia de la actualización del estímulo hemodinámico con el crecimiento, lo cual se ha estudiado en el caso de la geometría "B". Para el caso en el que se actualiza la geometría después de 15 años de proceso inflamatorio y se recalcula el flujo sanguíneo con la nueva geometría, el estímulo hemodinámico cambia, con lo que la placa final predecida es diferente a la obtenida con el modelo desacoplado: debido a esta actualización de la geometría, la placa de la ICA de este paciente es más alargada y se predice mejor la geometría real.

Por lo tanto, debido a este efecto, al final del Capítulo 4 se concluye que la actualización de la hemodinámica podría tener una gran influencia en las placas obtenidas con el modelo computacional. Por ello, en el Capítulo 5 se ha estudiado la influencia de dicha actualización en la aterosclerosis mediante un modelo FSI. Debido al coste computacional de las geometrías reales, el estudio de la influencia del FSI se ha desarrollado en la geometría de dos dimensiones axisimétrica ya presentada en el Capítulo 3.

En primer lugar, el modelo en dos dimensiones se ha mejorado incluyendo el flujo sanguíneo transitorio dependiente del ciclo cardíaco. Debido a que una de las conclusiones del Capítulo 4 es que NV predice las placas mejor que usar únicamente TAWSS u OSI, se ha empleado NV como el estímulo hemodinámico principal a considerar para el modelo con FSI.

Para poder analizar la influencia de la actualización de la hemodinámica en la placa generada, en primer lugar se calcula el modelo desacoplado dependiente de NV. Adicionalmente, debido a que las propiedades de la reparación endotelial causada por cambios hemodinámicos no están claras, se han desarrollado dos modelos diferentes de FSI: El primero de ellos considera reparación endotelial mientras que, el segundo considera que, una vez que el endotelio se ha dañado continúa permanentemente en este estado y, por lo tanto, no se modela la reparación endotelial.

Debido a la diferencia de las escalas temporales entre el ciclo cardíaco y el proceso inflamatorio, se ha desarrollado un modelo semiacoplado (actualizando la geometría cada determinados años) en lugar de un modelo con FSI completamente acoplado (actualizando la geometría en cada instante de tiempo). Por lo tanto, se ha realizado un análisis de la frecuencia de actualización de la geometría, empleando periodos de 5, 2.5 y 1.25 años para ambos modelos, con y sin reparación endotelial. En el caso del modelo con reparación endotelial, la convergencia de los resultados se alcanza para un periodo de actualización de la geometría igual a 1.25 años. Por el contrario, en el caso que no considera reparación endotelial, dicha convergencia no se alcanza debido a la creación de nuevas áreas de flujo de sustancias con cada actualización de la geometría.

Se ha observado una gran influencia del FSI en las placas obtenidas, tanto atendiendo a la forma de su geometría como a su ratio de estenosis. Las placas obtenidas con ambos modelos de FSI tienen una forma más longitudinal que las obtenidas con el modelo desacoplado. Adicionalmente, las placas resultantes son más grandes en el caso en el cual no

se considera reparación endotelial, lo cual se debe a la acumulación de flujos de entrada de sustancias producida por la actualización de la geometría que no se produce para los casos desacoplado y de actualización de la hemodinámica con reparación endotelial. Debido a la diferencia en las placas obtenidas con ambos modelos de FSI se puede concluir que el comportamiento real de las células endoteliales sería equivalente a un caso intermedio entre ambos. Sin embargo, debido a que dicho comportamiento no es conocido, el caso intermedio no se ha podido calcular, siendo por lo tanto una limitación del modelo.

En los modelos sí se observa el desarrollo de manera natural de nuevas placas de ateroma aguas abajo de la primera, lo cual valida el fenómeno de la doble estenosis empleada para producir la recirculación que provoca el crecimiento de una nueva placa. Dicho fenómeno se ha empleado para producir el inicio de la placa analizada en los dos casos de modelo axisimétrico en dos dimensiones empleados en esta Tesis.

A pesar de las limitaciones que presentan los modelos desarrollados durante esta Tesis, estos se pueden emplear para predecir formación de placas de ateroma en arterias, tanto de tipo vulnerable como no vulnerable. Dichos modelos también se pueden aplicar a geometrías de paciente específico. Adicionalmente, se puede concluir que el FSI tiene una gran influencia en las placas desarrolladas y, por lo tanto, no debería ser despreciado.

7.3 Contribuciones

La principal contribución de esta Tesis es el desarrollo de un modelo computacional de aterosclerosis capaz de reproducir la aparición de placas de ateroma en arterias. Otras contribuciones importantes de la presente Tesis son:

- Se ha mejorado la formulación y la convergencia del modelo matemático previo, por ejemplo, reemplazando los términos exponenciales de las ecuaciones del proceso inflamatorio en la pared arteria, entre otros cambios.
- Se ha comprobado que, atendiendo a la composición de las placas obtenidas, el modelo de referencia corresponde a un modelo de placas vulnerables.
- Se ha desarrollado un modelo de referencia de placa de ateroma no vulnerable basado en modificaciones en las ecuaciones y parámetros referidos a las células musculares de fenotipo sintético y al colágeno, dentro del rango encontrado en la literatura. Adicionalmente, dicho modelo se ha validado con resultados de imágenes IVUS reales de [Le Floc'h et al. \(2009\)](#).
- Debido al amplio rango de valores encontrado en la literatura, se ha realizado un análisis de sensibilidad del modelo ante variaciones en sus parámetros determinando cómo afectarían al crecimiento de la placa.

- Se ha añadido el cálculo de flujo sanguíneo en estado transitorio dependiente del ciclo cardíaco, tanto en el modelo 2d axisimétrico como en las geometrías de paciente específico.
- Se ha validado el modelo de placa vulnerable con geometrías reales de paciente específico. Además, se ha comprobado la estabilidad del modelo ya que no reproduce placa en el caso de geometrías sanas.
- Se han analizado diferentes variables hemodinámicas en las geometrías de paciente específico, analizando la influencia de ellas en las placas desarrolladas. En concreto, se han empleado TAWSS y OSI y se ha desarrollado una nueva variable dependiente de ambos. Se ha concluido que NV predice mejor las placas de los pacientes reales en la mayoría de los casos analizados, debido a que combina las principales ventajas de emplear TAWSS y OSI individualmente.
- Se ha realizado un cálculo simplificado de FSI en una de las carótidas reales para verificar que la consideración de la actualización de la hemodinámica supone una mejor predicción de algunas de las placas que presentan los pacientes reales y que el modelo desacoplado no es capaz de reproducir.
- Se han desarrollado dos modelos de interacción fluido-estructura para analizar la influencia de la actualización de la hemodinámica sobre las placas obtenidas, los cuales se han aplicado al modelo axisimétrico debido al alto coste computacional que supondría realizarlos en las geometrías de paciente específico. La conclusión principal obtenida es que dicha influencia en las placas es elevada, tanto en la geometría de las placas obtenidas como en el ratio de estenosis, por lo que no se debería despreciar el efecto de la actualización de la hemodinámica en el cálculo de placas de ateroma.
- Se ha analizado la importancia de la reparación endotelial en los modelos de FSI, concluyendo que tiene una gran influencia en las placas desarrolladas. El comportamiento real de las células endoteliales debería encontrarse en un caso intermedio entre los dos modelos analizados.

7.4 Líneas de trabajo futuras

Las líneas de trabajo futuras de esta Tesis se enfocan en mejorar el modelo desarrollado enfocándose, para ello, en sus limitaciones:

- Se está desarrollando un estudio de la influencia de la mecánica de la pared arterial en la formación de placas de ateroma. Para ello, se están analizando tres modelos computacionales diferentes: El primero de ellos tiene en cuenta los efectos de la tortuosidad de la pared arterial en las placas desarrolladas. El segundo modelo considera

los efectos de la porosidad de la pared arterial en las placas. Finalmente, el tercero de los modelos combina los efectos de los dos comentados previamente.

- Se está desarrollando un modelo con la pared arterial multicapa, más similar a la pared arterial real, para eliminar la simplificación de la pared monocapa de los modelos desarrollados en esta Tesis. Dicho modelo considera las capas íntima, media y adventicia de la pared arterial, modelando el endotelio y las láminas elástica interna y externa como membranas. Adicionalmente, se ha incluido el efecto de la quimiotaxis en el modelo multicapa, debido a que el cambio de fenotipo de las CSMCs en la capa media se produce por la presencia de citoquinas en la capa íntima. Actualmente se está ajustando la velocidad de dicha quimiotaxis en el modelo, empleando para ello datos experimentales de la literatura.
- Se tiene planteado incluir la mecanotaxis en el modelo, considerando las tensiones debidas a la deformación de la pared arterial.
- La influencia de la hipertensión en las placas de ateroma predecidas con el modelo debería ser analizada, debido a que existen evidencias de que la hipertensión aumenta el riesgo de formación de placas de ateroma.
- Tener en cuenta los cambios en las propiedades de transporte de la pared arterial debido a la aparición de las placas las cuales, en los modelos desarrollados, se han considerado constantes a lo largo de todo el proceso.
- La influencia de otros factores en las placas obtenidas, como cambios en las condiciones del paciente debido a la administración de fármacos o variaciones en las concentraciones de LDL o monocitos en sangre, deberían ser consideradas para lograr un modelo más realista.
- La validación del modelo mediante datos experimentales obtenidos, por ejemplo, de un estudio de seguimiento de pacientes con placa o con riesgo de desarrollar placa de ateroma
- Analizar el comportamiento real de la reparación de las células endoteliales debido a cambios en los estímulos hemodinámicos para, posteriormente, poder reproducir dicho comportamiento en el modelo FSI.
- Se pueden incluir en el modelo nuevas sustancias involucradas en el proceso de aterosclerosis, como lipoproteínas de alta densidad, distintos tipos de citoquinas, radicales de oxígeno libres que oxidan el LDL, o metaloproteasas, las cuales son las responsables de la degradación del colágeno.
- El modelo computacional es un modelo continuo el cual, como se ha comentado en el Capítulo 1, permite la simulación de geometrías reales debido a que no considera células individuales. Sin embargo, este modelo no puede reproducir el comportamiento aleatorio natural de las células, la cual es la principal ventaja de los mode-

los de agentes. Por ello, una línea futura es desarrollar una metodología que permita acoplar el modelo continuo con un modelo de agentes, combinando las ventajas de ambos.

7.5 Publicaciones y otras contribuciones

En esta sección se incluyen los artículos científicos y las diferentes presentaciones realizadas en congresos científicos derivados del trabajo desarrollado durante la presente Tesis.

7.5.1 Publicaciones en revistas científicas

- Hernández-López, P., Cilla, M., Martínez, M.A. and Peña, E.
Effects of the haemodynamic stimulus on the location of carotid plaques based on a patient-specific mechanobiological plaque atheroma formation model.
Frontiers in Bioengineering and Biotechnology, 2021, 9, 690685.
IF: 6.064 Q1. DOI: 10.3389/fbioe.2021.690685
- Hernández-López, P., Martínez, M.A., Peña, E. and Cilla, M.
Understanding the parameter influence on lesion growth for a mechanobiology model of atherosclerosis.
Mathematics, 2023, 11, 829.
IF: 2.542 Q1. DOI: 10.3390/math11040829
- Hernández-López, P., Cilla, M., Martínez, M.A., Peña, E. and Malvè, M.
Fluid-structure interaction influence on a mechanobiological model of atheroma plaques growth.
En preparación.
- Se va a desarrollar otro artículo sobre la influencia de la mecánica de la pared arterial:
Hernández-López, P., Laita-Dieste, N., Cilla, M., Martínez, M.A. and Peña, E.
Arterial wall mechanics influence on a model of atherosclerosis.

7.5.2 Presentaciones en congresos científicos

Internacionales

- Autores: **Hernández-López, P.**, Cilla, M., Martínez, M. A. y Peña, E.
Título: On modelling patient-specific carotid atherosclerotic plaque formation.
Formato: Póster and flash presentation.
Congreso: Virtual Physiological Human Conference 2018 (VPH2018).
Lugar de celebración: Zaragoza, España.
Fecha: 5-7 de septiembre de 2018.

- Autores: Hernández-López, P., **Cilla,M.**, Martínez, M. A. y Peña, E.
Título: Mechanobiological modeling of atheroma plaque formation in carotid patient-specific geometries.
Formato: Presentación.
Congreso: XIV Congreso de Métodos Numéricos en la Ingeniería.
Lugar celebración: Guimarães, Portugal.
Fecha: 1-3 de julio de 2019.
- Autores: **Hernández-López, P.**, Cilla,M.,Martínez, M. A. y Peña, E.
Título: Mechanobiological modelling of atheroma plaque formation in carotid patient-specific geometries.
Formato: Presentación.
Congreso: Congress of the European Society of Biomechanics 2019 (ESB2019).
Lugar de celebración: Viena, Austria.
Fecha: 7-10 de julio de 2019.
- Autores: Laita-Dieste, N., Hernández-López, P., Cilla,M., Mena, A., Martínez, M. A. y **Peña, E.**
Título: Effect of Mechanics On Atheroma Plaque Formation and Development: Mechanobiological Model Coupled with Wall Expansion and FSI.
Formato: Presentación.
Congreso: 25th Congress of the European Society of Biomechanics.
Lugar celebración: Viena, Austria.
Fecha: 7-10 de julio de 2019.
- Autores: **Hernández-López, P.**, Cilla,M.,Martínez, M. A. y Peña, E.
Título: Patient-specific atheroma plaque growth depending on the mechanical stimulus.
Formato: Póster
Congreso: 5th Barcelona VPH Summer School.
Lugar de celebración: Barcelona, España.
Fecha: 7-11 de junio de 2021.
Información adicional: Obtención del premio al mejor Hands-on.
- Autores: **Hernández-López, P.**, Cilla,M.,Martínez, M. A. y Peña, E.
Título: Analysis of the influence of different mechanical stimuli in atheroma plaques in patient-specific carotids.
Formato: Presentación.
Congreso: European Society of Biomechanics (ESB2021).
Lugar de celebración: Telemático.
Fecha: 11 - 14 de julio de 2021.
- Autores: **Hernández-López, P.**, Cilla,M.,Martínez, M. A. y Peña, E.
Título: Analysis of the influence of the arterial wall mechanics in a mechanobiological

model of atherosclerosis.

Formato: Póster.

Congreso: European Society of Biomechanics (ESB2022).

Lugar de celebración: Oporto, Portugal.

Fecha: 26 - 29 de junio de 2022.

- Autores: **Hernández-López, P.**, Cilla, M., Martínez, M. A., Peña, E. y Malvè, M.
Título: Mechanobiological model of atheroma plaque growth based on fluid-structure interaction.
Formato: Presentación.
Congreso: European Solid Mechanics Conference (ESMC2022).
Lugar de celebración: Galway, Irlanda.
Fecha: 4 - 8 de julio de 2022.

Nacionales

- Autores: **Hernández-López, P.**, Cilla, M., Martínez, M. A. y Peña, E.
Título: Modelado mecanobiológico del crecimiento de placa de ateroma en arteria carótida.
Formato: Presentación.
Congreso: VIII Reunión del Capítulo Español de la Sociedad Europea de Biomecánica (ESB).
Lugar de celebración: Castellón de la Plana, España.
Fecha: 22 y 23 de noviembre de 2018.
- Autores: **Hernández-López, P.**, Cilla, M., Martínez, M. A. y Peña, E.
Título: Modelo mecanobiológico de la formación de placa de ateroma en arteria carótida de paciente específico.
Formato: Póster.
Congreso: VIII Jornada de Jóvenes Investigadores del Instituto e Investigación en Ingeniería de Aragón (I3A).
Lugar de celebración: Zaragoza, España.
Fecha: 6 de junio de 2019.
- Autores: **Hernández-López, P.**, Laita, N., Cilla, M., Martínez, M. A. y **Peña, E.**
Título: Effect of wall expansion and hypertension on atheroma plaque formation and development: mecanobiological model.
Formato: Presentación.
Congreso: IX Reunión del Capítulo Español de la Sociedad Europea de Biomecánica.
Lugar de celebración: Las Palmas de Gran Canaria, España.
Fecha: 24 y 25 de octubre de 2019.
- Autores: **Hernández-López, P.**, Cilla, M., Martínez, M. A. y Peña, E.
Título: Crecimiento de placa de ateroma en arteria carótida de paciente específico

según diferentes estímulos mecánicos.

Formato: Póster.

Congreso: IX Jornada de Jóvenes Investigadores del I3A.

Lugar de celebración: Zaragoza, España.

Fecha: 11 de diciembre de 2020.

Información adicional: Obtención del premio a la Mejor Contribución Científica en la División de Ingeniería Biomédica.

- Autores: **Hernández-López, P.**, Cilla,M., Martínez, M. A. y Peña, E.
Título: Influencia del estímulo mecánico empleado en el crecimiento de placa de ateroma en arterias carótidas de paciente específico.
Formato: Presentación.
Congreso: VII Jornadas del Programa de Doctorado de Ingeniería Mecánica.
Lugar de celebración: Zaragoza, España.
Fecha: 17 y 18 de diciembre de 2020.
- Autores **Hernández-López, P.**, Cilla,M., Martínez, M. A., Peña, E.y Malvè M.
Título: Modelo de crecimiento de placa de ateroma con interacción fluido-estructura.
Formato: Póster.
Congreso: X Jornada de Jóvenes Investigadores del I3A.
Lugar de celebración: Zaragoza, España.
Fecha: 21 de octubre de 2021.
- Autores: **Hernández-López, P.**, Cilla,M., Martínez, M. A. y Peña, E.
Título: Análisis de la influencia de diferentes estímulos mecánicos en el crecimiento de placa de ateroma en arterias carótidas de paciente específico.
Formato: Presentación.
Congreso: X Reunión Anual del Capítulo Nacional Español de la Sociedad Europea de Biomecánica.
Lugar de celebración: Granada, España.
España Fecha: 25 y 26 de octubre de 2021.
- Autores: **Hernández-López, P.**, Cilla,M., Martínez, M. A., Peña, E.y Malvè M.
Título: Modelo mecanobiológico del crecimiento de placa de ateroma con interacción fluido-estructura.
Formato: Presentación.
Congreso: VIII Jornadas del Programa de Doctorado de Ingeniería mecánica.
Lugar de celebración: Zaragoza, España.
Fecha: 12 de noviembre de 2021.
- Autores: Hernández-López, P., Laita, N., Cilla,M., Martínez, M. A. y **Peña, E.**
Título: Effect of mechanics in a mechanobiological model of atherosclerosis.
Formato: Presentación.
Second Colloquium of the Spanish Theoretical and Applied Mechanics Society.

Lugar de celebración: Sevilla, España.

Fecha: 28 y 29 de marzo de 2022.

- Autores: **Hernández-López, P.**, Laita, N., Cilla, M., Martínez, M. A. y Peña, E.
Título: Influencia de la mecánica de la pared arterial en el crecimiento de placa de ateroma.
Formato: Presentación.
Congreso: XI Jornada de Jóvenes Investigadores del I3A.
Lugar de celebración: Zaragoza, España.
Fecha: 16 de julio de 2022.
- Autores: **Hernández-López, P.**, Laita, N., Cilla, M., Martínez, M. A. y Peña, E.
Título: Modelo mecanobiológico de crecimiento de placa de ateroma en arteria: Influencia de la mecánica de la pared arterial.
Formato: Presentación.
Congreso: XI Reunión Anual del Capítulo Nacional Español de la Sociedad Europea de Biomecánica.
Lugar de celebración: Zaragoza, España.
Fecha: 24 y 25 de octubre de 2022.

Appendices



Appendix A

Parameters

Appendix A

Parameters

In this appendix, the determination of all the parameters involved in the mathematical model is explained, following the same sections than in Chapter 2.

A.1 Blood flow

Parameters involved in the calculation of blood flow along the arterial lumen are:

- μ_b : Blood dynamic viscosity. $0.0035 Pa \cdot s$ (Milnor, 1989).
- ρ_b : Blood density. $1050 kg/m^3$ (Milnor, 1989).

A.2 Plasma flow

All the necessary parameters for the determination of the plasma flow from the lumen into the arterial wall, through the endothelium, are divided in three sections related to: parameters correspondent to physic properties, dimensions and pressures:

A.2.1 Physic properties

- k_w : Darcy permeability of the arterial wall. $1.2 \cdot 10^{-18} m^2$. It is within the range of $0.8 \cdot 10^{-18} m^2$ and $2 \cdot 10^{-18} m^2$ (Huang et al., 1994; Prosi et al., 2005).
- $L_{p,nj}$: Normal junction conductivity. Its value is dependent of the considered artery. *The specific hydraulic conductivities for the tissues of intact vessels are then $5 \cdot 10^{-10} cm^2/(s \cdot mmHg)$ at 70 mmHg and $2.4 \cdot 10^{-10} cm^2/(s \cdot mmHg)$ at 180 mmHg, whereas the respective values for deendothelialized vessels are $6.7 \cdot 10^{-10} cm^2/(s \cdot mmHg)$ at 70 mmHg and $5.3 \cdot 10^{-10} cm^2/(s \cdot mmHg)$ at 180 mmHg. (Tedgui and Lever (1984), p. H789).*
The total conductivity of the arterial wall, L_{p_t} , may be expressed by an equation for two resistances in series (Tedgui and Lever (1984), p. H790).

$$\frac{1}{Lp_t} = \frac{1}{Lp_e} + \frac{1}{Lp_m}, \quad (\text{A.1})$$

being Lp_e and Lp_m the hydraulic conductivities of the endothelium and the media layer, respectively. The total conductivity of the arterial wall corresponds to the case of intact endothelium. Assuming that, when the endothelium is damaged, all the difficulty for the plasma flow corresponds to the media layer and Lp_m is equal to the hydraulic conductivity.

Tedgui and Lever (1984) do not consider leaky junctions, so we can assume that:

$$Lp_e = Lp_{nj} \quad (\text{A.2})$$

For example, for the case of an intraluminal pressure of 70 mmHg , the hydraulic conductivity of normal junctions per area unit is:

$$Lp_{nj} = 1.478 \cdot 10^{-15} \frac{\text{m}^2}{\text{s} \cdot \text{Pa}} \quad (\text{A.3})$$

Dividing by the thickness of the arterial wall, for the case of the considered carotid arteries (0.58 mm), it is possible to determine the hydraulic conductivity of normal junctions per length unit:

$$Lp_{nj} = 2.159 \cdot 10^{-12} \frac{\text{m}}{\text{s} \cdot \text{Pa}} \quad (\text{A.4})$$

The process is analogue for all the intraluminal pressures and arteries. For other cases of intraluminal pressures, it is necessary to interpolate.

- ϵ_w : Intima porosity of the arterial wall. 0.96 (**Ai and Vafai (2006)**, p. 1574).
- μ_p : Plasma dynamic viscosity. $0.001 \text{ Pa} \cdot \text{s}$ (**Milnor, 1989**).
- ρ_p : Plasma density. $1050 \frac{\text{kg}}{\text{m}^3}$ (**Milnor, 1989**).

A.2.2 Dimensions

- A_{unit} : Unit area for the experimental correlations in **Lin et al. (1989)**. 0.64 mm^2 (**Lin et al., 1989; Olgac et al., 2008**).
- l_{lj} : Length of a leaky junction. $2 \mu\text{m}$ *The intercellular cleft has a typical length of 1 – 2 μm* (**Weinbaum et al. (1985)**, p. H955).
- R_{cell} : Endothelial cell radius. $15 \mu\text{m}$. (**Weinbaum et al. (1985)**, Figure 2).
- w_l : Half-width of a leaky junction. 20 nm *a leaky junction width of 20 nm* (**Weinbaum et al. (1985)**, p.H950).

A.2.3 Pressures

- P_{adv} : Pressure of the adventitia. 17.5 mmHg (Olgac et al. (2008)).
- ΔP_{End} : Pressure drop in the endothelium. Its value is dependent of the intraluminal pressure. Takes values of 18 mmHg and 28 mmHg for intraluminal pressures of 70 mmHg and 180 mmHg , respectively. *From our calculated value for endothelial conductivity and measured filtration rate, the pressure drop across the endothelium is estimated to be 18 mmHg . If the endothelial conductivity is unaltered between 70 and 180 mmHg , then the pressure drop across the endothelium at the higher pressure is calculated to be 28 mmHg .* (Tedgui and Lever (1984), p.H790). For intermediate cases of intraluminal pressure, the pressure drop in the endothelium can be determined by interpolating the previous values.

A.3 Substances flow along lumen

The parameters to determine LDL and monocyte flows along the lumen are:

- $C_{0,LDL,b}$: LDL concentration in blood. $6.98 \frac{\text{mol}_{LDL}}{\text{m}^3}$ for the pathological model (Cilla (2013), p. 276).
Range of variation in the literature: $3.1 - 6.98 \frac{\text{mol}_{LDL}}{\text{m}^3}$ (Cilla, 2013).
- $C_{0,m,b}$: Monocyte concentration in blood. $550 \cdot 10^9 \frac{\text{Monocyte}}{\text{m}^3}$ (Khan, 2009).
- $D_{LDL,b}$: LDL diffusion coefficient in blood. $5 \cdot 10^{-12} \frac{\text{m}^2}{\text{s}}$ (Olgac et al. (2008), p. H911).
- $D_{m,b}$: Monocyte diffusion coefficient in blood. $1 \cdot 10^{-10} \frac{\text{m}^2}{\text{s}}$ Cilla et al. (2015), Table 1).

A.4 Inflammatory process

The parameters that are necessary to calculate the inflammatory process of atheroma plaques apparition in the arterial wall due to the presence of all the considered substances are divided in: Substances properties and dimensions, initial and threshold concentrations, lumen-arterial wall flows, parameters of the reactive terms and conversion parameters:

A.4.1 Substances properties and dimensions

- $D_{r,LDL,w}$: LDL diffusion coefficient in the radial direction in the arterial wall. $8 \cdot 10^{-13} \frac{\text{m}^2}{\text{s}}$. *We set the porosity of the media to $\epsilon = 0.15$ and the diffusivity of LDL with respect to the gradient of the volume-averaged concentration to $D = 8 \cdot 10^{-9} \frac{\text{cm}^2}{\text{s}}$.* (Prosi et al. (2005), p. 909).

- $D_{\theta,LDL,w}$: LDL diffusion coefficient in the circumferential direction in the arterial wall. $2.4 \cdot 10^{-12} \frac{m^2}{s}$. (Prosi et al. (2005); Yuan et al. (1991)).
- $D_{z,LDL,w}$: LDL diffusion coefficient in the longitudinal direction in the arterial wall. $2.4 \cdot 10^{-12} \frac{m^2}{s}$. (Prosi et al. (2005); Yuan et al. (1991)).
- $D_{r,oxLDL,w}$: Oxidised LDL diffusion coefficient in the arterial wall. $8 \cdot 10^{-13} \frac{m^2}{s}$. (Prosi et al., 2005). Due to there is no data of this value in the bibliography and, to their similar sizes, we assume the same diffusion coefficient for LDL and oxidised LDL.
- $D_{\theta,oxLDL,w}$: Oxidised LDL diffusion coefficient in the circumferential direction in the arterial wall. $2.4 \cdot 10^{-12} \frac{m^2}{s}$. (Prosi et al. (2005); Yuan et al. (1991)).
- $D_{z,oxLDL,w}$: Oxidised LDL diffusion coefficient in the longitudinal direction in the arterial wall. $2.4 \cdot 10^{-12} \frac{m^2}{s}$. (Prosi et al. (2005); Yuan et al. (1991)).
- $D_{r,m,w}$: Monocyte diffusion coefficient in the radial direction in the arterial wall. $8 \cdot 10^{-15} \frac{m^2}{s}$ (Cilla et al. (2013)).
- $D_{\theta,m,w}$: Monocyte diffusion coefficient in the circumferential direction in the arterial wall. $2.4 \cdot 10^{-14} \frac{m^2}{s}$. (Cilla et al. (2013); Yuan et al. (1991)).
- $D_{z,m,w}$: Monocyte diffusion coefficient in the longitudinal direction in the arterial wall. $2.4 \cdot 10^{-14} \frac{m^2}{s}$. (Cilla et al. (2013); Yuan et al. (1991)).
- $D_{r,M,w}$: Macrophage diffusion coefficient in the arterial wall. $8 \cdot 10^{-15} \frac{m^2}{s}$ (Budugrajan et al. (2008), Table I). Due to there is no data of this value in the bibliography and, to their similar sizes, we assume the same diffusion coefficient for monocytes and macrophages.
- $D_{\theta,M,w}$: Macrophage diffusion coefficient in the circumferential direction in the arterial wall. $2.4 \cdot 10^{-14} \frac{m^2}{s}$. (Cilla et al. (2013); Yuan et al. (1991)).
- $D_{z,M,w}$: Macrophage diffusion coefficient in the longitudinal direction in the arterial wall. $2.4 \cdot 10^{-14} \frac{m^2}{s}$. (Cilla et al. (2013); Yuan et al. (1991)).
- k_{lag} : Solute lag coefficient of LDL. 0.893 (Dabagh et al., 2009). To determine the value of $k_{lag,LDL}$, we assume that the intima layer of the arterial wall is composed by a fibre matrix of proteoglycans and collagen, according to Dabagh et al. (2009). During all this Thesis, the subscript Pg will be referred to the proteoglycan matrix while Cg is referred to collagen.

$k_{lag,LDL}$ can be determined as:

$$k_{lag,LDL} = 1 - \Omega_{intima}, \quad (A.5)$$

where Ω_{intima} is the partition coefficient of the intima layer, that can be determined following Dabagh et al. (2009):

$$\Omega_{intima} = \exp \left[- (1 - \epsilon_{Pg}) \left(2 \frac{R_{LDL}}{R_{Pg}} + \frac{R_{LDL}^2}{R_{Pg}^2} \right) \right] (\epsilon_{Cg} + \epsilon_{Pg} - 1) \cdot \exp \left[- (1 - \epsilon_{Cg})^{1/2} \left(1 + \frac{R_{LDL}}{R_{Cg}} \right) \right], \quad (A.6)$$

being ϵ_{Pg} and ϵ_{Cg} the porosities of the proteoglycan matrix and of the collagen, respectively. R_{LDL} , R_{Pg} and R_{Cg} represent the radius of LDL, proteoglycan and collagen. The value of R_{LDL} has already been defined in Section 2.5 (11 nm) while R_{Cg} can be assumed to be 20 nm (Huang et al., 1994). In addition, the proteoglycan matrix is composed by central filaments of hyaluronic and proteoglycan monomers (subscripts Cf and Pm , respectively). Thus, R_{Pg} can be defined as (Huang et al., 1994):

$$R_{Pg} = \left[\frac{\alpha_{Pm-Cf} R_{Pm}^2 + R_{Cf}^2}{\alpha_{Pm-Cf} + 1} \right]^{1/2}, \quad (A.7)$$

where α_{Pm-Cf} is the ratio between the lengths of proteoglycan monomers and central filaments of hyaluronic, and has a value of 3 (Dabagh et al., 2009; Huang et al., 1994). R_{Cf} is the radius of the central filaments of hyaluronic, which corresponds to 2 nm (Huang et al., 1994). On the other hand, R_{Pm} is an effective radius of proteoglycan monomers, which are composed by glycosaminoglycan fibres attached to proteoglycan core proteins and, therefore, it can be calculated as:

$$R_{Pm} = [\beta_{G-Cp} R_G^2 + R_{Cp}^2]^{1/2}, \quad (A.8)$$

being R_G and R_{Cp} the radius of glycosaminoglycan fibres and proteoglycan core proteins, respectively which, according to Huang et al. (1994), have values of 0.6 nm and 2 nm. β_{G-Cp} is a ratio between the lengths of glycosaminoglycan fibres and proteoglycan core proteins, and takes a value of 5 (Dabagh et al., 2009; Huang et al., 1994). Thus, R_{Pm} takes a value of 2.408 nm and R_{Pg} is equal to 2.313 nm.

On the other hand, the porosity of the proteoglycan matrix can be calculated as:

$$\epsilon_{Pg} = 1 - \frac{t_{0,intima}}{t_{intima}} (1 - \epsilon_{0Pg}), \quad (A.9)$$

where $t_{0,intima}$ and t_{intima} are, respectively, the thickness of the intima for an intraluminal pressure of 0 Pa (zero pressure case) and for the considered intraluminal pressure in each case. $t_{0,intima}$ takes a value of 0.5 μm based on the literature, and t_{intima} is equal to 0.155 μm and 0.0575 μm for intraluminal pressures of 70 mmHg and 180 mmHg (Dabagh et al., 2009). ϵ_{0Pg} is the porosity of the proteoglycan matrix for the zero pressure, that, according to Dabagh et al. (2009), has a value of 0.9866.

Analogously to the case of the porosity of the proteoglycan matrix, the porosity of the collagen matrix can be calculated as:

$$\epsilon_{Cg} = 1 - \frac{t_{0,intima}}{t_{intima}} (1 - \epsilon_{0Cg}) \quad (A.10)$$

The parameters $t_{0,intima}$ and t_{intima} have already been defined, and ϵ_{0Cg} is the porosity of the collagen matrix for the zero pressure, and it can be determined by knowing that for the zero pressure case, the 5 % of the intima is formed by collagen (Dabagh et al., 2009).

Thus, the value of Ω_{intima} can be calculated and it takes a value of 0.1065 and, therefore, $k_{lag,LDL}$ is equal to 0.893.

Range of variation in the literature: 0.2016 – 1.8934 (Dabagh et al., 2009); 0.1486 – 0.8514 (Olgac et al., 2008); 0.1486 – 1.05 (Sun et al., 2007).

The Table A.1 contains all the parameters that are necessary to calculate the value of $k_{lag,LDL}$:

Parameter	Description	Value	Reference
R_{Cf}	Radius of the central filaments of hyaluronic	2 nm	Huang et al. (1994)
R_{Cg}	Radius of collagen	20 nm	Huang et al. (1994)
R_{Cp}	Radius of proteoglycan core proteins	2 nm	Huang et al. (1994)
R_G	Radius of glycosaminoglycan fibres	0.6 nm	Huang et al. (1994)
$t_{0,intima}$	Thickness of the intima at the zero pressure case	0.5 μm	Dabagh et al. (2009)
t_{intima}	Thickness of the intima at a pressure of 70 mmHg	0.155 μm	Dabagh et al. (2009)
α_{Pm-Cf}	Ratio between the lengths of glycosaminoglycan monomers and filaments of hyaluronic	3	Huang et al. (1994) Dabagh et al. (2009)
β_{G-Cp}	Ratio between the lengths of glycosaminoglycan fibres and proteoglycan core proteins	5	Huang et al. (1994) Dabagh et al. (2009)
ϵ_{0Cg}	Porosity of the collagen matrix for the zero pressure case	0.95	Dabagh et al. (2009)
ϵ_{0Pg}	Porosity of the proteoglycan matrix for the zero pressure case	0.9866	Dabagh et al. (2009)

Table A.1: Parameters to determine the value of K_{lag} .

- l_{ij} : Length of a leaky junction. 2 μm The intercellular cleft has a typical length of 1 – 2 μm (Weinbaum et al. (1985), p. H955).
- Mw_{LDL} : LDL molecular weight. 386.65 $\frac{g}{mol_{LDL}}$ (Cilla (2013)).

- R_{LDL} : LDL radius. 11 nm. *Intercellular junctions, as described in the preceding section, would not normally allow significant passage of LDL (diameter ~ 23 nm) (Tarbell (2003), p. 96).*
- w_l : Half-width of a leaky junction. 20 nm *a leaky junction width of 20 nm (Weinbaum et al. (1985), p.H950).*
- ρ_{LDL} : LDL density. $1063 \frac{kg}{m^3}$. *LDL is broadly defined as lipoprotein fraction with density ranging from 1.006 to 1.063 g/ml, which can be isolated by various laboratory methods. (Ivanova et al. (2017), p. 2).*

A.4.2 Initial and threshold concentrations

- $C_{0,CSMC}$: CSMC initial concentration. $3.16 \cdot 10^{13} \frac{CSMC}{m^3}$. (Table 3, Escuer et al. (2019)).
Range of variation in the literature: $2.794 \cdot 10^{12} \frac{CSMC}{m^3}$ (Zahedmanesh et al., 2014)-
 $3.16 \cdot 10^{13} \frac{CSMC}{m^3}$ (Escuer et al., 2019).
- $C_{c,w}^{th}$: Cytokine threshold. Its value depends of the considered artery. It is estimated by looking at the maximum value of cytokine concentration in the area of plaque development.
- $C_{LDL,adv}$: LDL concentration in the adventitia. It is dependent on the intraluminal pressure. Figure 1.a, Meyer et al. (1996):

$$P_{lumen} = 70 \text{ mmHg} \Rightarrow C_{LDL,adv} = 5 \text{ ‰} \cdot C_{LDLdep} \quad (A.11)$$

$$P_{lumen} = 120 \text{ mmHg} \Rightarrow C_{LDL,adv} = 16 \text{ ‰} \cdot C_{LDLdep} \quad (A.12)$$

$$P_{lumen} = 160 \text{ mmHg} \Rightarrow C_{LDL,adv} = 19 \text{ ‰} \cdot C_{LDLdep} \quad (A.13)$$

For intermediate cases, the value can be determined by interpolating between the previous values. For example, for the case of 100 mmHg, $C_{LDL,adv}$ will be equal to $11.6 \text{ ‰} \cdot C_{LDLdep}$.

- $C_{SSMC,w}^{th}$: Smooth muscle cell threshold. $4.764 \cdot 10^{13} \frac{SSMC}{m^3}$. Table 1, Tracy (1997): Average of density of intimal smooth muscle cells: $16.2 \frac{SSMC}{10000 \mu m^2}$. Therefore, dividing by the thickness the coronary artery (0.34mm), the threshold of SSMCs can be obtained.
Range of variation in the literature: $4.212 \cdot 10^{12} \frac{SSMC}{m^3}$ (Zahedmanesh et al., 2014) - $4.764 \cdot 10^{13} \frac{SSMC}{m^3}$ (Tracy, 1997).

A.4.3 Lumen-Arterial wall flows

- C_{LDLdep} : Concentration of LDL deposited at the endothelium. $10^{-2} \cdot C_{LDL,l}$ (Figure 1.a, Meyer et al. (1996)).
- m_r : Monocyte recruitment. It is dependent on the radius of the considered artery. According to Steinberg et al. (1997), Figure 2, the 90 % of all the monocytes contained in blood flow passes from the lumen into the arterial wall in 72 h. Therefore, the 30 % of them are deposited into the arterial wall in a day. Equally to LDL, monocyte flow through the arterial wall is dependent on the mechanical stimulus, and has to accomplish (Cilla, 2013):

$$\frac{\frac{m_r}{1 + \frac{WSS}{WSS_0}}}{Unit\ Surface} = 0.3 \frac{m^3}{mol_{oxLDL} \cdot day}, \quad (A.14)$$

being the unit surface equal to:

$$Unit\ Surface = \frac{\pi \cdot R^2 \cdot dh}{2 \cdot \pi \cdot R \cdot dh} = \frac{R}{2} \quad (A.15)$$

and assuming $WSS = WSS_0$.

It can be seen than m_r is dependent on the radius of the considered artery. Therefore, its value will be different for coronary and carotid arteries, for example. It takes a value of $6.636 \cdot 10^{-4} \frac{m^4}{mol_{oxLDL} \cdot day}$ for carotid arteries, for example, considering as the radius the mean radius of all the pathological carotid arteries in Chapter 4.

- WSS_0 : Reference WSS. It is dependent on the considered artery. It is estimated as the half of the maximum WSS that allows monocyte flow through the endothelium, to correctly determine the sigmoid of the function $J_{s,m}$. For example, for the case of carotid arteries, the maximum WSS that allows monocyte flow is 2 Pa. Therefore, the value of WSS_0 will be 1 Pa.

A.4.4 Parameters of reactive terms

- C_r : Cytokine production. $3 \cdot 10^{-10} \frac{mol_C \cdot m^3}{mol_{oxLDL} \cdot Macrophage \cdot s}$ (Table 1, Cilla et al. (2013)).
- d_c : Cytokine degradation. $2.3148 \cdot 10^{-5} s^{-1}$. The hundred percent of all the cytokines present in a culture are degraded in the first 12h (Figure 2.A, Zhao et al. (2005)):

$$d_c = \frac{\frac{100}{100}}{12h \cdot 3600 \frac{s}{h}} = 2.3148 \cdot 10^{-5} s^{-1} \quad (A.16)$$

Range of variation in the literature: $1.1574 \cdot 10^{-5} s^{-1} - 3.27 \cdot 10^{-5} s^{-1}$ (Zhao et al., 2005).

- d_{Cg} : Collagen degradation. $\frac{1}{30} d^{-1}$. Figure 9.4 shows the time course (in days) of $g(s)$ and $q(s)$ for the case of a 15-day half-life, (Humphrey (2002), p. 518).

$$d_g = \frac{1}{15 \cdot 2} d^{-1} \quad (A.17)$$

- d_{LDL} : LDL oxidation frequency. $2.85 \cdot 10^{-4} s^{-1}$ (Ai and Vafai (2006), Table 2).
Range of variation in the literature: $2.85 \cdot 10^{-4} s^{-1}$ (Ai and Vafai, 2006) - $3.55 \cdot 10^{-4} s^{-1}$ (?).
- d_m : Monocyte differentiation frequency. $1.15 \cdot 10^{-6} s^{-1}$ (Bulelzai and Dubbeldam (2012), Table 1).
- G_r : Collagen production. $2.472 \cdot 10^{-21} \frac{kg_{Cg}}{SSMC \cdot s}$ (Table 2, Zahedmanesh et al. (2014)).
- k_c : Citokine threshold factor. 0.65093. Estimated. It has been determined for the improvements of the equations, and it is explained in Section 2.8 of Chapter 2.
- $LDL_{ox,r}$: Oxidised LDL uptake. $2.45 \cdot 10^{-23} \frac{m^3}{Macrophage \cdot s}$. Figure 5.A, Zhao et al. (2006):
LDL uptaken by a cell protein in 24 h is equal to $180 \frac{\mu g LDL}{mg cell prot.}$. Knowing LDL density and that 10^6 macrophages are approximately $25 \cdot 10^{-9} kg$ of cell proteins (Since $25 \mu g$ of cell protein corresponds to $2 \cdot 10^6$ 24-hr old macrophages by direct cell counts, Steinman and Cohn (1972), p. 192):

$$LDL_{ox,r} = \frac{180 \frac{\mu g LDL}{mg cell prot.}}{24h} \cdot \frac{1}{\rho_{LDL}} \cdot \frac{25 \cdot 10^{-9} kg cell prot.}{2 \cdot 10^6 macr.} = 2.45 \cdot 10^{-23} \frac{m^3}{Macrophage \cdot s} \quad (A.18)$$

Range of variation in the literature: $1.837 \cdot 10^{-24} - 2.45 \cdot 10^{-23} \frac{m^3}{Macrophage \cdot s}$ (Zhao et al., 2006); $2.259 \cdot 10^{-24} - 1.413 \cdot 10^{-23} \frac{m^3}{Macrophage \cdot s}$ (Kruth et al., 2002).

- Macrophage ingest capacity: 1.44 times their radius. *The calculated phagocytic capacity of $19.8 \mu m$ indicates that those cells are capable of ingesting particles 1.44 times their diameter, or 3 times their volume.* (Cannon and Swanson (1992), p. 909).
- m_d : Monocyte natural death frequency. $\frac{1}{60} d^{-1}$. Monocyte lifespan goes from 30 days to 90 days. Taking the mean value of 60 days, monocyte natural death frequency is equal to $\frac{1}{60} d^{-1}$ (Krstic, 1997).
Range of variation in the literature: $\frac{1}{30} - \frac{1}{90} d^{-1}$ (Krstic, 1997)
- n_{FC} : Maximum oxidised LDL uptake. $2.72 \cdot 10^{-11} \frac{mol_{oxLDL}}{Macrophage}$. It is estimated knowing that the radius of a macrophage is $10.6 \mu m$ (Table 2, Krombach et al. (1997)), and assuming that the radius of a foam cell is equal to 1.44 times a macrophage radius (*The calculated phagocytic capacity of $19.8 \mu m$ indicates that those cells are capable of ingesting particles 1.44 times their diameter, or 3 times their volume.*, Cannon and Swanson (1992), p. 909). Therefore, the radius of a foam cell is equal to $15.264 \mu m$. Knowing the previous radius and assuming that both, macrophages and foam cells are spheres

and that their change of volume is due to the oxidised LDL that is phagocytosed, it is possible to determine the volume of LDL that macrophages ingest by subtracting the volume of macrophages to the volume of foam cells, obtaining that a single macrophage can ingest a volume of oxidised LDL equal to $9907.9 \mu m^3$.

Then, it is possible to determine the total quantity of oxidised LDL that a macrophage can ingest, multiplying the volume of oxidised LDL by oxidised LDL density and dividing by its molar weight (assuming that both are equal to LDL ones due to their similar properties):

$$n_{FC} = \frac{v_{oxLDL} \cdot \rho_{oxLDL}}{Mw_{oxLDL}} = 2.72 \cdot 10^{-11} \frac{mol_{oxLDL}}{Macrophage} \quad (A.19)$$

Range of variation in the literature: $1.372 \cdot 10^{-11} - 4.096 \cdot 10^{-11} \frac{mol_{oxLDL}}{Macrophage}$ (Cannon and Swanson, 1992).

- p_{ss} : SSMCs proliferation. $0.24 d^{-1}$ (Table 2, Boyle et al. (2011)).
Range of variation in the literature: $0.0202 d^{-1}$ (Budu-Grajdeanu et al., 2008) - $0.24 d^{-1}$ (Boyle et al., 2011).
- r_{apop} : SSMC apoptosis rate. $0.087 d^{-1}$. *In contrast, plaque-derived cells showed a significantly higher rate of spontaneous cell death in 20 % FCs over 24 h ($8.7 \pm 1.8 \%$)* (Bennett et al. (1995), p. 2269).
Range of variation in the literature: $0.04 - 0.168 d^{-1}$ (Bennett et al., 1995); $1.999 \cdot 10^{-3} - 1.69 \cdot 10^{-2}$ (Kockx et al., 1996).
- S_r : SMCs differentiation. $0.0036 d^{-1}$ (Table 1, Cilla et al. (2013)).

A.4.5 Conversion parameters

In the case of some terms of the equations of the inflammatory process, some conversion parameters are necessary to define that a substance becomes another one:

- $k_{(LDL-oxLDL)}$: Conversion parameter for LDL oxidation into oxLDL. $1 \frac{mol_{oxLDL}}{mol_{LDL}}$. Estimated.
- $k_{(M-FC)}$: Conversion parameter for macrophage death into foam cell. $1 \frac{SSMC}{CSMC}$. Estimated.
- $k_{(m-M)}$: Conversion parameter for monocyte differentiation into macrophage. $1 \frac{Macrophage}{Monocyte}$. Estimated.
- $k_{(SMC)}$: Conversion parameter for CSMC differentiation into SSMC. $1 \frac{SSMC}{CSMC}$. Estimated.

A.5 Arterial wall mechanical model

- K_w : Initial compression modulus of the arterial wall. $4.46 \cdot 10^4 \text{ Pa}$. [Laita \(2019\)](#).

Table A.2 contains the analysed values of K_w and the volumetric variation obtained for each one of them.

Initial compression modulus $K_w \text{ (Pa)}$	Volumetric Variation $J \text{ (-)}$
$4.46 \cdot 10^8$	1
$4.46 \cdot 10^6$	1
$4.46 \cdot 10^5$	0.981
$4.46 \cdot 10^4$	0.907
$4.46 \cdot 10^3$	0.839
$4.46 \cdot 10^2$	0.826

Table A.2: Arterial wall compressibility analysis ([Laita, 2019](#)).

A.6 Plaque growth

Finally, the parameters that are necessary to compute the plaque growth in the arterial wall are:

- l_{SSMC} : SMCs length. $115 \mu m$ ([Cilla et al., 2013](#)).
Range of variation in the literature: $30 - 200 \mu m$ ([Cilla et al., 2013](#)).
- R_{FC} : Foam cell radius. $15.264 \mu m$. The radius of a macrophage is $10.6 \mu m$ (Table 2, [Krombach et al. \(1997\)](#)). Assuming that the radius of a foam cell is equal to 1.44 times a macrophage radius (*The calculated phagocytic capacity of $19.8 \mu m$ indicates that those cells are capable of ingesting particles 1.44 times their radius, or 3 times their volume.*, [Cannon and Swanson \(1992\)](#), p. 909). The radius of a foam cell is equal to $15.12 \mu m$.
- R_{SSMC} : SMCs radius. $3.75 \mu m$. p. 286, [Cilla et al. \(2013\)](#).
Range of variation in the literature: $2.5 - 5 \mu m$. ([Cilla et al., 2013](#)).
- ρ_{Cg} : Collagen density. $1000 \frac{kg}{m^3}$. Table 3, [Sáez et al. \(2013\)](#).



Appendix B

Darcy's law for plasma flow

Appendix B

Darcy's law for plasma flow

Brinkman's equation is commonly used to determine the flow through a permeable media:

$$\mathbf{u}_p = -\frac{k_w}{\mu_p} [\nabla P_p - \rho_p \cdot g] + k_w \cdot \left[\frac{\mu_w}{\mu_p} \right] \nabla^2 \mathbf{u}_p, \quad (\text{B.1})$$

where \mathbf{u}_p , P_p , ρ_p and μ_p are, respectively, the velocity, pressure, density and dynamic viscosity of plasma. k_w is the Darcy permeability of the arterial wall while μ_w is its effective viscosity. Finally, g is the gravitational constant.

The last term of Equation B.1 represents viscous transport between the plasma and the arterial wall, which is considered as negligible due to the small pore area of the arterial wall. Therefore, the Brinkman's equation can be written as:

$$\mathbf{u}_p = -\frac{k_w}{\mu_p} [\nabla P_p - \rho_p \cdot g] \quad (\text{B.2})$$

Equation B.2, is known as Darcy's law for flow across porous media. It represents a linear relation between the velocity of a flow in a porous media with its pressure and the gravitational forces. However, since the circulatory system is pressurised, the gravitational forces term can be neglected. Therefore, Darcy's law can be rewritten as follows:

$$\mathbf{u}_p = -\frac{k_w}{\mu_p} \nabla P_p, \quad (\text{B.3})$$

These assumptions of Darcy's law are only valid for cases of saturated and continuous media with Reynolds number lower than 10. In this appendix, the Reynolds number of plasma flow across the endothelium will be determined to check if Darcy's law can be applied.

Reynolds number is defined as:

$$Re = \frac{\rho \cdot u \cdot D_H}{\mu}, \quad (\text{B.4})$$

where ρ and μ are, respectively, the density and dynamic viscosity of the fluid. u is the velocity of the flow, and D_H is the hydraulic diameter in which the fluid flows.

For the case of plasma, the density and hydraulic viscosity are $1050 \frac{kg}{m^3}$ and $0.001 Pa \cdot s$, respectively (Milnor, 1989).

The value of plasma flow velocity across the endothelium will be determined using experimental data of Tedgui and Lever (1984). They obtained plasma flow filtration velocities in the range of $2.80 \cdot 10^{-6} \frac{cm}{s}$ to $4.39 \cdot 10^{-6} \frac{cm}{s}$. As can be seen, an increase in the velocity of the flow will produce an increase in the Reynolds number. Therefore, as the Darcy's law can be applied if Reynolds number is lower than 10, only the worst case will be calculated, which corresponds to the highest filtration velocity.

On the other hand, the arterial wall is porous so, as commented in Section 2.3, plasma flow across the endothelium obeys the three-pore model (plasma can flow through normal junctions, leaky junctions and vesicular pathways). As explained, the plasma flow through vesicular pathways is considered negligible, and, due to leaky junctions are bigger than the normal ones, the more quantity of plasma flow occurs through leaky junctions. Therefore, the Reynolds number will be calculated for the case of a leaky junction, which will cause the higher Reynolds value.

The hydraulic diameter is defined as:

$$D_H = \frac{4 \cdot T_A}{W_p}, \quad (B.5)$$

where T_A and W_p are, respectively, the transversal area of the flow and the wetted perimeter of the transversal area.

The leaky junctions, as explained in Chapter 2 are considered as ring shaped. Therefore, the transversal area of the ring can be calculated as:

$$T_A = \pi \cdot (R_o^2 - R_i^2), \quad (B.6)$$

being R_o and R_i the external and internal radius of the ring, respectively.

The wetted perimeter of the ring will be:

$$W_p = 2 \cdot \pi \cdot (R_o - R_i) \quad (B.7)$$

Therefore:

$$D_H = \frac{4 \cdot (\pi \cdot (R_o^2 - R_i^2))}{2 \cdot \pi \cdot (R_o - R_i)} = 2 \cdot (R_o + R_i) \quad (B.8)$$

According to Figure 2.5 of this thesis, the internal radius of a leaky junction is equal to R_{cell} , while the external one can be calculated as $R_{cell} + 2w_l$. Thus, the hydraulic diameter of a leaky junction can be calculated as:

$$D_H = 2 \cdot (R_{cell} + 2w_l - R_{cell}) = 4 \cdot w_l, \quad (B.9)$$

and the Reynolds number is

$$Re = \frac{\rho_p \cdot u_p \cdot 4 \cdot w_l}{\mu_p} \quad (\text{B.10})$$

For the case of the maximum velocity determined experimentally (Tedgui and Lever, 1984), the Reynolds number is:

$$Re = \frac{1050 \frac{kg}{m^3} \cdot 4.39 \cdot 10^{-8} \frac{m}{s} \cdot 4 \cdot 20 \cdot 10^{-9} m}{0.001 Pa \cdot s} = 3.68 \cdot 10^{-9} \quad (\text{B.11})$$

Therefore, Darcy's law can be applied for the determination of plasma flow across the arterial wall.



Bibliography

Bibliography

- Ai, L. and Vafai, K. (2006). A coupling model for macromolecule transport in a stenosed arterial wall. *International Journal of Heat and Mass Transfer*, 49(9-10):1568–1591.
- Alimohammadi, M., Pichardo-Almarza, C., Agu, O., and Díaz-Zuccarini, V. (2017). A multiscale modelling approach to understand atherosclerosis formation: A patient-specific case study in the aortic bifurcation. *Proceedings of the Institution of Mechanical Engineers, Part H: Journal of Engineering in Medicine*, 231(5):378–390.
- Arshad, M., Ghim, M., Mohamied, Y., Sherwin, S. J., and Weinberg, P. D. (2020). Endothelial cells do not align with the mean wall shear stress vector. *Journal of the Royal Society Interface*, 18:20200772.
- Bennett, M. R., Evan, G. ., and Schwartz, S. M. (1995). Apoptosis of human vascular smooth muscle cells derived from normal vessels and coronary atherosclerotic plaques. *Journal of Clinical Investigation*, 95(5):2266–2274.
- Bhui, R. and Hayenga, H. N. (2017). An agent-based model of leukocyte transendothelial migration during atherogenesis. *PLoS Computational Biology*, 13(5):1–23.
- Boyle, C. J., Lennon, A. B., and Prendergast, P. J. (2011). In silico prediction of the mechano-biological response of arterial tissue: Application to angioplasty and stenting. *Journal of Biomechanical Engineering*, 133(8):1–10.
- Budu-Grajdeanu, P., Schugart, R. C., Friedman, A., Valentine, C., Agarwal, A. K., and Rovin, B. H. (2008). A mathematical model of venous neointimal hyperplasia formation. *Theoretical Biology and Medical Modelling*, 5:1–9.
- Bulelzai, M. A. K. and Dubbeldam, J. L. A. (2012). Long time evolution of atherosclerotic plaques. *Journal of Theoretical Biology*, 297:1–10.
- Calvez, V., Ebde, A., Meunier, N., and Raoult, A. (2009). Mathematical modelling of the atherosclerotic plaque formation. *European Series In Applied and Industrial Mathematics: Proceedings*, 28:1–12.
- Cancel, L. M., Fitting, A., and Tarbell, J. M. (2007). In vitro study of LDL transport under pressurized (convective) conditions. *American Journal of Physiology - Heart and Circulatory Physiology*, 293(1):126–132.

- Cannon, G. J. and Swanson, J. A. (1992). The macrophage capacity for phagocytosis. *Journal of Cell Science*, 101(4):907–913.
- Caro, C., Pedley, T., Schroter, R., and Seed, W. (1978). The mechanics of the circulation. Oxford University Press. Oxford.
- Cebollero-Burgués, M. (2017). Modelo computacional acoplado de la expansión mecánica de dispositivos intravasculares y liberación de fármaco asociada. *Master Thesis, University of Zaragoza, Spain*.
- Chien, S. (2003). Molecular and mechanical bases of focal lipid accumulation in arterial wall. *Progress in Biophysics and Molecular Biology*, 83(2):131–151.
- Chien, S. (2008). Effects of Disturbed Flow on Endothelial Cells. *Annals of Biomedical Engineering*, 36(4):554–562.
- Chung, S. and Vafai, K. (2012). Effect of the fluid–structure interactions on low-density lipoprotein transport within a multi-layered arterial wall. *Journal of Biomechanics*, (45):371–381.
- Cilla, M. (2013). Mechanical effects on the atheroma plaque appearance, growth and vulnerability. *PhD Thesis, University of Zaragoza, Spain*.
- Cilla, M., Martínez, M. A., and Peña, E. (2015). Effect of Transmural Transport Properties on Atheroma Plaque Formation and Development. *Annals of Biomedical Engineering*, 43(7):1516–1530.
- Cilla, M., Peña, E., and Martínez, M. A. (2013). Mathematical modelling of atheroma plaque formation and development in coronary arteries. *Journal of the Royal Society Interface*, 11(90):20130866.
- Corti, A., Chiastra, C., Colombo, M., Garbey, M., Migliavaca, F., and Casarin, S. (2020). A fully coupled computational fluid dynamics - agentn based model of atherosclerotic plaque development: multiscale modeling framework and parameter sensitivity analysis. *Computers in Biology and Medicine*, 118:103623.
- Curry, F. E. (1974). A hydrodynamic description of the osmotic reflection coefficient with application to the pore theory of transcapillary exchange. *Microvascular Research*, 8(2):236–252.
- Curtiss, C. F. and Hirschgelder, J. O. (1952). Integration of stiff equations. *Proceedings of the National Academy of Sciences*, 38(3):235–243.
- Dabagh, M., Jalali, P., and Tarbell, J. M. (2009). The transport of LDL across the deformable arterial wall: The effect of endothelial cell turnover and intimal deformation under hypertension. *American Journal of Physiology - Heart and Circulatory Physiology*, 297(3):983–996.

- Dai, G. H., Kaazempur-Mofrad, M. R., Natarajan, S., Zhang, Y. Z., Vaughn, S., Blackman, B. R., Kamm, R. D., Garcia-Gardena, G., and Gimbrone, M. A. (2004). Distinct endothelial phenotypes evoked by arterial waveforms derived from atherosclerosis-susceptible and -resistant regions of human vasculature. *Proceedings of the National Academy of Sciences of the United States of America*, (101):14871–14876.
- De Bruyne, B., Pijls, N. H. J., Heyndrickx, G. R., Hodeige, D., Kirkeeide, R. L., and Gould, K. L. (2000). Pressure-derived fractional flow reserve to assess serial epicardial stenoses: theoretical basis and animal validation. *Circulation*, 101(15):1840–7.
- Deyranlou, A., Niazmand, H., and Sadeghi, M. R. (2015). Low-density lipoprotein accumulation within a carotid artery with multilayer elastic porous wall: Fluid-structure interaction and non-Newtonian considerations. *Journal of Biomechanics*, 48(12):2948–2959.
- Díaz-Zuccarini, V., Di Tomaso, G., Agu, O., and Pichardo-Almarza, C. (2014). Towards personalised management of atherosclerosis via computational models in vascular clinics: Technology based on patient-specific simulation approach. *Healthcare Technology Letters*, 1(1):13–18.
- Escuer, J., Martínez, M. A., McGinty, S., and Peña, E. (2019). Mathematical modelling of the restenosis process after stent implantation. *Journal of The Royal Society Interface*, 16(157):20190313.
- Filipovic, N. (2010). Computer Simulation of Plaque Formation and Development in the Cardiovascular Vessels, Chapter 5. *New Trends in Technologies: Devices, Computer, Communication and Industrial Systems, IntechOpen, Rijeka*. Editor: Meng Joo Er.
- Filipovic, N., Teng, Z., Radovic, M., Saveljic, I., Fotiadis, D., and Parodi, O. (2013). Computer simulation of three-dimensional plaque formation and progression in the carotid artery. *Medical and Biological Engineering and Computing*, 51(6):607–616.
- Fok, P.-W. (2012). Mathematical model of intimal thickening in atherosclerosis: Vessel stenosis as a free boundary problem. *Journal of Theoretical Biology*, (314):23–33.
- Fung, Y. C. (1997). *Biomechanics circulation*. Springer Science+Business media.
- Fuster, V., Moreno, P. R., Fayad, Z. A., Corti, R., and Badimon, J. J. (2005). Atherothrombosis and high-risk plaque: Part I: Evolving concepts. *Journal of the American College of Cardiology*, 46(6):937–954.
- Gao, H., Long, Q., Graves, M., Gillard, J. H., and Li, Z. Y. (2009). Carotid arterial plaque stress analysis using fluid-structure interactive simulation based on in-vivo magnetic resonance images of four patients. *Journal of Biomechanics*, 42(10):1416–1423.
- Gear, C. W. (1967). The numerical integration of ordinary differential equations. *Mathematics of Computation*, 21(98):146–156.

- Gijssen, F. J., Wentzel, J. J., Thury, A., Mastik, F., Schaar, J. A., Schuurbijs, J. C., Slager, C. J., Van Der Giessen, W. J., De Feyter, P. J., Van Der Steen, A. F., and Serruys, P. W. (2008). Strain distribution over plaques in human coronary arteries relates to shear stress. *American Journal of Physiology - Heart and Circulatory Physiology*, 295(4):1608–1614.
- Glagov, S., Weisenberg, E., Zarins, C. K., Stankunavicius, R., and Kolettis, G. J. (1978). Compensatory enlargement of human atherosclerotic coronary arteries. *New England Journal of Medicine*, (316):1371–1375.
- Gray, H. (1918). *Anatomy of the human body*. Philadelphia: Lea & Febiger, 1918; Bartleby.com, 2000.
- Guarino, A. J., Tulenko, T. N., and Wrenn, S. P. (2006). Sphingomyelinase-to-LDL molar ratio determines low density lipoprotein aggregation size: biological significance. *Chemistry and Physics of Lipids*, 142(1-2):33–42.
- Holzapfel, G. A., Gasser, T. C., and Ogden, R. W. (2000). A new constitutive framework for arterial wall mechanics and a comparative study of material models. *Journal of Elasticity*, (61):1–48.
- Huang, Y., Rumschitzki, D., Chien, S., and Weinbaum, S. (1994). A fiber matrix model for the growth of macromolecular leakage spots in the arterial intima. *Journal of Biomechanical Engineering*, 116(4):430–445.
- Huang, Z. J. and Tarbell, J. M. (1997). Numerical simulation of mass transfer in porous media of blood vessel walls. *American Journal of Physiology - Heart and Circulatory Physiology*, 273(1 42-1).
- Humphrey, J. D. (2002). *Cardiovascular solid mechanics: Cells, tissues and organs*. Springer-Verlag, New York.
- Insull, W. (2009). The pathology of atherosclerosis: Plaque development and plaque responses to medical treatment. *American Journal of Medicine*, 122(1 SUPPL.):S3–S14.
- Ivanova, E. A., Myasoedova, V. A., Melnichenko, A. A., Grechko, A. V., and Orekhov, A. N. (2017). Small dense low-density lipoprotein as biomarker for atherosclerotic diseases. *Oxidative Medicine and Cellular Longevity*, 2017:1273042.
- Kedem, O. and Katchalsky, A. (1958). The conventional description of transport through membranes makes use of two equations, one for solute flow and one for volume flow. Consider an isothermal system. *Biochimica et Biophysica Acta*, 27(2):229–246.
- Kenjereš, S. and De Loor, A. (2014). Modelling and simulation of low-density lipoprotein transport through multi-layered wall of an anatomically realistic carotid artery bifurcation. *Journal of the Royal Society Interface*, 11:20130941.
- Khan, F. H. (2009). *The elements of immunology*. Pearson Education India.

- Kock, S. A., Nygaard, J. V., Eldrup, N., Fründ, E. T., Klærke, A., Paaske, W. P., Falk, E., and Yong Kim, W. (2008). Mechanical stresses in carotid plaques using MRI-based fluid-structure interaction models. *Journal of Biomechanics*, 41(8):1651–1658.
- Kockx, M. M., Muhring, J., Bortier, H., De Meyer, G. R. Y., and Jacob, W. (1996). Biotin- or digoxigenin-conjugated nucleotides bind to matrix vesicles in atherosclerotic plaques. *American Journal of Pathology*, 148(6):1771–1777.
- Krombach, F., Münzing, S., Allmeling, A. M., Gerlach, J. T., Behr, J., and Dörger, M. (1997). Cell size of alveolar macrophages: an interspecies comparison. *Environmental Health Perspectives*, 105(5):1261–1263.
- Krstic, R. V. (1997). Human microscopic anatomy: an atlas for students of medicine and biology. Berlin, Germany: Springer.
- Kruth, H. S., Huang, W., Ishii, I., and Zhang, W. Y. (2002). Macrophage foam cell formation with native low density lipoprotein. *Journal of Biological Chemistry*, 277(37):34573–34580.
- Laita, N. (2019). Mechanobiological model to the study the mechanical effect on the atheroma plaque formation and its application to the high blood pressure disease. *Master Thesis, University of Zaragoza, Spain*.
- Le Floc'h, S., Ohayon, J., Tracqui, P., Finet, G., Gharib, A. M., Maurice, R. L., Cloutier, G., and Pettigrew, R. I. (2009). Vulnerable atherosclerotic plaque elasticity reconstruction based on a segmentation-driven optimization procedure using strain measurements: Theoretical framework. *IEEE Transactions on Medical Imaging*, 28(7):1126–1137.
- Levesque, M. J., Liepsch, D., Moravec, S., and Nerem, R. M. (1986). Correlation of endothelial cell shape and wall shear stress in a stenosed dog aorta. *American Heart Association Journals*, 6:220–229.
- Libby, P. (2021). Inflammation during the life cycle of the atherosclerotic plaque. *Cardiovascular research*, 117(13):2525–2536.
- Libby, P., Ridker, P. M., and Hansson, G. K. (2011). Progress and challenges in translating the biology of atherosclerosis. *Nature*, 473(7347):317–325.
- Libby, P. and Theroux, P. (2005). Pathophysiology of coronary artery disease. *Circulation*, 111(25):3481–3488.
- Lin, S. J., Jan, K. M., Weinbaum, S., and Chien, S. (1989). Transendothelial transport of low density lipoprotein in association with cell mitosis in rat aorta. *Arteriosclerosis*, 9(2):230–236.
- Malek, A. M. and Alper, S. L. (1999). Hemodynamic shear stress and its role in atherosclerosis. *Stress: The International Journal on the Biology of Stress*, 282(21):2035–2042.

- Malvè, M., Chandra, S., García, A., Mena, A., Martínez, M. A., Finol, E. A., and Doblaré, M. (2014). Impedance-based outflow boundary conditions for human carotid haemodynamics. *Computer Methods in Biomechanics and Biomedical Engineering*, 17(11):1248–1260.
- Mathew, J., Sankar, P., and Matthew, V. (2022). Physiology, Blood Plasma. StatPearls Publishing.
- Meyer, G., Merval, R., and Tedgui, A. (1996). Effects of pressure-induced stretch and convection on low-density lipoprotein and albumin uptake in the rabbit aortic wall. *Circulation Research*, 79(3):532–540.
- Milnor, W. R. (1989). Hemodynamics. 2nd Edition. Williams and Wilkins, Baltimore, MD.
- Morbiducci, U., Mazzi, V., Domanin, M., Nisco, G. D., Vergara, C., Steinman, D. A., and Gallo, D. (2020). Wall shear stress topological skeleton independently predicts long-term restenosis after carotid bifurcation endarterectomy. *Annals of Biomedical Engineering*, 48:2936–2949.
- MUMPS (1999). Project PARASOL, CERFACs, IRIT-ENSEEIH and RAL, <https://panua.ch/products/pardiso/>.
- Nolan, D. R. and McGarry, J. P. (2016). On the Compressibility of Arterial Tissue. *Annals of Biomedical Engineering*, 44(4):993–1007.
- Ogunrinade, O., Kameya, G. T., and Truskey, G. A. (2002). Effect of fluid shear stress on the permeability of the arterial endothelium. *Annals of Biomedical Engineering*, 30:430–446.
- Ohayon, J., Gharib, A. M., Garcia, A., Heroux, J., Yazdani, S. K., Malvè, M., Tracqui, P., Martinez, M. A., Doblaré, M., Finet, G., and Pettigrew, R. I. (2011). Is arterial wall-strain stiffening an additional process responsible for atherosclerosis in coronary bifurcations?: An in vivo study based on dynamic CT and MRI. *American Journal of Physiology - Heart and Circulatory Physiology*, 301(3).
- Olgac, U., Kurtcuoglu, V., and Poulikakos, D. (2008). Computational modeling of coupled blood-wall mass transport of LDL: Effects of local wall shear stress. *American Journal of Physiology - Heart and Circulatory Physiology*, 294(2):909–919.
- Olivares, A. L., González Ballester, M. A., and Noailly, J. (2016). Virtual exploration of early stage atherosclerosis. *Bioinformatics*, 32(24):3798–3806.
- Pan, J., Cai, Y., Wang, L., Maehara, A., Mintz, G., Tang, D., and Li, Z. (2021). A prediction tool for plaque progression based on patient-specific multi-physical modeling. *PLoS Comput Biol*, 17(3):e1008344.
- PARDISO (2007). Panua Technologies, <https://panua.ch/products/pardiso/>.

- Patlak, C. S., Goldstein, D. A., and Hoffman, J. F. (1963). The flow of solute and solvent across a two-membrane system. *Journal of Theoretical Biology*, 3(5):426–442.
- Peiffer, V., Sherwin, S. J., and Weinberg, P. D. (2013). Computation in the rabbit aorta of a new metric - the transverse wall shear stress - to quantify the multidirectional character of disturbed blood flow. *Journal of Biomechanics*, 46:2651–2658.
- Perktold, K., Resch, M., and Florian, H. (1991). Pulsatile non-newtonian flow characteristics in a three-dimensional human carotid bifurcation model. *Journal of Biomechanical Engineering*, 113(4):464–75.
- Pijls, N. H. J., De Bruyne, B., Bech, G. J. W., Liistro, F., Heyndrickx, G. R., Bonnier, J. J. R. M., and Koolen, J. J. (2000). Coronary pressure measurement to assess the hemodynamic significance of serial stenosis within one coronary-artery: validation in humans. *Circulation*, 102(19):2371–7.
- Prosi, M., Zunino, P., Perktold, K., and Quarteroni, A. (2005). Mathematical and numerical models for transfer of low-density lipoproteins through the arterial walls: A new methodology for the model set up with applications to the study of disturbed luminal flow. *Journal of Biomechanics*, 38(4):903–917.
- Renkin, E. M. (1954). Filtration, diffusion, and molecular sieving through porous cellulose membranes. *The Journal of General Physiology*, 2(38):225–243.
- Saad, Y. and Schultz, M. H. (1986). GMRES: A generalized minimal residual algorithm for solving nonsymmetric linear systems. *SIAM Journal on Scientific and Statistical Computing*, 7:856–869.
- Sáez, P., Malvè, M., and Martínez, M. A. (2015). A theoretical model of the endothelial cell morphology due to different waveforms. *Journal of Theoretical Biology*, 379:16–23.
- Sáez, P., Peña, E., Ángel Martínez, M., and Kuhl, E. (2013). Mathematical modeling of collagen turnover in biological tissue. *Journal of Mathematical Biology*, 67(6-7):1765–1793.
- Siogkas, P., Sakellarios, A., Exarchos, T. P., Athanasiou, L., Karvounis, E., Stefanou, K., Fotiou, E., Fotiadis, D. I., Naka, K. K., Michalis, L. K., Filipovic, N., and Parodi, O. (2011). Multiscale - Patient-specific artery and atherogenesis models. *IEEE Transactions on Biomedical Engineering*, 58(12 PART 2):3464–3468.
- Sommer, G., Regitnig, P., Költringer, L., and Holzapfel, G. A. (2010). Biaxial mechanical properties of intact and layer-dissected human carotid arteries at physiological and supraphysiological loadings. *American Journal of Physiology - Heart and Circulatory Physiology*, 298(3):898–912.
- Steinberg, D., Khoo, J. C., Glass, C. K., Palinski, W., and Almazan, F. (1997). A new approach to determining the rates of recruitment of circulating leukocytes into tissues: Application

- to the measurement of leukocyte recruitment into atherosclerotic lesions. *Proceedings of the National Academy of Sciences of the United States of America*, 94(8):4040–4044.
- Steinman, R. M. and Cohn, Z. A. (1972). The interaction of particulate horseradish peroxidase (hrp)-anti hrp immune complexes with mouse peritoneal macrophages in vitro. *Journal of Cell Biology*, 55(3):616–634.
- Sun, N., Wood, N. B., Hughes, A. D., Thom, S. A., and Xu, X. Y. (2007). Effects of transmural pressure and wall shear stress on LDL accumulation in the arterial wall: A numerical study using a multilayered model. *American Journal of Physiology - Heart and Circulatory Physiology*, 292(6):3148–3157.
- Tang, D., Yang, C., Mondal, S., Liu, F., Canton, G., Hatsukami, T. S., and Yuan, C. (2008). A negative correlation between human carotid atherosclerotic plaque progression and plaque wall stress: In vivo MRI-based 2D/3D FSI models. *Journal of Biomechanics*, 41(4):727–736.
- Tarbell, J. M. (2003). Mass Transport in Arteries and the Localization of Atherosclerosis. *Annual Review of Biomedical Engineering*, 5(1):79–118.
- Tedgui, A. and Lever, M. J. (1984). Filtration through damaged and undamaged rabbit thoracic aorta. *American Journal of Physiology-Heart and Circulatory Physiology*, (247):784–791.
- Tomaso, G. D., Daz-Zuccarini, V., and Pichardo-Almarza, C. (2011). A multiscale model of atherosclerotic plaque formation at its early stage. *IEEE Transactions on Biomedical Engineering*, 58:3460–3463.
- Tracy, R. E. (1997). Declining density of intimal smooth muscle cells as a precondition for atheronecrosis in the coronary artery. *Virchows Archiv: European Journal of Pathology*, 430(2):155–162.
- Virmani, R., Burke, A. P., Farb, A., and Kolodgie, F. D. (2006). Pathology of the vulnerable plaque. *Journal of the American College of Cardiology*, 47(8, Supplement):C13–C18.
- Weinbaum, S., Tzeghai, G., Ganatos, P., Pfeffer, R., and Chien, S. (1985). Effect of cell turnover and leaky junctions on arterial macromolecular transport. *American Physiological Society*, (248):945–960.
- White, F. M. (1979). *Fluid Mechanics*, McGraw-Hill, New York.
- World Health Organisation (2019). <https://www.who.int/news-room/fact-sheets/detail/the-top-10-causes-of-death>.
- Yeoh, O. H. (1993). Some forms of the strain energy function for rubber. *Rubber Chemistry and Technology*, 66(5):754–771.

- Younis, H. F., Kaazempur-Mofrad, M. R., Chan, R. C., Isasi, A. G., Hinton, D. P., Chau, A. H., Kim, L. A., and Kamm, R. D. (2004). Hemodynamics and wall mechanics in human carotid bifurcation and its consequences for atherogenesis: Investigation of inter-individual variation. *Biomechanics and Modeling in Mechanobiology*, 3(1):17–32.
- Yuan, F., Chien, S., and Weinbaum, S. (1991). A new view of convective-diffusive transport processes in the arterial intima. *Journal of Biomechanical Engineering*, 113(3):314–329.
- Zahedmanesh, H., Van Oosterwyck, H., and Lally, C. (2014). A multi-scale mechanobiological model of in-stent restenosis: deciphering the role of matrix metalloproteinase and extracellular matrix changes. *Computer Methods in Biomechanics and Biomedical Engineering*, 17(8):813–828.
- Zhao, B., Li, Y., Buono, C., Waldo, S. W., Jones, N. L., Mori, M., and Kruth, H. S. (2006). Constitutive receptor-independent low density lipoprotein uptake and cholesterol accumulation by macrophages differentiated from human monocytes with macrophage-colony-stimulating factor (M-CSF). *Journal of Biological Chemistry*, 281(23):15757–15762.
- Zhao, S. Z., Ariff, B., Long, Q., Hughes, A. D., Thom, S. A., Stanton, A. V., and Xu, X. Y. (2002). Inter-individual variations in wall shear stress and mechanical stress distributions at the carotid artery bifurcation of healthy humans. *Journal of Biomechanics*, 35(10):1367–1377.
- Zhao, W., Oskeritzian, C. A., Pozez, A. L., and Schwartz, L. B. (2005). Cytokine production by skin-derived mast cells: Endogenous proteases are responsible for degradation of cytokines. *The Journal of Immunology*, 175(4):2635–2642.
- Zohdi, T. I., Holzapfel, G. A., and Berger, S. A. (2004). A phenomenological model for atherosclerotic plaque growth and rupture. *Journal of Theoretical Biology*, 227(3):437–443.



Universidad
Zaragoza